nagra.

TECHNICAL REPORT 24-20

Design and Performance Assessment of HLW Disposal Canisters

November 2024

Nagra | National Cooperative for the Disposal of Radioactive Waste
Hardstrasse 73 | 5430 Wettingen | Switzerland
T. +41 56 437 11 11 | info@nagra.ch | nagra.ch

nagra.

TECHNICAL REPORT 24-20

Design and Performance Assessment of HLW Disposal Canisters

November 2024

Nagra | **National Cooperative for the Disposal of Radioactive Waste**
Hardstrasse 73 | 5430 Wettingen | Switzerland
T. +41 56 437 11 11 | info@nagra.ch | nagra.ch

The report "Design and Performance Assessment of HLW Disposal Canisters" has been elaborated by a project team consisting of N. Diomidis[1], Y.J. Janin[2], M. Roy[2], R. Lunn[2], Ch. Schneider[2], T. Mitchell[2], K. Derekar[2], J. Nicholas[2], G. Schneider[2], St. Holdsworth[3] and F. King[4].

[1]Nagra
[2]TWI Ltd.
[3]EMPA
[4]Integrity Corrosion Consulting Ltd.

An earlier version of the report was reviewed by Satoru Suzuki, Yusuke Ogata and Shuhei Nagata (NUMO), and Peter G. Keech (NWMO). We are very grateful for their contributions to the improvement of the report.

ISSN 1015-2636

Abstract

Regulatory guidelines require the development and use of disposal canisters as an indispensable component of the multi-barrier system of a deep geological repository for high-level waste. The primary long-term safety function of the canisters is to provide complete containment of radionuclides for a certain period of time.

In this report, a potential method for manufacturing and sealing disposal canisters based on present day technology and satisfying all relevant requirements is presented. The provisional canister design consists of a cylinder with flat lids. Depending on the waste type to be disposed of the canisters are approximately 4 to 5 m long and have a diameter of approximately 0.7 to 1.1 m. The canisters are forged from a bespoke low carbon steel alloy. Both lids will be welded on the cylindrical body using electron beam welding. The bottom lid, which is welded prior to loading the canister with the waste, will undergo a global heat treatment in a furnace for stress relief. The top lid, which is attached with the closure weld to seal the canister after waste loading, will undergo a local heat treatment to relieve residual stresses. Both welds will be appropriately inspected for potential flaws using non-destructive examination methods.

The regulatory requirement for the canister lifetime during disposal is at least 1,000 years. The current provisional canister design was developed with the aim to demonstrate that this requirement can be satisfied with a significant safety margin. The prediction of the canister lifetime is based on the principle that the evolution of the repository is well understood, such that the behaviour of the canister material can be described, and the potential failure mechanisms can be assessed. The assessment of the structural integrity of the canister is achieved based on a standardised fracture mechanics methodology using a set of conservative assumptions, namely:

- the canister will have a reduced wall thickness, in accordance with a conservative corrosion rate,
- the canister material will exhibit a reduced fracture toughness, in accordance with conservative assumptions related to hydrogen embrittlement,
- the maximum anisotropic lithostatic stresses expected at repository depth act on the canister,
- the residual stresses calculated from the modelling of the weld process and the post-weld heat treatment are present in the weld region,
- and various types of weld flaws have escaped detection and are present in the weld.

Even based on these conservative assumptions, an engineering critical assessment approach demonstrates that the current provisional canister design can satisfy the regulatory lifetime requirement with a significant safety margin.

Zusammenfassung

Behördliche Anforderungen erfordern die Entwicklung und Nutzung von Endlagerbehältern als unverzichtbares Element des Mehrbarrierensystems eines geologischen Endlagers für hochradioaktiven Abfall. Die primäre Langzeitsicherheitsfunktion der Behälter besteht darin, über einen bestimmten Zeitraum, einen vollständigen Einschluss der Radionuklide zu gewährleisten.

In diesem Bericht wird eine mögliche Methode für Herstellung und Verschluss der Endlagerbehälter vorgestellt, die auf heutiger Technologie basiert und alle dafür relevanten Anforderungen erfüllt. Die Endlagerbehälter haben eine zylindrische Form mit flachen Deckeln. Je nach Abfalltyp sind die Behälter ca. 4 bis 5 m lang und haben einen Durchmesser von ca. 0,7 bis 1,1 m. Die Behälter werden aus einer spezifischen kohlenstoffarmen Stahllegierung geschmiedet und die beiden Deckel werden mithilfe des Elektronenstrahl-Schweissverfahrens an den zylindrischen Behälterkörper geschweisst. Der bodenseitige Deckel, der noch vor der Abfallbeladung an den Behälter geschweisst wird, wird zum Spannungsabbau einer umfassenden Wärmebehandlung in einem Ofen unterzogen. Der obere Deckel, der nach der Abfallbeladung mit einer Verschlussnaht an den Endlagerbehälter geschweisst wird, wird zum Abbau der Eigenspannungen lokal wärmebehandelt. Beide Schweissnähte werden mit zerstörungsfreien Prüfverfahren auf mögliche Mängel untersucht.

Die behördliche Anforderung an den Endlagerbehälter ist einen vollständigen Einschluss von mindestens 1,000 Jahren zu gewährleisten. Die derzeitige, beispielhafte Umsetzung wurde mit dem Ziel entwickelt, zu demonstrieren, dass diese Anforderung mit einer signifikanten Sicherheitsmarge erfüllt werden kann. Die erwartete Entwicklung der Bedingungen im Tiefenlager ist hinreichend bekannt, sodass das Verhalten des Behältermaterials beschrieben und potenzielle Versagensmechanismen bewertet werden können. Der Nachweis der Erfüllung dieser Langzeitsicherheitsanforderung erfolgt auf der Grundlage eines standardisierten bruchmechanischen Prüfverfahrens unter Berücksichtigung einer Reihe konservativer Annahmen, spezifisch:

- sich die Wanddicke des Endlagerbehälters unter Berücksichtigung einer konservativen Korrosionsrate verringert haben wird,
- das Material des Endlagerbehälters gemäss konservativen Annahmen zur Wasserstoffversprödung eine geringere Bruchfestigkeit aufweisen wird,
- die auf Tiefenlagerebene zu erwartenden anisotropen lithostatischen Spannungen auf den Behälter einwirken,
- die residuale Eigenspannung, simuliert auf Basis der Modellierung des Schweissprozesses und der nachgängigen Wärmebehandlung, an der Schweissnaht vorhanden ist,
- und verschiedene Arten von Schweissdefekten nicht erkannt wurden und in der Schweissnaht vorhanden sein können.

Selbst auf der Grundlage dieser konservativen Annahmen zeigt ein ingenieurtechnisches Bewertungsverfahren, dass der Endlagerbehälter die behördlichen Anforderungen mit grosser Sicherheitsmarge erfüllen wird.

Table of Contents

List of Tables

List of Figures

List of Acronyms

ATW	Alpha-toxic waste
b.g.l.	Below ground level
BWR	Boiling water reactor
CE	Carbon equivalent
CP	Cathodic protection
CMIC	Chemical microbiologically influenced corrosion
CTOD	Crack tip opening displacement
DBA	Design by analysis
DBF	Design by formulae
EB	Electron-beam (welding)
ECA	Engineering critical assessment
ECAT	Eddy current array testing
EDZ	Excavation-damaged zone
ENSI	Swiss Federal Nuclear Safety Inspectorate (*Eidgenössisches Nuklearsicherheitsinspektorat*)
ET	Eddy current testing
FAD	Failure assessment diagram
FA	Fuel assembly
FEA	Finite element analysis
FE	Full-scale emplacement experiment (at the Mont Terri Rock Laboratory)
GBM	Granular bentonite material
GCB	Gradient control band
GTA	Gas tungsten arc (welding), also referred to as Tungsten inert gas (TIG) welding
HAZ	Heat affected zone
HB	Heat band
HLW	High-level waste (spent fuel assemblies and vitrified high-level waste from reprocessing)
IC-A	Iron corrosion experiment (at the Mont Terri Rock Laboratory)
ID	Inner diameter
JO	Jura Ost (siting region)
L/ILW	Low- and intermediate-level waste
LoF	Lack of fusion

LoP	Lack of penetration
MAG-S or -M	Metal active gas (welding) with a single- or multiple-filler wire
MIG	Metal inert gas (welding)
MPI	Magnetic particle inspection
NAB	Nagra Work Report (*Nagra Arbeitsbericht*)
NDT	Non-destructive testing
NG-TIG	Narrow gap tungsten inert gas (welding)
NL	Nördlich Lägern (siting region)
NNpH	Near-neutral pH
NTB	Nagra Technical Report (*Nagra Technischer Bericht*)
OD	Outer diameter
OPA	Opalinus Clay
PAUT	Phased array ultrasonic testing
PM	Parent material
POD	Probability of detection
PWHT	Post weld heat treatment
pWPS	Preliminary welding procedure specification
PWR	Pressurised water reactor
RBG	General license application (*Rahmenbewilligungsgesuch*)
RH	Relative humidity
RP-HLW	Vitrified high-level waste from reprocessing
RT	Radiographic testing
SAW-S or -M	Submerged arc welding, single- or multi-wire
SB	Soak band
SCC	Stress corrosion cracking
SF	Spent fuel
SGT	Sectoral Plan for Deep Geological Repositories (*Sachplan geologische Tiefenlager*)
SIF	Stress intensity factor
SRB	Sulphate-reducing bacteria
TIG-C or -H	Tungsten inert gas (welding), also referred to as GTA welding with cold or hot filler wire
TOFD	Time of flight diffraction
TRL	Technology readiness level

TWE	Through-wall extent
URL	Underground rock laboratory
UT	Ultrasonic testing
UTS	Ultimate tensile strength
VT	Visual testing
WRS	Weld residual stress
YS	Yield strength
Z	Reduction of area at fracture
ZNO	Zürich Nordost (siting region)
Zwilag	Zwischenlager Würenlingen AG

1 Introduction

1.1 Context

In Switzerland, legal regulations (Nuclear Energy Act (KEG 2003) and Nuclear Energy Ordinance (KEV 2004)) and guidelines are in place for the management of radioactive waste. The Nuclear Energy Ordinance classifies Switzerland's radioactive waste into low- and intermediate-level waste (L/ILW), alpha-toxic waste[1] (ATW), and high-level waste (HLW), the latter comprising spent fuel (SF) and vitrified HLW from reprocessing (RP-HLW). The Nuclear Energy Act requires the disposal of all these types of radioactive waste in deep geological repositories. The feasibility of this disposal solution has been demonstrated for L/ILW in Nagra (1985) and for long-lived intermediate-level waste and HLW in Nagra (2002).

The Sectoral Plan for Deep Geological Repositories (SGT) regulates the search for suitable siting regions for deep geological repositories in Switzerland. This site selection process is conducted in three stages (BFE 2008). Stages 1 and 2 have already been completed and Nagra is currently in Stage 3. Clarifications on the safety-related specifications for this stage are provided in ENSI 33/649 (ENSI 2018), while ENSI Guideline G03 and the corresponding explanatory report (ENSI 2020, ENSI 2023) specify the protection objective, protection criteria and design principles for deep geological repositories.

In Stage 3 of the Sectoral Plan, three siting regions located in Northern Switzerland have been considered – Jura Ost (JO), Nördlich Lägern (NL) and Zürich Nordost (ZNO) – with the objective of selecting one siting region for an HLW repository, one for an L/ILW repository, or one for a combined repository for all waste types.

Following a comparison of the three siting regions, Nagra concluded that NL is the safest and most flexible siting region. Therefore, it is applying for a general licence for a repository for both HLW and L/ILW, with surface facilities at the Haberstal site (minicipality of Stadel, ZH).

The justification for this selection and the safety demonstration for a repository at the site are submitted as part of the general licence application (RBG[2]). The reports that relate to post-closure safety, shown in Fig. 1-1, are structured as follows:

- The overall safety-related argumentation, including post-closure and operational safety, is summarised in an overarching safety report ("*Sicherheitsbericht*", NTB 24-01) (Nagra 2025b) shown at the top of Fig. 1-1.
- The upper left side of Fig. 1-1 shows the reports supporting Nagra's site comparison. The available options are compared with respect to safety and technical feasibility and the results are synthesised in NTB 24-03 ("*Bericht zur Begründung der Standortwahl*") (Nagra 2025a).
- The upper right side of Fig. 1-1 shows the reports documenting the post-closure safety case for the combined repository at the site, including its synthesis in the post-closure safety report, NTB 24-10 (Nagra 2024e).
- The lower part of Fig. 1-1 shows the report that presents the safety and repository concept, including the provisional design, NAB 24-18 (Nagra 2024i), and reports which provide the assessment basis.

The present report is highlighted in Fig. 1-1 with a red box and is part of the assessment basis.

---

[1] According to Nagra (2024a), ATW can coexist with L/ILW within the same emplacement caverns. As a result, for the sake of simplicity, the term L/ILW encompasses ATW without explicit mention.

[2] From the German term *Rahmenbewilligungsgesuch.*

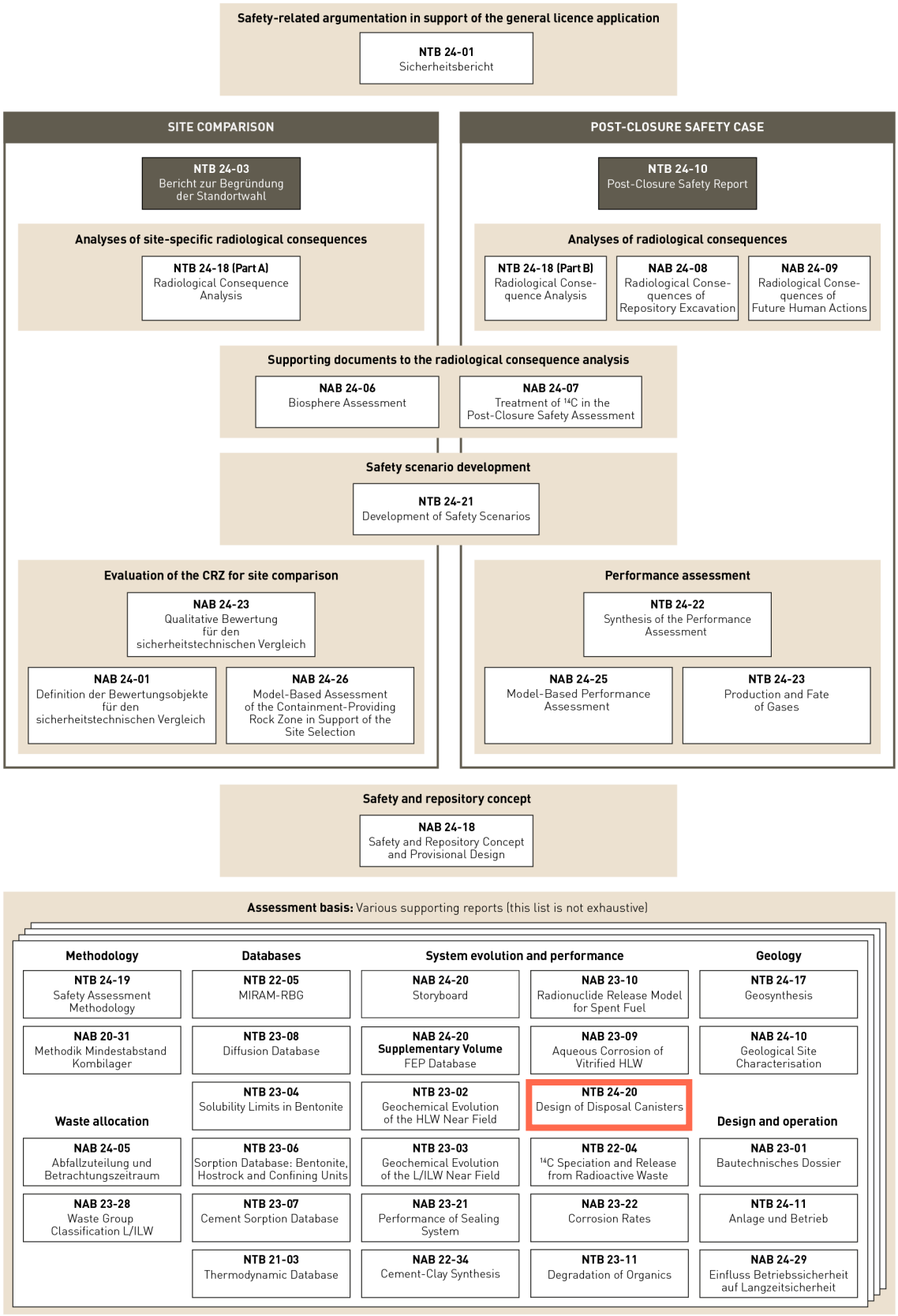

Fig. 1-1: Structure of reports covering post-closure safety aspects of the site comparison and the post-closure safety case

1.2 Scope of the report

The main objectives of this report are:

- to demonstrate the feasibility of manufacturing HLW disposal canisters using present-day technology,
- and to demonstrate that the current provisional design can satisfy the regulatory requirement on canister lifetime (at least 1,000 years) in a deep geological repository according to the Swiss disposal concept.

This report is an update and refinement of Patel et al. (2012). The scope is similar to that of the earlier report and focuses on the provisional canister design, fabrication, and structural performance. Much of the information on corrosion is available elsewhere, e.g., King (2008), Diomidis et al. (2023), Hesketh et al. (2023). Only brief details are given here, with a focus on the processes that are considered to be relevant for long-term canister performance.

This report is closely linked to Diomidis et al. (2023), which defines the reference corrosion rates for various metals present in the deep geological repository. Furthermore, outcomes of this report are used extensively elsewhere, such as Curti (2022), Johnson et al. (2023), Nagra (2024g), Nagra (2024f), Nagra (2024h), Curti et al. (2023), Nagra (2024d).

1.2.1 Structure of the report

Chapter 2 provides information about the repository and handling concepts with a focus on the conditions that an HLW disposal canister will encounter during disposal which may affect its long-term performance. The approach employed for designing and manufacturing the canister, providing a description of its as-built state, is given in Chapter 3. Chapter 4 covers subjects related to long-term performance of the canister as provided by the current provisional design, including degradation mechanisms and lifetime assessment. A summary and conclusions are given in Chapter 5.

2 Disposal conditions

This chapter provides a description of the deep geological repository and the conditions that a disposal canister will encounter after emplacement. Focus is given to processes and phenomena that are relevant to the long-term performance of the canisters during disposal, namely mechanical loading and environmental conditions that could influence corrosion. Further details on the evolution of the disposal environment of the HLW repository section are given in Nagra (2024d) and Curti et al. (2023).

2.1 Description of the repository and operations

The current Nagra project envisages two repository sections within a combined repository, one for HLW and one for L/ILW. The underground part of the combined repository will be constructed in the Opalinus Clay (OPA) at a depth between 850 and 900 m b.g.l., roughly in the middle of the OPA stratum. As illustrated in Fig. 2-1, it will include a series of parallel dead-end emplacement drifts for SF and RP-HLW and dead-end emplacement caverns for L/ILW. The HLW emplacement drifts will be spatially separated from the L/ILW emplacement caverns to minimise interactions between the two sections of the combined repository. The HLW emplacement drifts have lengths of about 1,000 m. The current concept envisages spacing between individual emplacement drifts of about 40 m. Access to the disposal areas will be provided through shafts and the construction and operations tunnels, which allow for simultaneous waste emplacement and construction activities.

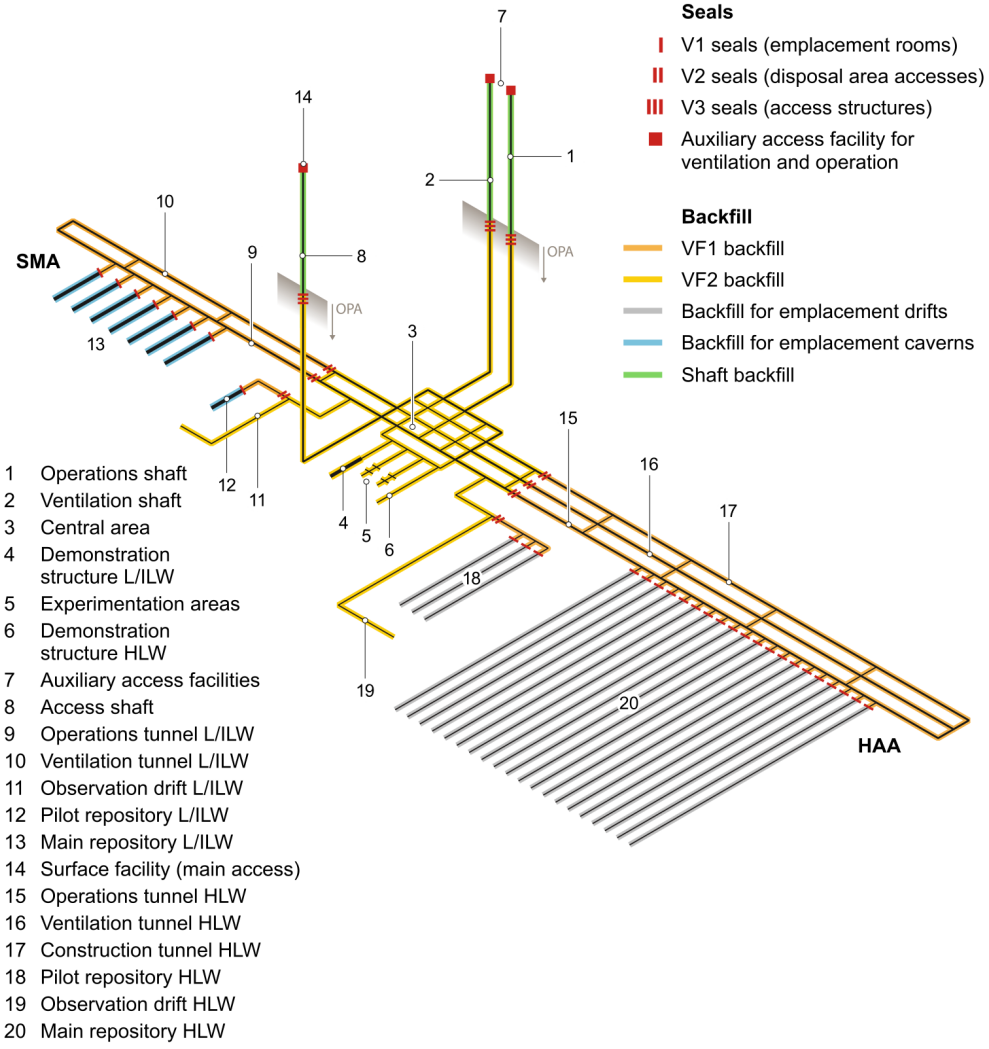

Fig. 2-1: Schematic view of the proposed combined repository and its main components after closure

From Nagra (2021). Note that the current repository design may be refined and modified in future stages of the project.

After arrival at the encapsulation plant, SF assemblies and flasks containing RP-HLW will be loaded into the disposal canisters. Relevant information on the SF and RP-HLW to be disposed of is given in App. A. The current overall waste management concept foresees the location of the encapsulation plant at the site of the interim storage facility for radioactive waste of the Zwischenlager Würenlingen AG (Zwilag). Details about the design and operations of the encapsulation plant are given in Nagra (2024b). Loading will be carried out with the objective of optimising the emplacement procedure to provide an evenly distributed thermal load (heat output is restricted to a maximum of 1,500 W per canister at the time of emplacement (Nagra 2023b)) and an optimum use of the available space underground.

After loading of the waste, the canister lid will be welded, and the weld will be inspected and heat-treated. Descriptions of these operations are provided in Chapter 3.

During waste loading, closure and transport, the canisters will be placed inside re-usable transport overpacks protecting the disposal canisters from mechanical loads, thereby ensuring their integrity in case of handling incidents. In addition, the overpacks protect, i.e., shield, the operating personnel from radiation during operations. Transport of the packaged waste to the underground facilities will take place through the main access shaft.

The disposal canisters will be emplaced co-axially at intervals of about 3 metres along the emplacement drifts (Fig. 2-2). The drifts have initial outer diameters of about 3.5 to 3.7 m and are supported by an approximately 0.4-m-thick lining composed of pre-cast concrete segments (Kosakowski 2023). The void space behind these elements is backfilled with a low viscosity, two-compound mortar (Kosakowski 2023).

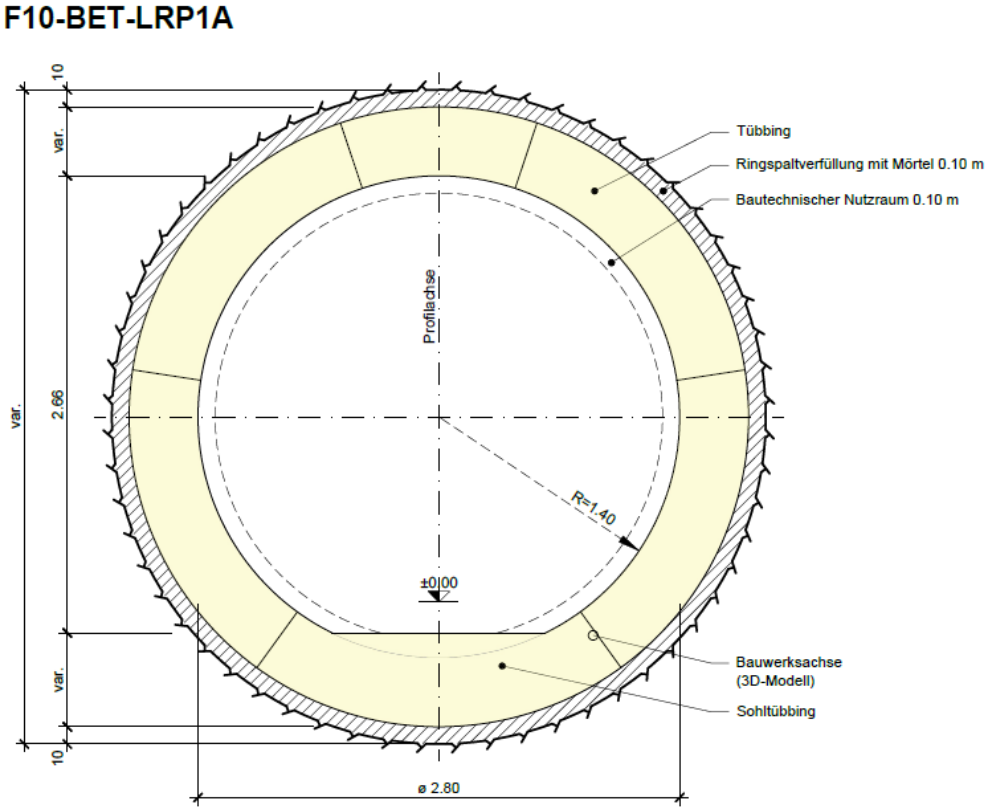

Fig. 2-2: Current design profile of a HLW emplacement drift

From Nagra (2023a).

Fig. 2-3 illustrates an emplaced SF canister in a section of an HLW emplacement drift, including subsequent backfilling. The canister is emplaced on a pedestal made of compacted MX-80 bentonite blocks with a water content of about 18% and a dry density of approximately 1.8 $g \cdot cm^{-3}$. Shortly afterwards, the tunnel is backfilled with granular MX-80 bentonite material with a water content of about 5% and a dry density of at least 1.45 $g \cdot cm^{-3}$. These steps are repeated as successive canisters are emplaced.

Together, the bentonite blocks and pellets form a protective mechanical, thermal and chemical buffer around the disposal canisters. Requirements on the bentonite buffer are derived and justified in Leupin et al. (2014). The required properties are described in more detail in Jenni et al. (2019).

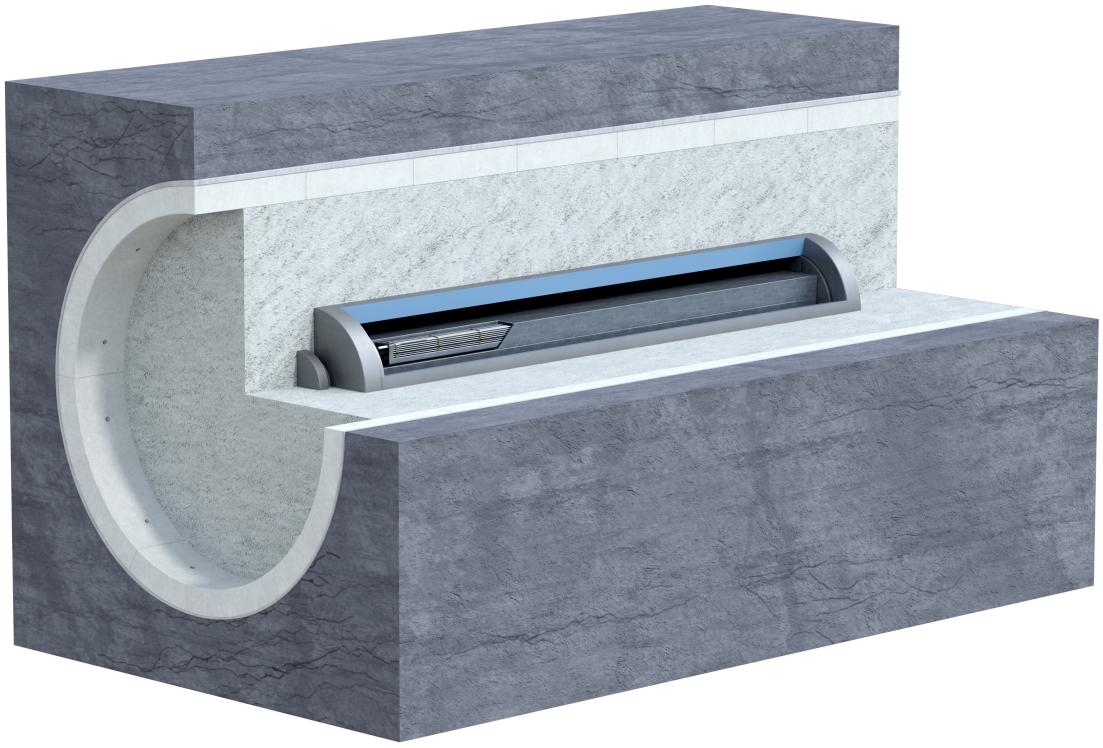

Fig. 2-3: Illustration of an SF canister emplaced in a backfilled HLW emplacement drift

2.2 Environmental conditions

2.2.1 Temperature & saturation

In the repository, the ambient temperature is predominantly a function of the depth for the majority of the repository lifetime, i.e., ~ 48 °C in the present case. However, upon emplacement the heat generated by the radioactive decay of the waste inside the canisters, leads to a transient temperature increase. A peak temperature at the canister surface is observed within the first 10 years after emplacement, and then, over a few thousand years, it decreases to the background temperature of the host rock. The peak temperature is calculated to be approximately 140 °C. After backfilling of the drift, the bentonite next to the canister dries due to evaporation, leading to a decreased saturation and relative humidity for approximately 30 years. Resaturation of the bentonite buffer occurs gradually, taking approximately 200 years for full saturation of the near-field to be reached. Thereafter, the buffer remains effectively fully water-saturated at all locations. The thermal and hydraulic evolution of the repository is discussed in detail in Nagra (2024f).

2.2.2 Redox conditions

The nature of the near-field redox conditions is an important factor in the corrosion behaviour of the disposal canister. Conditions will start off relatively oxidising due to the initially trapped O_2 in the sealing materials and due to the production of radiolytic oxidants from gamma radiation penetrating the container wall and interacting with water in the bentonite. Quite quickly, however, the environment will become anoxic and remain so indefinitely.

The amount of atmospheric O_2 trapped in the emplacement drift can be calculated based on the volumes of sealing and construction materials, the total porosity of each material, and the initial degree of saturation. Oxygen exists as both dissolved O_2 in the pore fluids in the bentonite and concrete and, more significantly, as gaseous O_2 in the unsaturated pore space. For a canister spacing of 3 m, the amount of O_2 for the emplacement drift design illustrated in Fig. 2-2 and Fig. 2-3 amounts to 164 mol per canister for the SF canister design. Of this total, 85% is in the granular bentonite material (GBM), 2% in the compacted bentonite pedestal, and 13% in the cast concrete tunnel liner. The vast majority of the O_2 (99%) is present as gaseous O_2, mainly in the relatively dry as-emplaced GBM (initial moisture content ~ 5%, corresponding to approximately 15% saturation) and in the concrete liner (assumed to have an initial degree of saturation of 50%). The initial O_2 inventory for the RP-HLW canister is slightly lower (162 mol per canister) because of the shorter length of the canister and, hence, the smaller amount of pre-cast concrete and bentonite sealing materials.

This initially trapped atmospheric O_2 will be consumed by a number of processes, which can include oxidation of pyrite and other oxidisable mineral phases in the GBM and OPA, consumption by aerobic microbes, sorption of gaseous O_2 by the bentonite, corrosion of metallic materials used for tunnel support, and corrosion of the canisters. The Full-Scale Emplacement (FE) experiment at the Mont Terri Rock Laboratory provides evidence for the expected evolution of the nearfield since it closely simulates an HLW emplacement drift and comprises three canister-sized carbon steel heaters mounted on buffer block pedestals, with the drift backfilled with GBM (Müller et al. 2017). The drift is extensively instrumented in order to measure the time-dependent temperature and relative humidity, as well as the concentration of gaseous O_2 at various locations along the drift. It was found that the O_2 concentration in all parts of the drift decreased rapidly following backfilling with GBM. The precise nature of the processes responsible for the disappearance of O_2 is still under investigation, but it is apparent that the initial oxic period will only last for a few days or weeks following sealing of the emplacement drifts (Giroud et al. 2018).

In addition to O_2 initially trapped in the emplacement drifts, oxidising species can be produced by the radiolysis of the humid atmosphere and/or the pore water in unsaturated and saturated bentonite, respectively. Due to shielding provided by the canister wall, the gamma dose rates at the outer surface of the canister are modest, with a maximum value of 0.2 $Gy \cdot h^{-1}$ (Gutiérrez et al. 2018). Initially, irradiation of humid air in the unsaturated buffer will produce gaseous HNO_3 (Morco et al. 2017) but, in the absence of a condensed H_2O phase on the canister surface this HNO_3 will diffuse away from the canister and react with the bentonite and other sealing materials where liquid water is present (Fig. 2-4(a)). With the onset of surface wetting of the canister, radiolytic oxidants will dissolve in either the surface droplets (Fig. 2-4(b)) or a condensed surface water film (Fig. 2-4(c)). However, it is expected that the initially trapped O_2 will have been consumed prior to the wetting of the surface so that HNO_3 formation will have essentially ceased, with radiolytically-produced molecular H_2O_2 and $OH^{\bullet}$ radicals being the primary oxidants of concern, along with trace amounts of O_2 produced either radiolytically or via the decomposition of H_2O_2. Eventually, the near-field will become water-saturated concurrently with the continuing but diminishing production of H_2O_2 and $OH^{\bullet}$ radicals (Fig. 2-4(d)), as the radiation field will have dropped to very low levels by then (< 0.01 $Gy \cdot h^{-1}$).

Following the consumption of the initial O_2 inventory and the decrease in the magnitude of the radiation field, the near-field will become anaerobic and remain so indefinitely. Thus, the redox conditions for the vast majority of the lifetime of the canister will be anaerobic. Under anaerobic conditions, corrosion of the canister will result in the production of H_2 as oxidation will be supported by the reduction of water. The generated H_2 will dissolve in the porewater but will also lead to the formation of an H_2 gas phase at the canister surface, at least temporarily. The evolution of saturation and gas pressure in the nearfield is discussed in detail in Nagra (2024f). The presence of H_2 will maintain reducing redox conditions in the near-field.

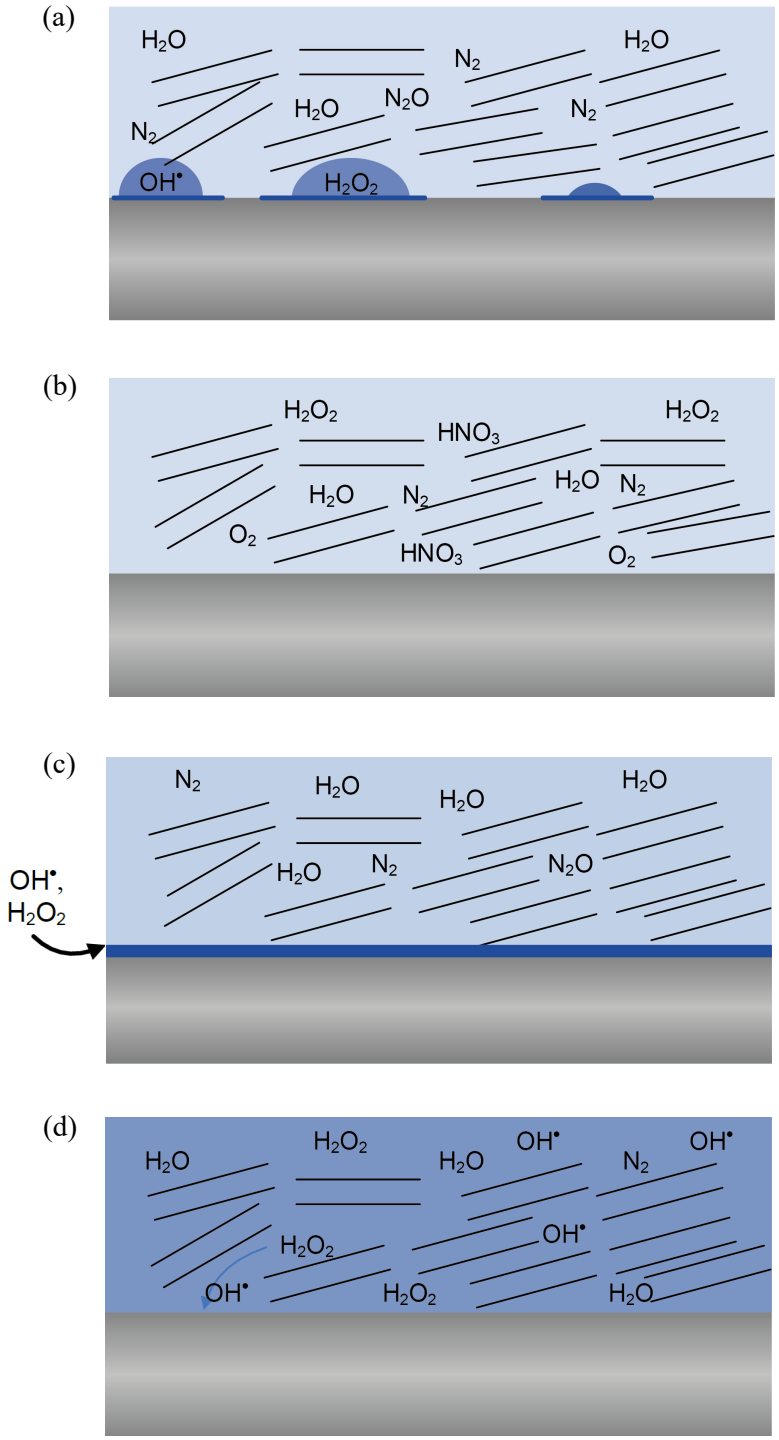

Fig. 2-4: Evolution of the environment adjacent to the canister surface

(a) Irradiation of humid air, (b) and (c) irradiation of N_2-H_2O atmospheres accompanied by oxidant generation in surface droplets or condensed surface water film, respectively, and (d) irradiation of saturated bentonite. Light and dark blue regions represent a humid atmosphere and condensed water, respectively. The sets of parallel lines represent clay particles, while grey represents the canister wall (modified from King & Behazin 2021).

2.2.3 Porewater chemistry

The gradual resaturation of the bentonite buffer surrounding the disposal canister occurs as OPA porewater from the surrounding rock enters the backfilled emplacement drift. As this happens, equilibration with bentonite minerals will occur, which will influence the species dissolved in the porewater. The bentonite porewater composition has been calculated by modelling cation exchange and solubility equilibria after reaction between the OPA porewater and MX-80 bentonite, and documented in Curti et al. (2023). An extensive sensitivity study has indicated that a narrow range of compositions, Eh and pH across all simulated bentonite porewaters is to be expected. The narrow pH and Eh windows are explained by internal chemical buffering mechanisms provided by the interplay of carbonate-CO_2, sulphate-sulphide and Fe(II)-Fe(III) mineral equilibria in conjunction with cation exchange. Details of the reference OPA and bentonite porewaters for the NL siting region are given as an example in Tab. 2-1.

Tab. 2-1: pCO_2 (bar), pH, Eh, ionic strength ($mol \cdot kg^{-1}$) and total elemental concentrations ($mol \cdot kg^{-1}$) of reference bentonite and OPA porewaters for the NL siting region

From Curti et al. (2023).

	Bentonite porewater	**OPA porewater**
log $p(CO_2)$	-2.20	-2.20
pH	7.24	7.10
Eh	-0.173	-0.167
Ionic strength	0.452	0.319
Al	2.08×10^{-8}	2.09×10^{-8}
Ba	7.19×10^{-8}	1.57×10^{-7}
C (in)	2.94×10^{-3}	2.21×10^{-3}
Ca	1.77×10^{-2}	2.03×10^{-2}
Cl	0.239	0.240
F	1.74×10^{-4}	1.74×10^{-4}
Fe	2.09×10^{-5}	2.56×10^{-5}
K	1.83×10^{-3}	2.13×10^{-3}
Mg	1.02×10^{-3}	1.45×10^{-2}
Mn	1.84×10^{-5}	8.24×10^{-5}
Na	0.375	0.215
S	7.86×10^{-2}	2.29×10^{-2}
Si	1.70×10^{-4}	1.72×10^{-4}
Sr	1.72×10^{-4}	3.70×10^{-4}

2.2.4 Microbial aspects

Microbial activity will be suppressed in the nearfield of an HLW emplacement drift because of the presence of highly compacted bentonite (Jenni et al. 2019, King 2009, Stroes-Gascoyne et al. 2010). After bentonite saturation, the low water activity, lack of physical space, and high swelling pressure are considered to be the principal reasons behind the empirical observations, although the details of the mechanism have yet to be established (Jenni et al. 2019). The threshold buffer dry density above which microbial activity is suppressed depends on various factors, including the type of clay, the porewater salinity, the availability of nutrients, temperature, etc., but target

densities in the range of 1,250 to 1,450 $kg \cdot m^{-3}$ (Smart et al. 2017) and as high as 1,600 $kg \cdot m^{-3}$ (Stroes-Gascoyne et al. 2010) have been suggested. The absence of microbial activity in the bentonite backfill implies that biofilm formation on the canister surface will not occur. Additionally, recent experimental results indicate that temperatures of 90 °C or higher for periods of at least one year tend to inhibit microbial survival in the bentonite (Morales Hidalgo et al. 2024), further supporting the assumption that no microbial activity will occur in the near-field. However, it is conceivable that some niches where microbial activity is possible could exist in the excavation-damaged zone (EDZ) in the OPA.

2.2.5 Evolution of environmental conditions and related uncertainties

The expected thermal-hydraulic evolution at the outer surface of a disposal canister can be conceptually divided into the three phases shown in Fig. 2-5 and described hereafter. While the temperature (T) and relative humidity (RH) phases given in the figure are conceptually correct, the values of time, T and RH are approximate. Probabilistic assessments in Nagra (2024f) and Nagra (2024k) explore in detail the related uncertainties and the variability of the disposal system.

Phase 1: Initial dry phase

The beginning of phase 1 is defined as the time at which the backfilling of the area around an emplaced canister is complete. Phase 1 continues until the time when the canister surface is first wetted with liquid water. There is a critical RH for the formation of moisture on the metal surface below which aqueous corrosion does not occur. For clean, smooth metal surfaces, this critical RH is in the order of 80%. Particulate covered and rough metal surfaces lower the critical RH. Here it is assumed that wetting of the canister surface will take place at a RH of 60% due to the presence of surface contaminants (such as salts and/or clay particles) and a porous surface oxide (which will promote capillary condensation), leading to a duration of Phase 1 of approximately 40 years. This is a hot and dry period, during which consumption of entrapped O_2 takes place and only high-temperature, dry oxidation of the canister is possible. Mass transport of species towards and away from the canister will take place primarily through the gas phase.

Phase 2: Anaerobic, unsaturated phase

Phase 2 lasts from the first wetting of the canister surface (~ 60% RH) until the complete saturation of the near-field, i.e., from approximately 40 years until approximately 200 years after emplacement. This phase is characterised by a gradual increase of the RH and a gradual decrease of the temperature down to approximately 80 °C. The canister surface is wet enough for electrochemical reactions to occur under anaerobic conditions. Wetting may be non-uniform at first, either because of the deliquescence of surface contaminants or because of non-uniform access of H_2O. Fe(III) corrosion products formed on the canister surface during Phase 1 will be reduced to Fe(II), and further anoxic corrosion of the canister will occur. Progressive saturation by water inflow will cause swelling of the bentonite starting at the periphery of the tunnel and gradually progressing towards the centre. By the end of this phase, the swelling pressure will have fully developed as bentonite reaches complete saturation. Previously precipitated salts will redissolve as the moisture content of the bentonite increases and the bentonite porewater will begin to equilibrate with the incoming water from the host OPA.

Phase 3: Anaerobic, saturated phase

At the onset of phase 3, the bentonite is completely saturated and the only oxidant available in the system is water since the yield of oxidising radiolysis products will be vanishingly small by this time. Corrosion under these conditions yields H_2 gas by reduction of protons and water. Metal

ions formed by corrosion may precipitate near the canister surface as carbonates or oxides/ hydroxides, or react with the bentonite. Mass transport towards and away from the canister surface occurs by diffusion of dissolved species. The temperature at the canister surface, and elsewhere in the repository, will continually decrease.

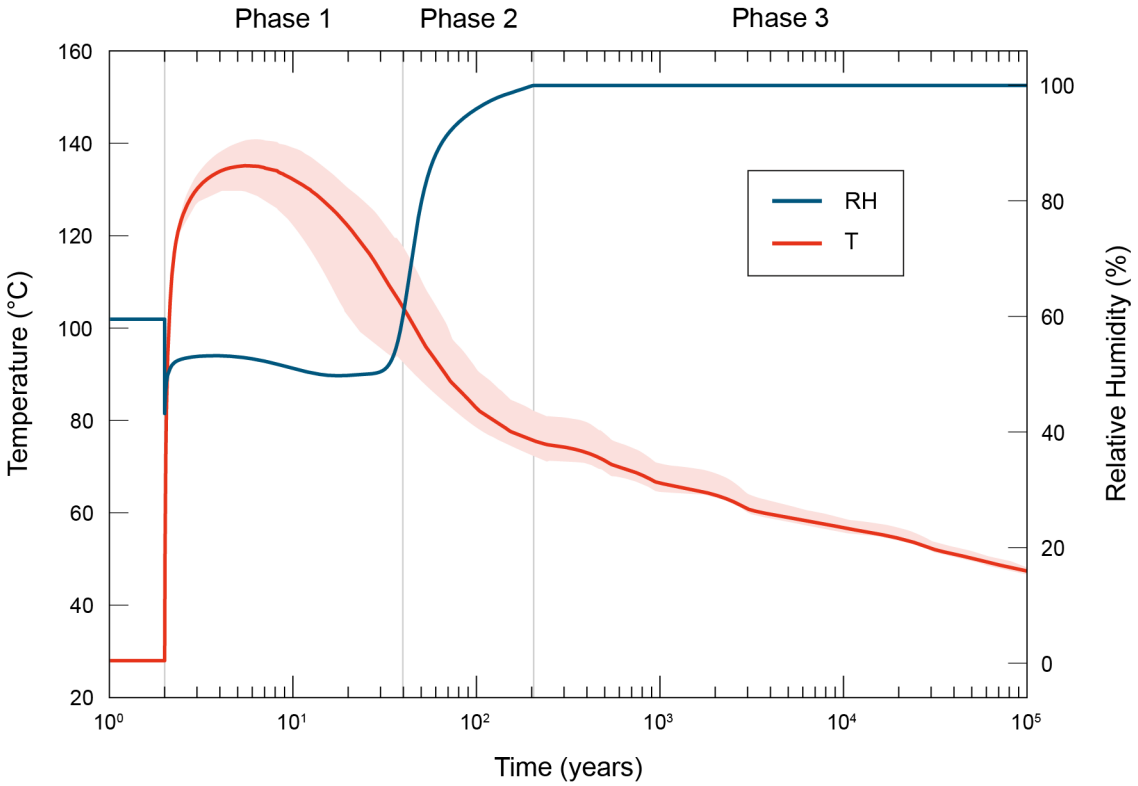

Fig. 2-5: Evolution of temperature (T) and relative humidity (RH) at the outer surface of a disposal canister with time

Emplacement of the canister and backfilling are assumed to take place instantaneously at year 2. Prior to this time, the shown T and RH represent the values expected in the emplacement drift during the ventilation period. For T, the band indicates the range of values for the various canisters in the repository, while the line indicates the average value.

2.3 Mechanical loading conditions

2.3.1 Swelling and pore pressures

The magnitude of the swelling pressure of the MX-80 bentonite after complete saturation will primarily depend on the emplaced dry density. The variation in emplaced buffer density is one of the factors that can result in a spatially variable load around the circumference and along the axis of the canister. Evidence from the FE experiment at Mont Terri (Müller et al. 2017) is useful for defining variations in density that could be expected in the repository (Köhler et al. 2015). Slope measurements of the granular bentonite material during emplacement indicated that the dry density varied between 1.444 and 1.555 g·cm^{-3} with an average dry density of 1.489 g·cm^{-3}. The bentonite blocks used for the pedestals exhibited dry densities between 1.74 and 1.80 g·cm^{-3}, with an average of 1.78 g·cm^{-3}. Such densities are expected to lead to swelling pressures in the range of 3 – 6 MPa at full saturation.

A system mimicking the FE experiment with inhomogeneously emplaced bentonite density was modelled by Bosch Llufriu (2021), with good agreement with the experimental results. The predicted development of swelling pressure in the buffer, expressed as the normal pressure on the canister, is shown in Fig. 2-6. The saturation phase is characterised by a non-monotonic development of stresses, including a period in which the total pressure of the block pedestal is lower than the pressure developed by the granular bentonite on the canister. Stresses during this period vary between 0 and 5 MPa. At the time of saturation (~ 200 years), a significant build-up of stress is observed, which is the result of the thermal pressurisation of the pore water, in turn a consequence of the differential thermal expansion of porewater and matrix pores. As heat dissipates through the rock, the porewater pressure eventually starts to decrease towards hydrostatic level. Accordingly, stress on the canister decreases as well. Throughout this period, the stress acting on the canister can be approximated as the sum of the swelling pressure of the bentonite and the pore pressure. For this model, the initial porewater pressure was set to 2.1 MPa as representative of the FE experiment at Mont Terri. The same porewater pressure is recovered after the dissipation of any thermal effects, at approximately 2,000 – 3,000 years and onwards.

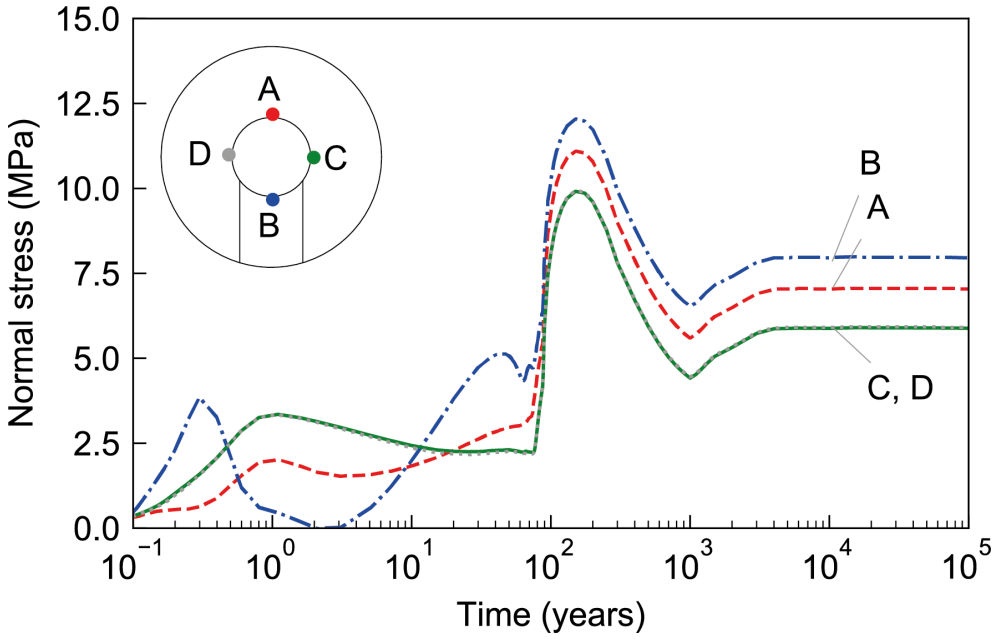

Fig. 2-6: Predicted development of total stress (swelling pressure) in the buffer shown as normal stress acting on the canister

From Bosch Llufriu (2021).

2.3.2 Lithostatic stresses

The quantification of the contemporary 3D in-situ stress tensor in the rock volume of the three candidate repository siting regions is reported in Nagra (2024j). This is done through a synthesis of stress data, including those obtained from Nagra's deep borehole campaign, as well as of results of geomechanical-numerical 3D stress models providing a continuous description of the stress tensor. The magnitudes of the minimum horizontal stress (S_{hmin}) and the maximum horizontal stress (S_{Hmax}) were determined by various measurements, while the vertical stress (S_v) was determined from integrated rock density and direct measurements. The S_{Hmax} orientation was also determined, and shows no variation with depth, especially across the OPA and geological

confining units. The HLW emplacement drifts will be constructed with an orientation parallel to S_{Hmax}, and consequently only S_{hmin} and S_v are relevant here. The stress magnitudes at a depth of 900 m b.g.l in the NL siting region are shown in Tab. 2-2.

Tab. 2-2: Minimum horizontal and average vertical stress magnitudes (MPa) at a depth of 900 m b.g.l. in the NL siting region

From Nagra (2024j).

Min. and max. possible values are P10 for the lowest and P90 for the highest bounds of S_{hmin} gradients for all tests conducted in OPA.

Likely lower and upper values are the median (P50) of the lowest and highest bounds of S_{hmin} gradients for all tests conducted in OPA.

Minimum horizontal stress magnitude S_{hmin} [MPa]				**Average vertical stress magnitude S_v** [MPa]
Min. possible value	Likely lower value	Likely upper value	Max. possible value	
15.2	16.7	17.9	19.6	21.6

2.3.3 Residual stresses

The final closure weld of the canister after loading of the waste using a fusion-based welding process will invariably result in tensile residual stresses in the weld region. The maximum residual stress is typically assumed to be equal to the yield strength of the material. High tensile residual stresses are undesirable because the threshold stress for initiation of stress corrosion cracking (SCC) in steel approximates to the yield strength of the material, and because the resistance to brittle fracture and tolerance to flaws can be significantly reduced by the presence of tensile residual stresses if the toughness is low. Therefore, the application of a stress relieving method is being considered for canister sealing and lid welding methodology and is further discussed in Section 3.7.

Post-weld heat treatment (PWHT) is generally used for stress relief of welded thick steel structures. However, PWHT does not completely eliminate the residual stress. This means that residual tensile stresses at the weld region will remain and should be taken into account in performance assessment. The PWHT parameters and predicted material properties are discussed in Section 3.7.

2.3.4 Evolution of stresses and related uncertainties

For a deep geological repository at a depth of 900 m b.g.l. in OPA, stress development at the canister during the early phase is expected to be dominated by the bentonite swelling pressure and the pore pressure (cf. Section 2.3.1). The main difference to the values shown in Fig. 2-6 would be the hydrostatic pressure, which is expected to be approximately 9 MPa at repository depth. Thus, higher values than those shown in Fig. 2-6 would be expected, but their evolution would follow the same trends.

At periods relevant to the required canister lifetime (i.e., beyond 1,000 years after closure), the stress acting on the canister is projected to be up to 15 MPa assuming no gas generation and a maximum swelling pressure of 6 MPa. If gas generation is considered, this could contribute an additional stress of around 3 MPa (Nagra 2024f), leading to a total stress of approximately 18 MPa. Notably, the difference between the normal stresses around the canister is minimal, with a maximum difference of less than 2 MPa.

While the abovementioned projections of stress evolution are based on the expected evolution of an HLW emplacement drift, several uncertainties must be considered to better evaluate the long-term evolution of stress on the canister. The following addresses three primary uncertainties that could impact these stress estimates over time:

- Gas pressure development: According to the recent performance assessment (Nagra 2024k), an excess gas pressure level of 5 MPa above the hydrostatic pressure is considered for the upper bounding case of gas generation. This additional gas pressure could contribute directly to the stress applied to the canister, potentially increasing the maximum stress to 20 MPa. This is based on the unrealistic assumption that all canisters would breach at the same time. With distributed canister breaching times, the gas-induced overpressure would be reduced.
- Tunnel convergence: Tunnel support, i.e. the concrete lining, will degrade over the long term, which could lead to tunnel convergence. In the event of complete support loss, ground movements could occur until a new equilibrium is reached. The buffer and the canister may then be subjected to mechanical compression up to the partial or full weight of the overburden (i.e., lithostatic stress level mentioned in Section 2.3.2). However, this extreme case is not expected, and a convergence with an order of magnitude of 2 – 3 cm is foreseen, which would cause additional compression of approximately 2 MPa to the canister.
- Evolution of in-situ stresses: The high clay content in the OPA formation could contribute to time-dependent deformation, known as creep. Although evidence of creep mechanisms in OPA is currently limited to the time scales and confining stress level applicable in the present study (Zhang et al. 2020, Naumann et al. 2007), a recent study by Sasaki & Rutqvist (2022) investigated the stress evolution in the near-field of a generic repository considering the creep effect in a shaly host rock formation and showed that the three main stress components (i.e., S_v, S_{Hmax}, S_{hmin}) approach the asymptote of the isotropic geostatic stress level (i.e., S_v). The most relevant finding is that the creep tends to relieve high deviatoric stresses in the long term (e.g., after tens of thousands of years) and thus increases buffer compaction.

To assess the structural integrity of disposal canisters in the long term, assumptions related to stresses acting on the canister must be chosen conservatively. Therefore, the principal stress components in the vicinity of the canister are considered: S_v (vertical lithostatic stress) and S_{hmin} (horizontal lithostatic stress perpendicular to the canister axis) as documented in Section 2.3.2. For S_{hmin}, the minimum possible value is selected as the most conservative due to increased stress anisotropy. As discussed above, repository-induced (i.e., buffer swelling and thermal pressure-isation) stress changes in the post-closure phase result in stress levels that are lower than lithostatic stresses. Considering the stress components S_v and S_{hmin} ensures that the assessment captures the maximum deviatoric stress state on the canister, which is significant in scenarios of tunnel support loss and substantial tunnel convergence. If pure isotropic compaction needs to be considered, adopting S_v as the stress component is appropriate, assuming the occurrence of significant creep.

3 Canister design

3.1 Canister requirements

Requirements inform and guide the development of the design since it is expected that a canister design must meet or exceed these requirements. The requirements that have been defined for the provisional design development of HLW disposal canisters for the RBG are summarised in Tab. 3-1. In this context, "failure" or "breaching" of the canister should be interpreted as any loss of containment through the existence of a leak path allowing gas and/or liquid to migrate between the inside and the outside of the disposal canister. This definition can cover various failure modes from a through wall crack to a more widespread structural failure. Deformation, degradation or instability of the canister are not necessarily failure modes if the containment remains intact. As an example, the analyses presented in this report demonstrate that the containment function provided by the current provisional canister design will remain for longer than 10,000 years.

The canister must be designed to meet the requirement defined for containment with an "adequate margin". This margin allows for deviations from design expectation in terms of loading, inaccuracies in analysis methods, quality lapses in materials, lack of knowledge of material performance and environment, uncertainties and potential construction defects. There is inevitably a level of engineering judgement implicit within this process as to what is acceptable so that the risk of failure is reduced to as low as reasonably practicable. Decisions will be based on the limit of current knowledge and experience, with an acknowledgement of existing gaps in knowledge and experience, which might be filled in the course of time.

In addition to the requirements shown below, a boundary condition currently foreseen in Nagra's reference concept is that the canisters are to be made of low carbon steel.

Tab. 3-1: Disposal canister requirements

A: Regulatory requirements (ENSI 2023). B: Waste related requirements. C: Long-term performance related requirements. D: Operational requirements.

Code	Name	Description
A1	Canister lifetime	The HLW disposal canisters must provide complete containment of radionuclides for a minimum of 1,000 years after emplacement.
A2	Criticality safety	Criticality safety of loaded SF disposal canisters is to be ensured during both the operational and post-closure phases. This matter is addressed in Nagra (2024c).
A3	Retrievability	The canister must remain retrievable until the end of the monitoring phase. This matter is addressed in Nagra (2022).
B1	Waste integrity	No handling operation should damage the SF or RP-HLW.
B2	Dimensions	The disposal canister should be adequately dimensioned to accommodate SF and/or RP-HLW according to the proposed loading plan. No alteration (e.g., cutting) of the waste is possible (see B1). If multiple SF assemblies are loaded into one canister, an internal structure (e.g., basket) with adequate clearance is needed.
C1	Structural integrity - disposal	The stresses in the canister wall, lid and base, including the seal joint region(s) must be below the failure limit for at least the required lifetime by an adequate margin for the structural loading in the repository.

Tab. 3-1: continued

Code	Name	Description
C2	Wall thickness	Mechanical loading during disposal provides the basis for determination of the wall thickness, which must ensure long-term structural integrity.
C2.1	Corrosion	Corrosion rates of the canister material and of the seal joint(s) must be low enough under disposal conditions to preclude premature canister breaching as a result of general and/or local loss of effective thickness. Furthermore, gas generation due to corrosion in the post-closure period must be low enough to avoid any damage to the engineered and geological barriers.
C3	Sealing	There must be a satisfactory method for sealing the wall thickness range in question. The sealing method must be suitable for remote application, given the radiation field.
C3.1	Seal integrity	The seal joint region must not be significantly more susceptible to stress-induced failure mechanisms than the parent material.
C3.2	Residual stress reduction	If post-sealing stresses are too high, they must be reduced to a suitable level. The stresses in the seal-joint region and heat-affected zone (HAZ) must be low enough to reduce the probability of stress-assisted failure processes.
C3.3	Inspection	The inspection process(es) must be able to detect defects that are smaller than the critical flaw size by an adequate margin. In addition, residual seal material must be cleaned/removed from the canister seal region if required by the selected inspection processes.
D1	Manufacturing best practice	Best available present-day technology should be adopted for the fabrication and sealing of the canisters.
D2	Production rate	Using the preferred manufacturing, sealing, stress reduction and inspection processes, it should be possible to completely package one canister per day in the encapsulation plant. Parallel processing can be implemented if necessary.
D3	Structural integrity - handling	The canister must remain structurally sound during normal handling and incidents that could occur during handling. Because the canister is surrounded by a transfer/shielding overpack while in the encapsulation plant and during transfer underground, it is not considered vulnerable to impacts from handling under this condition.
D4	Inner lid	An inner lid must be installed in the canister after loading of the SF. The lid must have an air-tight seal (gasket) to ensure that the next stage of operations (placement of the main lid and final welding) poses no risk of spread of contamination.
D5	Repackaging or repair	There should be a method to allow repackaging or repairs in case of significant damage to a canister during a handling incident.

3.2 Design methodology

Most pressure vessel specifications or design codes (e.g., PD 5500 (BSI 2024b) and BS EN 13445 (BSI 2021a, BSI 2021b)) provide requirements for the design of components or their parts using design by formulae (DBF). DBF is based on a simplified and empirical approach to engineering design. It employs rules prescribed in established codes, standards and recommended practices that dictate design specifications for various types of structures, based on findings from extensive testing, historical data and expert knowledge. This approach relies on conservative assumptions and standardised values, which may lead to overdesign and can be unsuitable for unique or non-standard design requirements.

The work presented in this report employs a design-by-analysis (DBA) approach that involves advanced analysis to evaluate the response and performance of a design under various conditions. It involves finite element analysis (FEA) to support the subsequent engineering critical assessment (ECA) in order to establish the structural integrity of the canisters.

Using FEA, the through-thickness stress distributions due to external pressure can be established, whereas most handbook solutions are based on an internally pressurised component. Coupled with ECA, the design approach presented here also considers the combined effects of material properties, loading conditions and environmental effects on the longevity of the canisters.

In this work, a sequentially coupled thermo-mechanical approach is adopted for the closure weld of the canister consisting of four simulations, as summarised below:

1. A heat transfer simulation is used to model the transient temperature field due to the welding process as the beam travels along the circular path around the canister.
2. The transient temperature field from the welding process is then mapped on to a mechanical model to predict the resulting as-welded residual stress field.
3. A heat transfer simulation of the local PWHT process is used to model the transient temperature field as the canister is heated by the heat bands.
4. The transient temperature field from the PWHT process is then mapped onto a mechanical model to predict the resulting residual stresses after PWHT.

The residual stresses after PWHT are then employed in ECA calculations to determine critical flaw sizes.

ECA is an analysis based on fracture mechanics principles and is used to assess the integrity of a flaw (in this case, a postulated flaw) against failure due to fracture, fatigue or plastic collapse under specified loading conditions. As no cyclic loading of the canister is expected, fatigue is not considered. The three elements involved in an ECA are material properties (fracture toughness and tensile properties), applied stresses (primary and secondary) and the geometric information about the flaw and component under consideration.

A failure assessment diagram (FAD) shows the interaction between the two relevant failure modes, as illustrated in Fig. 3-1:

- On the X-axis, L_r (the collapse ratio) determines the proximity to plastic collapse; and
- On the Y-axis, K_r (the fracture ratio) determines the proximity to brittle fracture.

The area bounded by the axes and by the assessment line is called the safe zone. If the assessment point lies within the safe zone, the flaw is acceptable; if it lies on the line, it is critical; and a flaw is considered unacceptable if it is outside the line.

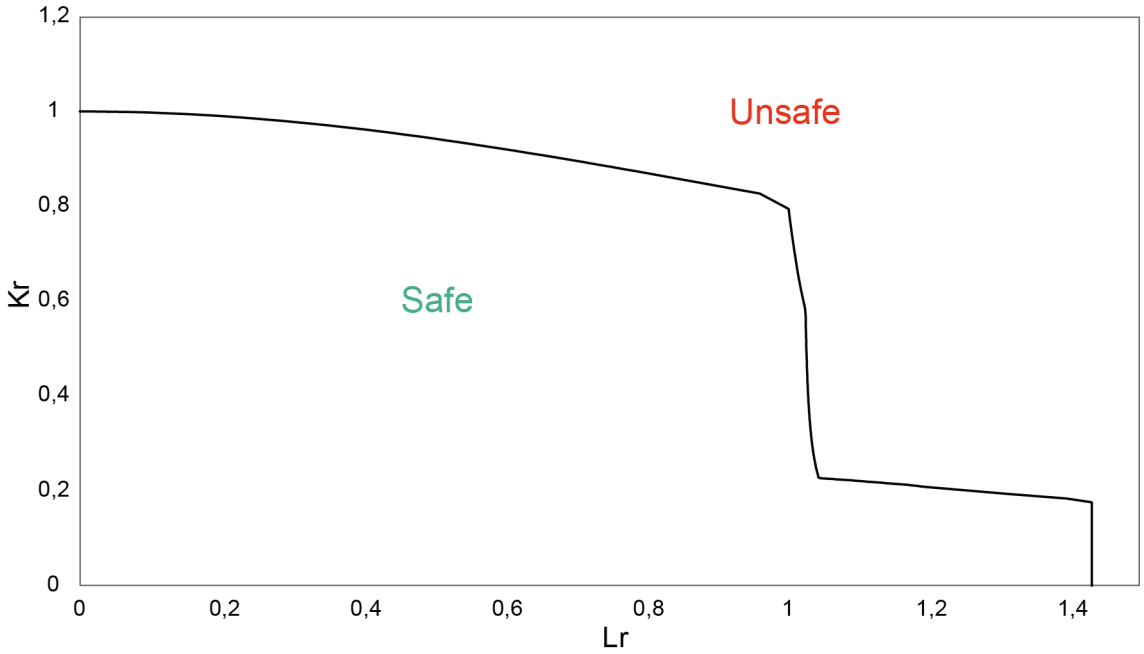

Fig. 3-1: BS 7910 Option 2 FAD with yield discontinuity used in this work
From (BSI 2019b).

ECA calculations are performed to determine the acceptable welding flaws in accordance with the Option 2 material-specific procedure of the flaw assessment procedure BS 7910 (BSI 2019b). All calculations were performed using the CrackWISE®6 commercial software which automates the fracture clauses in BS 7910 (BSI 2019b).

The handbook solutions given in BS 7910 (BSI, 2019a) are based on sound fracture mechanics principles. Hadley (2007), Hadley (2018a), Hadley (2018b), Hadley & Moore (2006), Hadley & Smith (2016), Hadley et al. (2020) describe the validation work carried out against full-scale test data and numerical analyses in order to demonstrate that the solutions are safe, user-friendly, practically useful and not excessively conservative. The stress intensity factor (SIF) and reference stress/limit load solutions included in BS 7910 (BSI 2019b) annexes were established based on the loading conditions under which the stresses (membrane, bending or both) acting upon the crack faces open the crack.

For the ECA calculations, disposal canisters were assessed with the following flaws:

- A surface-breaking flaw, see Fig. 3-2;
- A long surface-breaking flaw, see Fig. 3-3;
- An embedded flaw, see Fig. 3-4.

In Fig. 3-2, Fig. 3-3 and Fig. 3-4, B is thickness, a and 2a are flaw height, 2c is flaw length, p is ligament thickness, and W is width.

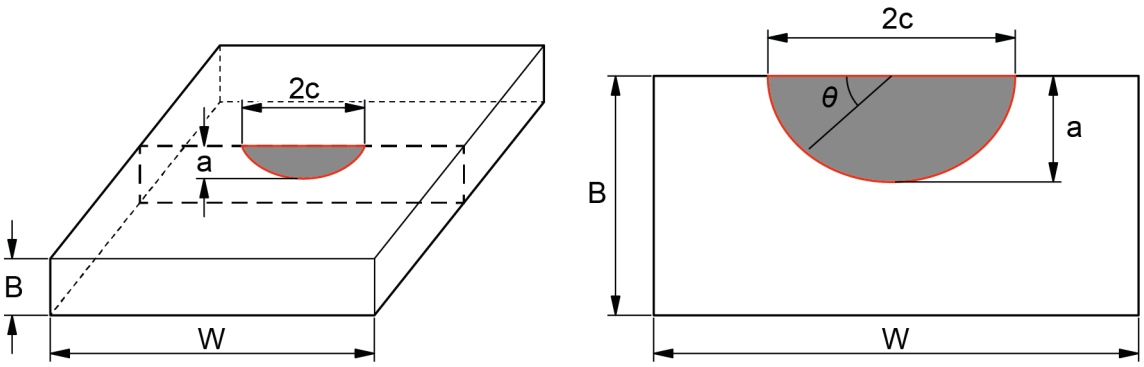

Fig. 3-2: Surface-breaking flaw in a plate

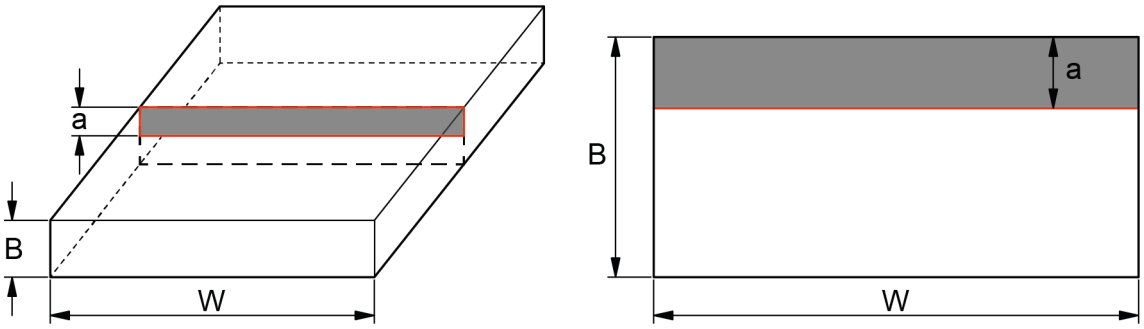

Fig. 3-3: Long surface flaw in a plate

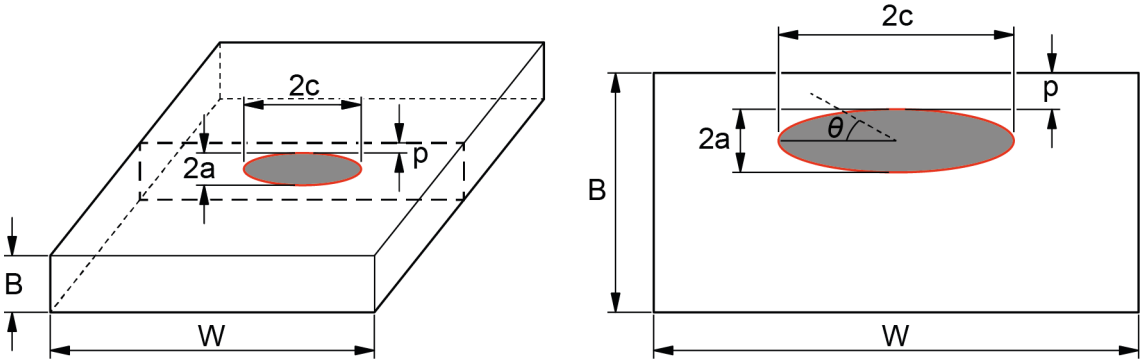

Fig. 3-4: Embedded flaw in a plate

Since the closure weld in the canister is between a flat lid and a cylindrical shell body, the analytical solutions, which assume a circumferential joint between two cylindrical parts, do not apply. For this reason, the BS 7910 (BSI 2019b) flat plate solutions (which provide stress intensity factors for a wide range of geometries) were employed in this work. The flaw types shown in Fig. 3-2, Fig. 3-3 and Fig. 3-4 bound both external and internal diameters of the weld as the analytical solutions remain unchanged regardless of flaw position i.e., outer diameter (OD) or inner diameter (ID), see Fig. 3-5 and Fig. 3-6. The postulated flaws assumed bound both the top and bottom lids.

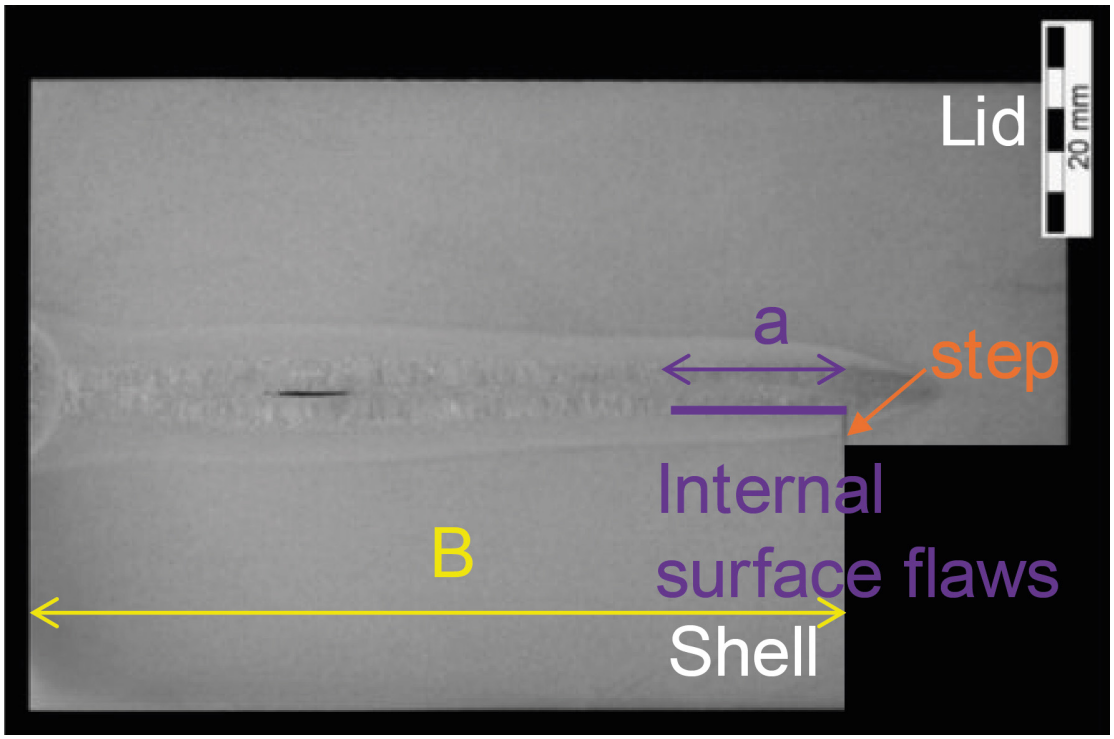

Fig. 3-5: Internal surface flaws
B is thickness, a is postulated flaw height.

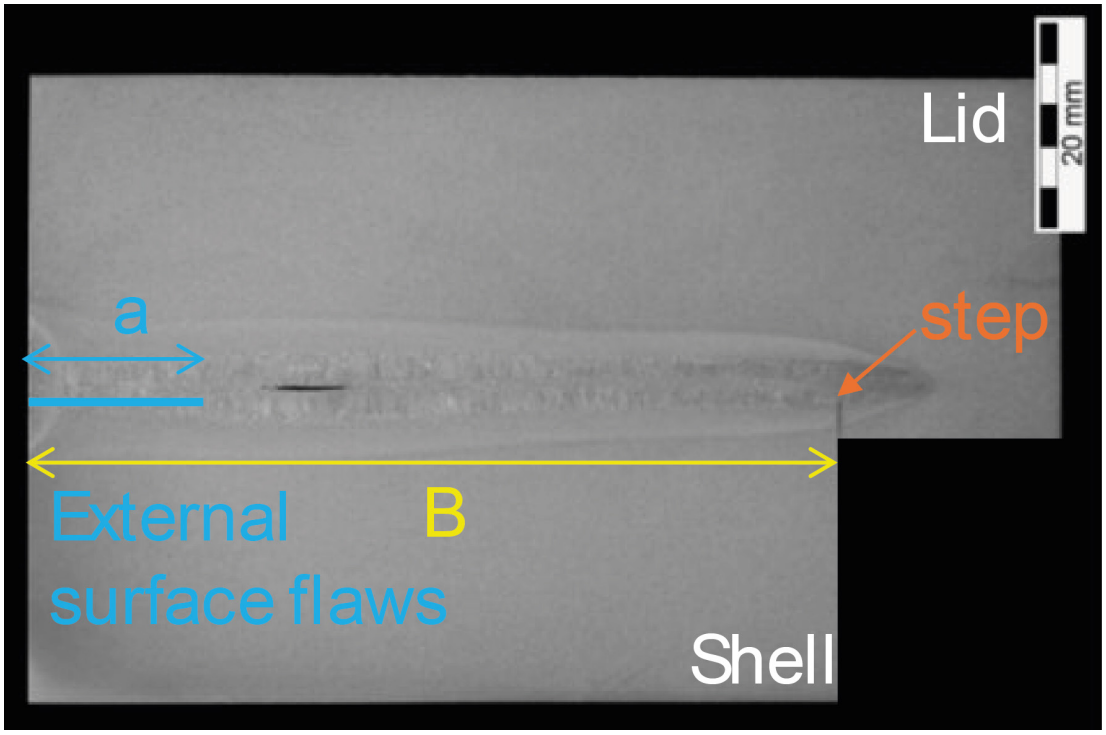

Fig. 3-6: External surface flaws
B is thickness, a is postulated flaw height.

For the analyses, it was assumed that the wall thickness after 10,000 years was decreased due to corrosion (see Section 4.2.1) and was 133 mm instead of the as built thickness of 140 mm, for both SF and RP-HLW canisters. As discussed in detail in Section 3.8, the presence of sub-surface flaws is possible between 20 and 100% of section thickness from the external surface. Thus, it is appropriate to assume that the shortest distance between the external surface and the flaw is 20% of the thickness, i.e., p = 28 mm. With a 7 mm wall thickness loss after 10,000 years, the final ligament is p = 21 mm, as shown in Fig. 3-7. This value was employed to determine the acceptance limit of an embedded flaw close to the OD of the canisters. The calculations also considered the possibility of such a flaw located at the step where the lid and shell body meet. It was assumed that the ligament of a root spiking was 1 mm. Any embedded flaws located closer to the step than this were bound by the acceptance limit of a surface flaw, as the ligament became so small that it was appropriate to treat such embedded flaws as an internal surface-breaking flaw.

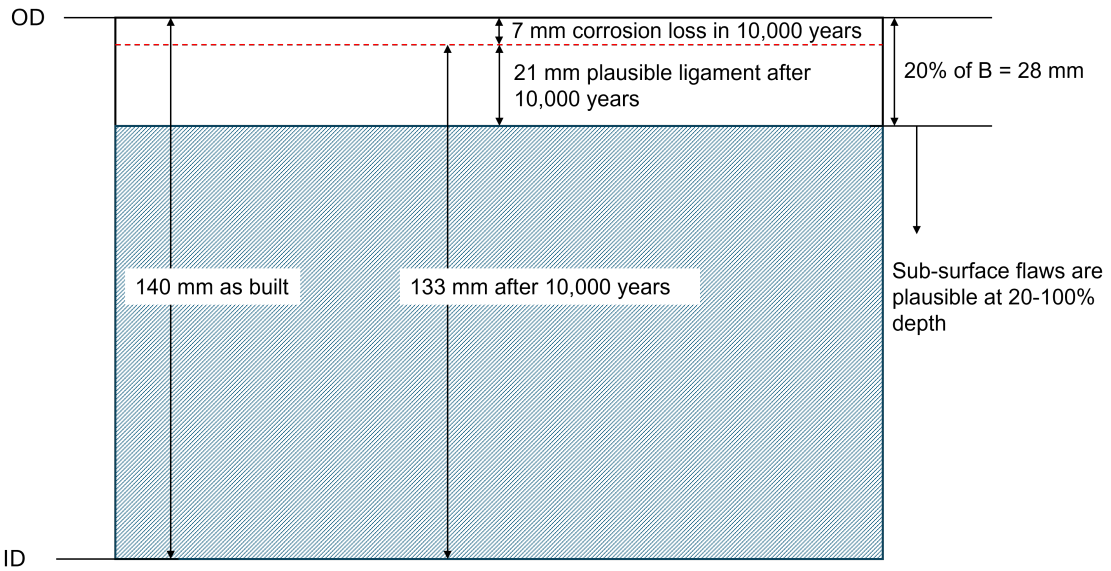

Fig. 3-7: Schematic illustration of potential wall thickness loss after 10,000 years and likely location of sub-surface flaws

The remainder of Chapter 3 is structured as follows. The design and dimensions of all canister types are shown in Section 3.3. The material specification and properties are described in Section 3.4. The manufacture of the canister is detailed in Section 3.5, which includes forging of the cylindrical body and lids, and welding of the bottom lid. Section 3.6 focuses on the closure weld. Section 3.7 provides the details of the selected PWHT approach and recommended material properties after PWHT for numerical analyses and ECA calculations. The plausible flaws in the weld are elaborated in Section 3.8, which also includes suitable inspection methods and their associated detection limits.

All findings from the activities described in this chapter are then fed into the structural assessment in Section 4.3, which describes the structural performance of the canister 10,000 years after emplacement in the repository under disposal loads. This section also includes the determination of critical flaw acceptance criteria and the assessment of the structural integrity of canisters with flaws possibly missed by inspection.

3.3 Design drawings and description

The disposal canisters for SF can accommodate either 4 PWR fuel assemblies (FAs) (Fig. 3-8) or 12 BWR FAs (Fig. 3-9). The two SF canister variants (SF-PWR and SF-BWR) share identical designs except for the shape of the inner basket that holds the FAs. Each basket type is designed according to the dimensions of the respective FA type. The cross-section of each square element of the basket provides a clearance of 10 mm on either side of the largest FA it is designed to host, i.e. the inner dimensions of each element are 159 × 159 mm for BWR and 235 × 235 mm for PWR FAs.

The outer shell of the SF disposal canister is made up of three main pieces: two lids and a cylindrical body. The canister length from top to bottom lid (excluding handles[3]) is 4,960 mm. The cylindrical shell body measures 4,660 mm in length and 1,100 mm in OD. It is 140 mm thick as built. The top and bottom lids measure 1,100 mm in diameter and 150 mm in thickness. There is a 10 mm step along the circumference of the inner face to allow accurate positioning of the lid when welding takes place.

The RP-HLW disposal canisters (Fig. 3-10) are designed to hold three RP-HLW flasks, stacked on top of each other. Similar to the SF canister, each RP-HLW canister is made up of three main pieces: two lids and a cylindrical body. These canisters measure 4,267 mm in length and 720 mm in OD. The top and bottom lids are 150 mm thick with a 10 mm step on the inner face along the circumference.

[3] The handles have a length of 160 mm each.

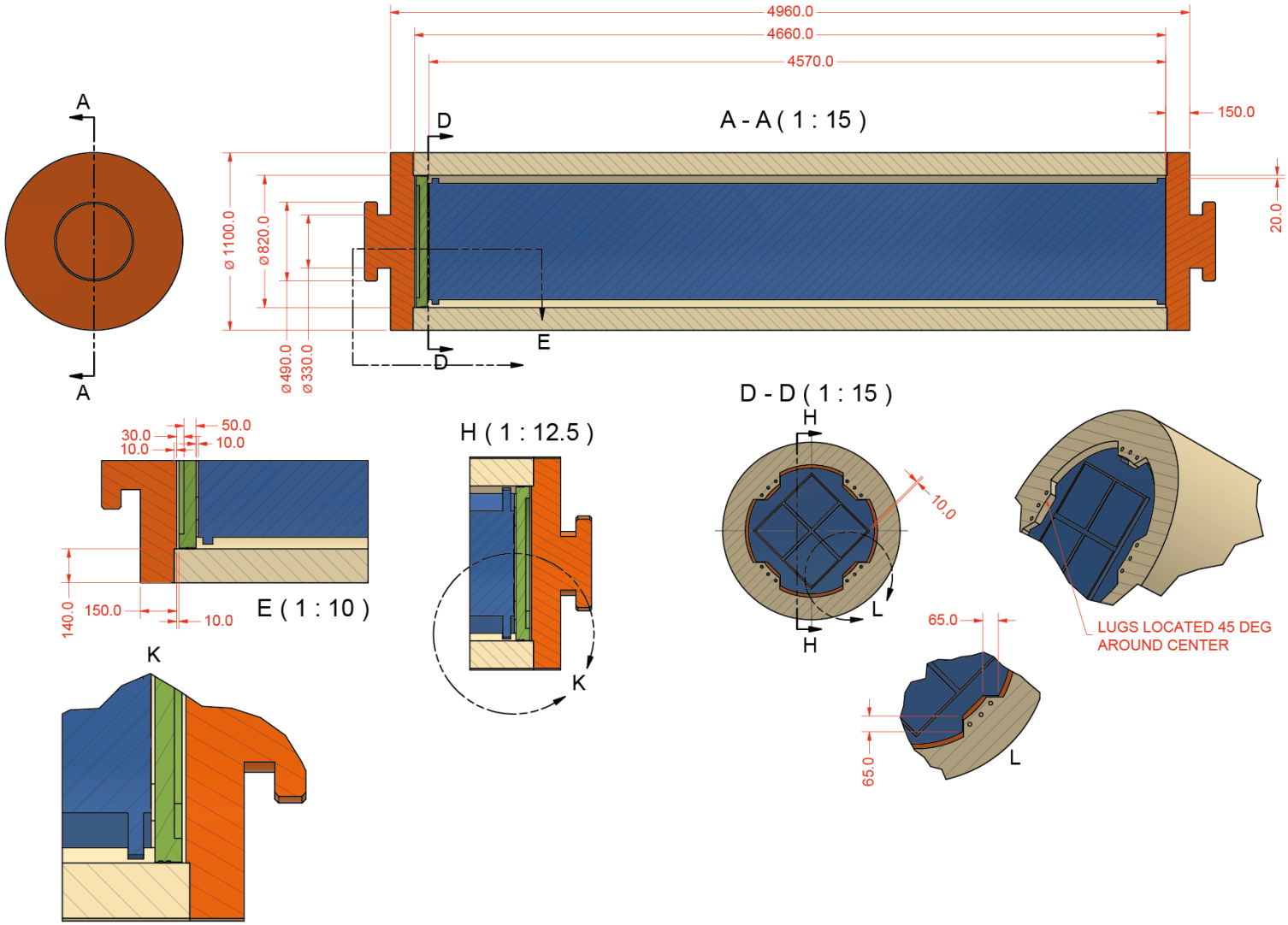

Fig. 3-8: Engineering drawings of a SF-PWR disposal canister

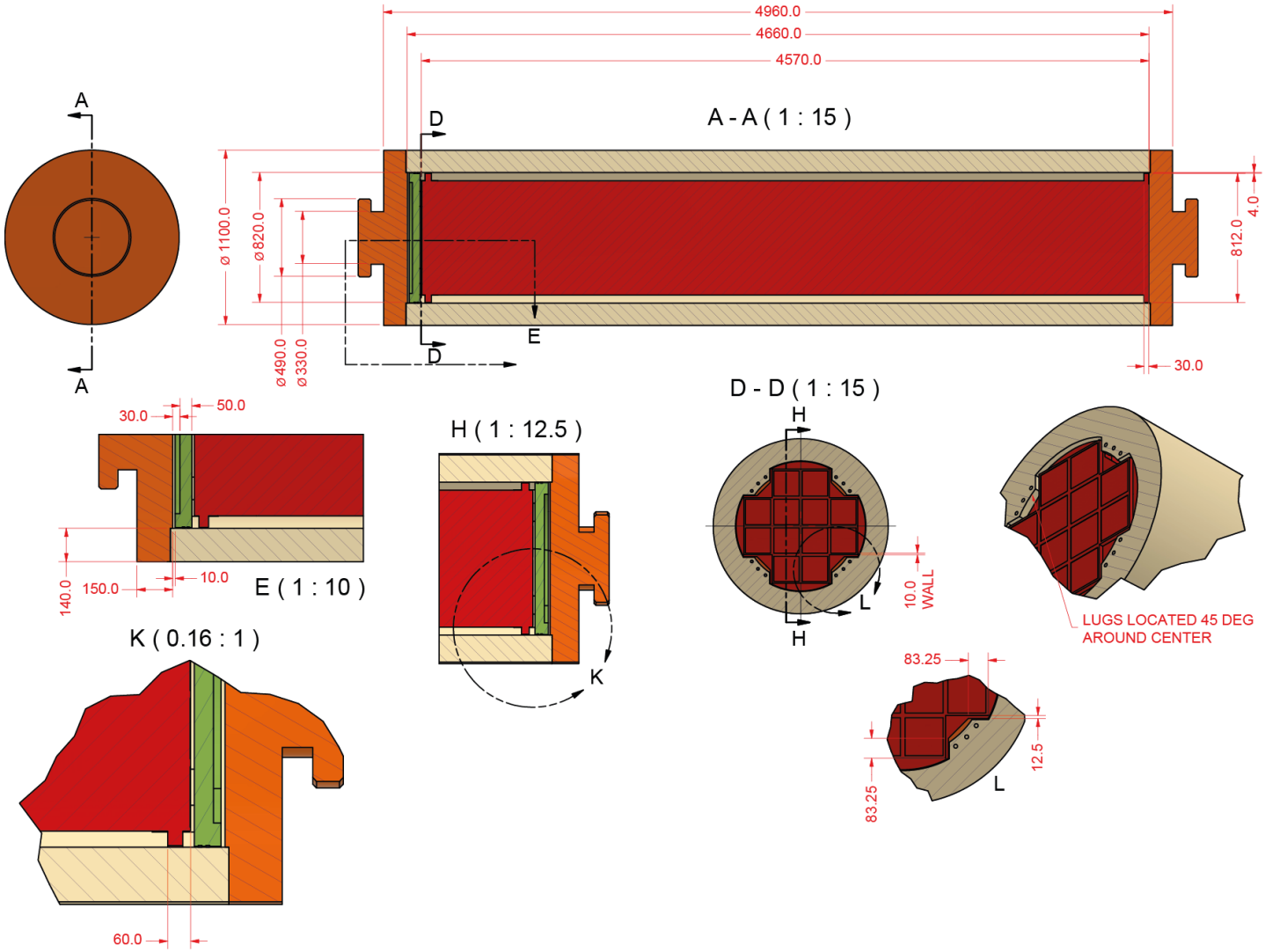

Fig. 3-9: Engineering drawings of a SF-BWR disposal canister

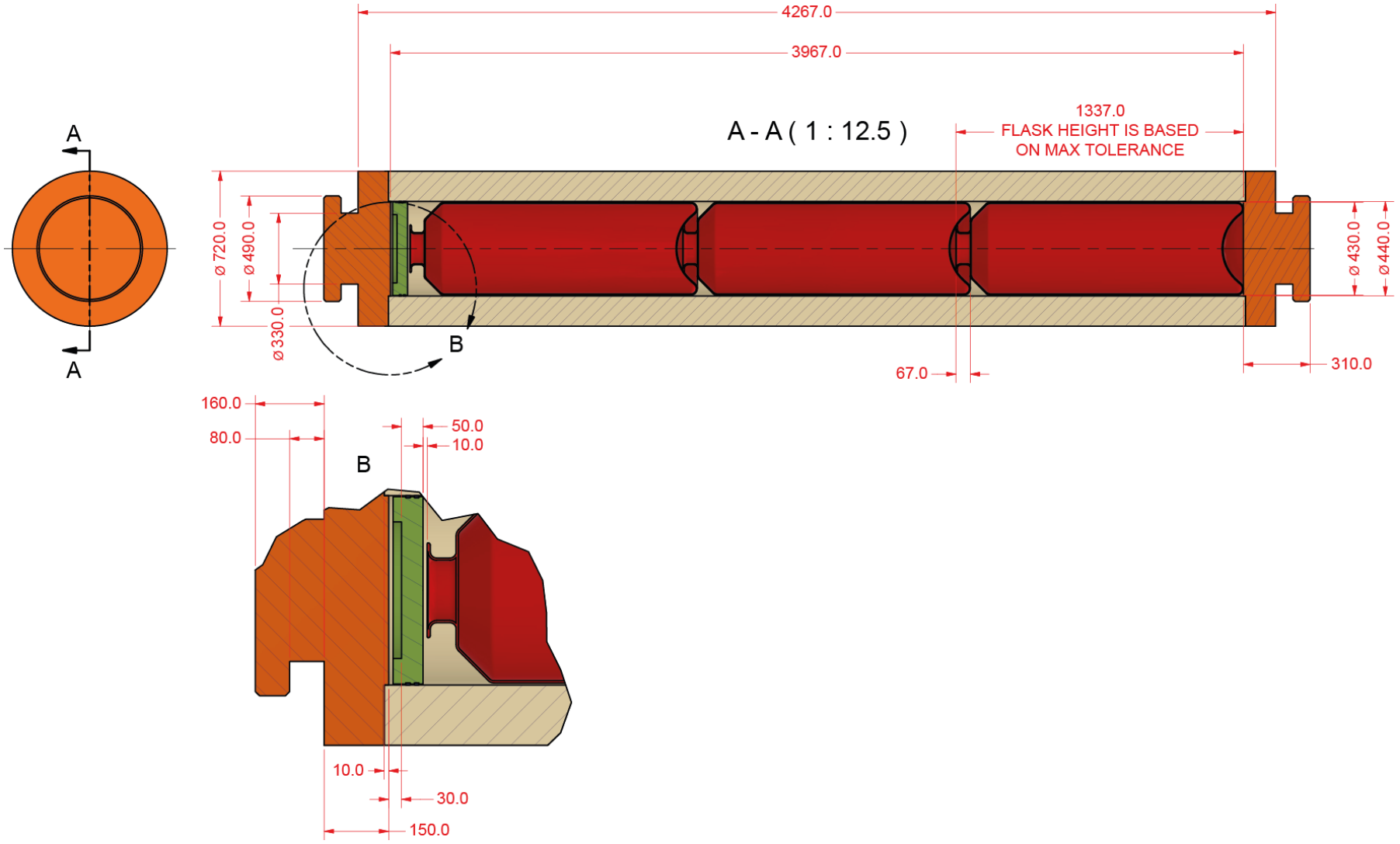

Fig. 3-10: Engineering drawings of a loaded RP-HLW disposal canister

For operational reasons (see Tab. 3-1), an inner lid, currently assumed to be made of carbon steel, is required. This uses metal seals to provide a gas-tight closure until the outer lid has been welded, heat treated and inspected. Given the radiation field of a loaded HLW disposal canister, the inner lid must be mountable within a hot cell (or a service bay) following a robust and easy remote mounting procedure. To fill the canister with inert gas and test gas tightness, appropriate valves or another system allowing for vacuum degassing of the interior and filling with inert gas are required. The pressure differential between the inside and outside of the canister can be conservatively estimated as atmospheric pressure inside and the local vacuum required for the EB welding (5×10^{-2} mbar) on the outside.

Literature relating to lid attachment mechanisms in the nuclear waste management industry was reviewed, and the selected inner lid designs were:

- For the SF disposal canister, a push-fit lid with support lugs and bolts, see Fig. 3-11.
- For the RP-HLW disposal canister, a push-fit lid with metal seals and the addition of a small fillet weld to secure the lid in place, see Fig. 3-12.

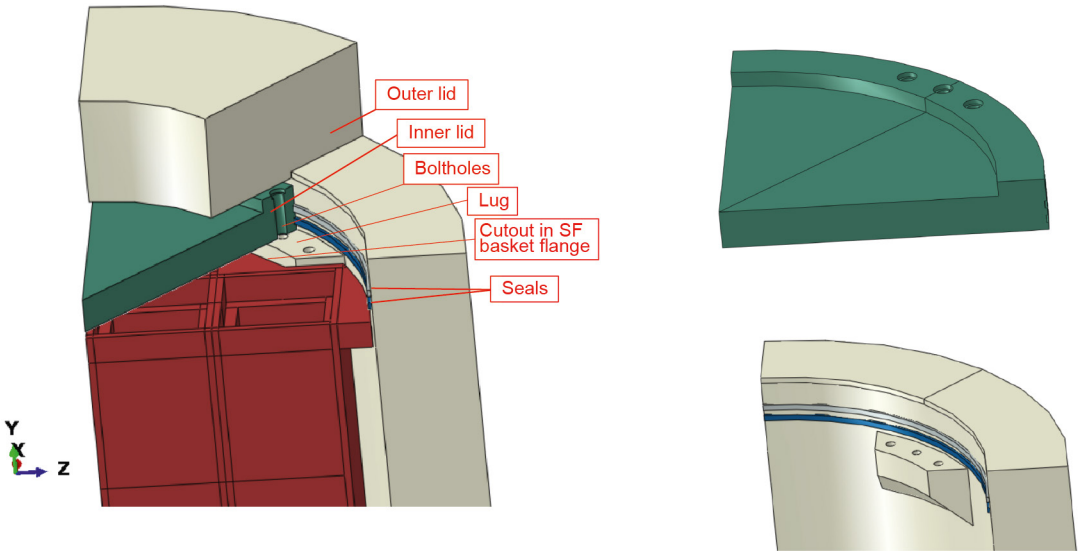

Fig. 3-11: Push-fit lid with support lugs and bolts foreseen for the SF canister: cutaway view (left), inner lid (top right) and lug showing bolt-holes (bottom right)

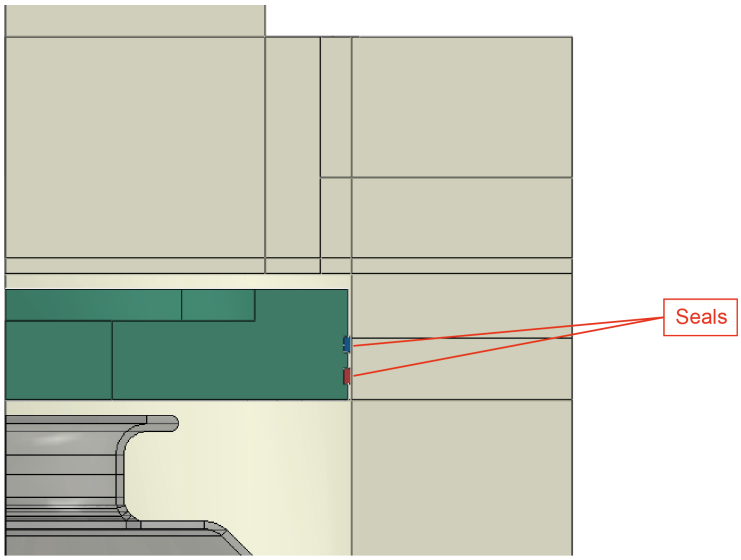

Fig. 3-12: Push-fit inner lid with seals on cylindrical face foreseen for the RP-HLW canister (The fillet weld foreseen to secure the inner lid is not shown).

3.4 Material specification and properties

The material specification presented here covers the cylinder, base and lid forgings for the manufacture of carbon steel HLW disposal canisters and applies to forging thicknesses of up to 150 mm. For this application, a low carbon steel is preferred, to minimise the risk of failure from hydrogen embrittlement (see Section 4.2.4) in the presence of a tensile stress while maintaining an adequate uniform corrosion performance. Importantly, plain carbon steel with the appropriate control of impurities and production related alloy additions is readily weldable. The carbon steel compositional limits are given in Tab. 3-2.

Tab. 3-2: Maximum compositional limits (wt.%) and carbon equivalent (CE_{IIW}) for low carbon steel disposal canister forgings

$CE_{IIW} = C + Mn/6 + (Cr + Mo + V)/5 + (Ni + Cu)/15$

C	Si	Mn	P	S	Cr	Ni	Cu	CE_{IIW}	Notes
0.12	0.30	0.8	0.015	0.010	0.2	0.2	0.02	0.30	Cr + Ni + Mo < 0.25 H < 1 ppm Vacuum degassed (low O, N)

The defined material conforms to the requirements of EN 10250-2 S235J2G3 and EN 10222-2 P245GH, but with additional realisable limitations. In particular, there is a requirement for vacuum degassing and a hydrogen release treatment. In addition to the elements specified in the table, the amounts of Pb, Sn, As and Sb must be provided by the material supplier. Individual forgings shall be supplied in a normalised heat treatment condition. The forgings shall have been normalised at a temperature between 890 and 950 °C.

The mechanical property limits for carbon steel disposal canister forgings with thicknesses of up to 150 mm are given in Tab. 3-3.

Tab. 3-3: Mechanical property limits for carbon steel disposal canister forgings

$R_{p0.2}/R_m < 0.8$

$R_{p0.2}$ is the 0.2% proof strength, R_m is the ultimate tensile strength, A is the tensile elongation at fracture, Z is the reduction of area at fracture, and CVN is the Charpy V-notch impact energy.

	$R_{p0.2}$ [MPa]	**R_m** [MPa]	**A** [%]	**Z** [%]	**CVN(-20°C)** [J]
Max	320	640	-	-	-
Min	220	400	17 (long)	15 (trans)	27

The average surface roughness should be lower than 3.2 µm to facilitate inspection during manufacture and non-destructive testing of the closure weld.

3.5 Canister manufacture

3.5.1 Forging

Following the review by Patel et al. (2012), it was determined that the long forging with the welded base option is the most desirable manufacturing route. The main driver for this decision is primarily associated with the inherent high integrity of hollow forgings.

The ingots used to manufacture the forging will need to be vacuum degassed to achieve the tight compositional control described in Section 3.4. The ingots will need to be rough-forged to a cylindrical blank with a diameter close to that of the canisters. To make one shell body and two lids that form one canister, the ingots will need to undergo open die forging to produce a hollow cylinder and two plain discs, as respectively presented in Fig. 3-13 and Fig. 3-14.

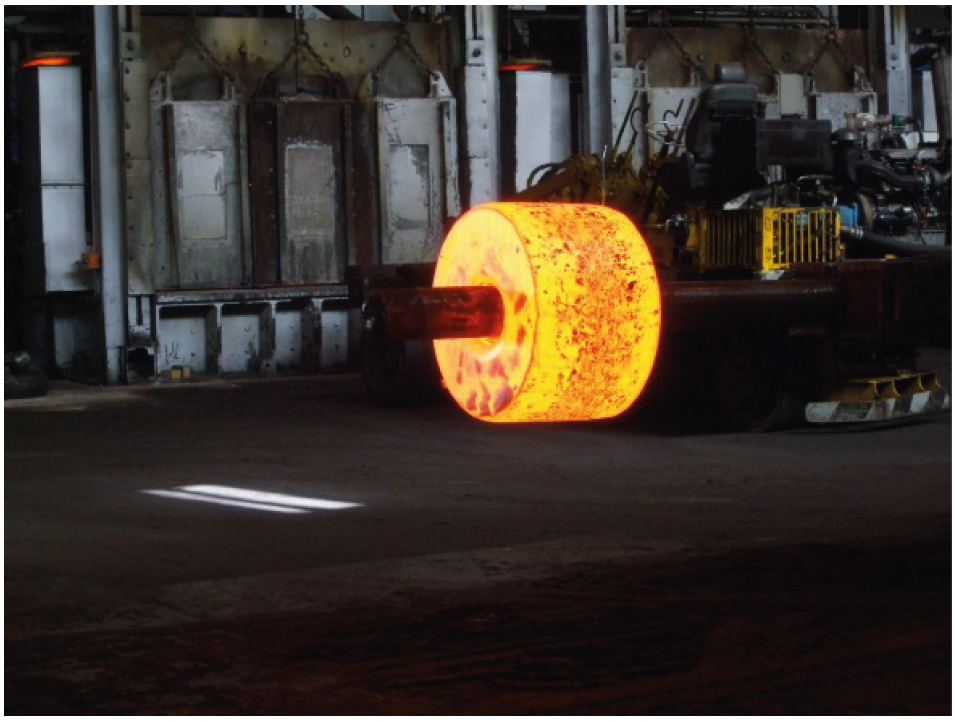

Fig. 3-13: Hollow forging of tubular section

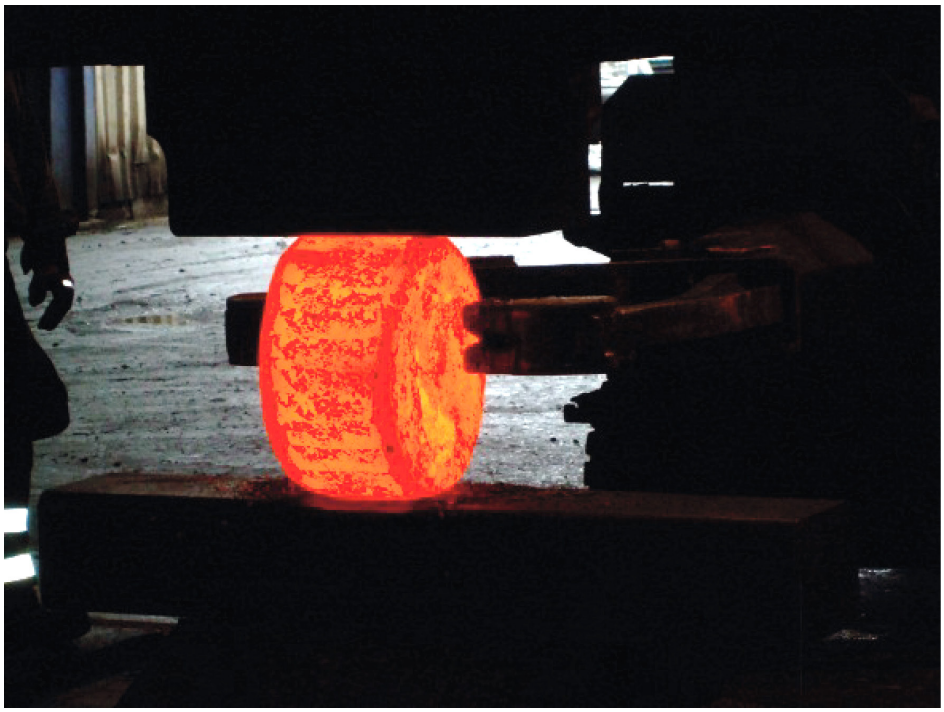

Fig. 3-14: Forging of lid disc

The black forgings will be subsequently machined to produce a hollow tube, representing a canister body with a wall thickness slightly exceeding 140 mm and several mm of positive tolerance on other dimensions; and two lids, with a suitable preparation.

3.5.2 Welding of bottom lid

Similar to the top closure weld (see Section 3.6), the bottom weld of both canister types is too thick (> 100 mm) for conventional arc welding edge preparations such as single or double vee grooves. These edge preparations require a relatively large amount of weld metal, which necessitates a large number of weld passes and welding time. This large volume of weld metal would also generate significant residual stress and distortion. These considerations indicated that a narrow gap welding process would be necessary. The narrow gap welding process is well proven and is in use in a wide range of industries for high thickness welds, similar to the one under consideration. Potential narrow gap processes identified were:

- reduced pressure electron beam (EB);
- narrow gap Tungsten inert gas cold filler wire (TIG-C);
- narrow gap Tungsten inert gas hot filler wire (TIG-H);
- narrow gap submerged arc welding single filler wire (SAW-S);
- narrow gap submerged arc welding multi-filler wire (SAW-M);
- narrow gap gas metal arc welding single filler wire (MAG-S);
- narrow gap gas metal arc welding multi-filler wire (MAG-M).

For the selection of the weld process, a Pugh Matrix decision matrix was used. Tab. 3-4 shows the total rating factors for each welding process. EB outperformed all arc welding processes and was thus deemed the most appropriate for welding the bottom lid of both SF and RP-HLW disposal canisters. The full Pugh Matrix, including criteria, weighting factors, scores and rating factors, is included in App. B.

Tab. 3-4: Comparison of total rating factors obtained for each considered welding process for the bottom lid weld

EB	**TIG-C**	**TIG-H**	**SAW-S**	**SAW-M**	**MAG-S**	**MAG-M**
303.5	240	240	255	265	265	265

The joint design and preparation, as well as the welding procedure for the bottom lid will be the same as those for the top lid and closure weld. These are described in Section 3.6. Just like for the closure weld, only welding from the outer diameter is considered.

Upon completion of EB welding of the bottom lid, the long forging with the welded base will be inspected, after machining to remove residual weld material. If no indications are reported, the canister will be stress-relieved in a global furnace. Any corrective action required will depend on the types of indications reported by inspection and their location. For near-surface and pore-like indications, repair using EB welding could be an option. If planar indications are reported, it will be difficult to perform repairs. Even if it is possible, it could introduce further issues, such as weld shrinkage. Where repair is not an option, the original weld and lid will be removed, and a new lid will be welded and re-inspected.

A commonly used guideline for PWHT is that the joint should be soaked at peak temperature for 2 hours, plus 15 minutes for each additional inch when thickness exceeds 125 mm in accordance with Table NB-4622.1-1 of ASME BPVC.III.1.NB (ASME 2023a). Ferritic joints are typically stress-relieved at temperatures between 580 and 620 °C when a global furnace is used. Machining to final dimensions will then take place since global PWHT typically introduces a layer of oxide crust on all exposed surfaces.

In a structure subject to PWHT, the residual stress is not generally reduced to zero. The level of residual stress remaining in welds after PWHT can be estimated on the basis of stress relaxation tests for all-weld or parent metal specimens, as appropriate. Where these data are not available, it can be assumed that for the bottom lid, the stresses after heat treatment in a global furnace within the range 580 to 620 °C are as follows, according to BS 7910 (BSI 2019b):

- For a flaw lying in a plane parallel to the welding direction (i.e., the stresses to be considered are perpendicular to the weld), the residual stress (Q_m) should be assumed to be 20% of the lesser of the yield strengths of the weld or parent metal.
- For a flaw lying in a plane transverse to the welding direction (i.e., the stresses to be considered are parallel to the weld), Q_m should be assumed to be equal to 30% of the room temperature yield strength of the material in which the flaw is located, or 30% of the greater of the yield strengths of the weld or parent metal for a flaw that lies partly in weld metal and partly in parent metal.

3.6 Closure weld and joint design

3.6.1 Weld process selection

For the selection of a suitable welding process for the top lid closure weld of SF and RP-HLW canisters, two welding processes were compared, namely EB and narrow-gap Tungsten inert gas (NG-TIG). These processes were initially selected due to their applicability to a controlled or hot cell environment as required for the closure weld of a loaded canister. The comparison was based on a decision matrix analysis. The two welding processes were scored against 25 weighted criteria. A numerical score was assigned to each welding process against these 25 criteria using a consistent scoring system, in which 1 represented low confidence and 10 represented high confidence. For each criterion, a rating factor was obtained by multiplying each score by its corresponding weighting. The total rating factor for each welding process was the sum of all the rating factors. The total rating factors for the two processes are shown in Tab. 3-5.

Tab. 3-5: Comparison of total rating factors obtained for each considered welding process for the top lid closure weld

EB	**NG-TIG**
1393	1137

Tab. 3-5 indicates that EB welding scores higher than the NG-TIG welding process and is thus selected. This is predominantly due to its higher productivity and reliability for remote operation. Although hardness and toughness properties after welding are more of a challenge, heat treatment is expected to restore these properties. The details of the comparison for the selection of the canister closure weld process are included in App. B.

3.6.2 Welding procedure specification

Draft preliminary welding procedure specifications (pWPS) have been prepared for the SF disposal canister and for the RP-HLW disposal canister (see App. C). The pWPS contain the information required in accordance with BS EN ISO 15609-3 (BSI 2004), with further data on the potential controls and/or parameter variations which can be used to minimise flaws in thick section welds especially at the start-stop position. The specifications also address the inspection and assembly requirements for the canister, stating initial fit-up limits. In addition, the proposed welding sequences are described in detail and key process parameters are identified. Suggested ranges are stated, which will form the basis of suitable welding conditions that will need to be experimentally refined and tested in order to complete the weld qualification exercise.

The materials presented for welding must be sufficiently clean (locally degreased using acetone) and free from surface residual magnetic field levels above 5 Gauss. Prior to welding, the parts (cylindrical shell body and lid) should be checked to ensure that any surface oxide, mill scale or protective coating has been removed from 25 mm around the joint line. Some light surface oxide is allowed to remain on the canister lid and body 25 mm below the weld region. Fit-up between parts needs to be controlled and should be less than the limits specified in the pWPS. No filler material is intended to be used during the welding process and no preheat is required (the initial temperature of the steel is expected to be between 15 °C and 50 °C at the time of welding due to the decay heat of the HLW). A fronting bar of mild steel is to be used as a weld bead support feature.

The welding operations will be conducted in the following sequence:

- tacking (stitch tacks);
- tacking (full 360° circumferential tack);
- welding (single pass full 360° circumferential weld with 30° slope up and 60° slope down).

To help accommodate the weld cap reinforcement, the joint preparation consists of a V-groove of 60° included angle and with a depth of 7 mm as shown in Fig. 3-15, with a circumferential joint gap between 0 and 0.25 mm. The fronting bar is positioned 7 mm away from the weld groove.

Additional details related to the pWPS proposed for EB welding of the lids of both SF and RP-HLW disposal canisters is given below:

- Welding position: 2G position (PC) or horizontal weld orientation.
- Welding parameters: current: 225 mA ± 5%; voltage: 150 kV ± 1%; welding speed: 80 mm·min^{-1} ± 1%; heat input: ~ 25 kJ·mm^{-1}.
- Gas: local vacuum with a reduced pressure of ~ 5 × 10^{-2} mbar with background helium gas with a flow rate of 0.6 litre·min^{-1}.

The weld is a full penetration butt joint into integral backing type. The minimum joint depth is estimated to be 140 mm (which is the shell thickness) plus ~ 20 mm extending beyond the step into the integral backing of the lid.

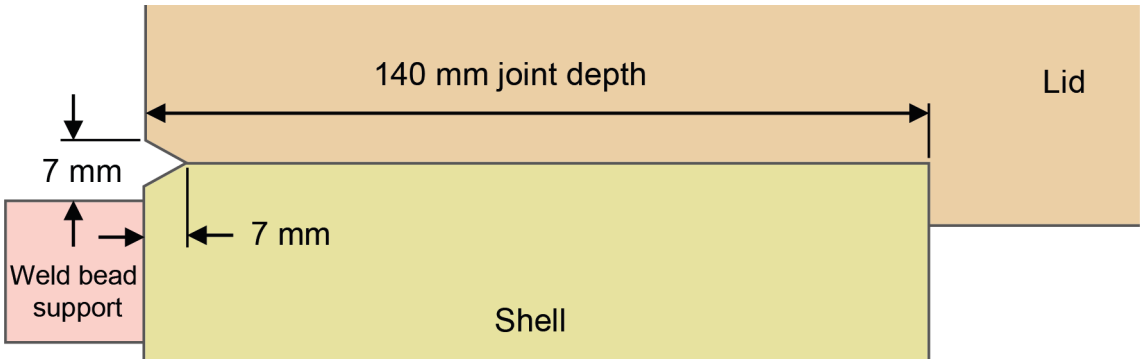

Fig. 3-15: Basic joint profile

The weld region of both top and bottom lids should be cleaned (machined) to remove residual weld material or scale resulting from heat treatment during the manufacture of the closure weld.

3.6.3 Thermal model of the EB weld

This section covers step 1 of the modelling approach discussed in Section 3.2.

The purpose of the thermal model of the welding process, which was developed in Abaqus, is to evaluate the temperature of the canister material in the region surrounding the EB weld resulting from the welding process. Two models were developed, one of the SF disposal canisters and one of the RP-HLW disposal canister. The canister was the only part included in the weld simulation thermal model, as the internal basket structure does not significantly influence the behaviour of the canister body during welding.

Regarding the canister geometries (Fig. 3-16), the SF canister geometry was modelled in accordance with Fig. 3-8 and Fig. 3-9, and the RP-HLW canister geometry was modelled in accordance with Fig. 3-10. The full material properties used to model the SF and HLW canister are given in App. E.

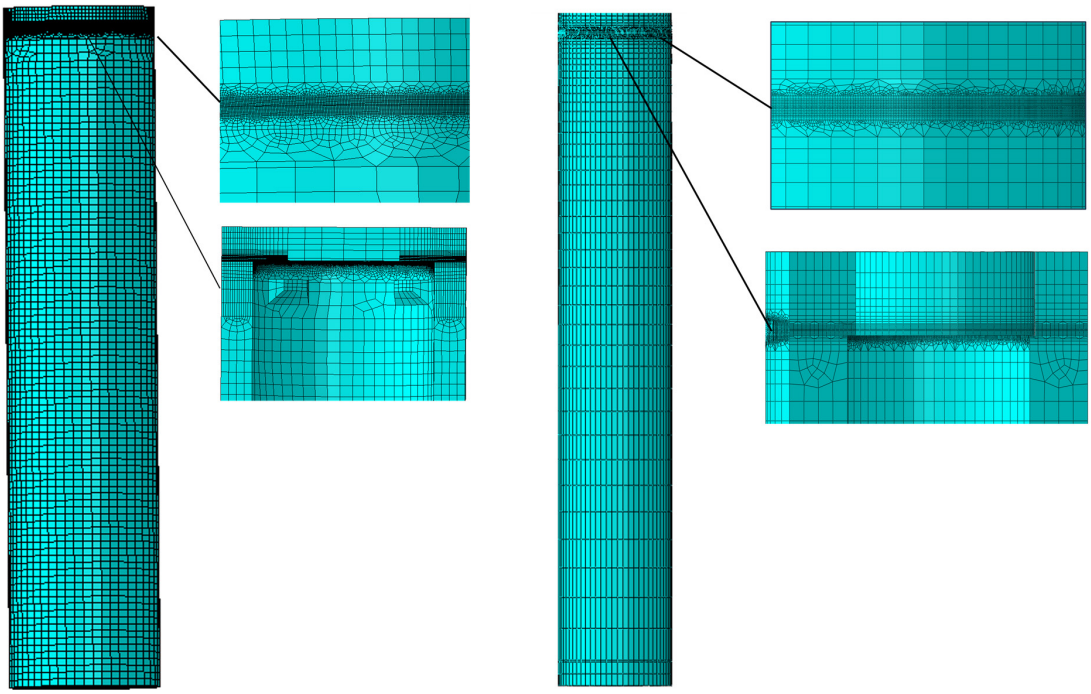

Fig. 3-16: Views showing the mesh used in the thermal model of the SF disposal canister (left) and RP-HLW disposal canister (right), with details showing internal and external views of the highly refined mesh in the weld region

The slope-in and slope-out described in App. C were included in the model such that the beam travelled a total of 451° around the circumference. The slope-in and slope-out were the same for both canisters. After heating, a cooling step was simulated to return the canister to ambient temperature. Radiation boundary conditions were prescribed on the inner and outer surfaces of the model (using an emissivity of 0.8) and convection to ambient conditions was also specified over the lower length of the canisters on the basis that this part would be outside the vacuum chamber.

Fig. 3-17 illustrates typical resulting temperature fields during the simulations; the keyhole is indicated by the grey region in each figure.

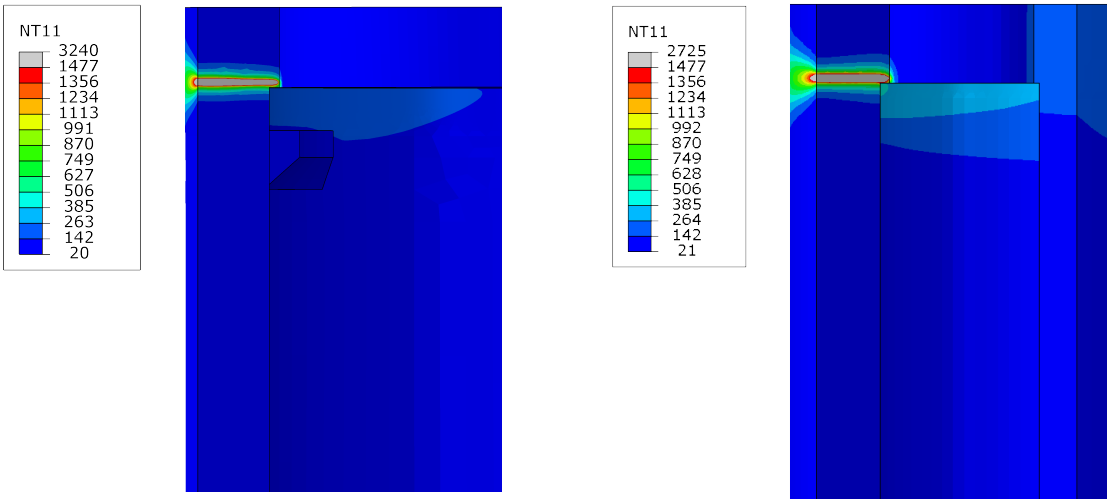

Fig. 3-17: Illustrative cut-away images of the weld simulations in progress, showing temperature (°C) where the grey region represents the keyhole: SF disposal canister (left) and RP-HLW disposal canister (right)

3.6.4 Mechanical model of the EB weld

This section covers Step 2 of the modelling approach discussed in Section 3.2.

The transient temperature field (heating and subsequent cooling) described in Section 3.6.3 was mapped on to a mechanical model to predict the resulting stress field. The mechanical model, shown in Fig. 3-18, represents a one-degree segment of the canister body, with symmetry conditions modelled on the appropriate faces.

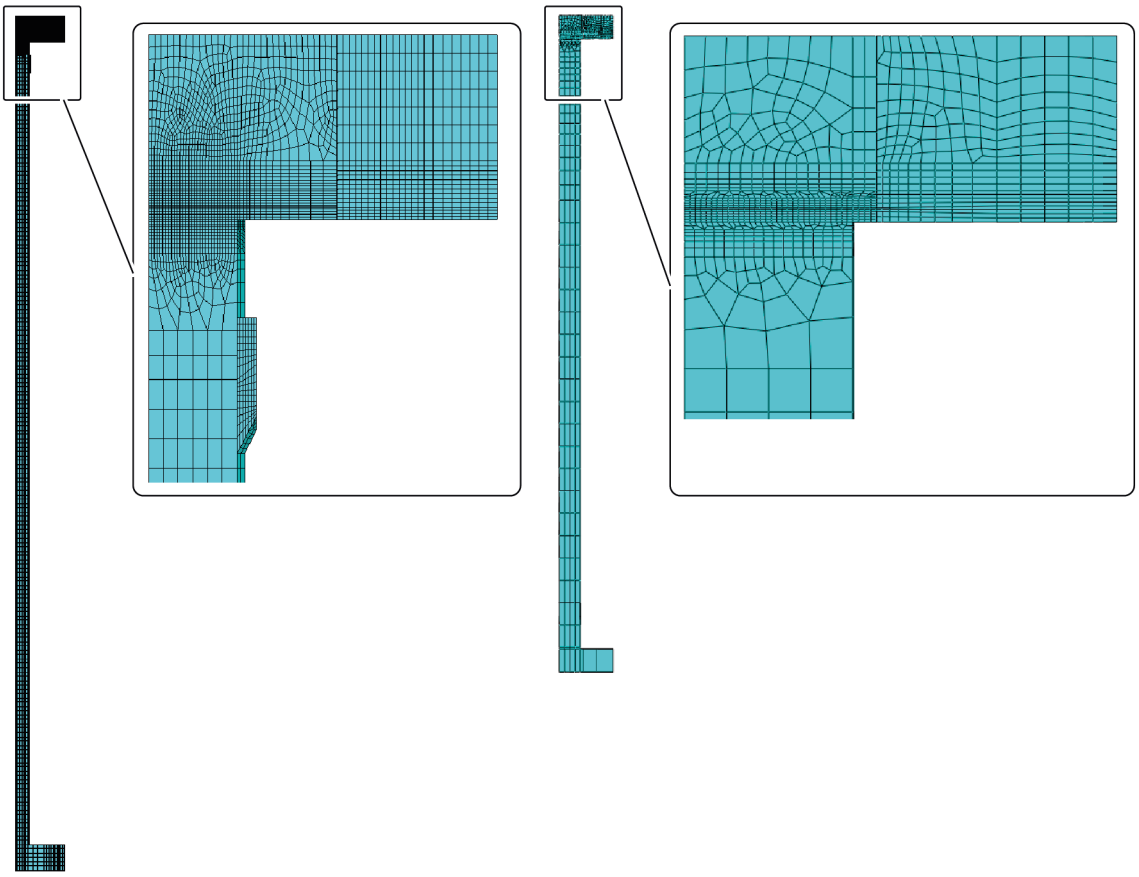

Fig. 3-18: Mechanical welding process model, showing the finite element mesh; (left) SF disposal canister model and (right) RP-HLW disposal canister model

The elastic material properties and the post-yield stress-strain behaviour were derived from testing and included rate- and temperature-dependent stress-strain curves (App. D). It should be noted that these test data had a room temperature yield strength of 294 MPa; therefore, the yield stress obtained from testing is at the upper end of the yield stress range for this material (220 MPa to 320 MPa). The residual stresses evaluated from the modelling are at the conservative end of the expected range. The thermal expansion coefficient is shown in App. E.

Significant features of the mechanical model are:

- Hoop symmetry was modelled on all appropriate faces.
- Edges on the central axis were constrained in the radial direction.
- The base was restrained in the vertical direction.
- The model was meshed predominantly with first-order hexahedral stress elements (Abaqus element C3D8R) and mesh convergence was verified.
- Young's modulus was modelled as temperature-dependent.
- Material annealing was included in the model by setting the equivalent plastic strain to zero when the temperature exceeded 1,150 °C.

The computed stress field after simulated cooling to ambient temperature is shown in Fig. 3-19. These stresses represent the as-welded residual stresses in the canister, before PWHT.

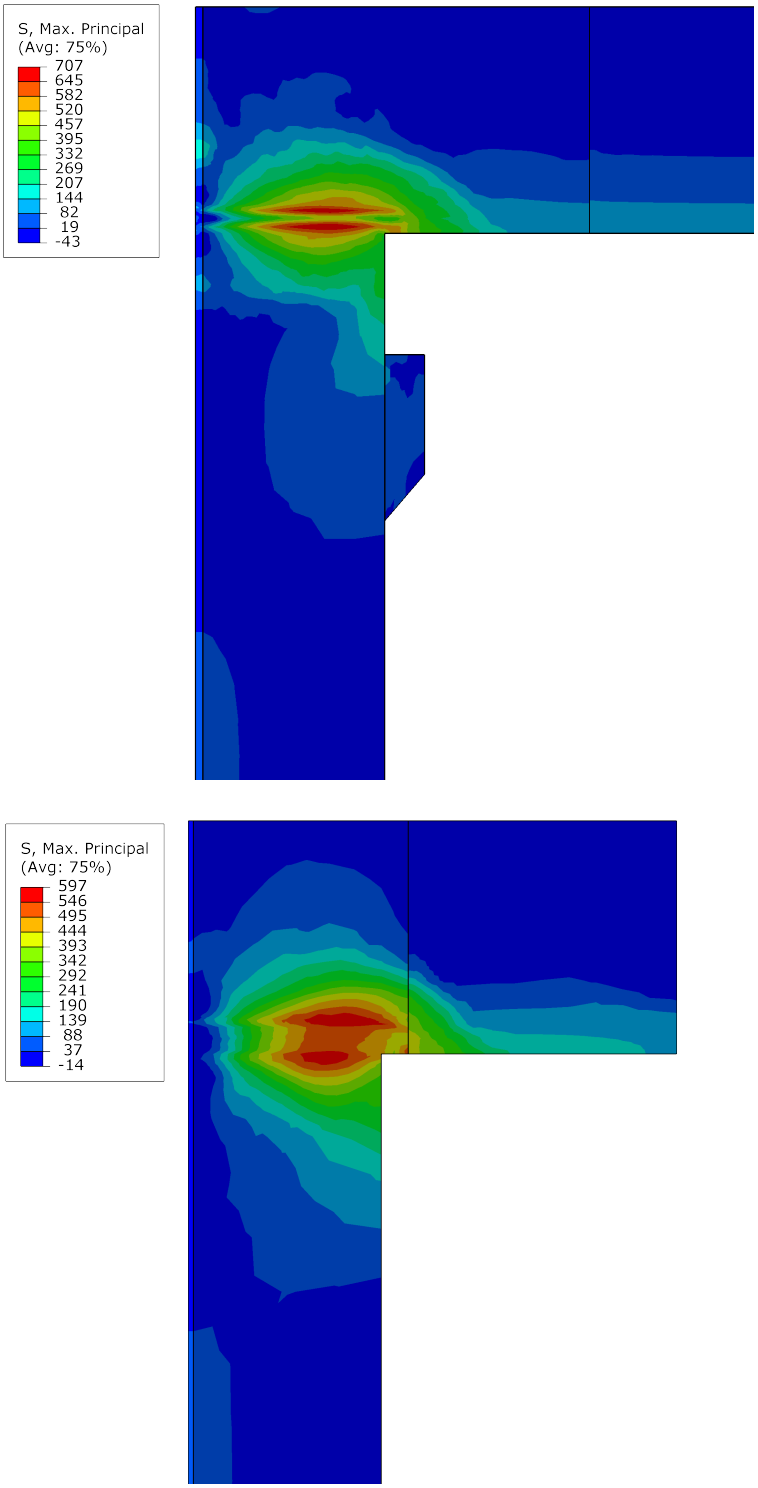

Fig. 3-19: As-welded maximum principal stress (MPa) computed for the SF disposal canister (top) and the RP-HLW disposal canister (bottom) after completion of welding and cooling to ambient temperature

3.7 Post-weld heat treatment

Upon completion of the closure weld, it is no longer possible to heat treat the canisters in a furnace as is done for the bottom lid (see Section 3.5.2) due to the risk of overheating the contained waste. The temperature limits employed are 400 °C for SF and 500 °C for RP-HLW. Therefore, the only practical approach is to apply local PWHT. This can result in a higher level of residual stress than that expected for heat treatment carried out in a global furnace. The level of residual stress depends on factors such as the temperature attained, the width of the heated band and the width of the insulated region. Because of the wide range of variables, most flaw assessment procedures do not offer general recommendations. For this reason, numerical simulation is employed to predict the welding residual stresses after local PWHT. The inclusion of higher residual stresses due to the lower efficiency of local heat treatment in the assessment of the closure weld bounds the acceptance limit of the bottom lid weld. The sizes and requirements of the heating bands are discussed in Section 3.7.1. The modelling of residual stresses after PWHT is discussed in Section 3.7.2.

The effects of PWHT on tensile properties of C-Mn steels have been studied extensively. A reduction in strength of the parent material is expected following PWHT, but the effect varies significantly based upon the temperature and the duration. Watkins et al. (1963) identified that the temperature of PWHT was critical in determining the extent of strength reduction or improvement in toughness for welds and HAZs. They employed relatively long PWHT times (up to 72 hours, nominally 4.5 hours per 25 mm of thickness), and not all material types were tested in all conditions. They reported 6% drop in yield strength after PWHT. Similar observations were reported by Gulvin et al. (1972) in C-Mn pressure vessel steels (25 and 50 mm thick). There was a scatter band of ± 7% in change in yield strength, ± 5% in change in ultimate tensile strength (UTS). Salkin (1987) identified that PWHT at temperatures of 600 °C resulted in a reduction in yield strength of approximately 2% in C-Mn steels. Furthermore, it is known (Goldak & Nguyen 1977, Punshon & Elliott 1985, Hesse et al. 2016) that electron beam welds have low fracture toughness in the as-welded condition, and that this is significantly improved by the application of PWHT.

It is very rare that in modern steel making processes, the tensile properties of a steel would be lower than the specified minimum limits. Until specific testing identifies the actual properties to be used in calculations, it is recommended that the specified minimum properties of the parent steel are used in desktop analyses and assessments. This is reflected in the ECA calculations presented in Section 4.3.

3.7.1 Thermal model of PWHT

This section covers step 3 of the modelling approach discussed in Section 3.2.

The PWHT thermal model has two objectives:

- Computation of the transient temperature field in the canister during PWHT to simulate the stress relaxation (in the subsequent mechanical model, see Section 3.7.2) and residual stress after PWHT.
- Computation of the temperatures in the SF (both BWR and PWR) and RP-HLW disposal canisters during the PWHT process to verify that the maximum temperature experienced did not exceed the specified limit.

Considering the geometries used in the PWHT models, quarter symmetry was employed in all cases.

For the SF-BWR canister geometry, in addition to the canister, the internal structure, i.e., the FAs and basket, were modelled in the PWHT thermal model. The basket was drawn in accordance with Fig. 3-9. The FAs were modelled with a simplified geometry with a total length of 4,481 mm as shown in Fig. 3-20. The stainless-steel handle had a mass of 1.97 kg and was 139 × 139 mm in cross-section. The length of the assembly representing the Zircaloy rods (shown in red in Fig. 3-20) had a length of 4,280 mm and was modelled with a 159 × 159 mm cross-section. By modelling a larger cross section, a simplified and conservative model was attained. The SF is in contact with the basket and so heat transfer is by conduction, which is a more efficient method of heat transfer than radiation. The density of the SF was corrected to ensure that the mass of the SF in each fuel assembly was 294 kg.

A sensitivity study was undertaken to compare different simplifications of the FA geometry. In the first case, there was a 21.4 mm gap between the handle and SF; this was compared to the case where there was no gap. The wall thickness of the handle was adjusted to ensure that the total length of the FA and mass of the stainless-steel handle was the same in both geometries. It was found that the maximum temperature in the cladding was 1.3 °C higher in the case where the stainless-steel handle was in contact with the spent fuel rods, and so this result is reported below. The wall thickness of the stainless-steel handle used was 1.4 mm with a base thickness of 5 mm and a handle height of 201 mm.

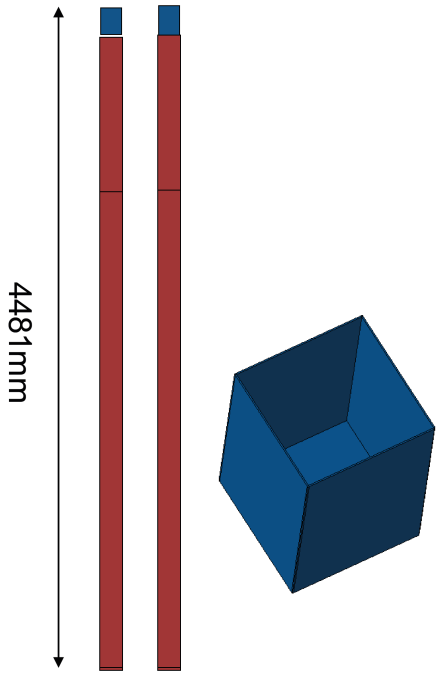

Fig. 3-20: Simplified geometry of BWR fuel assembly employed in the PWHT thermal model

A sensitivity study was undertaken whereby there was a 21.4 mm gap between the handle and SF (left) and no gap (middle). The detail of the stainless-steel handle is shown on the right.

For the SF-PWR model, the canister was the same as for the SF-BWR. However, the FAs and basket differed. Based on the results of the SF-BWR sensitivity study, the stainless-steel handle was modelled in contact with the Zircaloy rods. A total basket length of 4,570 mm and FA length of 4,293 mm was used with a handle height of 284 mm. The Zircaloy rod length was therefore 4,009 mm. The handle had the same shape as the SF-BWR handle, but with a cross section of 215 × 215 mm and a base wall thickness of 10 mm. The thickness of the side walls was adjusted to preserve the overall handle mass of 10.17 kg.

In the case of the RP-HLW model, three flasks containing vitrified HLW were added to the model as shown in Fig. 3-21. The key dimensions of the flasks were taken from Fig. 3-10.

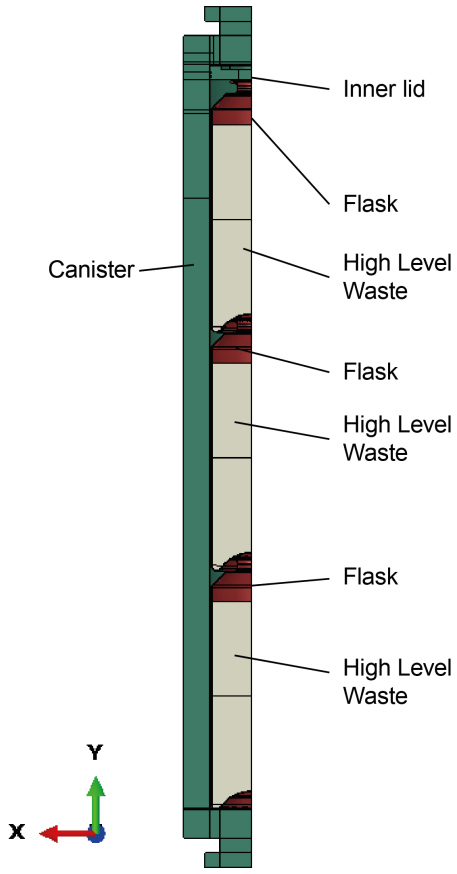

Fig. 3-21: PWHT thermal model of RP-HLW disposal canister

The material properties used in the thermal model are shown in App. E. These properties were the same as those used in previous work (Patel et al. 2012). They have been compared to the literature (Popov et al. 2000) and found to be comparable. For the SF models, the basket was assigned the same material properties as the canister. The SF was assigned the properties of UO_2. Considering the stainless steel handle, the thermal material properties for AISI 304L stainless steel were used for the SF-BWR canister and AISI 321 for the SF-PWR canister models. For the RP-HLW canister model, the flasks were AISI 309 stainless steel.

The models were meshed using linear heat transfer elements (Abaqus element DC3D8), refined in the areas of interest. Mesh convergence was verified. Views of the mesh in the three geometries modelled are shown in Fig. 3-22 and Fig. 3-23.

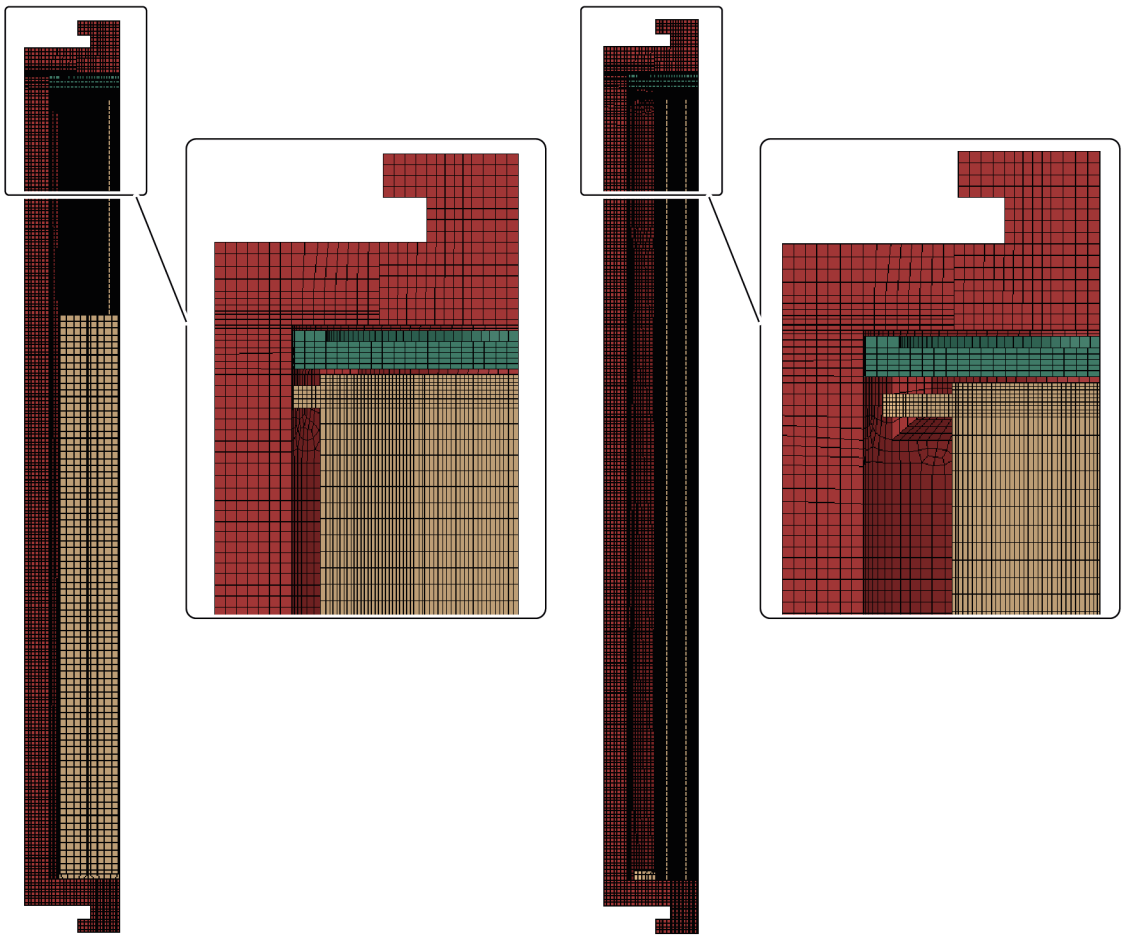

Fig. 3-22: PWHT thermal model of the SF-BWR disposal canister (left) and SF-PWR disposal canister (right) showing the mesh in the area of interest around the soak band and weld

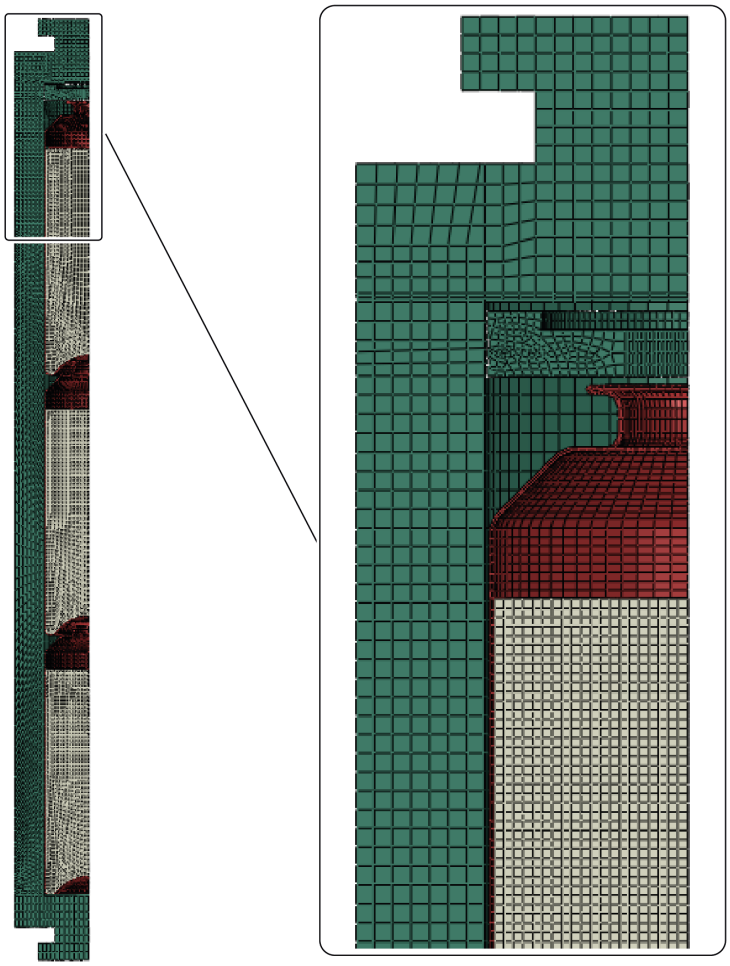

Fig. 3-23: PWHT thermal model of the RP-HLW disposal canister showing the mesh in the area of interest around the soak band and weld

The PWHT processes modelled use the three zones defined in AWS D10.10 (AWS 2009). These are the soak band (SB), the heat band (HB) and the gradient control band (GCB).

The SB is the area which must have a certain temperature to activate the creep mechanisms that relieve the residual stresses at the weld. This temperature was controlled to 600 °C ± 25 °C. In accordance with AWS D10.10 (AWS 2009), the length of the SB was 51 mm either side of the weld, resulting in a total SB length of 102 mm (assuming the weld thickness to be negligible).

The HB is the area where heat is applied. In the FE models, a surface heat flux was applied to the outer surface of the canister over the length of the HB. Using the adapted formula from AWS D10.10 (AWS 2009), the length of the HB was calculated using the equation below:

$$HB = SB + \sqrt{Rt} \qquad [1]$$

where HB is the heated band half-length; SB is soak band half-length, in this case 51 mm; R is the outer radius; t is the wall thickness.

This gave an HB half-length of 328 mm for the SF canisters, and 275 mm for the RP-HLW canister.

The GCB is the area outside the heated band in which thermal insulation material can be placed to decrease heat loss. Equation [2] was used to calculate the length of the GCB either side of the weld (AWS 2009).

$$GCB = HB + 2\sqrt{Rt} \qquad [2]$$

where GCB is the gradient control band half-length.

This gave a GCB of 883 mm for the SF disposal canisters, and 724 mm for the RP-HLW disposal canister.

In addition, a body heat flux was included to model the decay heat generated by the SF and RP-HLW. In the SF models the total heat from the SF is 1,500 W per canister. In the RP-HLW model it is taken as 1,250 W per canister.

Heat transfer by radiation was accounted for between the basket and the interior of the canister chamber, and for the space between the lid and the canister interior, using Abaqus gap radiation, which approximates the radiation direction as normal to the canister surface. The Abaqus cavity radiation method was applied in the space between the top of the FAs and the lid, accounting for symmetry in the cavity definition. External radiation and convection were modelled on the outer surface of the canister outside the GCB, with a sink temperature of 20 °C. The heat transfer coefficient for convection is 0.025 $mW \cdot (mm^2 \cdot K)^{-1}$ and the emissivity of all surfaces was 0.8 (Patel et al. 2012). A sensitivity study was undertaken which varied the emissivity between 0.07 and 0.9; it was found that the maximum temperature in the SF changed by less than 10%, indicating that the temperature of the SF is insensitive to the value of the canister emissivity. The regions covered by the GCB, HB and SB were assumed to be perfectly insulated. Fig. 3-24 illustrates the heat band area as modelled for the SF-BWR and RP-HLW canisters.

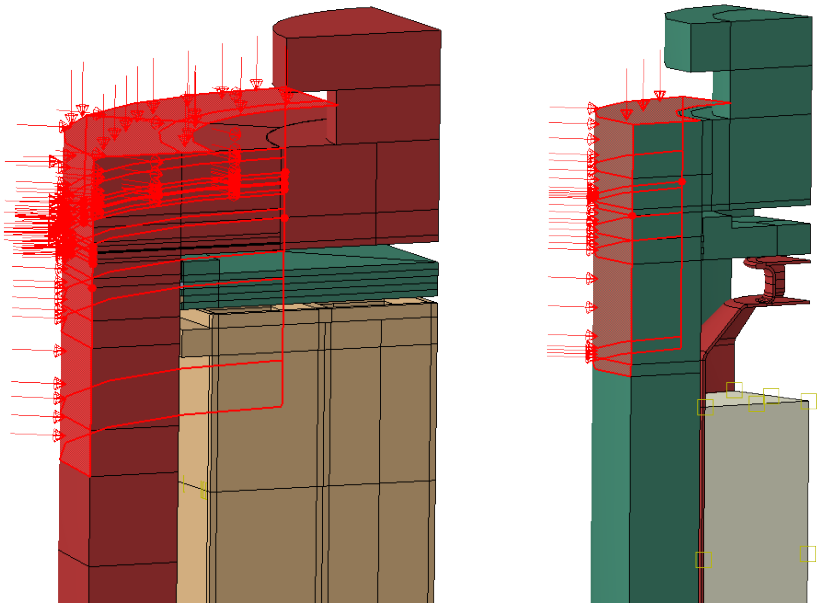

Fig. 3-24: PWHT model showing the HB area over which heat is applied to the model: SF-BWR disposal canister (left) and RP-HLW disposal canister (right)

The models were run using a transient procedure in which the heat flux on the soak band was uniformly increased such that the temperature at the outer surface of the closure weld followed the prescribed temperature increase over 7.1 hours, and was then held at this temperature for 2.8 hours (Tab. 3-6). This simulates the heat input from an external heat mat controlled by a thermocouple placed adjacent to the weld. This is depicted in Fig. 3-25 to Fig. 3-28. Fig. 3-25 summarises the computed temperature distribution at the end of the hold period over the whole model for the three cases analysed. Fig. 3-26 to Fig. 3-28 show the temperature at the control point compared to the prescribed heating profile for the three canisters. The diffusion of the heat through the thickness over time is then calculated by the simulation, so that it accurately represents the through-thickness temperature distribution from the transient external heating. The difference across the weld at the end of the hold period was found to be between 15 and 28 °C for the various models.

Following the completion of the hold period, the heat input was turned off and the canister was allowed to cool naturally. It was assumed that the insulation would remain in place until the canister cooled to approximately 400 °C before being removed to allow uncontrolled cooling to ambient.

Tab. 3-6: PWHT steps, duration and temperature

Step	**Elapsed time** [hours]	**Temperature** [°C]
	0	20
Heat to 425 °C	4.0	425
Heat to 600 °C	7.1	600
Hold	9.9	600
Cool to approximately 400 °C	13 (minimum, may be longer depending on cooling rate)	400
Insulation removed, cool to ambient	Depends on cooling rate	20

For the SF-BWR canister, the results of the PWHT thermal model shown in Fig. 3-26 indicate that the maximum temperature in the Zircaloy was evaluated to be 366.3 °C. For the SF-PWR canister (Fig. 3-27), the maximum temperature in the Zircaloy was evaluated to be 296.7 °C. For the RP-HLW canister, the results shown in Fig. 3-28 indicate that the maximum temperature in the glass was evaluated to be 354 °C. Note that in Fig. 3-26 to Fig. 3-28 the temperature shown for the Zircaloy or glass is the maximum at any point of the top surface at a given time.

Therefore, it was concluded that the proposed PWHT regime can be used as specified for all canister variants. These analyses also computed the temperature distribution in the canister body over time, which was then used in the final stage of the residual stress modelling (see Section 3.7.2).

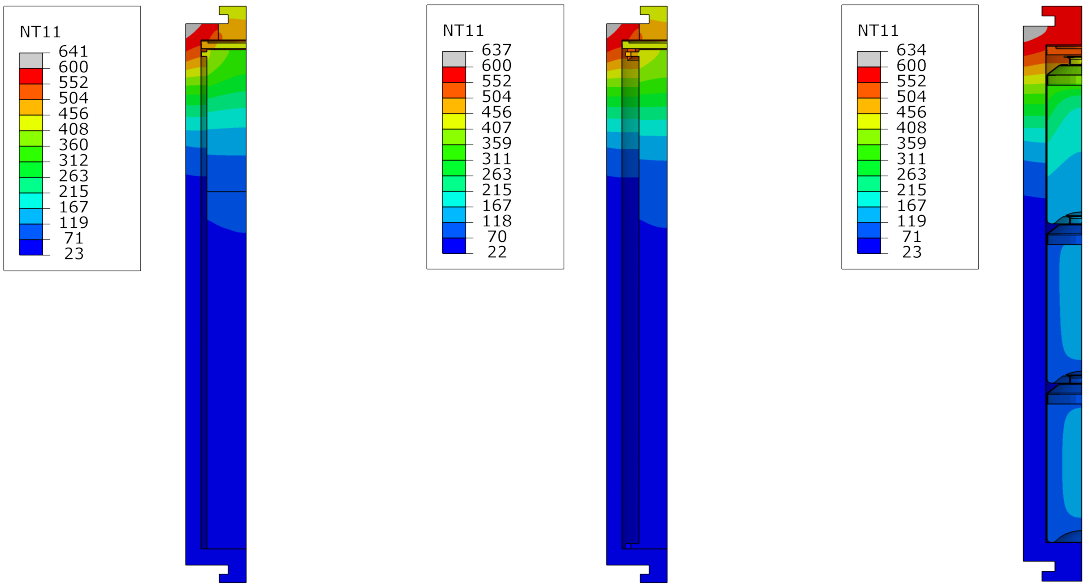

Fig. 3-25: The temperature distribution at the end of the hold step (°C) for the SF-BWR (left), SF-PWR (middle) and RP-HLW (right) disposal canisters

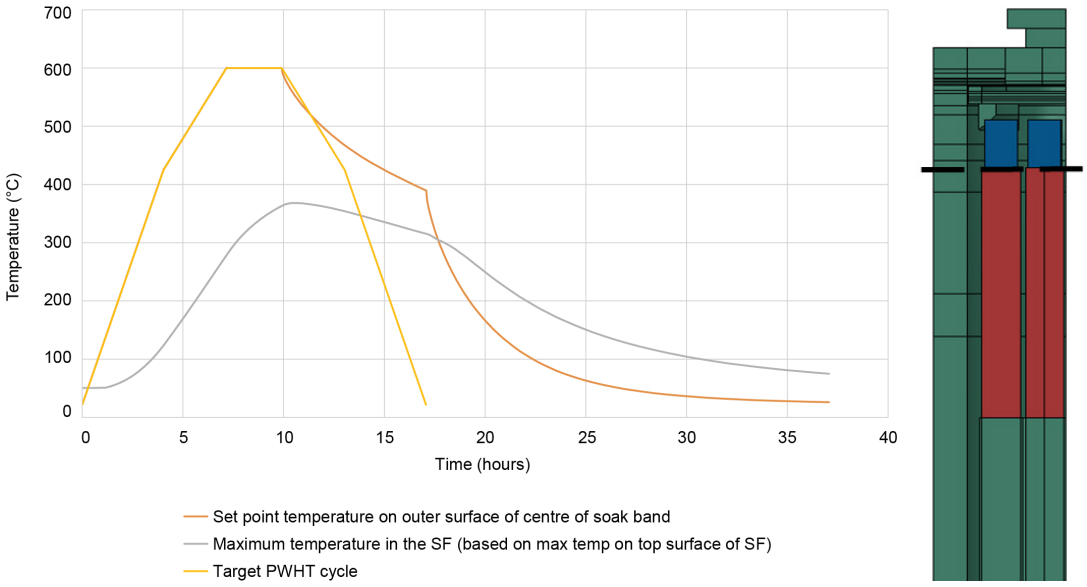

Fig. 3-26: Maximum temperature (°C) at the top of the SF (location of the dotted line) over time for the SF-BWR disposal canister; compared to the actual and target temperatures at the control location on the outer surface of the weld. Stainless-steel handle in blue, SF in red, basket removed for visibility

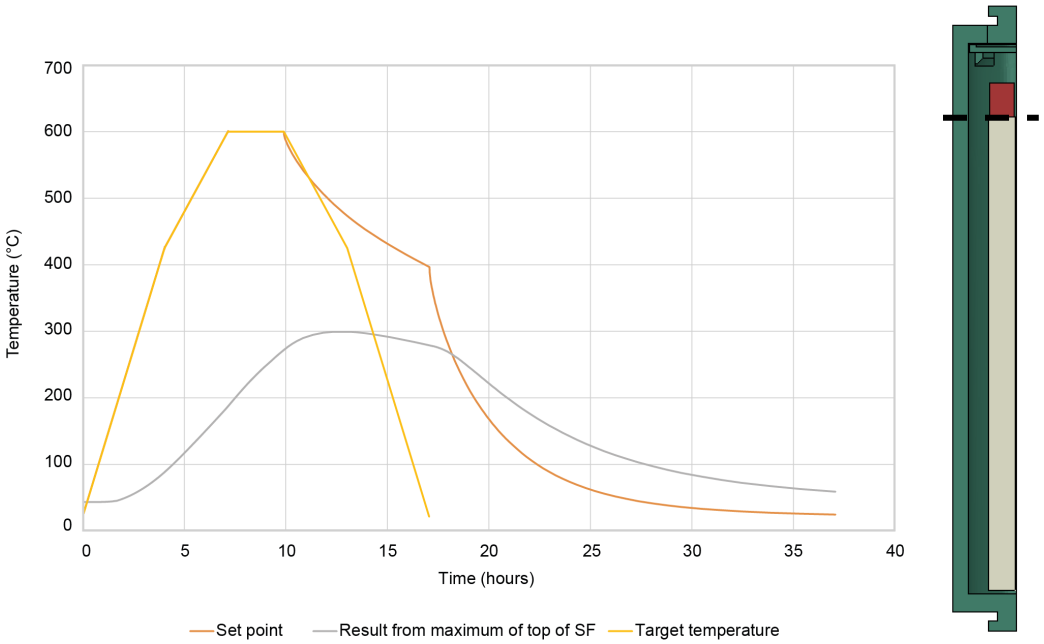

Fig. 3-27: Maximum temperature (°C) at the top of the SF (location of the dotted line) over time for the SF-PWR disposal canister; compared to the actual and target temperatures at the control location on the outer surface of the weld. Stainless-steel handle in red, SF in cream, basket removed for visibility

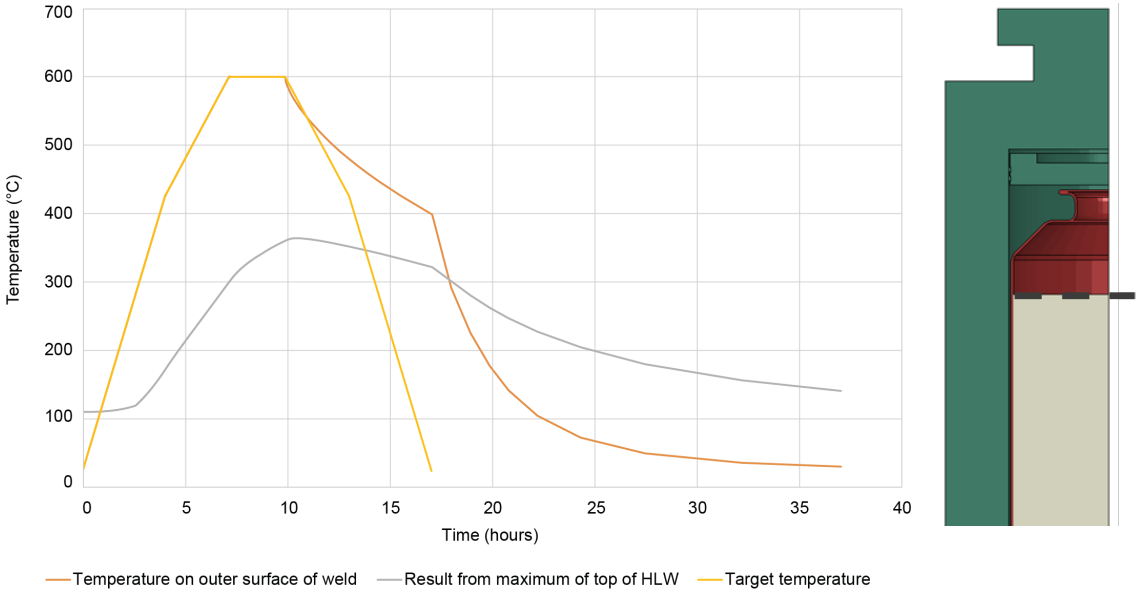

Fig. 3-28: Maximum temperature (°C) at the top of the glass (location of the dotted line) over time for the RP-HLW disposal canister; compared to the actual and target temperatures at control location on the outer surface of the weld. Stainless-steel flask in red, glass in cream

3.7.2 Mechanical model of PWHT

This section covers step 4 of the modelling approach discussed in Section 3.2.

The final stage of the PWHT modelling was to compute the reduction in residual stress (i.e., the stress relaxation) during PWHT for the SF and RP-HLW disposal canisters. The PWHT mechanical models used the same geometry, mesh, boundary conditions and temperature-dependent material properties (including temperature-dependent Young's modulus) as the mechanical model for the welding process (see Section 3.6.4). The models were initialised with the final stress-strain state of the welding process model (after cooling); the temperature field from the relevant PWHT heat transfer simulation was then applied, with the model temperature being increased gradually over the appropriate time, held at that temperature and then cooled (see Section 3.7.1). The accuracy of the welding residual stress simulation was refined using test data generated from a P245GH grade steel, which has similar properties to the specifications described in Section 3.4. Details of the experimental data and analyses are included in App. D.

The computed maximum principal stresses after completion of the PWHT cycle and cooling to ambient temperature are shown in Fig. 3-29 and can be compared to Fig. 3-19. As before, axial stresses (i.e., perpendicular to the weld) were extracted along a radial path through the closure weld centreline for each canister. These are shown, along with the comparable as-welded residual stress results, in Fig. 3-30 and Fig. 3-31 for the SF and RP-HLW disposal canisters respectively. These results constitute the computed residual stress field in the as-built canister after PWHT.

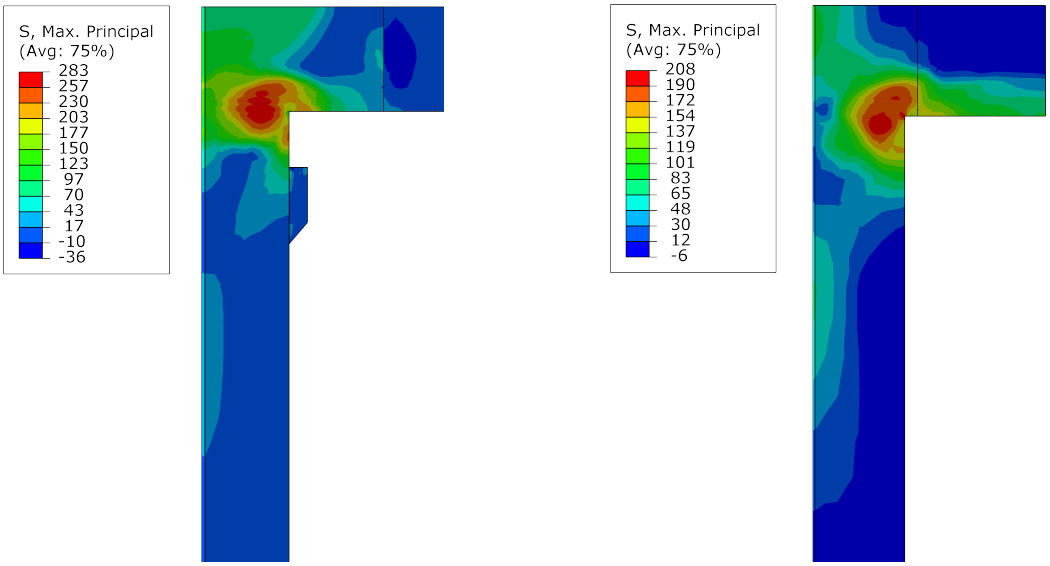

Fig. 3-29: Maximum principal stress (MPa) computed for SF disposal canister (left) and RP-HLW disposal canister (right) after completion of PWHT and cooling to ambient temperature

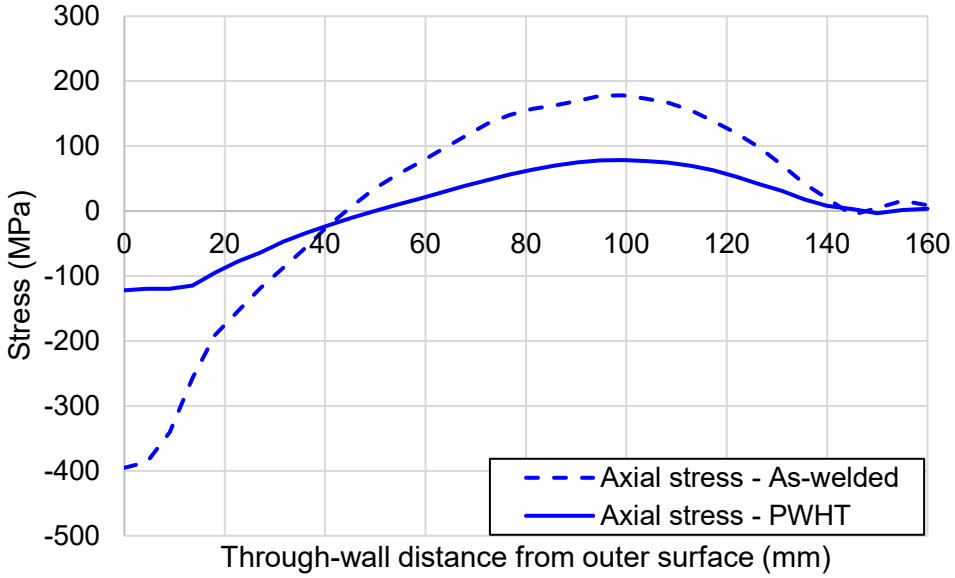

Fig. 3-30: Axial stress along a radial path through weld centreline before and after PWHT of the SF disposal canister

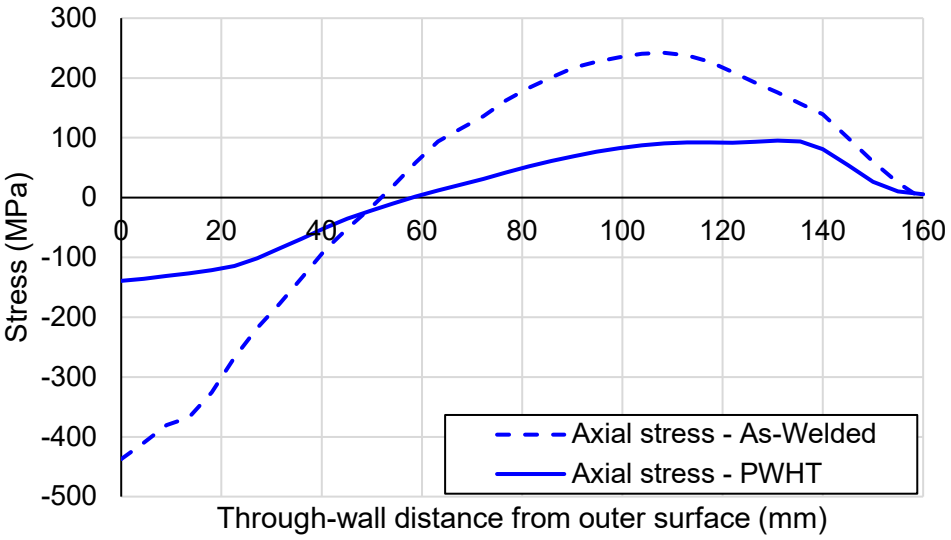

Fig. 3-31: Axial stress along a radial path through weld centreline before and after PWHT of the RP-HLW disposal canister

The weld residual stress (WRS) distributions shown above are characteristic of EB joints. The inner and outer surfaces of the section always see lower magnitude than the bulk section, where a peak is typically observed in the second half of the thickness. This is consistent with those observations reported in the literature (Vasileiou et al. 2016, Vasileiou et al. 2019, Vasileiou et al. 2021, Smith et al. 2014, Kingston et al. 2010, Hurrell et al. 2014, Ficquet et al. 2012).

As it is difficult to apply a polynomial fit or linearisation to such distributions, the ECA calculations described in Section 4.3 employ the peak value from these profiles, with an 5% uplift to account for the YS upper limit of 320 MPa, though tensile tests of a similar material grade with a less stringent composition indicated a YS of 305 MPa (see App. D). The secondary axial stress values employed in ECA are therefore:

- A peak value of 82.4 MPa for SF disposal canisters.
- A peak value of 100.1 MPa for RP-HLW disposal canisters.

3.8 Inspection

The discussion of inspection in the following sections is focused on the closure weld but is also applicable to the weld of the bottom lid. In all cases, the canister weld region should be cleaned (machined) to remove residual weld material or scale resulting from heat treatment to allow inspection. On completion of the bottom lid weld, there will, in principle, be access for inspection from the inner surface as well as the outer surface (unlike for the closure weld). However, the root of the EB weld will be ~ 10 mm from the inner surface (see Fig. 3-5), which means that the EB weld cannot be inspected effectively by surface non-destructive testing (NDT) methods such as eddy current testing (ET), magnetic particle inspection (MPI) or remote visual testing (VT) from the inner surface. In principle, ultrasonic testing (UT) could be deployed from the inner surface and would provide some extra redundancy in the inspection of the bottom lid weld. However, this extra inspection would have marginal benefit, because root flaws will give a strong pulse-echo response using a 0° UT beam from the lid as well as strong corner echoes using angle beams from the OD of the canister shell. Embedded centre-line flaws are also ideally oriented for 0° UT from the lid. By contrast, angle beams from the inner surface would give relatively weak responses from sub-surface planar flaws on the weld centreline. Angle beams deployed from the inner surface would generate strong corner echoes from planar flaws at the OD, but are still likely to be less effective than ET or eddy current array testing (ECAT).

3.8.1 Foreseeable flaws

A review of the knowledge database of The Welding Institute (TWI) was conducted on EB welds of thick section steels (i.e., 50 mm and above), along with a review of Patel et al. (2012). Further assessment of the references targeted those containing either NDT evaluation of production/ qualification welds or those that had comments on the weld quality. Of special interest were any comments on assessment criteria such as ASME IX (ASME 2023b) or BS EN ISO 13919-1 (BSI 2019a) or which NDT techniques were used such as phased array ultrasonic testing (PAUT), time-of-flight-diffraction (TOFD) and X-ray.

Approximately 20 digital references were accessible for review, covering a range of EB weld thicknesses from 50 mm to 200 mm. However, only two references used a weld geometry similar to that of the disposal canisters. The remaining welds were all fully penetrating welds with no backing. Splitting the references into two thickness regimes, there were 11 covering 40 - 100 mm and 9 references for thicknesses of 100 to 200 mm.

Information on weld quality fell into two categories: those with general comments on weld quality, and those that had been assessed/qualified based on ASME IX (ASME 2023b) or BS EN ISO 13919-1 (BSI 2019a). The references that contained general comments on weld quality were usually generated from X-ray inspection of development welds. It is common during weld development of thick sections to cut the welds into a longitudinal slice. This enables transverse X-ray inspection through a much thinner section rather than a sample of at least 100 mm, thus increasing the effectiveness of the evaluation. The number of defects is assessed and commented.

In these references, comments such as “no significant defects” were common. These types of comments are based on the evaluation of X-ray results from the sliced weld samples normally assessed based on BS EN ISO 13919-1 (BSI 2019a) requirements. If the volumetric quality is satisfactory, the weld quality is normally deemed acceptable and reported as thus. This destructive inspection is only used during development and where other forms of NDT are inappropriate, because of the thicknesses involved.

Among the other references reviewed, there were 6 cases where national or international standards were used to qualify the welds (mechanical testing and inspection): 3 for welds of under 100 mm thickness and 3 for thicknesses over 100 mm. The remaining unqualified and uncommented references contained notes on several NDT inspections using PAUT or TOFD.

Excerpts from some of the reviewed reports are as follows:

- Seven ~ 1 m long development blocks EB welded at a thickness of 200 mm with no identified defects, examined via PAUT.
- A demonstration tubular article with over 18 m of EB weld in 60 mm material. There were some reported defects, such as four cases of lack of fusion (LoF) in the root and a number of near surface start/stop defects; on average these were 0.5 – 1 mm in size and at ~ 15 mm deep.
- Four circumferential welds with a thickness of 180 mm and a length of 9 m evaluated using TOFD:
  - No detectable flaws.
  - Long region of LoF 300 mm with a suspected hole. Repair attempted, two indications were still evident, through-wall extent (TWE) ~ 1.5 – 2 mm but lengths of 150 mm and 40 mm at a depth of 140 mm.
  - Some LoF and root spiking detected, LoF tended to be 0 mm length ~ 1 mm TWE.
  - One weld had a longer LoF flaw, 60 mm length but less than 1 mm TWE. Longer (~ 200 mm long) root spiking was evident.

The comments noted in the thickest sections were generally good and there were large weld sections where no flaws were found. The main flaws/defects were LoF in the root, which had average TWE of less than 2 mm. These types of flaws can be small planar defects such as cracks or true LoF/LoP (lack of penetration) events when the beam and/or high voltage become unstable. As a result the penetration drops leaving these small LoF flaws. The reported root spiking is probably a non-optimised slope out region, where in the development welds not enough trials were performed to fully optimise the transition from full penetration to partial penetration.

The canister designs considered in this work do not see a transition from an open keyhole at the root to a closed keyhole, so these types of flaws are less likely. It is still possible to get some flaws in the slope down as the intensity in the beam is changing but these are likely to be minimised during development of the process. If such flaws did occur, they would be of similar size i.e., a TWE of 1 – 2 mm and a length of 0 – 1 mm.

The most significant defects identified in the above references are the larger LoF instances in the mid-thickness of the weld. These are likely to be cracks, possibly caused by inclusions in the weld or changes in local composition.

Overall, the biggest flaw sizes occurred when attempting weld sections of 200 mm, which is challenging due to the amount of molten metal requiring support. Welds of 150 mm and below show acceptable weld quality in line with national and international standards, with the infrequent occurrence of some root spiking and LoF indications. Taking this into account, flaw sizes from ~ 80 mm to 150 mm are directly relevant to the current case when considering the bulk of the

weld. The flaws for the root of the weld in backing are not reported and cannot be easily commented on. However, as mentioned above they would be similar in nature to the flaws with a TWE of 1 – 2 mm and a length of 0 – 1 mm.

On reviewing the references and some of the lessons-learnt logs, the major factors which impact weld quality are the stability of the equipment, i.e., not running at near maximum power, the level of residual magnetism, the robustness of the fronting and backing bars, and the level of contamination in the material (e.g., inclusions). Cases of tack welds breaking and the bar moving were directly responsible for gross through thickness flaws.

3.8.2 Inspection of sub-surface flaws

Of the various NDT methods, only UT and radiographic testing (RT) are well-suited to detect of sub-surface flaws in thick-section ferritic steel. However, RT is not recommended for the set-on flat cylindrical lid design considered in this report. There is no existing RT system that could penetrate the full 1,100 mm width of the lid. RT of the closure weld would therefore require a double-wall technique with the RT beam offset from the weld centreline, meaning that the RT beam would not be ideally aligned. The technique would be especially ineffective for flaws near the weld root because of the variation in the penetrated thickness (in both the axial and circumferential direction). This would tend to mask indications of any planar flaws, making it impossible to effectively sentence the weld. For these reasons, Patel et al. (2012) considered that the use of RT in addition to UT would require a more complex canister design without any clear benefit, and would have a negative impact on costs.

Ronneteg et al. (2006), Pitkänen et al. (2009), Pitkänen (2010) describe the inspection procedures for EB welds in copper disposal canisters. Copper is more difficult to inspect effectively by UT than carbon steel because it is highly attenuative. These projects therefore adopted more complex set-in lid designs, which allowed the use of RT in addition to PAUT, thereby providing diversity and redundancy for the volumetric inspections. A high-energy (9 MeV) linear accelerator was used for the RT for both projects. By contrast, Nakamura et al. (2010) achieved diversity and redundancy for carbon steel welds through the use of four diverse ultrasonic techniques, namely PAUT, TOFD and two creeping wave techniques (pulse-echo and pitch-catch, respectively). These techniques achieved 100% detection for flaw heights above 2 mm at depths of up to 190 mm (50 mm deeper than the depth required for the disposal canisters considered here). This demonstrates that, for carbon steel, it is in principle possible to achieve diversity and redundancy through the use of diverse ultrasonic techniques. For example, diversity and redundancy could be achieved for sub-surface flaws through a combination of 0° beams, angled pulse-echo beams and TOFD.

UT is generally effective at detecting planar defects and particularly effective in fine-grained ferritic steels, because these steels are ultrasonically isotropic. The flaws of greatest structural concern are generally planar flaws, e.g., lack of fusion and cracking. Various studies, e.g., Goujon (2005) and Moran et al. (2015), show that ultrasonic methods have very good capability for such flaws, especially for carbon steel welds with unrestricted access (such as the disposal canister). UT capability for volumetric flaws (e.g., porosity and inclusions) in the studies above is adequate but reduced sensitivity is expected at smaller sizes. Patel et al. (2012) concluded that well-designed conventional UT would reliably detect a high proportion of foreseeable planar flaws of size 4 mm (TWE) × 15 mm (length). This conclusion was largely based on Chapman & Bowker (2001), which is now also the primary reference cited in Annex T of BS 7910 (BSI 2019b) for the capability of conventional UT, and is unaffected by any of the recent changes in the canister dimensions. Chapman & Bowker (2001) do not quantify the reliability of detection in terms of a probability of detection (POD). However, their study of rough defects serves to demonstrate that

90% of the modelled defects give a peak UT response above the reporting threshold, which is equivalent to a probability of detection (POD) of at least 90%. A literature search revealed no evidence specific to the POD of defects in EB welds made of ferritic steel.

Additionally, the use of UT permits concurrent working with welding and NDT personnel on the same shift, and can offer the benefit of near real-time feedback to welders from examination results, which could reduce potential further re-work being required. For applications in the power industry, Overton et al. (2013) indicate that UT can take half the time of RT.

The ASME III (ASME 2023a) Boiler and Pressure Vessel Code (BPVC) categorises both the closure weld and the bottom weld as "Category C" corner welded joints. The ASME code requires volumetric NDT of such joints, but allows the volumetric NDT method to be either UT or RT. Whichever method is used, the code requires it to be performed according to a detailed written procedure, which has been proven by "actual demonstration". The ASME code is very widely used and represents general good practice for such inspections.

3.8.3 Inspection of surface flaws

Patel et al. (2012) recommended ET and VT to supplement UT, thereby enhancing the reliability of detection of flaws at the outer surface of the closure weld. Again, this recommendation, and the reasons for it, are unchanged since the 2012 study. ET is essentially a non-contact inspection method and is therefore inherently more adaptable for remote deployment than MPI or penetrant testing (Watkins et al. 2006). ET (and VT) techniques have also been successfully demonstrated for other canister projects (Stępiński 2003, Holmberg & Kuusela 2011, Smith 2003). Compared to conventional ET, the use of ECAT would offer a further reduction in inspection time, and would provide a permanent record of the collected data. Diversity and redundancy can be achieved for near-surface flaws through a combination of 0° beams, angled pulse-echo beams, ET and (if necessary) UT creeping waves.

Patel et al. (2012) concluded that well-designed ET can reliably detect flaws with a TWE of 1 mm and a length of 5 mm as long as the outer surface is smooth and flush. At the time, this conclusion was largely based on Ahmad et al. (1989). ASME V (ASME 2023c) Article 8 Mandatory Appendix X requires that the detection performance of ECAT systems be demonstrated on various notches and flat-bottomed holes, including 12 notches with maximum dimensions of 1.6 mm (length) by 1 mm (depth) by 0.25 mm (width). These values are indicative of the size of flaws that can be detected by ECAT. However, the detection limits for the height/length of tight cracks may be somewhat larger.

Holmberg & Kuusela (2011) present POD curves for ET and VT of man-made holes in copper versus their diameter. They reported that 90% POD was achieved with 95% confidence for the following hole diameters:

- 0.53 mm for high frequency ET;
- 0.36 mm for low frequency ET;
- 0.31 mm for VT.

3.8.4 Safety margins on flaw sizes

The RWMC canister design work (Asano et al. 2011) proposed a safety factor of 10 on critical flaw height based on a criterion within the ASME XI and Japanese codes for in-service inspection of nuclear power plants. For the canister considered by Asano et al. (2011), the critical flaw height was calculated to be 46 mm, so they proposed that the maximum allowable flaw height should be 4 mm. As explained in Section 10.4.1 of Patel et al. (2012), these safety factors set a sentencing criterion for the repair or toleration of a real flaw detected by inspection. They do not set a size by which the capability of the inspection is to be determined or judged. This capability is characterised by another size of flaw which the inspection is qualified to detect with high confidence, and there should be an appropriate margin between the minimum size detection limit and the maximum allowable flaw size.

The factor by which the critical flaw sizes are reduced to set the minimum flaw sizes that manufacturing inspections of the canisters must be qualified to detect with high confidence has yet to be established. For this purpose, Marshall (1982) proposed a qualification size factor “approaching 2”. The long-term structural performance of SF and RP-HLW disposal canisters in this report will be based on a safety factor of 10.

4 Canister performance

The as-built canister described in Chapter 3 has been designed to withstand the expected external loads during disposal. Exposure to the repository environment, however, will result in slow, long-term corrosion of the canister which will ultimately determine its service life. Corrosion will not only reduce the load-bearing wall thickness of the canister, but may also degrade the material properties due to the absorption of hydrogen produced during the long-term anaerobic phase. A short discussion on the various approaches employed for the assessment of long-term performance of disposal canisters is given in Section 4.1. The effects of various corrosion processes are discussed in Section 4.2. The structural integrity of the canister 10,000 years after emplacement in the repository is assessed in Section 4.3. The methodologies used for building confidence in lifetime predictions are discussed in Section 4.4.

4.1 Assessment of long-term performance

King et al. (2024b) have recently reviewed the various approaches employed for predicting the lifetimes of carbon steel and copper disposal canisters. For both materials, a common approach is to assess the mechanical and corrosion performance of the canister separately. Thus, the canister is designed to remain structurally sound for the expected service loads and a minimum necessary wall thickness, the so-called "mechanical allowance", is defined. The remaining wall thickness is then defined as the "corrosion allowance" with the canister lifetime calculated based on the time required to consume this allowance according to the different corrosion mechanisms expected to occur under repository conditions. In addition, a series of "reasoned arguments" are developed to justify the exclusion of corrosion processes not expected to occur. This approach was followed in two recent safety cases involving carbon steel disposal canisters, in France (Andra 2022) and in Japan (Ogawa et al. 2017, NUMO 2021).

An alternative approach, which is followed here, is to consider the effects of both mechanical and corrosion degradation processes simultaneously. Such an approach is important for a single-shell carbon steel canister design as interactions between mechanical and corrosion processes are expected in the repository. In particular, the absorption of hydrogen produced by anaerobic corrosion of carbon steel can result in a decrease in fracture toughness of the canister material and an increased probability of brittle fracture.

4.2 Corrosion behaviour

The nature of the corrosion processes that will impact the canister will change over time as the environmental conditions within the repository evolve. The aim of this section is to describe the mechanisms of corrosion processes that are, and that are not, expected to occur under repository conditions. For corrosion processes that are expected to occur, a further aim is to define the rate or extent of those processes, as well as to demonstrate that the underlying mechanisms are understood sufficiently well. For those processes that are not considered possible, and which are excluded from the lifetime assessment, the aim is to again demonstrate sufficient mechanistic understanding to justify their exclusion.

4.2.1 Uniform corrosion

4.2.1.1 Oxic corrosion

Evidence from the FE experiment at Mont Terri indicates that the atmospheric O_2 initially trapped in the emplaced bentonite buffer is consumed within a matter of days or weeks following backfilling of the tunnel (Section 2.2.2). This period of O_2 consumption corresponds to the hottest and driest period in the evolution of the nearfield environment at a time at which there is insufficient adsorbed water on the canister surface to support aqueous corrosion processes. Fig. 4-1 shows a comparison between the observed and the predicted rates of O_2 consumption in the FE-G experiment based on an extension of the 3-D reactive-transport model described by Giroud et al. (2018). Simulations were performed with and without the possibility of heater corrosion, in addition to other O_2-consumption reactions involving corrosion of the steel tunnel support materials, irreversible reaction with the bentonite and OPA, and reversible sorption of gaseous O_2 by the bentonite (King & Briggs 2024). Consumption reactions for dissolved O_2, including corrosion of the heaters, are assumed to only occur in the model if the relative humidity exceeds 60%, representing the threshold RH for the formation of a thin water film or water droplets on the surface. As can be seen from a comparison of the solid and dashed curves, there is virtually no difference in the rate of O_2 consumption regardless of whether heater corrosion is, or is not, included in the model. This suggests that heater corrosion is an insignificant contributor to the overall consumption of O_2 in the experiment, in large part because the heater surfaces are too dry during the period of rapid O_2 consumption. Similar behaviour would be expected in the repository itself.

The observations from, and the interpretation of the results of, the FE-G experiment suggest that there may be no aerobic corrosion of the canisters. Instead, all of the initially trapped O_2 will be consumed by other processes prior to the wetting of the canister surfaces.

During Phase 1 of the evolution of the repository environment (see Fig. 2-5), oxidation could occur in the absence of a condensed moisture on the canister surface. Oxidation kinetics are slow at the temperatures expected in the repository (Desgranges et al. 2003, Hélie et al. 2006). Fig. 4-2 shows the time dependence of the depth of corrosion due to dry air oxidation based on the experimental measurements of Desgranges et al. (2003) estimated by Diomidis (2014). Oxidation kinetics were found to follow a parabolic rate law and to vary with temperature with an activation energy of ~ 98 $kJ \cdot mol^{-1}$ for the temperature range of interest. It can be seen from the figure that the extent of oxidation is minor, even over an extended period of dry conditions. If we assume that the duration of Phase 1 is 40 years (Fig. 2-5) and that, conservatively, the temperature is a constant 180°C, then the depth of dry air oxidation is < 1 μm. A corrosion depth of 1 μm would correspond to the consumption of approximately 1% of the initially trapped atmospheric O_2.

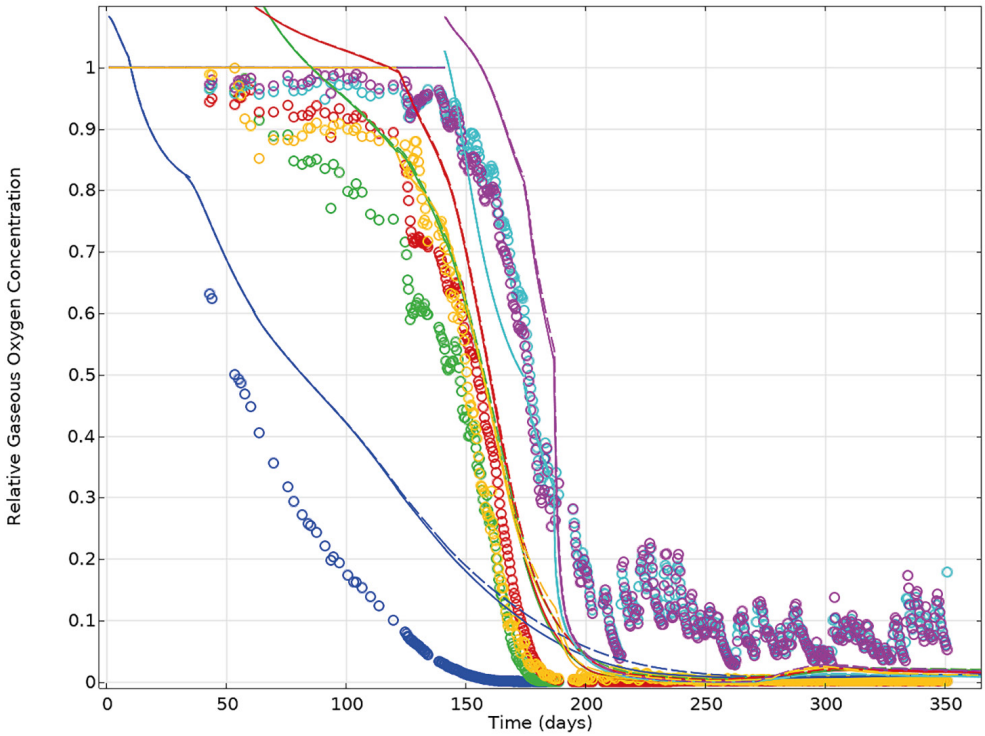

Fig. 4-1: Comparison of the observed and predicted consumption of O_2 in the FE-G experiment with and without corrosion of the heaters

(King & Briggs 2024)

Coloured open circles represent the experimental measurements from each of six O_2 gas sensors (expressed relative to the concentration in air), and the corresponding coloured curves represent predictions including (solid curves) or excluding (dashed curves) the possible corrosion of the heaters. Day 0 on the time axis corresponds to the day on which the first section of the tunnel was backfilled. The O_2 concentrations are expressed relative to that at a temperature of 25°C (calculated as the corresponding dissolved O_2 concentration in equilibrium with gaseous O_2). Since the initial temperature within the FE experiment was less than 25°C, the relative O_2 concentration can exceed a value of 1 at early times

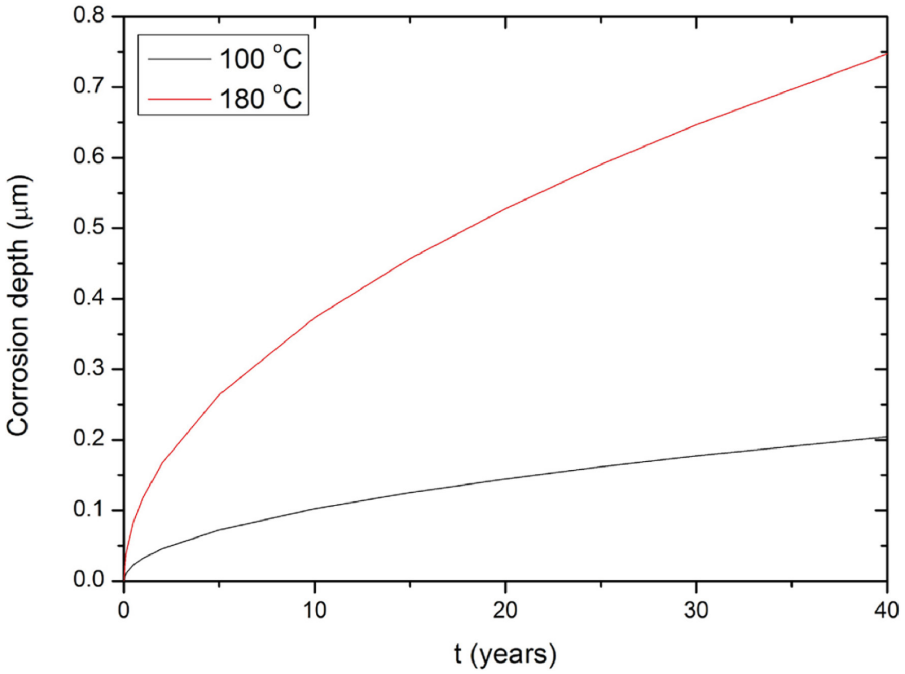

Fig. 4-2: Time dependence of the corrosion depth due to dry air oxidation at assumed constant temperatures of 100 °C and 180 °C

From Diomidis (2014).

Regardless of the expected absence of a surface moisture film, it is useful to quantify the maximum possible extent of aerobic corrosion of the canisters. Aerobic corrosion would result in the formation of Fe(III) corrosion products, such as goethite (α-FeOOH), lepidocrocite (γ-FeOOH), hematite (α-Fe_2O_3), or maghemite (γ-Fe_2O_3):

$$4Fe + 3O_2 + 2H_2O \rightarrow 4FeOOH \quad [3]$$

$$2Fe + 3O_2 \rightarrow Fe_2O_3 \quad [4]$$

Even if these reactions do occur, the extent of corrosion would be minimal, with the initial O_2 inventory (see Section 2.2.2) being equivalent to a wall loss of only 80 µm on the assumption that 100% of the O_2 supported corrosion of an SF canister, while the corresponding depth of corrosion for a smaller RP-HLW canister would be 150 µm.

4.2.1.2 Anaerobic corrosion

Like other ferrous alloys, carbon steel will corrode in O_2-free H_2O accompanied by the evolution of H_2. Based on the expected evolution of the nearfield environment illustrated in Fig. 2-5, anaerobic corrosion will start prior to complete saturation of the repository in Phase 2 and continue in Phase 3 following saturation.

The mechanism of the anaerobic corrosion of carbon steel in aqueous environments, including compacted bentonite and other soil media, has been extensively studied (Féron et al. 2009, JNC 2000, King 2008). Iron oxidises to ferrous (Fe(II)) species accompanied by the generation of H_2:

$$Fe \rightarrow Fe^{2+} + 2e^- \quad [5]$$

$$2H_2O + 2e^- \rightarrow 2OH^- + H_2 \quad [6]$$

Overall:

$$Fe + 2H_2O \rightarrow Fe(OH)_2 + H_2 \quad [7]$$

Ferrous hydroxide is unstable, especially at elevated temperatures, and is converted to magnetite Fe_3O_4 via the Schikorr reaction, accompanied by additional H_2 production:

$$3Fe(OH)_2 \rightarrow Fe_3O_4 + 2H_2O + H_2 \quad [8]$$

The growth of the corrosion product layer results in a decrease of the corrosion rate with time. Carbonate-containing corrosion products, including siderite ($FeCO_3$), are observed in the presence of compacted bentonite:

$$Fe + HCO_3^- + H_2O \rightarrow FeCO_3 + H_2 + OH^- \quad [9]$$

Magnetite surface films exhibit a duplex structure, with a thin inner barrier layer (of nm dimensions) and an outer porous layer formed by a dissolution-precipitation process (King 2008). The corrosion reaction in the repository is under anodic control, governed by the rate of ion transport across the thin barrier film. The outer porous layer thickens over time but remains porous. In the presence of compacted bentonite, the corrosion product film grows into the clay layer, creating a zone of altered material immediately adjacent to the corroding surface (Féron et al. 2009). Since the properties of the inner barrier film determine the corrosion rate, periodic spalling of the outer porous film would not impact the corrosion behaviour, and there is no mechanism by which the corrosion rate could increase over time. Therefore, the use of a constant corrosion rate based on empirical measurements is a valid approach to estimating the long-term corrosion behaviour of the canister. Indeed, since the corrosion rate generally continues to decrease with time (due to thickening of the barrier layer) over extended periods (Hesketh et al. 2023), it can be argued that the use of a corrosion rate determined from an experiment of finite duration is conservative as the long-term rate would be expected to be lower.

Corrosion experiments in a humid anoxic atmosphere, relevant to Phase 2 of the nearfield evolution, have been conducted over 5 years (Senior & Martino 2022). During this period, the corrosion rate decreases with time to rates below 1 $nm \cdot a^{-1}$. In those experiments, the corrosion rate was determined by measuring the amount of evolved H_2 using a sensitive solid-state H_2 probe with a corrosion rate sensitivity better than 0.1 $nm \cdot a^{-1}$ (Senior & Martino 2022).

Corrosion experiments in saturated compacted bentonite, relevant to Phase 3 of the nearfield evolution, have been conducted for longer durations, i.e., up to ~ 12 years (Hesketh et al. 2023). As shown in Fig. 4-3, the corrosion rate continues to decrease with time over this period, with the long-term rate in the order of tens of $nm \cdot a^{-1}$.

Diomidis et al. (2023) have reviewed long-term corrosion rates for carbon steel in contact with saturated compacted bentonite (as well as for other materials and for alkaline systems) and derived best-estimate and upper and lower bound values (Tab. 4-1). Only data from experiments with a

duration of 4 years or longer and for temperatures ≤ 80 °C were selected. Time-averaged corrosion rates, such as those determined from mass loss, were converted to "instantaneous" corrosion rates for ease of comparison with rates measured from the rate of H_2 evolution. The corrosion rates are not strongly dependent on temperature (Fig. 4-4).

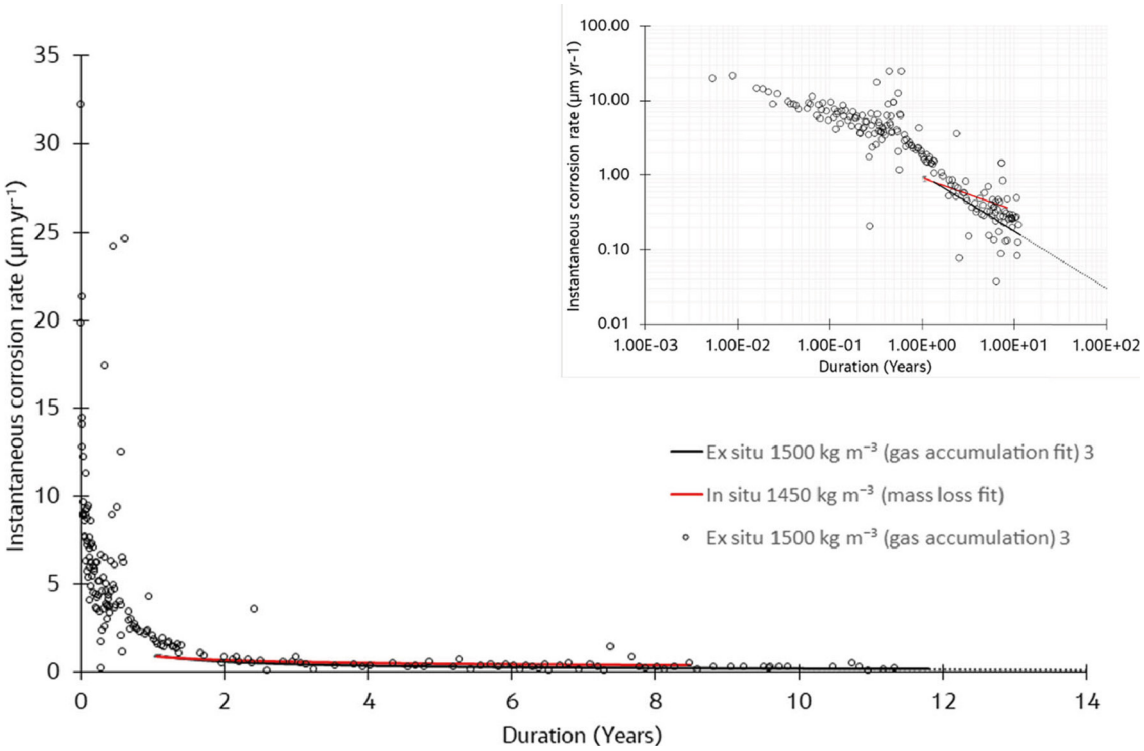

Fig. 4-3: Time dependence of the corrosion rate of carbon steel in contact with saturated compacted bentonite under anaerobic conditions based on in-situ and ex-situ tests

From Hesketh et al. (2023). The insert shows the same data plotted on a log scale with a dotted line indicating a forecast up to 100 years.

Tab. 4-1: Best-estimate and upper and lower bound long-term corrosion rates for carbon steel in contact with saturated compacted bentonite under anaerobic conditions

From Diomidis et al. (2023).

	Corrosion rate [µm·a^{-1}]
Best estimate	0.30
Lower bound	0.026
Upper bound	0.70

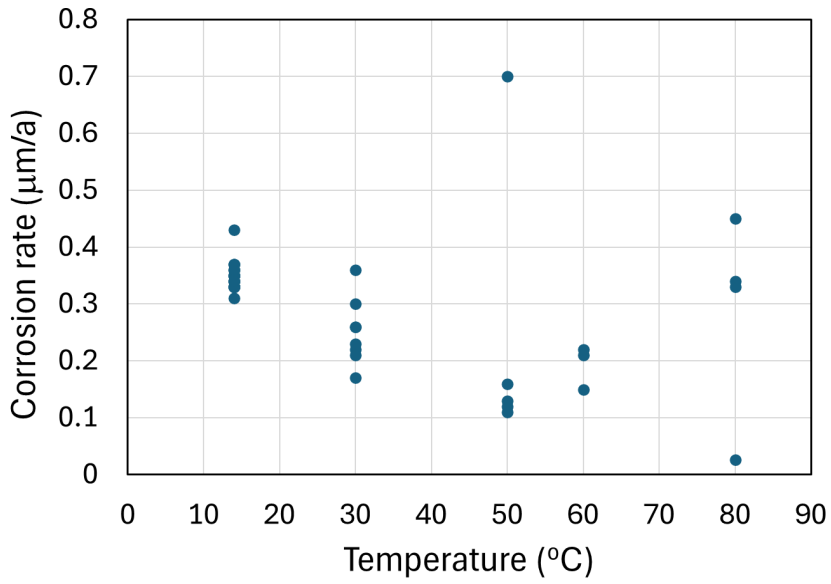

Fig. 4-4: Temperature dependence of the long-term corrosion rate of carbon steel in anaerobic saturated compacted bentonite

Based on data from Diomidis et al. (2023).

4.2.1.3 Effect of radiolysis

In addition to O_2 initially trapped in the repository, oxidising species can be produced by the radiolysis of the humid atmosphere and/or the pore water in unsaturated and saturated bentonite, respectively (Section 2.2.2). Under saturated conditions, the impact of irradiation is a function of the absorbed dose rate. Fig. 4-5 shows the dependence of the enhancement factor[4] for uniform corrosion of carbon steel on the dose rate for saturated systems in bulk solution and compacted bentonite for both oxic and anoxic conditions. It is apparent that, within experimental variability, there is no significant enhancement of the rate of uniform corrosion (defined here as an enhancement factor of greater than ~ 2) in bulk solution for dose rates < 10 $Gy \cdot h^{-1}$. This critical dose rate for an effect of irradiation is consistent with the findings from a recent parametric study of the effects of dose rate and total absorbed dose on the corrosion of carbon steel (Bevas et al. 2024). In compacted bentonite, there is no significant effect of irradiation in any of the reported studies at dose rates of up to 3,500 $Gy \cdot h^{-1}$. The beneficial effect of bentonite may be because of the scavenging of radiolytic oxidants by the oxidation of pyrite impurities in the clay (JAEA 2013) or because of changes to the yields of oxidising and reducing radiolysis products due to energy transfer with clay minerals (King & Behazin 2021, Behazin et al. 2023).

[4] The enhancement factor is the ratio of the corrosion rate in the presence of radiation to the corrosion rate under unirradiated conditions measured by the same authors in the same environment and for the same exposure period.

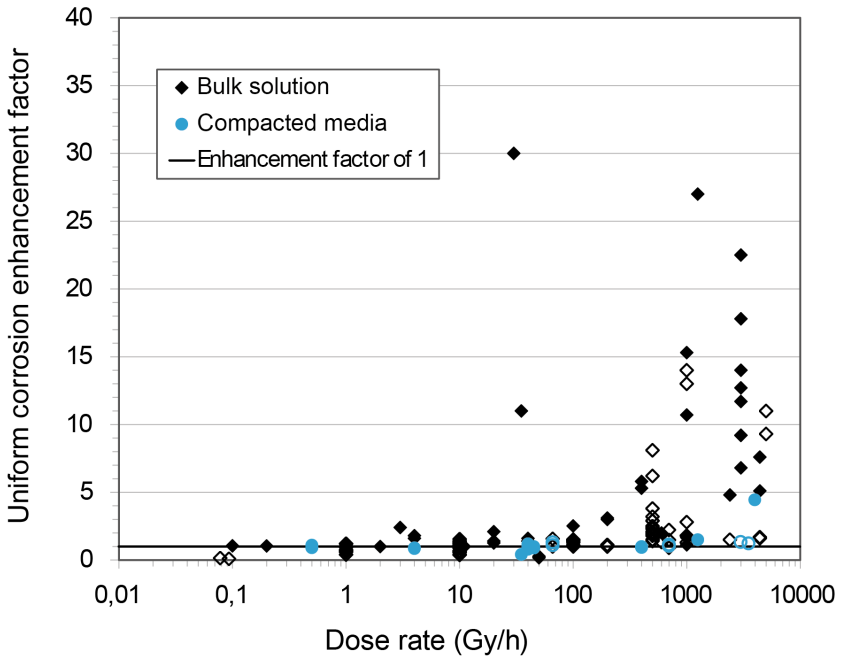

Fig. 4-5: Dependence of the enhancement factor for uniform corrosion of carbon steel on the gamma dose rate in bulk solution (black diamonds) and saturated compacted bentonite (blue circles)

Open symbols indicate oxic conditions, while closed symbols indicate anoxic conditions. The enhancement factor is the ratio of the corrosion rate in the presence of radiation to the corrosion rate measured under unirradiated conditions by the same authors in the same environment and for the same exposure period. The figure is based on a compilation of results for carbon steel and cast iron from 32 separate studies (King 2024).

There have been fewer studies of the effect of irradiation on the corrosion of carbon steel under atmospheric conditions or in the presence of unsaturated bentonite (Fig. 4-6). As in saturated systems, there is no apparent significant effect of radiolysis for dose rates up to 700 $Gy \cdot h^{-1}$. It has recently been reported that irradiation can induce corrosion in an anaerobic humid atmosphere at 60% RH at a dose rate of 400 $Gy \cdot h^{-1}$, whereas no corrosion was observed in an equivalent unirradiated experiment (Sarrasin et al. 2024). This observation may indicate an enhancement in the corrosion rate at higher dose rates under atmospheric conditions, although no enhancement has been observed in unsaturated bentonite at a dose rate of 700 $Gy \cdot h^{-1}$.

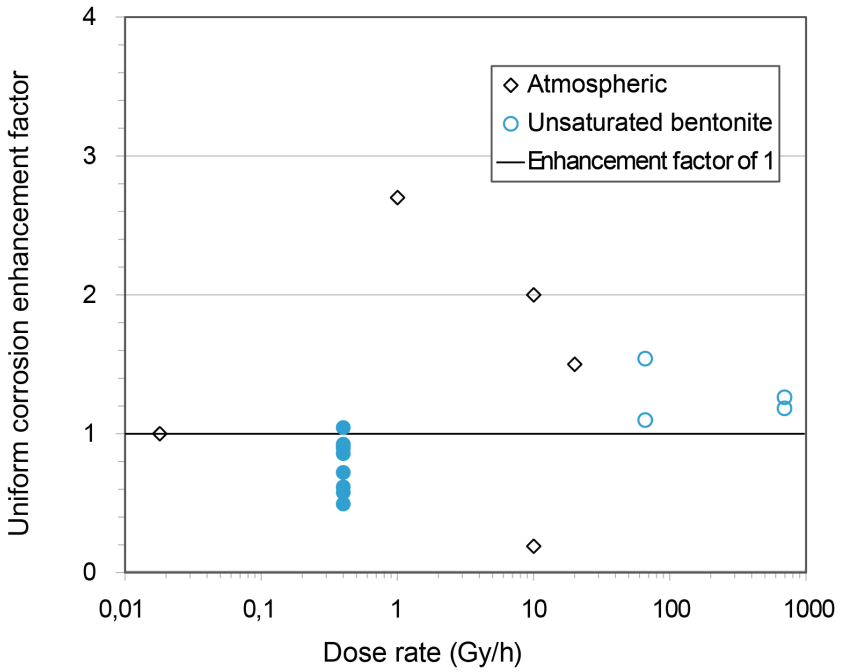

Fig. 4-6: Dependence of the enhancement factor for uniform corrosion of carbon steel on the gamma dose rate in humid atmospheres (black diamonds) and in unsaturated compacted bentonite (blue circles)

From King (2024). Open symbols indicate oxic conditions, while closed symbols indicate anoxic conditions. The enhancement factor is the ratio of the corrosion rate in the presence of radiation to the corrosion rate measured under unirradiated conditions by the same authors in the same environment and for the same exposure period.

4.2.1.4 Treatment of uniform corrosion in canister lifetime assessment

Based on the discussion above, uniform corrosion is treated as follows in the performance assessment of HLW disposal canisters:

- Dry air oxidation during Phase 1 is excluded from consideration because the extent of wall loss is insignificant.
- Aqueous corrosion due to the initially trapped O_2 is excluded from consideration primarily because the evidence indicates that the O_2 will be consumed by other processes prior to the wetting of the canister surface. Furthermore, even for the unrealistic assumption that 100% of the initial O_2 inventory resulted in uniform corrosion, the extent of wall loss would be insignificant.
- Radiolysis effects are implicitly included in the assessment, although the empirical evidence shows no significant effect on the corrosion rate of carbon steel in compacted bentonite for the maximum dose rate of 0.2 $Gy \cdot h^{-1}$ at the canister outer surface.
- The long-term anaerobic corrosion rate is defined as 0.7 $\mu m \cdot a^{-1}$, corresponding to the upper bound of the distribution of long-term empirical rates reviewed by Diomidis et al. (2023). This rate corresponds to the saturated conditions during Phase 3 of the repository evolution but is also used to represent the rate for the unsaturated conditions during Phase 2. The selected rate is conservative both because it is based on experiments of relatively short duration compared to the required canister lifetime, and because it is the upper bound value. Based on this rate, 7 mm of wall loss are expected after 10,000 years of disposal.

4.2.2 Localised corrosion

Localised corrosion is the result of the spatial separation of the anodic and cathodic reactions. In natural systems, the cathodic reaction is typically the reduction of O_2. For passive systems, the spatial separation is generally initiated by the localised breakdown of the passive film, whereas for active systems, differential [O_2] cells can be established due to geometric factors or the formation of spatially heterogenous corrosion products.

In aqueous systems, the supply of H_2O to the corroding surface is relatively rapid and it is difficult to create spatial gradients in the concentration of H_2O. Furthermore, the large potential difference that results from the spatial separation of the anodic dissolution of Fe and the cathodic reduction of O_2 is not present when the cathodic reaction is the reduction of H_2O, so there is a much-diminished electrochemical driving force for localised corrosion under anaerobic conditions. Thus, localised corrosion under anaerobic conditions is unlikely and would, in any case, cause limited damage. Oxidising radiolysis products can ennoble the corrosion potential of carbon steel at high dose rates (several $kGy \cdot h^{-1}$) and, hence, increase the likelihood of localised film breakdown in passive systems (Farnan et al. 2019). However, the extent of such ennoblement for the dose rates of concern here would be insignificant.

The arguments made to this point have addressed whether localised corrosion can initiate under repository-relevant conditions. However, even if pits or localised attack do initiate, the extent of propagation and the degree of localisation would be limited. Fig. 4-7 shows a compilation of pitting factors for carbon steel expressed as a function of the average depth of corrosion. The pitting factor is the ratio of the depth of the deepest penetration (as measured from the original surface) to the mean depth of corrosion, so that a pitting factor of one corresponds to uniform corrosion. Both laboratory and field measurements indicate that the magnitude of the pitting factor, i.e., the degree of localisation, decreases with increasing depth of (average) corrosion. In other words, corrosion that starts as pitting transforms into something resembling surface roughening and eventually to uniform corrosion. From the figure, the average depth of corrosion corresponding to a pitting factor of one, i.e., the depth at which there is no further localisation, is smaller than 10 mm. This depth is similar to the corrosion depth expected after 10,000 years of disposal (7 mm) and only a small fraction of the wall thickness of 140 mm, implying that even if localised corrosion does initiate, it will cease to propagate as discrete pits long before the structural integrity of the canister is compromised.

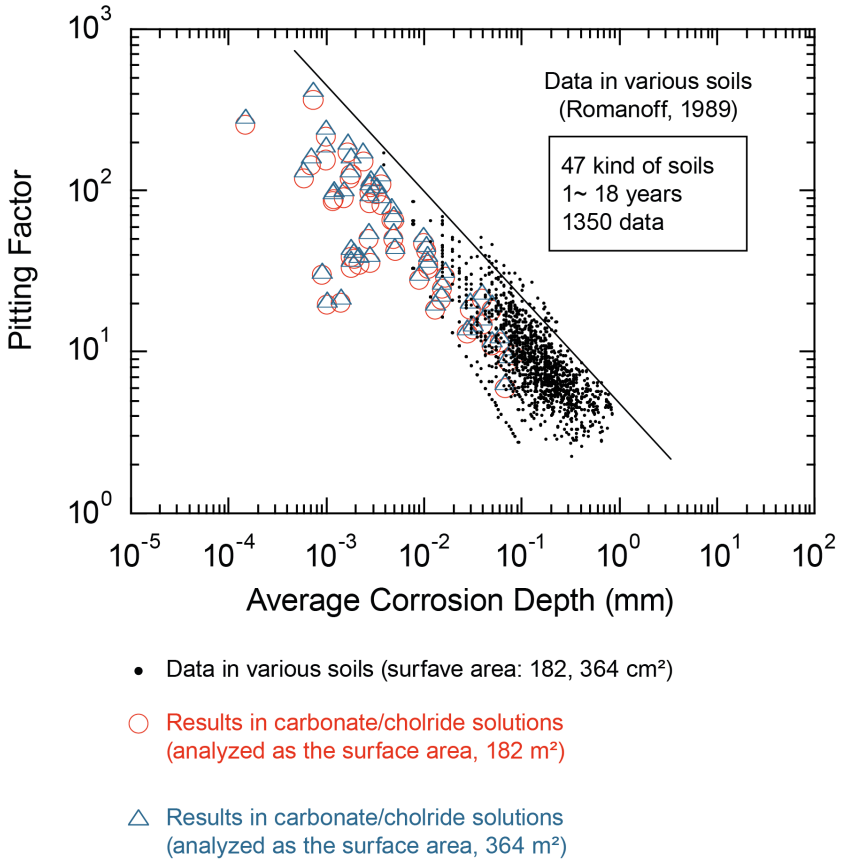

Fig. 4-7: Dependence of the pitting factor for carbon steel on the average depth of corrosion based on various laboratory sources and data from analogue studies

From JNC (2000).

4.2.2.1 Treatment of localised corrosion in canister lifetime assessment

Localised corrosion is not expected to occur or adversely impact the long-term performance of the canister and is, therefore, excluded from further consideration. Initiation of localised corrosion is considered unlikely since the initially trapped O_2 is expected to be consumed prior to wetting of the canister surface. Even if localised corrosion does initiate, evidence suggests that it will evolve into relatively uniform corrosion before the wall thickness has been reduced significantly.

4.2.3 Stress corrosion cracking

The possibility of stress corrosion cracking (SCC) of disposal canisters can be assessed based on the three pre-requisite conditions for cracking, namely: a suitable environment, sufficient tensile stress, and a susceptible material. All three of these requirements must be met for SCC to be possible. If just one of the pre-requisites is not met, then cracking cannot occur.

Carbon steel is known to be susceptible to SCC in a number of environments (King 2010b). Of the environments in which SCC of carbon steel has been reported, many can be excluded from consideration because the environment will clearly not exist in the repository, such as concentrated nitrate, caustic or phosphate solutions, or high-temperature (> 200 °C) water. However,

certain aspects of the environments in which the SCC of underground pipelines has been reported are not very dissimilar from those expected in the repository. Two forms of SCC of pipeline steels are recognised (King 2010b, King 2010a):

- Near-neutral pH SCC (NNpH SCC) is associated with a dilute bicarbonate solution (in the range of 0.001 to 0.01 $mol \cdot L^{-1}$) with a pH in the range of 5.5 to 7.5 and potentials corresponding to the corrosion potential in anaerobic environments. Carbon steel is in the active state under these conditions. Cracking is transgranular and is promoted by the more aggressive cyclic loading found on liquid pipelines, although NNpH SCC also occurs under less aggressive cyclic loading associated with gas pipelines.
- High-pH SCC occurs in a concentrated carbonate/bicarbonate solution (0.1 to > 1 $mol \cdot L^{-1}$) at pH values > 9.3. Under these conditions, the steel surface is passive. Cracking occurs in a specific range of potentials associated with the "nose" of the active-passive transition, in the range of -0.525 to -0.675 V_{SCE} at room temperature. The crack growth rate increases exponenttially with temperature, with an activation energy of ~ 40 $kJ \cdot mol^{-1}$. Crack propagation is intergranular and dynamic crack-tip strain is required for crack growth.

In NNpH SCC cracking occurs under anaerobic conditions, which will prevail for the majority of the lifetime of the canister. However, the reference bentonite porewater shown in Tab. 2-1 after saturation with incoming OPA porewater is more saline than the dilute bicarbonate-based water in which cracking is observed. In terms of the mechanical loading requirements, crack propagation does not occur under static load. Instead, NNpH SCC is an example of corrosion fatigue promoted by the effects of absorbed hydrogen (Chen 2016). A cyclic load is a pre-requisite for NNpH SCC and will be absent on the canister under repository conditions.

The latter environment is typically generated on underground pipelines by the action of cathodic protection (CP) on the pipe surface in areas where the protective coating has failed and allows ground-water to contact the pipe (Been et al. 2005). The increase in pH due to the cathodic reduction of O_2 or H_2O causes CO_2 to dissolve in the surface water and create the concentrated CO_3^{2-}/HCO_3^- environment. If the CP current is subsequently interrupted, the potential of the pipe surface can move into the potential window for cracking which is relatively noble compared with the corrosion potential in anaerobic environments. Clearly, such environments are unlikely to exist at the canister surface in the absence of CP. Furthermore, the relatively noble potential window implies the need for aerobic conditions, the duration of which is limited to a few days or weeks in the repository (see Section 2.2.2). High-pH SCC is an example of a slip-dissolution mechanism involving the periodic rupture of a passive film at the crack tip (Parkins 2000). Cracking is promoted by cyclic loading in order to create dynamic crack-tip strain to rupture the passive film. Therefore, it is concluded that the environmental and mechanical loading conditions for high-pH SCC will not occur in a repository in OPA.

Despite the unlikelihood of SCC under repository conditions, the possibility of cracking of carbon steel canisters has been investigated in the French (Bulidon et al. 2021, Didot et al. 2017, Necib et al. 2017) and Japanese programmes (Mitsui et al. 2008, Ogawa et al. 2017).

The French programme has focussed on the possibility of SCC in anaerobic Callovo-Oxfordian porewater solutions, which are similar to environments that support NNpH SCC in pipeline steels. A range of carbon steels for pressure vessel applications has been studied with varying microstructure and strengths (P235, P265, P275, P285NH, where the three digits indicate the minimum value of the yield strength for plate material ≤ 16 mm in thickness) and including a standard pipeline steel (API 5L X65, minimum specified yield strength 448 MPa), which is the reference material for the casing of the micro-tunnels in the French disposal concept. As-received and EB-welded material has been investigated. Both crack initiation and propagation were studied, using both plain and notched coupons under slow straining and constant load conditions,

as well as pre-cracked compact tension specimens. Indications of crack initiation have been reported for all grades investigated, although the cracks were often shallow (< 200 µm deep) and filled with corrosion products (Didot et al. 2017, Necib et al. 2017). Shallow, apparently dormant, SCC cracks are typical of NNpH SCC on underground pipelines, with only relatively few cracks (<< 1%) propagating under cyclic loading conditions that are required to maintain a sharp crack tip and to counteract the blunting effect due to corrosion. However, Necib et al. (2017) reported one indication of crack growth for P275 steel (but not the API X65 or P285NH grades) at a stress intensity of 15 MPa√m (but not at 40 MPa√m, where crack blunting was observed). The clearest indications of SCC were observed with steels with a banded ferrite-pearlite microstructure, and this has led the French programme to focus on optimising the steel grade, particularly the microstructure (Crusset et al. 2017).

In contrast to the focus on NNpH SCC environments in the French programme, the Japanese studies focused on the concentrated carbonate/bicarbonate environments associated with high-pH SCC (Haruna et al. 2000a, Haruna et al. 2000b, JNC 2000, Mitsui et al. 2008, Ogawa et al. 2017). Evidence for crack initiation has been reported, although no measurements of the crack growth rate have been made. When studying welded material (TIG, EB, and MAG welding), the parent material was found to be more susceptible than either the weld metal or heat-affected zone (Asano et al. 2011). The current approach appears to be the use of post-weld heat treatment to reduce the residual tensile stress (and even to induce compressive residual stress), although it is acknowledged that the success of this approach in reducing the SCC susceptibility will need to be demonstrated during further development of the canister design (Ogawa et al. 2017).

The results from the French and Japanese programmes provide evidence of crack initiation on carbon steel under severe loading conditions when exposed to repository environments, which, however, will not be present in a repository in OPA according to the Swiss disposal concept. Consequently, in the absence of a relevant mechanism and due to the lack of convincing evidence and data for sustained crack growth, there is no basis for including SCC in the current disposal canister lifetime prediction.

4.2.3.1 Treatment of SCC in canister lifetime assessment

Stress corrosion cracking is excluded from consideration for the assessment of canister lifetimes because of the absence of a suitable chemical environment in the repository and the absence of cyclic loading found necessary to sustain crack growth.

4.2.4 Hydrogen induced cracking

4.2.4.1 Hydrogen uptake in steel

Hydrogen is generated at the external surface of carbon steel canisters as a consequence of the corrosion process in moist anaerobic conditions (see Section 4.2.1.2). Although the bentonite porewater is relatively benign, a H_2 partial pressure of up to ~ 11 MPa is expected to be present at the external surface of the canister (Nagra 2024f). Hydrogen will begin to accumulate both within the steel itself and inside the canister as atomic H diffuses through the canister wall and desorbs as H_2 on the inner surface of the canister wall (Turnbull 2009). The absorption of hydrogen into the low strength carbon steel matrix structure can be responsible for a reduction in tensile ductility and fracture toughness (Xu & Rana 2008, Lam et al. 2009, Xu 2012, Matsunaga et al. 2015), with the susceptibility to hydrogen-induced cracking increasing in carbon steel at increasing strength level.

The material specification for the carbon steel forgings is defined in Section 3.4. However, due to the sparsity of material property data for low-strength carbon steels in H_2 the characteristics for a number of other notionally similar steels have also been considered in the following. The material pedigrees for these are given in Tab. 4-2.

Tab. 4-2: Summary of specified low-strength carbon steel forging characteristics

The values are shown as lower limit / upper limit.

	Nagra spec.	**ASTM A106-B**	**ASTM A285-C**	**ASTM A516 70**	**API 5L X42**	**API 5L X70**	**BS4360 50D**
C, wt.%	- /0.12	- /0.30	- /0.28	- /0.31	- /0.22	- /0.12	- /0.20
Si, wt.%	- /0.30	- /0.10		0.13/0.45	- /0.45	- /0.45	- /0.50
Mn, wt.%	- /0.80	0.29/ 1.06	- /0.98	0.79/1.30	- /1.20	- /1.70	- /1.50
P, wt.%	- /0.015	- /0.035	- /0.025	- /0.025	- /0.025	0.025	- /0.040
S, wt.%	- /0.010	- /0.035	- /0.025	- /0.025	- /0.015	0.015	- /0.040
Cr, wt.%	- /0.20	- /0.40					
Ni, wt.%	- /0.20	- /0.40			- /0.30	- /0.50	
Cu, wt.%	- /0.02	- /0.40			- /0.50	. /0.50	
Mo, wt.%		- /0.15			- /0.15	- /0.50	
Nb, wt.%							0.003/ 0.10
V, wt.%		- /0.08					0.003/ 0.15
CE_{IIW}	- /0.30	0.05/ 0.64	- /0.44	0.13/0.53	- /0.43	- /0.57	- /0.45
Norm (AC), °C	890/950						
$R_{p0.2}$, MPa	220/320	240/ -	205/ -	260/ -	290/495	485/ -	345/ -
R_m, MPa	400/640	415/ -	380/515	485/620	415/655	570/ -	490/640
A, %	17/ -		27/ -				21/ -
Z, %	15/ -						
C_v (-20 °C), J	27/ -						27/ -

4.2.4.2 Tensile properties

While there is a general consensus that H_2 impacts the tensile properties of low-strength carbon steels, in particular at low strain rates, it seems that the main effect is on tensile ductility rather than on smooth-specimen strength properties (e.g., Fig. 4-8, Lam et al. 2009, Xu 2012 and Matsunaga et al. 2015). Nevertheless, there is a significant effect of H_2 on the notched-specimen strength properties. Reductions in uniaxial elongation and reductions of area at fracture of up to ~ 60% have been observed for low-strength steels (e.g., Xu & Rana 2008). The evidence appears to indicate that the tensile ductility decreases with increasing H_2 pressure up to ~ 25 MPa, above which it remains relatively constant.

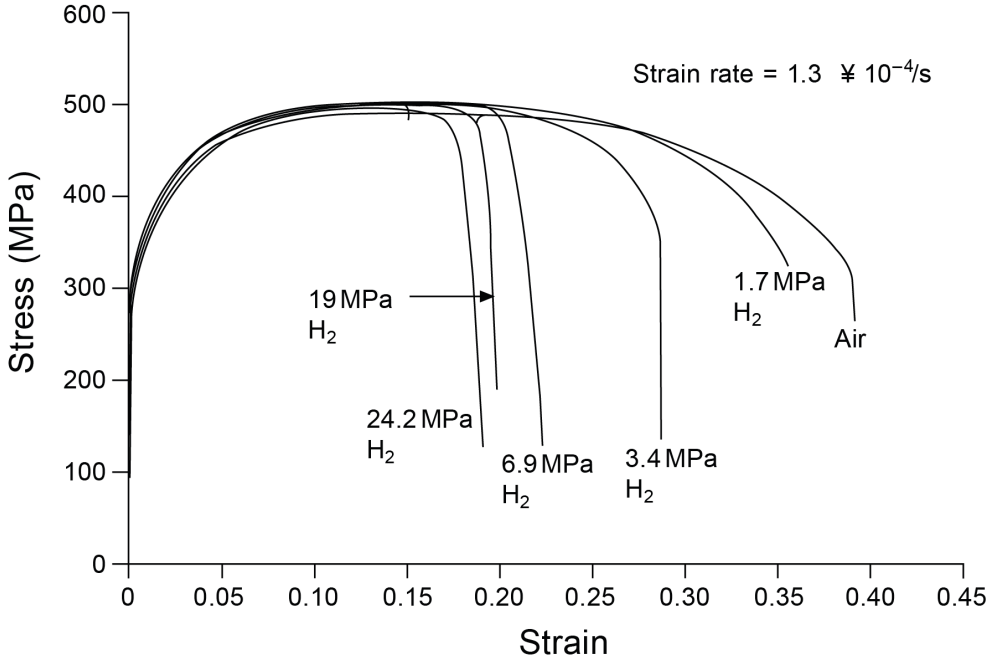

Fig. 4-8: Influence of hydrogen on room temperature tensile properties of A106-B at different pressures

From Xu & Rana (2008).

A range of carbon steel weldment types have been reported to exhibit similar tensile properties to their parent materials in high-pressure H_2 (Spingarn 1979).

4.2.4.3 Fracture toughness properties

In the literature, the influence of H_2 on the fracture toughness of low-strength carbon steels has been expressed both in terms of H_2 gas pressure (P_{H2}) and the concentration of dissolved atomic hydrogen (C_H). H_2 pressure is related to fugacity (f_{H2}), which in turn relates to the concentration of dissolved atomic H_2 by means of Sievert's law (Liu & Atrens 2013):

$$C_H = S_H\sqrt{(f_{H2})} \qquad [10]$$

where S_H is the solubility of atomic H_2 in the steel.

Parent material

In Fig. 4-9, K_{IH} fracture toughness data and K_{TH} threshold stress intensity data are presented as a function of H_2 gas pressure for carbon steel parent materials with a yield strength, $R_{p0.2}$ < ~ 600 MPa. In general, H_2 cracking rates are very high, such that the magnitudes of K_{IH} are only marginally above those of K_{TH}. K_{IH} for a given carbon steel decreases with increasing P_{H2} to a minimum at ~ 25 MPa, above which the magnitude of K_{IH} remains relatively constant. While the minimum value of K_{IH} for low strength carbon steel parent materials (for P_{H2} > ~ 25 MPa) is ~ 45MPa√m, the minimum value of K_{IH} for P_{H2} ~ 11 MPa is ~ 55 MPa√m. While this is significantly lower than the 71MPa√m defined by Turnbull (2009), it is consistent with the value of 55 MPa√m cited by ASME (2019).

On the basis of the data reviewed, lower and upper bound $K_{IH}(P_{H2})$ relationships have respectively been defined as:

$$K_{IH} = 45.7 + 100.67 \exp(-0.225 P_{H2}) \quad [11]$$

$$K_{IH} = 167.5 + 100.67 \exp(-0.225 P_{H2}) \quad [12]$$

with P_{H2} in MPa and K_{IH} in MPa√m.

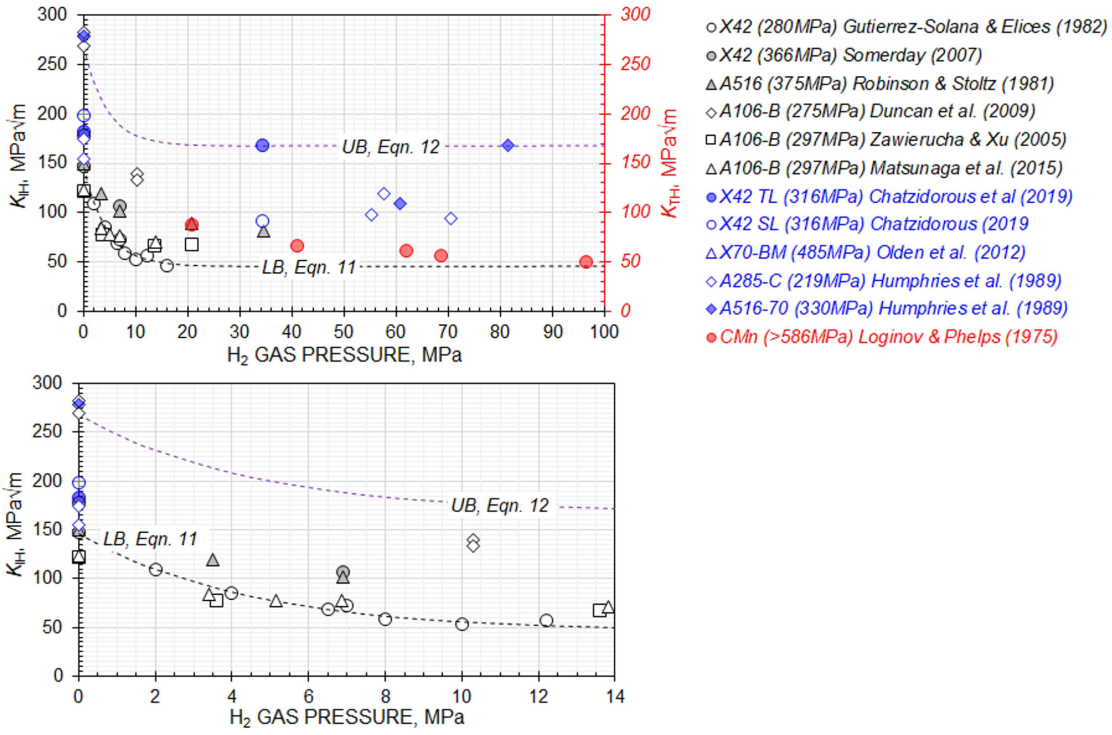

Fig. 4-9: Influence of hydrogen pressure on fracture toughness and threshold stress intensity factor of low-strength carbon steels

Top: complete dataset. Bottom: H_2 pressure range of 0 – 14 MPa (Gutiérrez-Solana & Elices 1982, Somerday et al. 2008, Robinson & Stoltz 1981, Zawierucha & Xu 2005, Chatzidouros et al. 2019, Olden et al. 2012, Loginow & Phelps 1975, Humphries et al. 1993).

When the source reference K_{IH} data are expressed in terms of C_H, an equivalent P_{H2} was determined using Equation [10]. The K_{IH} data directly determined as a function of P_{H2} in the source references are given as black symbols, while those originally determined as a function of C_H are represented by blue symbols. K_{TH} data are represented with red symbols.

The legend gives the yield strength of the material ($R_{p0.2}$) and the source reference.

EB weldments

The availability of fracture toughness data for thick section (140 mm thick) PWHTed EB-welded carbon steel HAZ and fusion zone are limited, even in air, and what is available typically applies to lower section thicknesses, e.g., 75 mm (Elliott 1984), 100 mm (Kihara et al. 1984). It is likely that the fracture toughness of PWHTed low-strength carbon steel EB weldments in H_2 is not significantly lower than that of the equivalent parent steel, and usually of a similar magnitude, although actual K_{IH} data for such joints are even scarcer than those for parent materials. The evidence presented in Somerday et al. (2008) for an electrical resistance weldment appears to indicate that the minimum K_{IH} may be lower than that for low-strength carbon steel parent material in H_2, but the applicability of the data to EB welds is questionable. Hence, on the basis of available knowledge, the minimum K_{IH} for PWHTed low-strength, carbon steel EB weldments in H_2 (i.e., with P_{H2} ~11 MPa) is assumed to be the same as that of the parent steel (i.e., 55 MPa√m).

4.2.4.4 Treatment of HIC in canister lifetime assessment

Hydrogen-induced cracking is included in the assessment of the canister integrity through the specification of a reduced fracture toughness (K_{IH}) due to the absorption of H_2 by the canister material during anaerobic corrosion. The value of K_{IH} is given by the minimum value of 55 MPa√m discussed above and cited in ASME (2019). This value is considered conservative primarily because it has been determined at room temperature, and fracture toughness increases with temperature (Turnbull 2009).

4.2.5 Microbially influenced corrosion

As discussed in Section 2.2.4, microbial activity is only expected to occur in the EDZ of the OPA around the emplacement drift where there is more physical space and moisture to support such activity. Aerobic microbial activity in the EDZ is thought to be one of the processes responsible for the rapid consumption of the initially trapped O_2 in the FE-G experiment (Fig. 4-1). Once anaerobic conditions have been established, sulphate reduction by sulphate reducing bacteria (SRB) in the EDZ will produce sulphide that could diffuse to the canister surface and result in chemical microbially influenced corrosion (CMIC) (Enning & Garrelfs 2014).

Various models have been developed to predict the extent of CMIC by the remote activity of SRB (King et al. 2024b). These models are generally based on the use of Monod kinetics to predict the rate of sulphate production via either organotrophic (using organic carbon as an electron donor) or lithotrophic (using H_2 as the electron donor) pathways. The resulting flux of sulphide to the canister surface in the repository has been estimated by Cloet et al. (2017). For well-emplaced bentonite, the flux of sulphide to the canister surface from the EDZ where it is assumed to be produced is predicted to increase with time, reaching a steady-state value of approximately 6×10^{-6} mol·m^{-2}·a^{-1}. For the reaction,

$$Fe + HS^- + H_2O \rightarrow FeS + H_2 + OH^- \quad [13]$$

this steady-state flux corresponds to a maximum corrosion rate of 0.04 nm·a^{-1}. The flux calculated by Cloet et al. (2017) included attenuation of the supply of sulphide due to the precipitation of HS^- with Fe(II)/Fe(III) species present as accessory minerals in the bentonite clay and OPA (e.g., siderite). However, there will also be a substantial release of Fe(II) from the canister due to anaerobic corrosion supported by the reduction of H_2O (Reactions [5]-[9]). If these additional attenuation reactions are taken into account, then virtually no sulphide reaches the canister surface and causes corrosion (Smart et al. 2024). Of the total wall thickness of 140 mm, only 0.25 µm is predicted to be corroded via Reaction [13], with the vast majority of corrosion being the result of anaerobic corrosion by H_2O.

4.2.5.1 Treatment of MIC in canister lifetime assessment

MIC is not explicitly included in the assessment of the long-term performance of the canister in this report. Nearfield microbial activity and the possibility of biofilm formation are excluded because of the inhibiting effect of compacted bentonite on microbial activity. Microbial activity in the EDZ and undisturbed OPA can produce aggressive metabolic by-products such as sulphide, but the flux of corrosive species to the canister is predicted to be much lower than the corresponding rate of anaerobic corrosion due to the reduction of H_2O. Therefore, the additional corrosion due to the remotely produced sulphide by SRB is not accounted for in the canister lifetime prediction.

4.3 Structural assessment

The structural performance of SF and RP-HLW disposal canisters has been assessed both for an "as-built" canister and for one after 10,000 years of disposal (with a wall loss of 7 mm, see Section 4.2.1.4). The main differences between the two assessment points are that, at the time of emplacement, the canister has its design wall thickness and the as-received material toughness, while after 10,000 years both wall thickness and toughness are decreased due to corrosion and the effect of hydrogen, respectively. A summary of inputs employed in the ECA calculations are given in Tab. 4-3.

Tab. 4-3: Inputs used in ECA calculations

Input	**SF**		**RP-HLW**	
	As built	10,000 years	As built	10,000 years
Thickness, mm	140	133	140	133
Width, mm	3,455.8	3,411.8	2,262	2,218
Yield strength, MPa	211.8			
Tensile strength, MPa	394.9			
Elastic modulus, MPa	203,610			
Poisson's ratio	0.3			
Fracture toughness, MPa√m	68.0	55.0	68.0	55.0
Primary membrane stress, MPa	0	-20.4	0	-19.1
Bending stress, MPa	0	66.8	0	7.0
Secondary stress, MPa	82.4		100.1	

It can be seen that the fracture toughness of the closure weld after PWHT (i.e., at the time of emplacement) was estimated to be 68 MPa√m using Equations J.2 and J.5 of BS 7910 based on a wall thickness of 140 mm, a toughness requirement of T_{27J} = - 20 °C (see Section 3.4), an assessment temperature T = 20 °C, a temperature scatter in Charpy versus fracture toughness correlation T_k = 25 °C and a probability of exceedance, P_f = 0.05.

Equations J.2 and J.5 of BS 7910 are as follows:

$$T_0 = T_{27J} - 18°C \quad [14]$$

$$K_{mat} = 20 + \{11 + 77exp[0.019(T - T_0 - T_k)]\}\left(\frac{25}{B}\right)^{0.25}\left[\ln\left(\frac{1}{1-P_f}\right)\right] \quad [15]$$

4.3.1 Stresses under long-term disposal loads

The stresses assuming long-term disposal loads were computed using FEA. Models were developed for the SF and RP-HLW disposal canisters using the loads and corroded wall thickness. The maximum principal stress profiles in the vicinity of the weld were extracted for use in the ECA calculations. The peak values of axial welding residual stress profiles determined from transient simulations were used.

These FEA models are shown in Fig. 4-10 and Fig. 4-11 below. Symmetry was exploited to model 1/8 of the actual canister. The models of the long-term loading accounted for potential corrosion by removing 7 mm from all outer surfaces (equivalent to a corrosion rate of 0.7 $\mu m \cdot a^{-1}$ for 10,000 years; see also Section 4.2.1) to give a wall thickness of 133 mm. This loss of wall thickness due to corrosion means that after 10,000 years for the SF canisters the radius is 543 mm and the circumference is 3,411 mm, while for the RP-HLW canisters the radius is 353 mm and the circumference is 2,218 mm. Hexahedral quadratic stress elements (Abaqus element C3D20R) were used throughout, with the mesh refined in the region around the closure weld and at least four elements across all sections.

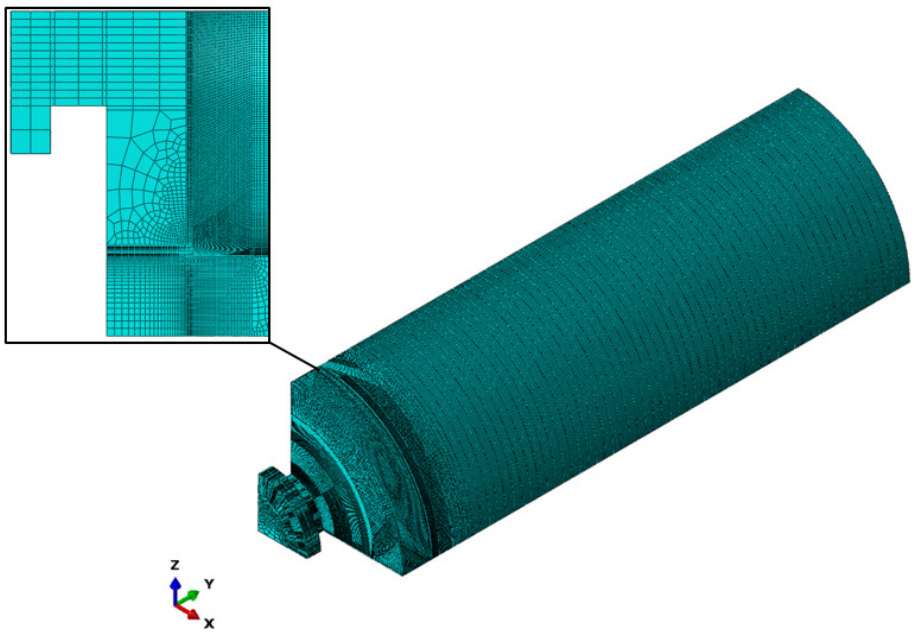

Fig. 4-10: Model showing mesh used to compute stresses under long-term loads for the SF disposal canister

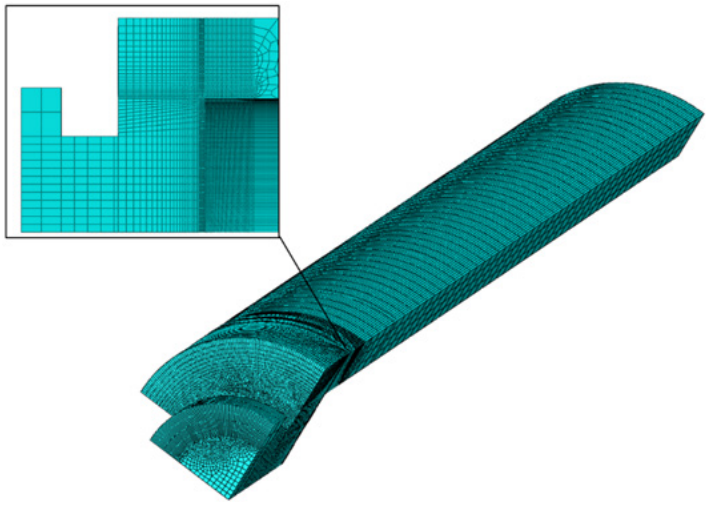

Fig. 4-11: Model showing mesh used to compute stresses under long-term loads for the RP-HLW disposal canister

In these models, only linear elastic material properties were employed for simplicity.

The loads experienced by the canister were modelled as an external pressure distribution varying from 15.2 MPa to 21.6 MPa around the circumference according to a cosine function (see Section 2.3.2) but remaining constant along the length of the canister (Fig. 4-12). A uniform, normal pressure of 21.6 MPa was applied to the surface of the flat ends.

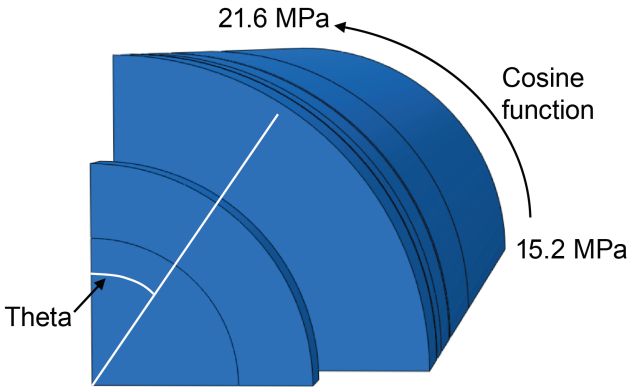

Fig. 4-12: Circumferential pressure applied to the canister in the long-term loading models, varying as a cosine function of the angle theta

The computed stresses are shown in Fig. 4-13 for the SF canister and Fig. 4-14 for the RP-HLW canister. It can be seen that the stresses are all below the minimum $Rp_{0.2}$ of the canister material (220 MPa) apart from an extremely localised high stress around the singularity at the tip of the unfused land, which is considered to be a numerical artefact.

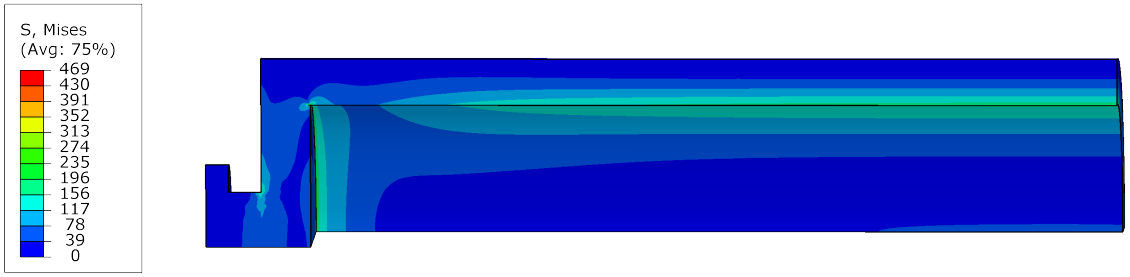

Fig. 4-13: von Mises stress (MPa) in the SF disposal canister under long-term loading

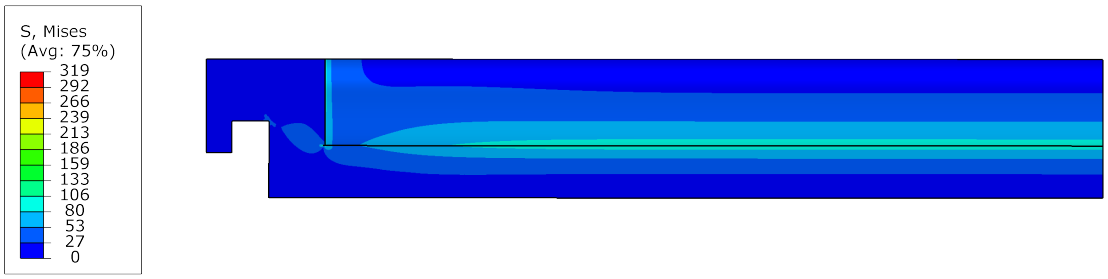

Fig. 4-14: von Mises stress (MPa) in the RP-HLW disposal canister under long-term loading

For use in the ECA, stresses were extracted along radial paths on the two long symmetry planes through the weld centreline from each model. The profiles that gave the highest linearised stress in each case were selected for use in the ECA (i.e., worst case). These are shown in Fig. 4-15 for the SF canister and Fig. 4-16 for the RP-HLW canister. In each case, there is a peak in stress which corresponds to the position through the weld where it passes across the unfused land. Again, this is considered to be a numerical artefact.

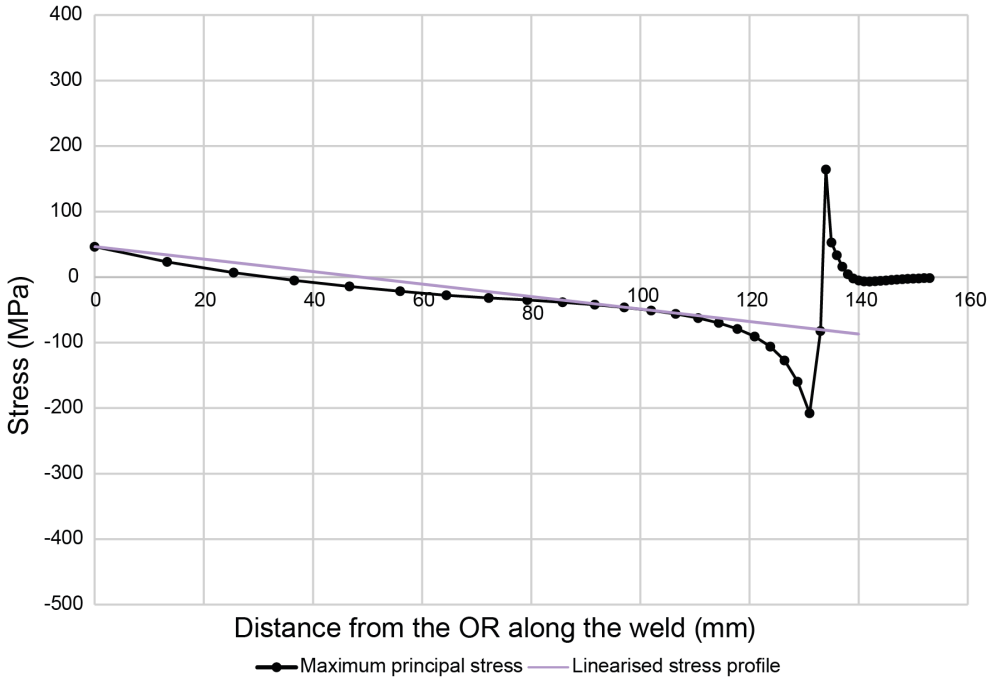

Fig. 4-15: Stress along the most highly stressed radial path on symmetry plane through weld centreline for the SF disposal canister

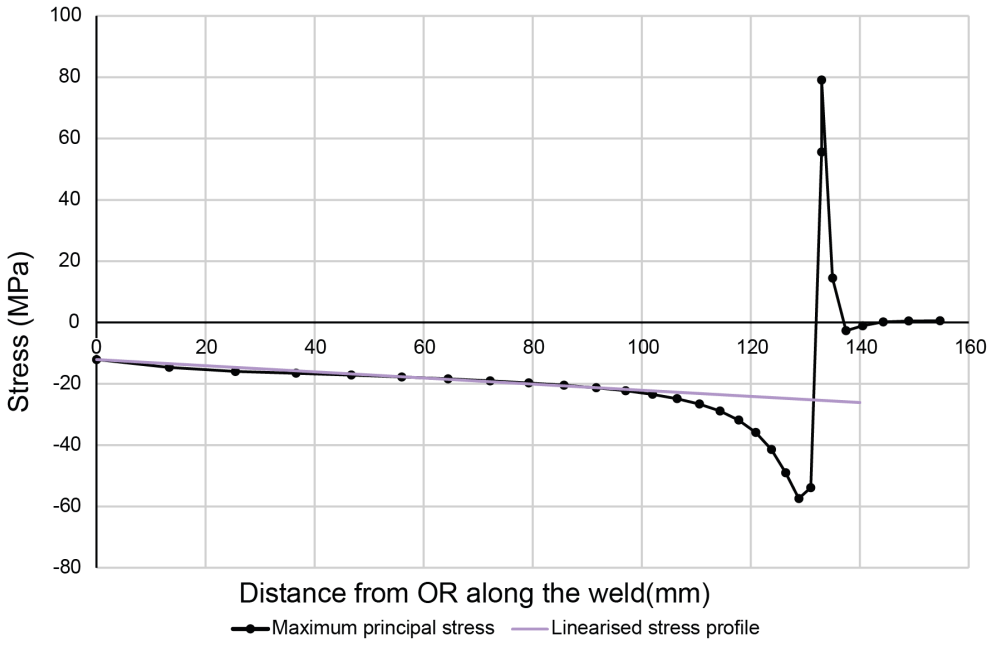

Fig. 4-16: Stress along the most highly stressed radial path on symmetry plane through weld centreline for the RP-HLW disposal canister

These linearised stresses were used in the ECA calculations, together with the residual stresses after PWHT described in Section 3.7. A summary of the stress values employed in ECA is shown in Tab. 4-4. Bending stress components were kept as positive values to bound both external and internal flaws.

Tab. 4-4: Stress values employed in ECA

Canister type	**Primary membrane stress** [MPa]	**Primary bending stress** [MPa]	**Secondary membrane stress** [MPa]
SF	-20.4	66.8	82.4
RP-HLW	-19.1	7.0	100.1

4.3.2 Critical flaw size estimates

The structural performance of the canisters was established using the ECA approach and assumptions described in Section 3.2. In short, three types of flaws were examined: surface-breaking, long surface-breaking and embedded with a ligament height greater than 2 mm. Flaws located very close to the surface i.e., 2 mm or less, can be bound by the limiting sizes of surface or long surface flaws. Since the analytical solutions for flaws in a plate do not change whether the flaws are located in the outer or inner surface, the bounding condition used to consider both internal and external surfaces was a positive bending stress value.

The critical flaw sizes presented here assumed a wall thickness of 133 mm, specified minimum tensile properties corrected to 48 °C, maximum principal primary stresses and peak magnitude from PWHT WRS profiles.

The critical flaw size plots are included in App. F. In SF canisters, when flaws are 33 mm deep or less, the maximum tolerable length was estimated to be 2,729.4 mm. This is the validity limit of the BS 7910 (BSI 2019b) analytical solutions. For a surface flaw with a depth of 113 mm, the maximum tolerable flaw length was 113.1 mm. If a long surface flaw was present, a height up to 29.7 mm could be tolerated. All critical embedded flaw sizes (after application of the safety factor of 10) are well above inspection detection limits.

The RP-HLW canister can tolerate a flaw length up the validity limit of BS 7910 solutions (BSI 2019b) when the flaw is 53 mm deep. If a long surface flaw is present, a height up to 42.7 mm is acceptable. App. F also provides a summary of critical sizes of embedded flaws located at a distance > 2 mm from the surface. It can be seen that these critical flaw sizes can be readily detected by surface and sub-surface inspection methods.

It is worth noting that for any embedded flaws located at a distance greater than the largest ligament size reported here to mid thickness from either ID or OD, they will be bound by the limiting sizes of the largest ligament. This is because as the ligament size increases, the load-bearing capacity of that local ligament also increases. In these cases, the largest tolerable flaw height (a) is taken as the sum of half the section thickness plus ligament height, i.e., $0.5 \cdot B + p$.

As the absolute value of primary bending stress was employed in the ECA, the results represented here would bound an embedded flaw on either the ID or OD of the canister at a given ligament (p).

The recommendation in Patel et al. (2012) includes a safety factor of 10 on the critical flaw sizes:

- The largest acceptable surface flaw is 113 × 113.1 mm in SF canisters. After incorporating a factor of 10, the critical size is 11.3 × 11.3 mm. This is greater than the surface inspection detection limit of 1 × 10 mm.
- The largest acceptable surface flaw is 123 × 261.9 mm in RP-HLW canisters. After incurporating a factor of 10, the critical size is 12.3 × 6.2 mm. This is greater than the surface inspection detection limit of 1 × 10 mm.
- The largest acceptable embedded flaw is 127 × 178.1 mm at 3 mm from the SF canister surface. After the safety factor correction, it becomes 12.7 × 17.8 mm. This is above the subsurface detection limit of 4 × 15 mm.
- The largest acceptable embedded flaw is 127 × 333.8 mm at 3 mm from the RP-HLW canister surface. After the safety factor correction, it becomes 12.7 × 33.4 mm. This is above the subsurface detection limit of 4 × 15 mm.

The critical flaw sizes predicted by ECA are well above the inspection detection limit. This means if there are any unacceptable flaws, they will be readily detectable by inspection.

4.3.3 Structural integrity of canisters

It is theoretically possible that the flaws that fall within the detection limits (Tab. 4-5) can be missed during inspection. This section describes the ECA calculations to establish if such missed flaws could remain safe. The inputs used in these assessments are listed in Tab. 4-3, while the results are presented in Fig. 4-17 to Fig. 4-24.

Tab. 4-5: Inspection detection limit

Flaw location	**Detectable flaw height** [mm]	**Detectable flaw length** [mm]
Outer surface	1	10
Inner surface near weld root	4	15

If a 1 × 10 mm surface flaw on the OD was missed during inspection, it could remain safe, as illustrated by the square symbol in Fig. 4-17. As there will be no external loadings present during this time, there is no risk of plastic collapse, hence $L_r = 0$. In addition, after 10,000 years, the flaw would be corroded away.

If a flaw of 4 × 15 mm on the ID was missed, the ECA demonstrates that it would remain safe throughout the canister lifetime, although it does move, as expected, towards the failure assessment line as the canister corrodes. Similar to the previous flaw, there will be no primary stresses after PWHT. The long-term stresses, the reduced thickness and degraded material properties lead to an increase in L_r and K_r but the assessment point still sits well within the FAD, as per Fig. 4-17. Similar remarks can be made on the RP-HLW canisters if flaws within the detection limit were missed during inspection, see Fig. 4-18. The increase in K_r in both Fig. 4-17 and Fig. 4-18 for a 4 × 15 mm flaw is not significant as the primary membrane stresses are largely compressive.

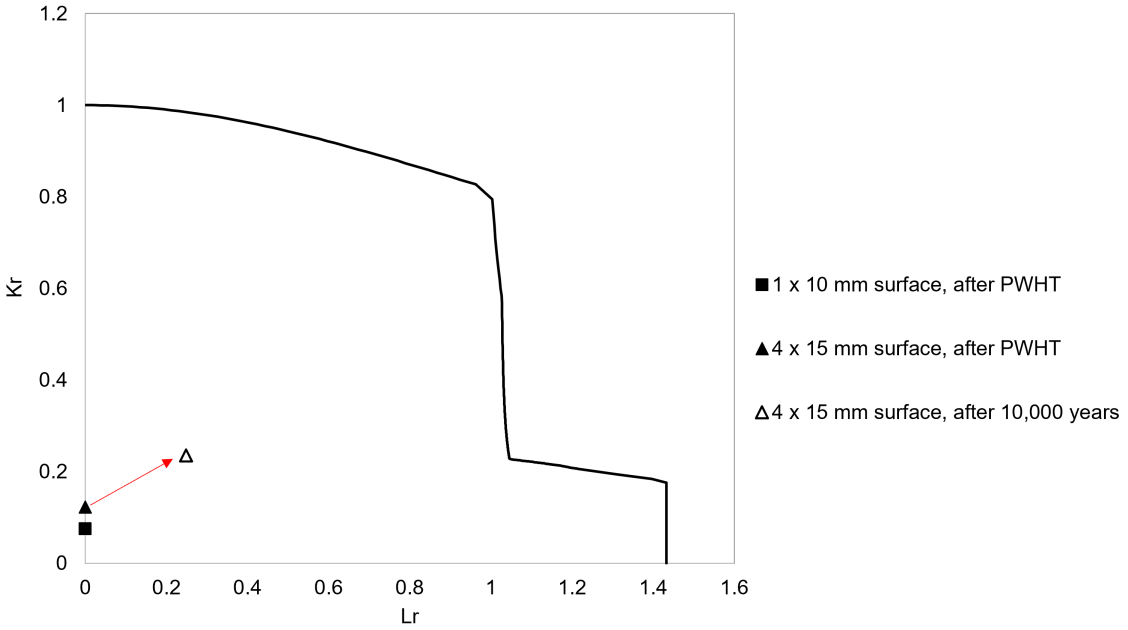

Fig. 4-17: Assessment results showing acceptability of flaws missed by inspection in SF disposal canisters

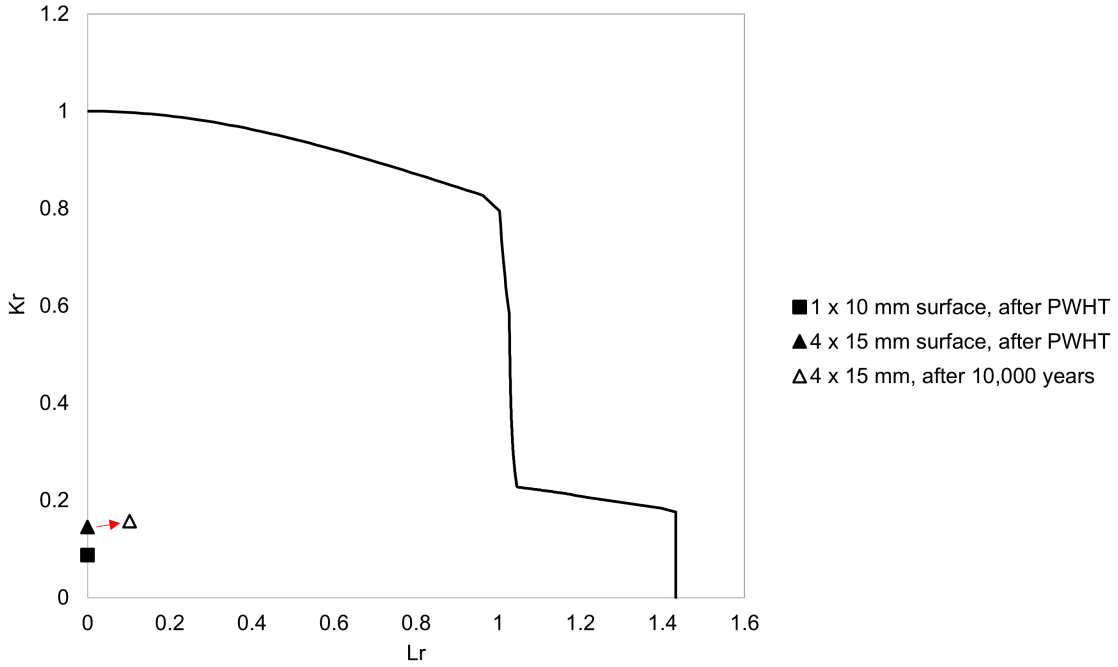

Fig. 4-18: Assessment results showing the evolution of flaws missed by inspection in RP-HLW disposal canisters

Further considerations were given to embedded flaws that may experience a change in ligament size in 10,000 years:

- After 10,000 years, the ligament of a 4 × 15 mm flaw located at 28 mm from the OD, is reduced to 21 mm due to corrosion loss. This considers lack-of-fusion or lack-of–penetration and root spiking defects that are possible between 20 and 100% of section thickness from the external surface. They may be sufficiently close together to be considered as a single flaw and yet small enough to missed by inspection:
  - Fig. 4-19 shows that the flaw after 10,000 years remains safe in SF canisters. The shift of the assessment point to the left is a result of long-term stresses, reduced thickness and toughness properties.
  - Similar observations are reported for RP-HLW canisters, see Fig. 4-20. There is a small increase in K_r but it is sufficiently small that it is not pronounced in the FAD.
- After 10,000 years, a 4 × 15 mm flaw initially located 9 mm from the OD will be closer to the OD with a ligament of 2 m or less. As it is sufficiently close to the surface, this is recharacterised as 6 × 17 mm flaw in line with BS 7910 Annex E rules:
  - Fig. 4-21 illustrates the acceptance of this flaw in SF canisters. It can be seen that after 10,000 years, the recharacterised flaw of 6 × 17 mm remains acceptable.
  - The same can be concluded for RP-HLW canisters (Fig. 4-22). A larger recharacterised flaw of 6 × 17 mm remains acceptable.
- A 4 × 15 mm flaw located 7 mm from the OD. After 10,000 years, the ligament would have been corroded away turning the embedded flaw into surface breaking flaw of 4 × 15 mm:
  - Fig. 4-23 shows that after a thickness loss of 7 mm, a 4 × 15 mm surface flaw remains acceptable in SF canisters.
  - Fig. 4-24 shows the same observation for RP-HLW canisters.

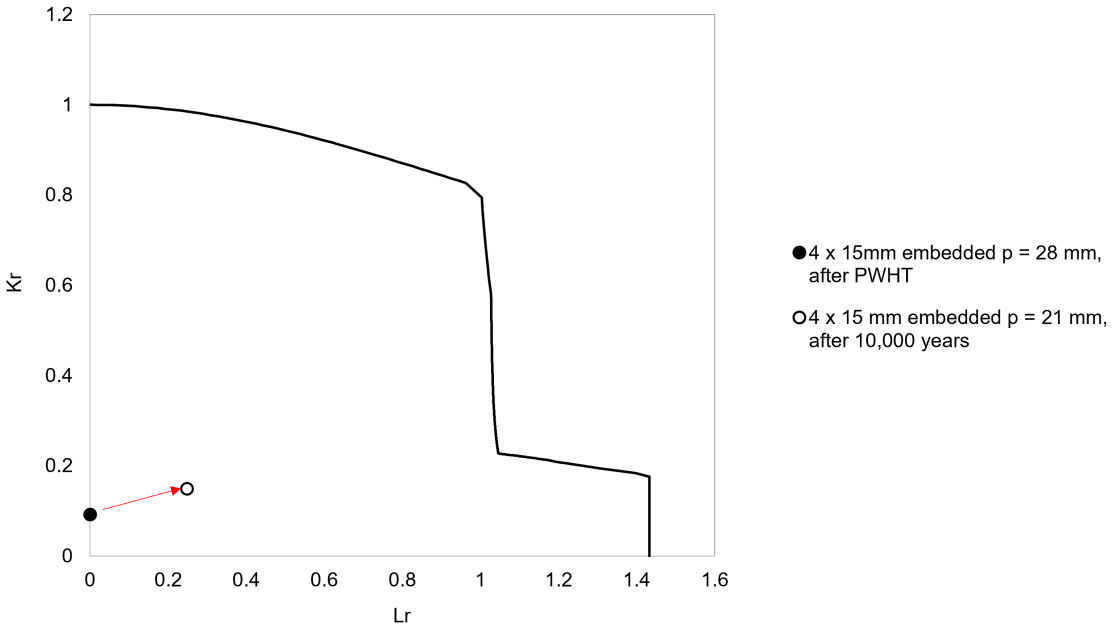

Fig. 4-19: Assessment results showing the evolution of a 4 × 15 mm flaw located at 28 mm from the OD in the SF disposal canisters

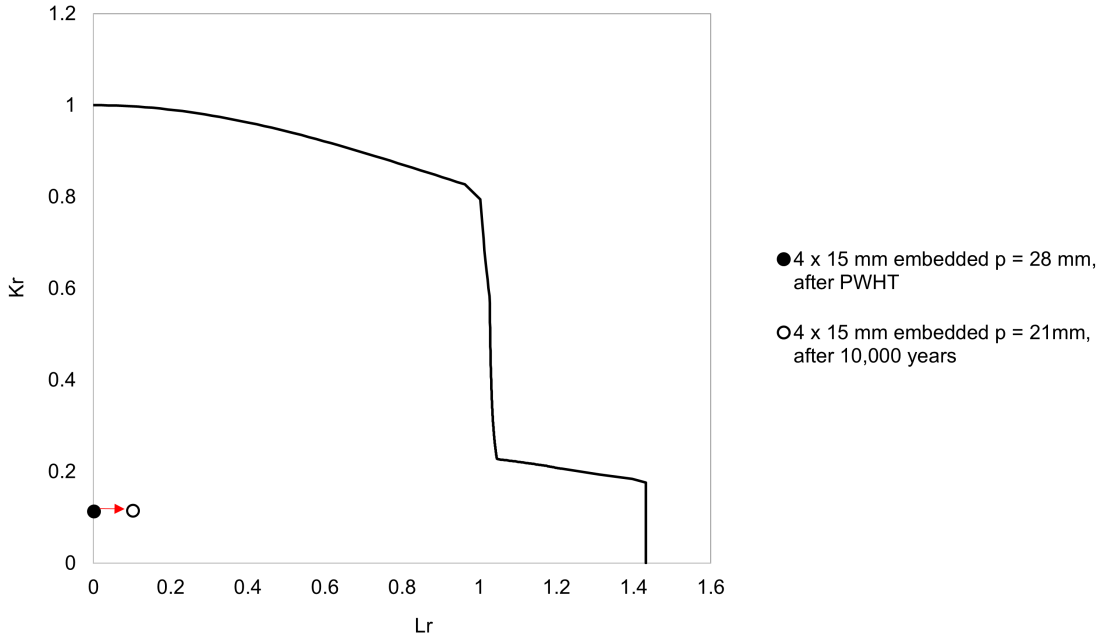

Fig. 4-20: Assessment results showing the evolution of a 4 × 15 mm flaw located at 28 mm from the OD in the RP-HLW disposal canisters

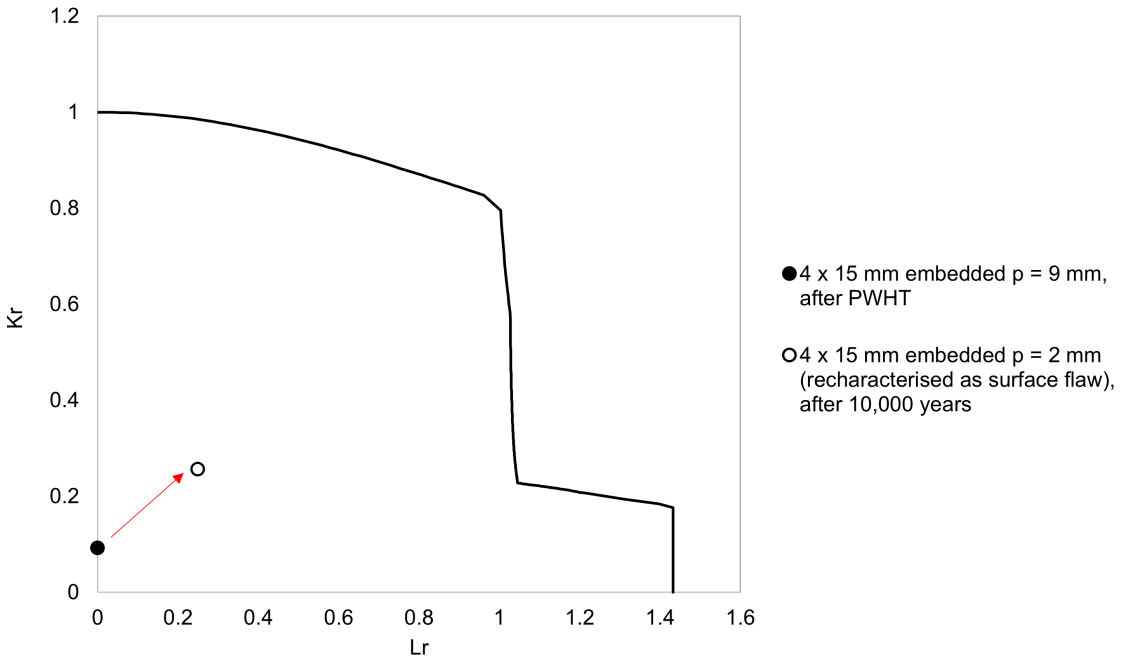

Fig. 4-21: Assessment results showing the evolution of a 4 × 15 mm flaw located at 9 mm from the OD in the SF disposal canisters

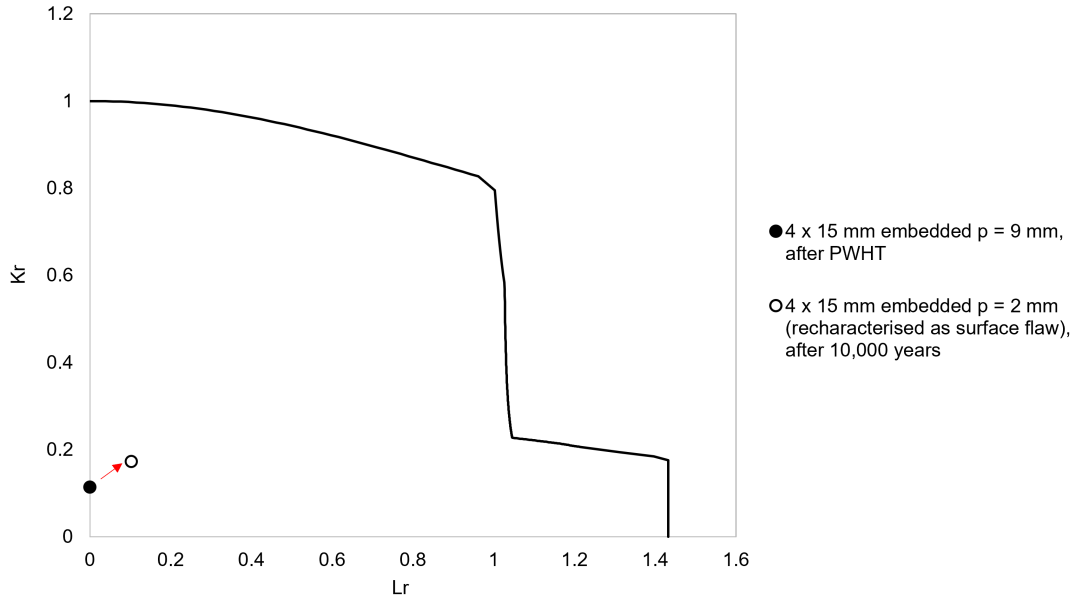

Fig. 4-22: Assessment results showing the evolution of a 4 × 15 mm flaw located at 9 mm from the OD in the RP-HLW disposal canisters

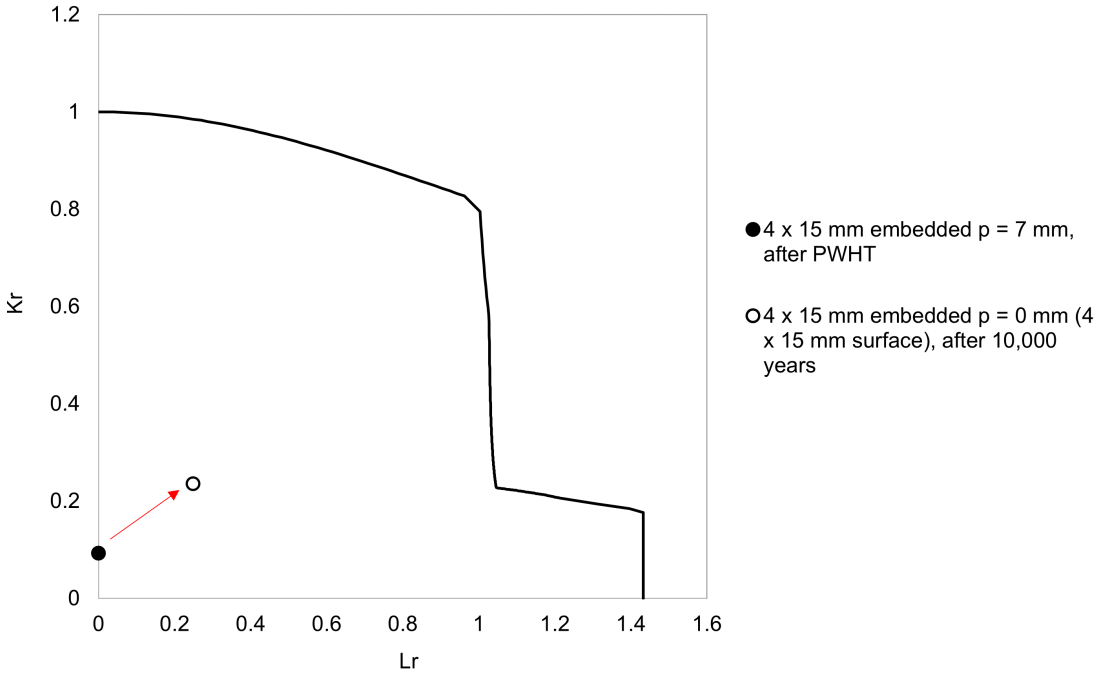

Fig. 4-23: Assessment results showing the evolution of a 4 × 15 mm flaw located at 7 mm from the OD in the SF disposal canisters

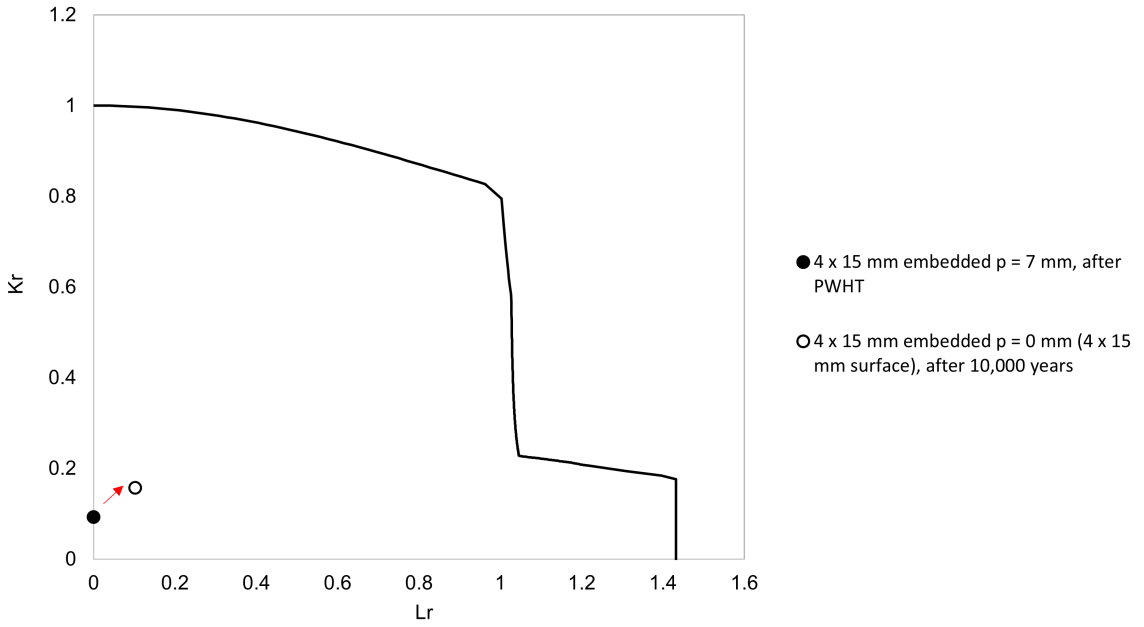

Fig. 4-24: Assessment results showing the evolution of a 4 × 15 mm flaw located at 7 mm from the OD in the RP-HLW disposal canisters

It is worth noting that the assessment points of flaws in SF disposal canisters are always higher in K_r because the long-term bending stresses of SF disposal canisters are greater than those of RP-HLW disposal canisters.

4.4 Confidence in lifetime prediction

Mathematical models for predicting the extent of corrosion processes are often validated against the results of experimental data (King et al. 2024a, King et al. 2024b). However, because of the long timescales involved and because of the large physical scale of the repository, it is generally impossible to validate canister lifetime prediction models against short-term laboratory observations. Therefore, several methodologies have been developed to build confidence in the prediction of corrosion processes over the long timescales involved, including:

- Evidence from in-situ experiments that closely simulate the repository environment.
- Evidence from archaeological analogues dating from periods that may, in some cases, exceed the minimum and/or design lifetimes of the canisters.
- The use of complementary models for predicting the rate and extent of different corrosion processes to which the canister may be exposed.
- Demonstration of a sound mechanistic understanding of the corrosion and mechanical degradation processes to which the canisters will be subjected.

After construction of the repository, it may be possible to further support confidence building by monitoring the integrity of the initially emplaced canisters in the pilot repository.

4.4.1 In-situ experiments

Information from in-situ experiments can be used to justify long-term predictions of the canister performance in a number of ways. By "in-situ experiments", we refer to tests that are typically performed in an underground research laboratory (URL) in a geological setting similar to that of the proposed repository (Diomidis & King 2020). Such experiments are often on a physical scale similar to that of the repository, as in the case of the FE experiment at Mont Terri (Müller et al. 2017), and in this way bridge the gap between small-scale laboratory experiments and the much larger scale of the repository. Because in-situ experiments are performed in URLs, it may also be possible to replicate certain environmental conditions specific to the repository location, such as the natural groundwater or the presence of indigenous microbial populations. Lastly, in-situ tests are commonly conducted for longer durations than laboratory experiments and, in the case of the initial aerobic phase, these durations can equal or exceed those expected in the repository itself.

The results of in-situ experiments are used for a number of purposes, including:

- Development of conceptual models for the performance of the repository that is not possible from small-scale laboratory tests.
- Synergistic studies, where parameters may be coupled.
- Validation of process models.
- Provision of data that can be used for canister lifetime predictions.

Nagra has made extensive use of in-situ experiments, particularly those located in the URLs at Mont Terri and Grimsel (Diomidis & King 2020). For example, the FE-G experiment at Mont Terri has provided information about the initial aerobic transient period and, in particular, the evidence that the initially trapped atmospheric O_2 is consumed within a matter of days or weeks following backfilling (Fig. 4-1). A mechanistically based process model has been developed to account for the observed behaviour and has provided valuable insights into the processes responsible for the consumption of O_2 during the redox transient (Giroud et al. 2018, King & Briggs 2024). When the test is eventually decommissioned, inspection of the heater surfaces and

specially prepared corrosion coupons will indicate the extent, if any, of localised corrosion. In particular, this will address the issue of whether a differential [O_2] cell could be established on the canister surface at the interface between the compacted bentonite block pedestal and the drier GBM, i.e., the so-called "focused corrosion" mechanism described by Landolt et al. (2009). The results of the process model to date (Fig. 4-1) suggest that no significant oxic corrosion will have occurred, but post-test inspection will provide definitive evidence. The FE-G experiment has proven to be a particular useful in-situ experiment, in large part because the timescale spans the entire duration of the aerobic-anaerobic transient.

The other major use of in-situ experiments in the Nagra canister programme is the measurement of long-term anaerobic corrosion rates (Reddy et al. 2021a, Reddy et al. 2021b). Results from the iron corrosion experiment at Mont Terri (IC-A) (Reddy et al. 2021b) are included in the analysis of reference corrosion rates of Diomidis et al. (2023) and contribute to the estimation of the best-estimate and upper and lower bound rates in Tab. 4-1. To date, these experiments have been running for a period of > 9 years and will continue to provide long-term corrosion rate data in the future.

4.4.2 Analogue studies

Along with copper, carbon steel is one of the few candidate canister materials for which there are natural and/or archaeological analogues that can help support long-term predictions of the corrosion behaviour (King 2021, Neff et al. 2010, Alexander & Reijonen 2024). Uniquely among the various confidence-building methods, analogues have representative timescales that match and, in the case of artefacts from the Iron Age and Roman era, exceed the regulatory canister lifetime requirement of 1,000 years.

Analogue studies can be used to support canister lifetime predictions in a number of ways, including:

- the provision of corrosion damage data, typically in the form of either corrosion rates or pit depths,
- evidence for the nature of corrosion products,
- the development of conceptual models,
- validation of mechanistically based corrosion models, and
- to generally build confidence in long-term predictions.

Analogue studies are often included in a well-structured canister development programme that combines the results from short-term laboratory experiments, simulation and modelling, large-scale *in situ* tests, and analogue studies (Dillmann et al. 2014). In general, analogues are used to support predictions of the rate and extent of uniform and localised corrosion rather than environmentally assisted cracking mechanisms, for which there are few, if any, analogues (King et al. 2023). However, analogue studies are not widely used to support predictions of the mechanical stability of the canister.

Although analogues are useful because of their longevity, there are also certain disadvantages. The composition and microstructure of the iron or steel artefacts are invariably different from those from which the canister is fabricated. Furthermore, the nature of the "disposal" environment is usually different from that expected in the repository.

Analogues owe their continued existence to either kinetic or thermodynamic stability (King et al. 2023). Thermodynamic stability results when the metal artefact is in equilibrium with the dissolved metal ions in a closed system (i.e., one in which there is no mass transport of reactants

or products). Cases of thermodynamic stability are rare and the majority of analogues, including all of those for iron or steel, are the result of kinetic stability. Artefacts may be kinetically stable due to the presence of a protective surface film or because of the slow transport rate of reactants and/or products. Examples of protective surface films include the hoard of Roman nails at the Inchtuthil site in Scotland which have remained largely intact due to the formation of a protective surface oxide, even though they were exposed to aerobic conditions for a period of approximately 2,000 years (Mapelli et al. 2009, Milodowski et al. 2015).

Nagra uses evidence from analogue studies to support canister lifetimes predictions as described below, and is a partner in a study of artefacts from the Aventicum Roman site near Avenches, Vaud, Switzerland. Iron-based artefacts, such as nails, are being studied as part of the Corint (Elucidating Corrosion of Iron by New Quantitative Multimodal In Situ Tomography[5]) project with the aims of developing new methodologies for characterisation of artefacts in an undisturbed state, understanding the long-term corrosion mechanisms and developing improved conservation methods for archaeological artefacts.

As well as providing mechanistic information, the study of archaeological artefacts can provide an estimate of the long-term corrosion rate of buried iron objects (Neff et al. 2006). Fig. 4-25 shows a comparison of the time-dependence of the depth of corrosion from laboratory experiments and from iron objects from a 1,500-years-old analogue site in Japan (Yoshikawa et al. 2008). The range of "estimated realistic corrosion" depths proposed by the authors is equivalent to a corrosion rate of 0.3 – 2.0 $\mu m \cdot a^{-1}$ after 10,000 years. In comparison, the range of long-term anaerobic corrosion rates for carbon steel estimated from experimental studies in compacted bentonite is 0.026 – 0.7 $\mu m \cdot a^{-1}$ (Tab. 4-1). Thus, evidence from analogue studies provides good support for the long-term rate used in canister lifetime predictions.

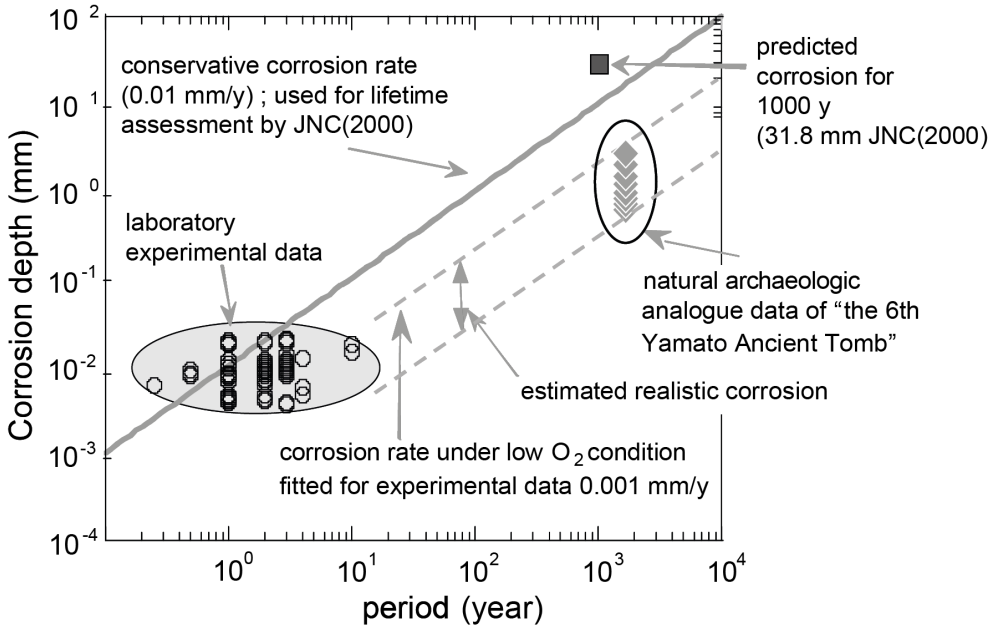

Fig. 4-25: Comparison of anaerobic corrosion rates from laboratory experiment and those derived from a 1,500-years-old analogue site in Japan

Adapted from Yoshikawa et al. (2008).

[5] www.corrosion-corint.ch

Another corrosion mechanism for which evidence from analogues is used is localised corrosion and, specifically, the pitting factor. The pitting factor decreases with increasing depth (equivalent to increasing time of exposure), indicating that corrosion becomes less localised and more uniform with increasing time (Fig. 4-7). These data are used in Section 4.2.2 to assess the extent of localised corrosion during the early aerobic phase and also to support the argument that, at longer time periods, corrosion will be essentially uniform in nature.

In summary, Nagra makes extensive use of analogues to support canister lifetime predictions. The evidence from analogue studies is primarily used to build confidence in the long-term predictions by supporting the distribution of anaerobic corrosion rates and the argument that corrosion is generally uniform in nature.

4.4.3 Complementary models

The aim of the use of complementary models is to demonstrate that both the models themselves and the predictions made using the models are robust.

Robustness of the models themselves can be demonstrated by comparing the predictions from similar models. As part of Posiva and SKB's Integrated Sulfide Project, three reactive-transport models for the microbial production, transport, and consumption of sulphide were benchmarked against each other (Posiva & SKB 2021). Although the structures and, in some respects, the mechanistic basis for the three models were quite different, the results of comparative analyses were similar, providing confidence in the robustness of the modelling approach. One of these models, developed by the University of Bern, has been used by Nagra to estimate the flux of sulphide and the resulting extent of canister corrosion (see Section 4.2.5).

Another example of the use of complementary models is the treatment of the HIC of carbon steel canisters. In this case, quite different approaches are used for a given corrosion process but with the same outcome, thus providing confidence in the robustness of the long-term prediction. The approach of Andra (Andra 2022) and NUMO (Ogawa et al. 2017, NUMO 2021) to predicting HIC is to develop a reasoned argument based on the results of laboratory experiments and/or well-established industrial experience that HIC will not occur under repository conditions for the particular canister material. A similar approach could have been adopted in the Nagra programme. Instead, the possibility of HIC has been explicitly included in the structural assessment described in Section 4.3 through the use of a lower value for the fracture toughness parameter consistent with embrittlement due to absorbed hydrogen. However, the results of the analysis demonstrate that HIC does not lead to canister failure within the assumed lifetime of 10,000 years, as provided by the canister provisional design. Thus, the outcome is the same for the two approaches, providing confidence that hydrogen-related degradation will not adversely impact the long-term performance of the canister within the relevant time frame.

4.4.4 Mechanistic understanding

The development of mechanistic understanding is a natural outcome of the conduct of laboratory and in-situ experiments and is useful for justifying long-term model predictions. Mechanistic understanding is used to:

- Develop conceptual models for different processes, either detailed process models (King et al. 2024a) or abstracted performance assessment models (King et al. 2024b).
- Support the exclusion of various corrosion processes by the development of mechanistically based reasoned arguments (for example, the exclusion of SCC of copper based on a mechanistically based decision tree (Diomidis & King 2022), or the exclusion of the crevice corrosion of Alloy 22 waste packages based on an electrochemically-derived criterion for initiation (DOE 2008)).
- Support and justify the extrapolation of (relatively) short-term empirical observations over long timescales (for example, justification that the growth of a porous Fe_3O_4 corrosion product layer will not lead to an increase in corrosion rate due to enhancement of the rate of the cathodic reaction (Taniguchi 2003)).

5 Summary and conclusions

This report describes a method for manufacturing and sealing canisters for the deep geological disposal of SF and RP-HLW in Switzerland based on present day technology. The development of the disposal canister concept is based on specific requirements linked to regulatory guidelines, waste-related aspects, and operational and post-closure safety considerations. Based on those requirements, preliminary designs and material specifications are defined. The design development was done based on a design-by-analysis approach consisting of an evaluation of the response and performance of a design under various conditions.

The two canister types, one for SF and one for RP-HLW, have a cylindrical shape with flat lids and are forged from a bespoke low carbon steel alloy. The primary differences between the canister types are the dimensions and their internal components, which are tailored to the waste type to be disposed of. SF disposal canisters are approximately 5 m long and have a diameter of approximately 1.1 m, while RP-HLW canisters are about 4 m long and have a diameter of approximately 0.7 m.

Electron beam welding will be used to weld the bottom lid. This will be followed by a global heat treatment to relieve residual stresses and by inspection. At that stage the canisters can be loaded with SF or RP-HLW. After loading of the waste and installation of the inner lid, the final closure weld will be performed to seal the canister. Electron beam welding will be used for the closure weld, and preliminary weld process specifications have been developed. Following closure welding, a local post-weld heat treatment cycle is foreseen to relieve stresses. Coupled thermal and mechanical models of the weld process and of the post-weld heat treatment were used to estimate the residual stresses.

After the final heat treatment, the closure weld is to be inspected to ensure the quality of the weld. Inspection processes able to detect both surface-breaking and sub-surface flaws, applicable to the current weld and canister design have been selected. The detection capabilities of the inspection techniques, defined from a literature review, were applied with a safety margin of 10.

After final inspection, the canister is to be emplaced in the repository. The evolution of the provisional repository system is well understood, such that the behaviour of the canister material can be described. The material degradation mechanisms that can act on the canister and influence its long term performance were identified and quantified. The potential failure mechanisms are known allowing the prediction of the canister lifetime with confidence using standard fracture mechanics methodologies.

The structural integrity of the canister is demonstrated based on:

- a reduced wall thickness, in accordance with a conservative uniform corrosion rate,
- a reduced fracture toughness, in accordance with conservative assumptions related to hydrogen embrittlement of the canister material,
- the assumption of the lithostatic stresses expected at repository depth acting on the canister,
- the residual stresses calculated from the modelling of the post-weld heat treatment,
- and the assumption of the presence of various types of weld flaws.

All cases assessed indicated that the current provisional canister design will remain structurally intact, and thus provide a complete containment of radionuclides, for significantly longer than the regulatory minimum lifetime requirement of 1,000 years.

6 References

Ahmad, A., Bond, L.J., Davis, J.R. & Mills, K.M. (eds.) (1989): Nondestructive evaluation and quality control. 9th ed. (ASM Handbook, 17). ASM International, Materials Park, Ohio.

Alexander, W.R. & Reijonen, H.M. (2024): Natural analogues - a catalogue. Research Report for NWS Ltd. (UK). Geological Survey of Finland GTK, Espoo, Finland.

Andra (2022): Dossier d'autorisation de creation de l'installation nucléaire de base (INB) Cigéo. Pièce 7: Version préliminaire du rapport de sûreté. Partie III: Démonstration de sûreté. Volume 8: La demonstration de sûreté après fermeture. Technical Report CG-TE-D-NTE-AMOA-SR0-0000-21-0007/A. Agence Nationale pour la Gestion des Déchets Radioactifs Andra, Châtenay-Malabry, France.

Asano, H., Nakamura, A. & Kobayashi, M. (2011): Long term integrity of overpack closure weld for HLW geological disposal. Part 1: Prediction and evaluation method for structural integrity of weld joint. Corrosion Engineering, Science and Technology 46/2, 165-170. DOI: 10.1179/1743278210Y.0000000016.

ASME (2019): Hydrogen Piping and Pipelines. ASME Code for Pressure Piping, B31.12.

ASME (2023a): Boiler and Pressure Vessel Code (BPVC). BPVC Section III – Rules for Construction of Nuclear Facility Components-Divison 3 – Containment Systems & Transport Packagings for Spent Nuclear Fuel & High Level Radioactive Waste, Subsection WC – Class SC Storage Containments, BPVC.III.3 - 2023. American Society of Mechanical Engineers.

ASME (2023b): Boiler and Pressure Vessel Code (BPVC). BPVC Section IX – Welding, Brazing, and Fusing Qualifications, BPVC.IX - 2023. American Society of Mechanical Engineers.

ASME (2023c): Boiler and Pressure Vessel Code (BPVC). BPVC Section V – Nondestructive Examination, BPVC.V - 2023. American Society of Mechanical Engineers.

AWS (2009): Recommended Practices for Local Heating of Welds in Piping and Tubing, AWS D10.10/D10.10M:1999 (R2009).

Barth, N., George, D., Bouyer, F., Schwartz, A., Lambert, C.-H., Ahzi, S. & Rémond, Y. (2020): An inverse method predicting thermal fluxes in nuclear waste glass canisters during vitrification and cooling. Nuclear Engineering and Design 364, 110686. DOI: 10.1016/j.nucengdes.2020.110686.

Basoalto, H. (2001): Modelling and Validation of Anisotropic Creep Deformation in Single Crystal Superalloys: Variable and Multiaxial Loading. *In:* Parker, J.D. (ed.): Creep and Fracture of Engineering Materials and Structures. Proceedings of the 9th International Conference. University of Wales Swansea, April 1-4, 2001. Institute of Materials, London.

Been, J., King, F., Yang, L., Song, F. & Sridhar, N. (2005): The Role of Coatings in the Generation of High- and Near-Neutral pH Environments that Promote Environmentally Assisted Cracking. Paper No. NACE-01567. *In:* NACE International: Proceedings of the CORROSION Conference 2005. Houston, April 3-7, 2005. NACE International.

Behazin, M., Briggs, S. & King, F. (2023): Radiation-induced corrosion model for copper-coated used fuel containers. Part 1. Validation of the bulk radiolysis submodel. Materials & Corrosion 74/11-12, 1834-1847. DOI: 10.1002/maco.202313770.

Bevas, C., Hesketh, J., Rance, A., Stevenson, L.-A., Uthayakumaran, S., Pateman, B., Padovani, C., Šachlová, Š., Kašpar, V., Dobrev, D., Götz, D., Kolomá, K. & Večerník, P. (2024): Elucidation of the effect of radiation on the corrosion of canister materials. Final version as of 06/02/2024 of deliverable D15.7 of the HORIZON 2020 project EURAD. EC Grant agreement no: 847593. European Joint Programme on Radioactive Waste Management EURAD.

BFE (2008): Sachplan Geologische Tiefenlager: Konzeptteil. BFE 2. April 2008 (Revision vom 30. November 2011). Departement für Umwelt, Verkehr, Energie und Kommunikation UVEK, Bern.

Bosch Llufriu, J.A. (2021): Studies on the Mechanical Evolution of Compacted Bentonite Subjected to Environmental Actions. PhD. École Polytechnique Fédérale de Lausanne, Lausanne, Switzerland.

BSI (2004): Specification and qualification of welding procedures for metallic materials. Welding procedure specification – Electron beam welding. BS EN ISO 15609-3:2004.

BSI (2013): Guide to methods for assessing the acceptability of flaws in metallic structures. BS 7910:2013.

BSI (2019a): Electron and laser-beam welded joints. Requirements and recommendations on quality levels for imperfections. Part 1: Steel, nickel, titanium and their alloys BS EN ISO 13919-1:2019.

BSI (2019b): Guide to methods for assessing the acceptability of flaws in metallic structures. BS 7910:2019.

BSI (2021a): Unfired pressure vessels. Part 1: General. BS EN 13445-1:2021.

BSI (2021b): Unfired pressure vessels. Part 3: Design. BS EN 13445-3:2021.

BSI (2024a): Eurocode 3. Design of steel structures – Beams with large web openings. BS EN 1993-1-13:2024.

BSI (2024b): Specification for unfired pressure vessels. PD 5500:2024.

Bulidon, N., Deydier, V., Bumbieler, F., Duret-Thual, C., Mendibide, C. & Crusset, D. (2021): Stress corrosion cracking susceptibility of P285NH and API 5L X65 steel grades in the high-level radioactive waste repository cell concept. Materials & Corrosion 72/1-2, 154-165. DOI: 10.1002/maco.202011842.

Chapman, R.K. & Bowker, K.J. (2001): The production of capability statements for standard NDT procedures. Insight 43/1, 36-38.

Chatzidouros, E.V., Traidia, A., Devarapalli, R.S., Pantelis, D.I., Steriotis, T.A. & Jouiad, M. (2019): Fracture toughness properties of HIC susceptible carbon steels in sour service conditions. International Journal of Hydrogen Energy 44/39, 22050-22063. DOI: 10.1016/j.ijhydene.2019.06.209.

Chen, W. (2016): An Overview of Near-Neutral pH Stress Corrosion Cracking in Pipelines and Mitigation Strategies for Its Initiation and Growth. Corrosion 72/7, 962-977. DOI: 10.5006/1967.

Cloet, V., Pekala, M., Smith, P., Wersin, P. & Diomidis, N. (2017): An Evaluation of sulphide fluxes in the near field of a HLW repository. Nagra Technical Report NTB 17-04.

Crusset, D., Deydier, V., Necib, S., Gras, J.-M., Combrade, P., Féron, D. & Burger, E. (2017): Corrosion of carbon steel components in the French high-level waste programme: evolution of disposal concept and selection of materials. Corrosion Engineering, Science and Technology 52/sup1, 17-24. DOI: 10.1080/1478422X.2017.1344416.

Curti, E. (2022): Aqueous Corrosion of Vitrified Nuclear Waste: Current Process Understanding, Literature Review and Recommended Rates. Nagra Arbeitsbericht NAB 23-09.

Curti, E., Thoenen, T., Kosakowski, G., Baeyens, B., Van Loon, L.R., Leupin, O.X. & Martin, L. (2023): The Geochemical Evolution of the Near-Field in the HLW Section of the Combined Repository at Nördlich Lägern. Nagra Technical Report NTB 23-02.

Desgranges, C., Abbas, A. & Terlain, A. (2003): Model for Low Temperature Oxidation during Long Term Interim Storage. *In:* Féron, D. & Macdonald, D.D. (eds.): Prediction of Long Term Corrosion Behaviour in Nuclear Waste Systems. Proceedings of an International Workshop. Cadarache, November 26-29, 2001. (European Federation of Corrosion publications, 36). Maney, London, 194-207.

Didot, A., Herms, E., Féron, D., Chêne, J. & Crusset, D. (2017): Stress corrosion cracking in the context of deep geological nuclear disposal – investigations on P235 and P265 steels. Corrosion Engineering, Science and Technology 52/sup1, 131-135. DOI: 10.1080/1478422X.2017.1320156.

Dillmann, P., Neff, D. & Féron, D. (2014): Archaeological analogues and corrosion prediction: from past to future. A review. Corrosion Engineering, Science and Technology 49/6, 567-576. DOI: 10.1179/1743278214Y.0000000214.

Diomidis, N. (2014): Scientific basis for the production of gas due to corrosion in a deep geological repository. Nagra Arbeitsbericht NAB 14-21.

Diomidis, N., Guillemot, T. & King, F. (2023): Definition of Reference Corrosion Rates for Performance and Safety Assessments. Nagra Arbeitsbericht NAB 23-22.

Diomidis, N. & King, F. (2020): The corrosion of radioactive waste disposal canisters based on in situ tests. *In:* Ritter, S. (ed.): Nuclear Corrosion. Research, progress and challenges. (European Federation of Corrosion publications, 69). Elsevier, Duxford, 371-389.

Diomidis, N. & King, F. (2022): Development of Copper Coated Canisters for the Disposal of SF and HLW in Switzerland. Nagra Technical Report NTB 20-01.

DOE (2008): Yucca Mountain Repository License Application. Technical Report DOE/RW-0573, Update No. 1, Docket No. 63–001. U.S. Department of Energy DOE, Washington, DC, USA.

Dyson, B.F. & McLean, M. (1990): Creep Deformation of Engineering Alloys: Developments from Physical Modelling. ISIJ International 30/10, 802-811. DOI: 10.2355/isijinternational.30.802.

Elliott, S. (1984): Electron Beam Welding of C/Mn Steels. Toughness and Fatigue Properties. Welding Journal 63/1 (Welding Research Supplement), 8s-16s.

Enning, D. & Garrelfs, J. (2014): Corrosion of iron by sulfate-reducing bacteria: new views of an old problem. Applied and environmental microbiology 80/4, 1226-1236. DOI: 10.1128/AEM.02848-13.

ENSI (2018): Präzisierungen der sicherheitstechnischen Vorgaben für Etappe 3 des Sachplans geologische Tiefenlager. Sachplan geologische Tiefenlager, Etappe 3. ENSI 33/649. Eidgenössisches Nuklearsicherheitsinspektorat ENSI, Brugg.

ENSI (2020): Geologische Tiefenlager. Erläuterungsbericht zur Richtlinie ENSI-G03/d. Eidgenössisches Nuklearsicherheitsinspektorat ENSI, Brugg.

ENSI (2023): Geologische Tiefenlager. Ausgabe Dezember 2020 (Änderung vom 1. November 2023). Richtlinie für die schweizerischen Kernanlagen ENSI-G03/d. Eidgenössisches Nuklearsicherheitsinspektorat ENSI, Brugg.

Farnan, I., King, F., Roberts, D., Smith, V., Swanton, S. & Thetford, R. (2019): Effects of Ionising Radiation on Engineered Barrier Systems. NDA Report RWM/Contr/19/041, Issue 4. (Contractor Report to RWM). Radioactive Waste Management RWM, available online at https://webarchive.nationalarchives.gov.uk/ukgwa/20211004151639mp_/https://rwm.nda.gov.uk/publication/effects-of-ionising-radiation-on-engineered-barrier-system-performance/?download.

Féron, D., Crusset, D. & Gras, J.-M. (2009): Corrosion Issues in the French High-Level Nuclear Waste Program. Corrosion 65/3, 213-223. DOI: 10.5006/1.3319129.

Ficquet, X., Goudar, D.M., Kingston, E.J., Ayres, K., Hurrell, P. & Gill, C. (2012): Measurement of Residual Stresses in Thick Reduced Pressure Electron Beam Welded Components. Paper 11435. *In:* SFEN: International Congress on Advances in Nuclear Power Plants 2011 (ICAPP 2011). Nice, May 2-6, 2011. Curran, Red Hook, NY, 2295-2300.

Filoni, L. & Rocchini, G. (1987): Thermal condictivity of iron, plain carbon and stainless steel, and Inconel 718 from 360 K to 900 K. High Temp.-High Press. 19/4, 381-387.

Fratini, L., Buffa, G., Campanella, D. & La Spisa, D. (2012): Investigations on the linear friction welding process through numerical simulations and experiments. Materials & Design 40, 285-291. DOI: 10.1016/j.matdes.2012.03.058.

Geng, P., Qin, G. & Zhou, J. (2019): Numerical and experimental investigation on friction welding of austenite stainless steel and middle carbon steel. Journal of Manufacturing Processes 47, 83-97. DOI: 10.1016/j.jmapro.2019.09.016.

Giroud, N., Tomonaga, Y., Wersin, P., Briggs, S., King, F., Vogt, T. & Diomidis, N. (2018): On the fate of oxygen in a spent fuel emplacement drift in Opalinus Clay. Applied Geochemistry 97, 270-278. DOI: 10.1016/j.apgeochem.2018.08.011.

Goldak, J.A. & Nguyen, D.S. (1977): A Fundamental Difficulty in Charpy V-Notch Testing Narrow Zones in Welds. Welding Journal 56/4 (Welding Research Supplement), 119s-125s.

Goujon, N.S. (2005): Replacement of Radiography by Ultrasonic Inspection. Research Report 301. Health and Safety Executive HSE, Suffolk.

Gulvin, T.F., Scott, D., Haddrill, D.M. & Glen, J. (1972): The Influence of Stress Relief on the Properties of C and C-Mn Pressure-Vessel Plate Steels. Paper 621. Journal of the West of Scotland Iron and Steel Institute 80, 149–175 & 282–285.

Gutiérrez, M.M., Caruso, S. & Diomidis, N. (2018): Effects of materials and design on the criticality and shielding assessment of canister concepts for the disposal of spent nuclear fuel. Applied Radiation and Isotopes 139, 201-208. DOI: 10.1016/j.apradiso.2018.05.016.

Gutiérrez-Solana, F. & Elices, M. (1982): High Pressure Hydrogen Behaviour of a Pipeline Steel. *In:* Interrante, C.G. & Pressouyre, G.M. (eds.): Current Solutions to Hydrogen Problems in Steels. Proceedings of the First International Conference. Washington DC, November 1-5, 1982. American Society for Metals ASM, Metals Park, OH, 181-185.

Hadley I. (2007): Validation of the European FITNET Fitness-for-Service Procedure: Incorporation of Weld Strength Mismatch into Fracture Assessment (Options 2 and 3). TWI Industrial Member Report 890/2007. The Welding Institute TWI, Cambridge.

Hadley, I. (2018a): Validation of BS 7910:2013 and R6 Fracture Assessment Procedures: Uniaxial and Biaxial Wide Plate Tests on A533B Steel. TWI Industrial Member Report 1107/2018. The Welding Institute TWI, Cambridge.

Hadley, I. (2018b): Validation of BS 7910:2013 Fracture Assessment Procedures: Uniaxial and Biaxial Wide Plate Tests on A533B Steel. TWI Core Research Report 30736/01/18. The Welding Institute TWI, Cambridge.

Hadley, I., Kouzoumis, K. & Janin, Y.J. (2020): Validation of BS 7910:2013 and R6 Fracture Assessment Procedures: Summary Report, Including Treatment of Plastic Collapse, Weld Strength Mismatch and Probabilistic Data. TWI Industrial Member Report 1125/2020. The Welding Institute TWI, Cambridge.

Hadley, I. & Moore, P. (2006): Fracture Case Studies for Validation of Fitness-for-Service Procedures. TWI Industrial Member Report 850/2006. The Welding Institute TWI, Cambridge.

Hadley, I. & Smith, S. (2016): Effects of Mechanical Loading on Residual Stress and Fracture: A Re-examination of the BS 7910 Rules. TWI Industrial Member Report 1074/2016. The Welding Institute TWI, Cambridge.

Haruna, T., Zhu, L., Murakami, M. & Shibata, T. (2000a): Effects of Potential and Concentration of Bicarbonate Solution on Stress Corrosion Cracking of Annealed Carbon Steel. Zairyo-to-Kankyo 49/3, 144-149. DOI: 10.3323/jcorr1991.49.144.

Haruna, T., Zhu, L. & Shibata, T. (2000b): Effects of Annealing Conditions on Stress Corrosion Cracking of Carbon Steel in Aqueous Bicarbonate Solution. Zairyo-to-Kankyo 49/3, 138-143. DOI: 10.3323/jcorr1991.49.138.

Hélie, M., Desgranges, C. & St. Perrin (2006): Prediction of Corrosion Behavior of HLW Containers in the Framework of the French Interim Storage Concept. Nuclear Technology 155/2, 120-132. DOI: 10.13182/NT06-A3751.

Hesketh, J., Haynes, H., Reddy, B., Rance, A., Bevas, C., Padovani, C. & Diomidis, N. (2023): Carbon steel corrosion in a bentonite buffer: A comparison between in situ exposure and lab based experiments. Materials & Corrosion 74/11-12, 1728-1745. DOI: 10.1002/maco.202313767.

Hesse, A.-C., Nitschke-Pagel, T. & Dilger, K. (2016): Fracture Toughness of Electron Beam Welded Fine Grain Steels. Procedia Structural Integrity 2, 3523-3530. DOI: 10.1016/j.prostr.2016.06.439.

Ho, C.Y. & Chu, T.K. (1977): Electrical Resistivity and Thermal Conductivity of Nine Selected AISI Stainless Steels. AD A129160. (DTIC Source Code 413571). Defense Technical Information Center.

Holmberg, J.-E. & Kuusela, P. (2011): Analysis of Probability of Defects in the Disposal Canisters. Posiva Working Report 2011-36. Posiva Oy, Eurajoki.

Humphries, M.J., McLaughlin, J.E. & Pargeter, R. (1993): Toughness Characteristics of Hydrogen Charged Pressure Vessel Steels. *In:* Prager, M. (ed.): Interaction of Steels with Hydrogen in Petroleum Industry Pressure Vessel Service. Proceedings of the International Conference. Paris, March 28-30, 1989.

Hurrell, P.R., Pellereau, B.M.E., Gill, C.M., Kingston, E., Smith, D. & Bouchard, P.J. (2014): Development of Residual Stress Profiles for Defect Tolerance Assessments of Thick Section Electron Beam Welds. PVP2014-28809. *In:* Brongers, M. (ed.): Proceedings of the ASME 2014 Pressure Vessels and Piping Conference, Vol. 6B: Materials and Fabrication. Anaheim, California, USA, July 7-24, 2014. American Society of Mechanical Engineers ASME, New York, NY.

JAEA (2013): Project for assessment methodology development of chemical effects on geological disposal system – summary of 6-year study. JAEA report. Japan Atomic Energy Agency JAEA, Tōkai, available online at https://warp.da.ndl.go.jp/collections/content/info:ndljp/pid/11457033/www.enecho.meti.go.jp/category/electricity_and_gas/nuclear/rw/library/2012/24-7-2.pdf.

Jenni, A., Wersin, P., Thoenen, T., Baeyens, B., Ferrari, A., Gimmi, T., Mäder, U., Marschall, P., Hummel, W. & Leupin, O. (2019): Bentonite backfill performance in a high-level waste repository: a geochemical perspective. Nagra Technical Report NTB 19-03.

JNC (2000): H12: Project to Establish the Scientific and Technical Basis for HLW Disposal in Japan : Project Overview Report : Second Progress Report on Research and Development for the Geological Disposal of HLW in Japan. JNC TN1410 2000-001. Japan Nuclear Cycle Development Institute JNC, Tokyo.

Johnson, L.H., Curti, E. & Spahiu, K. (2023): A Radionuclide Release Model for Spent UO2 and MOX Fuel for Safety Assessment with Application to Waste to be Disposed of in a Deep Geological Repository in Switzerland. Nagra Arbeitsbericht NAB 23-10.

Kang, J.-H. & Kim, S.-J. (2019): Critical Assessment 33: Dislocation density-based constitutive modelling for steels with austenite. Material Science and Technology 35/10, 1128-1132. DOI: 10.1080/02670836.2019.1618030.

KEG (2003): Kernenergiegesetz (KEG) vom 21. March 2003, Stand am 1. January 2024. Systematische Sammlung des Bundesrechts SR 732.1, Schweiz.

KEV (2004): Kernenergieverordnung (KEV) vom 10. December 2004, Stand am 1. January 2024. Systematische Sammlung des Bundesrechts SR 732.11, Schweiz.

Kihara, H., Arita, K., Numata, A. & Izuchi, S. (1984): A study on high power electron beam welding (Report 2). Mechanical properties and some characteristics of heavy section steel welds for pressure vessels. Welding in the World 22/1-2, 2-20.

Kim, C.S. (1975): Thermophysical properties of stainless steels. ANL-75-55. Argonne National Laboratory ANL, Argonne.

King, F. (2008): Corrosion of carbon steel under anaerobic conditions in a repository for SF and HLW in Opalinus Clay. Nagra Technical Report NTB 08-12.

King, F. (2009): Microbiologically Influenced Corrosion of Nuclear Waste Containers. Corrosion 65/4, 233-251. DOI: 10.5006/1.3319131.

King, F. (2010a): Development of Guidelines for Identification of SCC Sites and Estimation of Re-Inspection Intervals for SCC Direct Assessment. Pipeline Research Council Report, Catalog No. L5XXXX US Department of Transportation project DTPH56-06-T-000013, available online at https://primis.phmsa.dot.gov/matrix/FilGet.rdm?fil=6401&s=B4CEAE1D38BF43B4BF53702E48E8D0B3&c=1.

King, F. (2010b): Stress Corrosion Cracking of Carbon Steel Used Fuel Containers in a Canadian Deep Geological Repository in Sedimentary Rock. Nuclear Waste Management Organization Report NWMO TR-2010-21. Nuclear Waste Management Organization NWMO, Toronto.

King, F. (2021): Natural analogues and their use in supporting the prediction of the long-term corrosion behaviour of copper-coated UFC. Nuclear Waste Management Organization Report NWMO TR-2021-19. Nuclear Waste Management Organization NWMO, Toronto.

King, F. (2024): Radiation effects on copper-coated steel used fuel containers. NWMO TR-2021-08. Nuclear Waste Management Organization NWMO, Toronto.

King, F. & Behazin, M. (2021): A Review of the Effect of Irradiation on the Corrosion of Copper-Coated Used Fuel Containers. CMD 2/4, 678-707. DOI: 10.3390/cmd2040037.

King, F., Behazin, M. & Keech, P. (2023): Natural and archaeological analogues for corrosion prediction in nuclear waste systems. Materials & Corrosion 74/11-12, 1811-1822. DOI: 10.1002/maco.202313764.

King, F. & Briggs, S. (2024): FE-G gas modelling. Phase 28 report. Mont Terri Project internal report (unpublished).

King, F., Kolàř, M., Briggs, S., Behazin, M., Keech, P. & Diomidis, N. (2024a): Review of the Modelling of Corrosion Processes and Lifetime Prediction for HLW/SF Containers – Part 1: Process Models. CMD 5/2, 124-199. DOI: 10.3390/cmd5020007.

King, F., Kolàř, M., Briggs, S., Behazin, M., Keech, P. & Diomidis, N. (2024b): Review of the Modelling of Corrosion Processes and Lifetime Prediction for HLW/SF Containers – Part 2: Performance Assessment Models. CMD 5/2, 289-339. DOI: 10.3390/cmd5020013.

Kingston, E., Smith, D.J., Zheng, G., Gill, C. & Hurrell, P. (2010): Measurement of Residual Stresses in Thick Section Steel Electron Beam Welds. PVP2010-25314. *In:* Wiersma, B.J. (ed.): Proceedings of the ASME 2010 Pressure Vessels and Piping Conference, Vol. 6, Part A. Bellevue, Washington, USA, July 7-22, 2010. American Society of Mechanical Engineers ASME, New York, NY, 1307-1316.

Köhler, S., Garitte, B., Weber, H. & Müller, H. (2015): LUCOEX Deliverable D2.5: Emplacement Report LUCOEX – WP2. Euratom 7th Framework Programme Project, Brussels.

Kosakowski, G. (2023): Reactive Transport Modellling of Material Interface Evolution in the HLW Near-field. Nagra Arbeitsbericht NAB 23-33.

Lam, P.-S., Sindelar, R.L., Duncan, A.J. & Adams, T.M. (2009): Literature Survey of Gaseous Hydrogen Effects on the Mechanical Properties of Carbon and Low Alloy Steels. Journal of Pressure Vessel Technology 131/4 August. DOI: 10.1115/1.3141435.

Landolt, D., Davenport, A., Payer, J. & Shoesmith, D.W. (2009): A review of materials and corrosion issues regarding canisters for disposal of spent fuel and high-level waste in opalinus clay. Nagra Technical Report NTB 09-02.

Leupin, O.X., Birgersson, M., Karnland, O., Korkeakoski, P., Sellin, P., Mäder, U. & Wersin, P. (2014): Montmorillonite stability under near-field conditions. Nagra Technical Report NTB 14-12.

Liu, Q. & Atrens, A. (2013): A critical review of the influence of hydrogen on the mechanical properties of medium-strength steels. Corrosion Reviews 31/3-6, 85-103. DOI: 10.1515/corrrev-2013-0023.

Loginow, A.W. & Phelps, E.H. (1975): Steels for Seamless Hydrogen Pressure Vessels. Corrosion 31/11, 404-412. DOI: 10.5006/0010-9312-31.11.404.

Luo, Y., Gu, W., Peng, W., Jin, Q., Qin, Q. & Yi, C. (2020): A Study on Microstructure, Residual Stresses and Stress Corrosion Cracking of Repair Welding on 304 Stainless Steel: Part I-Effects of Heat Input. Materials (Basel, Switzerland) 13/10. DOI: 10.3390/ma13102416.

Mapelli, C., Nicodemi, W., Riva, R.F. & Vedani, M. (2009): Analysis of the Nails from the Roman Legionary at Inchtuthil. La Metallurgia Italiana 101/1 January, 51-58, available online at https://www.aimnet.it/allpdf/pdf_pubbli/gen09/mapelli.pdf.

Marshall, W. (1982): An assessment of the integrity of PWR pressure vessels. Second Report by a Study Group under the Chairmanship of Dr. W. Marshall. United Kingdom Atomic Energy Authority UKAEA.

Matsunaga, H., Yoshikawa, M., Kondo, R., Yamabe, J. & Matsuoka, S. (2015): Slow strain rate tensile and fatigue properties of Cr–Mo and carbon steels in a 115 MPa hydrogen gas atmosphere. International Journal of Hydrogen Energy 40/16, 5739-5748. DOI: 10.1016/j.ijhydene.2015.02.098.

Milodowski, A.E., Alexander, W.R., West, J.M., Shaw, R.P., McEvoy, F.M., Scheidegger, J.M. & Field, L.P. (2015): A Catalogue of Analogues for Radioactive Waste Management. British Geological Survey Commissioned Report CR/15/106, available online at https://www.natural-analogues.com/nawg-library/na-overviews/253-catalogue-of-natural-analogues-for-radioactive-waste-management-bgs-commissioned-report-cr-15-106/file.

Mitsui, H., Takahashi, R., Asano, H., Taniguchi, N. & Yui, M. (2008): Susceptibility to Stress Corrosion Cracking for Low-Carbon Steel Welds in Carbonate-Bicarbonate Solution. Corrosion 64/12, 939-948. DOI: 10.5006/1.3294409.

Morales Hidalgo, M., Povedano Priego, C., Martinez Moreno, M.F., Jroundi, F., Merroun, M.L., Alonso, U., Fernández, A.M., García-Gutiérrez, M., Mingarro, M., Jesus Morejón, T.M., Nieto, P., Valdivieso, P.P., Shree Bartak, D., Říha, J., Černá, K., Šachlová, Š., Kašpar, V., Dobrev, D., Večerník, P., Jakus, N., Jermann, E., Bena, P., Zarkali, C., Bernier-Latmani,R., Wei, T.-S., Sushko, V., Cherkouk, A., Smolders, C., Kursten, B. & Mijnendonckx, K. (2024): Integration of the findings on the impact of irradiation, dry density and particle size on the microbial community. Final version as of 04/04/2024 of deliverable D15.9 of the HORIZON 2020 project EURAD. EC Grant agreement no: 847593. European Joint Programme on Radioactive Waste Management EURAD.

Moran, T.L., Prowant, M., Nove, C.A., Pardini, A.F., Crawford, S.L., Cinson, A.D. & Anderson, M.T. (2015): Applying Ultrasonic Testing in Lieu of Radiography for Volumetric Examination of Carbon Steel Piping. US NRC report NUREG/CR-7204, PNNL-24232. Nuclear Regulatory Commission NRC.

Morco, R.P., Joseph, J.M., Hall, D.S., Medri, C., Shoesmith, D.W. & Wren, J.C. (2017): Modelling of radiolytic production of HNO 3 relevant to corrosion of a used fuel container in deep geologic repository environments. Corrosion Engineering, Science and Technology 52/sup1, 141-147. DOI: 10.1080/1478422X.2017.1340227.

Müller, H.R., Garitte, B., Vogt, T., Köhler, S., Sakaki, T., Weber, H., Spillmann, T., Hertrich, M., Becker, J.K., Giroud, N., Cloet, V., Diomidis, N. & Vietor, T. (2017): Implementation of the full-scale emplacement (FE) experiment at the Mont Terri rock laboratory. Swiss J Geosci 110/1, 287-306. DOI: 10.1007/s00015-016-0251-2.

Nagra (1985): Project Gewähr 1985: Nuclear Waste Management in Switzerland: Feasibility Studies and Safety Analyses. Nagra Project Report NGB 85-09.

Nagra (2002): Project Opalinus Clay: Safety report: Demonstration of disposal feasibility for spent fuel, vitrified high-level waste and long-lived intermediate-level waste (Entsorgungs-nachweis). Nagra Technical Report NTB 02-05.

Nagra (2021): Verschlusskonzept für ein geologisches Tiefenlager. Nagra Arbeitsbericht NAB 21-12.

Nagra (2022): Rückholungskonzept für ein geologisches Tiefenlager. Nagra Arbeitsbericht NAB 21-13.

Nagra (2023a): Bautechnisches Dossier Standortvergleich – Band 9: Bautechnische Risikoanalyse. Nagra Arbeitsbericht NAB 23-01 Band 9.

Nagra (2023b): Modellhaftes Inventar für radioaktive Materialien MIRAM-RBG. Nagra Technischer Bericht NTB 22-05.

Nagra (2024a): Abfallzuteilung und Betrachtungszeiträume. Nagra Arbeitsbericht NAB 24-05.

Nagra (2024b): Anlagen- und Betriebskonzept für das geologische Tiefenlager. Nagra Technischer Bericht NTB 24-11.

Nagra (2024c): Kritikalitätssicherheit. Nagra Arbeitsbericht NAB 24-03.

Nagra (2024d): Phenomenological Description of the Evolution of a Combined Geological Repository for Radioactive Waste in Opalinus Clay. Nagra Arbeitsbericht NAB 24-20.

Nagra (2024e): Post-closure safety report. Nagra Technical Report NTB 24-10.

Nagra (2024f): Production and Fate of Gases in a Combined Repository at NL. Nagra Technical Report NTB 24-23.

Nagra (2024g): Radiological Consequences of Deep Geological Repository Excavation by Erosive Processes. Nagra Arbeitsbericht NAB 24-08.

Nagra (2024h): Radiological Consequences of Future Human Actions. Nagra Arbeitsbericht NAB 24-09.

Nagra (2024i): Safety and Repository Concept and Provisional Design. Nagra Arbeitsbericht NAB 24-18.

Nagra (2024j): Stress field in the siting regions Jura Ost, Nördlich Lägern and Zürich Nordost. Nagra Arbeitsbericht NAB 24-19.

Nagra (2024k): Synthesis of the Performance Assessment for a Combined Repository. Nagra Technical Report NTB 24-22.

Nagra (2025a): Rahmenbewilligungsgesuch für das geologische Tiefenlager – Begründung der Standortwahl. Nagra Technischer Bericht NTB 24-03.

Nagra (2025b): Rahmenbewilligungsgesuch für das geologische Tiefenlager – Sicherheitsbericht. Nagra Technischer Bericht NTB 24-01.

Nakamura, A., Asano, H., Kawakami, S., Ito, T., Furukawa, T. & Fujisawa, K. (2010): Full-Scale Test of Overpack Closure Techniques for HLW Repository Operation: Welding Methods and UT Systems for Long-Term Structural Integrity of Weld Joints. *In:* ASME: Proceedings of the ASME 2010 13th International Conference on Environmental Remediation and Radioactive Waste Management. Spent fuel, fissile material, transuranic and high-level radioactive waste management, vol. 2. Tsukuba, Japan, October 3-7, 2010. American Society of Mechanical Engineers ASME, New York, NY, 375-382.

Naumann, M., Hunsche, U. & Schulze, O. (2007): Experimental investigations on anisotropy in dilatancy, failure and creep of Opalinus Clay. Physics and Chemistry of the Earth, Parts A/B/C 32/8-14, 889-895. DOI: 10.1016/j.pce.2005.04.006.

Necib, S., Bumbieler, F., Duret-Thual, C., Bulidon, N., Crusset, D. & Combrade, P. (2017): Assessment of the resistance to environmentally assisted cracking (EAC) of C-steel casing and overpack in the COx claystone. Corrosion Engineering, Science and Technology 52/sup1, 95-100. DOI: 10.1080/1478422X.2017.1336003.

Neff, D., Dillmann, P., Descostes, M. & Beranger, G. (2006): Corrosion of iron archaeological artefacts in soil: Estimation of the average corrosion rates involving analytical techniques and thermodynamic calculations. Corrosion Science 48, 2947-2970. DOI: 10.1016/j.corsci.2005.11.013.

Neff, D., Saheb, M., Monnier, J., Perrin, S., Descostes, M., L'Hostis, V., Crusset, D., Millard, A. & Dillmann, P. (2010): A review of the archaeological analogue approaches to predict the long-term corrosion behaviour of carbon steel overpack and reinforced concrete structures in the French disposal systems. Journal of Nuclear Materials 402/2-3, 196-205. DOI: 10.1016/j.jnucmat.2010.05.003.

NUMO (2021): The NUMO Pre-siting SDM-based Safety Case. Technical Report NUMO-TR-21-01. Nuclear Waste Management Organization of Japan NUMO, Tokyo, Japan.

Ogawa, Y., Suzuki, S., Kubota, S. & Deguchi, A. (2017): Re-evaluation of the required thickness of the carbon steel overpack for high-level radioactive waste disposal in Japan based on the latest scientific and engineering knowledge. Corrosion Engineering, Science and Technology 52/sup1, 204-209. DOI: 10.1080/1478422X.2017.1294355.

Olden, V., Alvaro, A. & Akselsen, O.M. (2012): Hydrogen diffusion and hydrogen influenced critical stress intensity in an API X70 pipeline steel welded joint – Experiments and FE simulations. International Journal of Hydrogen Energy 37/15, 11474-11486. DOI: 10.1016/j.ijhydene.2012.05.005.

Overton, D., Richardson, J. & Halsey, J. (2013): The Practical Use of UT in lieu of RT in the Power Industry. *In:* IET (ed.): Proceedings of the 9th International Conference on NDE in Relation to Structural Integrity for Nuclear and Pressurized Components. Seattle, Washington, USA, May 22-24, 2012. Institute for Energy and Transport IET, Luxembourg.

Parkins, R.N. (2000): A Review of Stress Corrosion Cracking of High Pressure Gas Pipelines. Paper No. NACE-00363. *In:* NACE International: Proceedings of the CORROSION Conference 2000. Orlando, March 26-31, 2000. NACE International.

Patel, R., Punshon, C., Nicholas, J., Bastid, P., Zhou, R., Schneider, C., Bagshaw, N., Howse, D., Hutchinson, E., Asano, R. & King, F. (2012): Canister Design Concepts for Disposal of Spent Nuclear Fuel and High Level Waste. Nagra Technical Report NTB 12-06.

Perović, N., Maglić, K., Stanimirović, A. & Vuković, G. (1995): Transport and calorimetric properties of AISI 321 by pulse thermal diffusivity and calorimetric techniques. High Temp.-High Press. 27/28/1, 53-58. DOI: 10.1068/htrt39.

Piekarska, W., Kubiak, M. & Bokota, A. (2011): Numerical Simulation of Thermal Phenomena and Phase Transformations in Laser-Arc Hybrid Welded Joints. Archives of Metallurgy and Materials 56/2, 37. DOI: 10.2478/v10172-011-0044-6.

Piekarska, W., Kubiak, M. & Saternus, Z. (2012): Numerical Modelling of Thermal and Structural Strain in Laser Welding Process. Archives of Metallurgy and Materials 57/4, 1219-1227. DOI: 10.2478/v10172-012-0136-y.

Pitkänen, J. (2010): Inspection of Bottom and Lid Welds for Disposal Canisters. Posiva Report 2010-04. Posiva Oy, Eurajoki.

Pitkänen, J., Salonen, T., Bertovic, M., Müller, C. & Pavlovic, M. (2009): NDT Reliability in Risk Minimization during Manufacturing and Welding of Spent Nuclear Fuel Disposal Components – A Realistic Tool for Reliable Inspections. Paper Fr.1.A.2. *In:* DGZfP: 4th European-American Workshop on Reliability of NDE. Berlin, Germany, June 24-26, 2009. Deutsche Gesellschaft für Zerstörungsfreie Prüfung DGZfP, Berlin.

Plansee Composite Materials (2024): EN 10222-2 Grade P245GH normalized or normalized formed (+N). (Matmatch), available online at https://matmatch.com/materials/minfm35589-en-10222-2-grade-p245gh-normalized-or-normalized-formed-n-, status as of June 8, 2024.

Popov, S.G., Carbajo, J.J., Ivanov, V.K. & Yoder, G.L. (2000): Thermophysical Properties of MOX and UO_2 Fuels Including the Effects of Irradiation. ORNL/TM-2000/351. Oak Ridge National Laboratory ORNL, Oak Ridge.

Posiva & SKB (2021): The Integrated Sulfide Project – Summary report. Posiva SKB Report 09. Posiva Oy & Svensk Kärnbränslehantering AB SKB, Eurajoki, Stockholm, available online at https://www.skb.com/publication/2497620/Posiva+SKB+Report+09.pdf.

Punshon, C.S. & Elliott, S. (1985): Toughness of Electron Beam Welds in Thick Section C-Mn and Microalloyed Steels. TWI Research Report 259/1985. The Welding Institute TWI, Cambridge.

Reddy, B., Padovani, C., Rance, A.P., Smart, N.R., Cook, A., Haynes, H.M., Milodowski, A.E., Field, L.P., Kemp, S.J., Martin, A. & Diomidis, N. (2021a): The anaerobic corrosion of candidate disposal canister materials in compacted bentonite exposed to natural granitic porewater containing native microbial populations. Materials & Corrosion 72/1-2, 361-382. DOI: 10.1002/maco.202011798.

Reddy, B., Padovani, C., Smart, N.R., Rance, A.P., Cook, A., Milodowski, A., Field, L., Kemp, S. & Diomidis, N. (2021b): Further results on the in situ anaerobic corrosion of carbon steel and copper in compacted bentonite exposed to natural Opalinus Clay porewater containing native microbial populations. Materials & Corrosion 72/1-2, 268-281. DOI: 10.1002/maco.202011785.

Robinson, S.L. & Stoltz, R.E. (1981): Toughness Losses and Fracture Behavior of Low Strength Carbon-Manganese Steels in Hydrogen. *In:* Bernstein, I.M. & Thompson, A.W. (eds.): Hydrogen Effects in Metals. Proceedings of the Third International Conference on Effect of Hydrogen on Behavior of Materials. Moran, WY, August 26-31, 1980. The Metallurgical Society of AIME, Warrendale, PA, 987-993.

Ronneteg, U., Cederqvist, L., Rydén, H., Öberg, T. & Müller, C. (2006): Reliability in sealing of canister for spent nuclear fuel. SKB Report R-06-26. Svensk Kärnbränslehantering AB SKB, Stockholm.

Salkin, R.V. (1987): The Stress Relaxation heat Treatments after Welding. *In:* Bramat, M. (ed.): Proceedings of the International Conference on Stress Relieving Heat Treatments of Welded Steel Constructions. Sofia, July 6-7, 1987. Pergamon Press, Oxford, xvii-lxxv.

Sarrasin, L., Tisyadi, M.F., Abdelouas, A., Šachlová, Š., Kašpar, V., Dobrev, D., Gõtz, D., Kolomá, K., Večerník, P., Zuna, M., Alonso, U., Diéguez, M., Soto, C., Fernández, A.M., Gutiérrez, M.G., Valdivieso, P. & Missana, T. (2024): Synthesis of irradiation results under repository conditions. Final version as of 13.05.2024 of deliverable D.15.8 of the HORIZON 2020 project EURAD. EC Grant agreement no: 847593. European Joint Programme on Radioactive Waste Management EURAD.

Sasaki, T. & Rutqvist, J. (2022): Effects of time-dependent deformation of shale on the integrity of a geological nuclear waste repository. International Journal of Rock Mechanics and Mining Sciences 158, 105206. DOI: 10.1016/j.ijrmms.2022.105206.

Schwartzberg, F.H., Osgood, S.H., Bryant, C. & Knight, M. (1970): Cryogenic Materials Data Handbook. Vol. 1, sections A, B, C Technical Documentary Report AFML-TDR-64-280, AD0713620. Revised, available online at https://apps.dtic.mil/sti/tr/pdf/AD0713619.pdf.

Senior, N. & Martino, T. (2022): Nuclear Waste Consortium Research Programme on Corrosion and Gas Genereation: Phase 1 Final Report. Nagra Technical Report NTB 22-07.

Smart, N., Abdelouas, A., Alonso De los Rios, Ursula, Bernier-Latmani, R., Bevas, C., Bosch, C., Cerná, K., Cherkouk, A., Cornu, I., Cassia Costa Dias, R. de, Debelle, A., Diéguez, M., Diomidis, N., Dobrev, D., Fernández, A.M., Finck, N., Gaggiano, R., Ganster, P., García-Gutiérrez, M., Götz, D., Hesketh, J., Idiart, A., Kašpar, V., Kolditz, O., Kolomá, K., Kuprin, A., Ma, J., Matulová, M., Merroun, M., Mijnendonckx, K., Mingarro, M., Missana, T., Montoya, V., Müller, N., Muñoz, A., Nieto, P., Padovani, C., Pakarinen, J., Pateman, B., Pont, A., Rance, A., Riba, O., Rossignol, F., Šachlová, Š., Sarrasin, L., Sayenko, S., Schild, D., Schmidt, M., Shao, H., Singh, A.R., Soto, C., Stevenson, L.-A., Tamisier, M., Tisyadi, Muhammad Faiz Al Rasyid, Trentin, A., Uthayakumaran, S., Valdivieso, P., Večerník, P., Vogt, C., Wersin, P. & Zuna, M. (2024): ConCorD Synthesis Report. Final version as of 31.05.2024 of deliverable D15.14 of the HORIZON 2020 project EURAD. EC Grant agreement no: 847593. European Joint Programme on Radioactive Waste Management EURAD.

Smart, N.R., Reddy, B., Rance, A.P., Nixon, D.J., Frutschi, M., Bernier-Latmani, R. & Diomidis, N. (2017): The anaerobic corrosion of carbon steel in compacted bentonite exposed to natural Opalinus Clay porewater containing native microbial populations. Corrosion Engineering, Science and Technology 52/sup1, 101-112. DOI: 10.1080/1478422X.2017.1315233.

Smith, D. (2003): Weld Flaw Evaluation and Nondestructive Examination Process Comparison Results for High-Level Radioactive Waste Package Manufacturing Program. TDR-EBS-ND-000007 REV 01. U.S. Department of Energy DOE.

Smith, D.J., Zheng, G., Hurrell, P.R., Gill, C.M., Pellereau, B.M.E., Ayres, K., Goudar, D. & Kingston, E. (2014): Measured and predicted residual stresses in thick section electron beam welded steels. International Journal of Pressure Vessels and Piping 120-121/August–September, 66-79. DOI: 10.1016/j.ijpvp.2014.05.001.

Somerday, B.P., Sofronis, P., Jones, R. & Somerday, B. (eds.) (2008): Effects of Hydrogen on Materials. Proceedings of the 2008 International Hydrogen Conference. Jackson, WY, September 7-10, 2008. American Society for Metals ASM, Materials Park, Ohio.

Spingarn, J.R. (1979): Hydrogen embrittlement of pipeline weldments. *In:* Hoover, W.R.: Hydrogen Compatibility of Structural Materials for Energy Storage and Transmission. Sandia Report SAND79-8202. Sandia National Laboratories SNL.

Stępiński, T. (2003): NDE of copper canisters for long-term storage of spent nuclear fuel from the Swedish nuclear power plants. *In:* Doctor, S.R., Bar-Cohen, Y. & Aktan, A.E. (eds.): Nondestructive Detection and Measurement for Homeland Security. NDE for Health Monitoring and Diagnostics. San Diego, CA, March 2, 2003. International Society for Optical Engineering SPIE. (SPIE Proceedings), 25-33.

Stroes-Gascoyne, S., Hamon, C.J., Maak, P. & Russell, S. (2010): The effects of the physical properties of highly compacted smectitic clay (bentonite) on the culturability of indigenous microorganisms. Applied Clay Science 47/1-2, 155-162. DOI: 10.1016/j.clay.2008.06.010.

Taniguchi, N. (2003): Effect of magnetite as a corrosion product on the corrosion of carbon steel overpack. *In:* Féron, D. & Macdonald, D.D. (eds.): Prediction of Long Term Corrosion Behaviour in Nuclear Waste Systems. Proceedings of an International Workshop. Cadarache, November 26-29, 2001. (European Federation of Corrosion publications, 36). Maney, London, 424-438.

thyssenkrupp Materials (UK) (2017): Stainless Steel 1.4541 - Material Data Sheet, available online at https://d2zo35mdb530wx.cloudfront.net/_legacy/UCPthyssenkruppBAMXUK/assets.files/material-data-sheets/stainless-steel/stainless-steel-1.4541-321.pdf, updated on June 6, 2017.

Turnbull, A. (2009): A review of the possible effects of hydrogen on lifetime of carbon steel nuclear waste canisters. Nagra Technical Report NTB 09-04.

Vasileiou, A.N., Smith, M.C., Francis, J.A., Balakrishnan, J., Wang, Y.L., Obasi, G., Burke, M.G., Pickering, E.J., Gandy, D.W. & Irvine, N.M. (2021): Development of microstructure and residual stress in electron beam welds in low alloy pressure vessel steels. Materials & Design 209, 109924. DOI: 10.1016/j.matdes.2021.109924.

Vasileiou, A.N., Smith, M.C., Francis, J.A., Rathod, D.W., Balakrishnan, J. & Irvine, N.M. (2019): Residual stresses in arc and electron-beam welds in 130 mm thick SA508 steel: Part 2 – measurements. International Journal of Pressure Vessels and Piping 172, 379-390. DOI: 10.1016/j.ijpvp.2019.03.035.

Vasileiou, A.N., Smith, M.C., Gandy, D., Ferhati, A., Romac, R. & Paddea, S. (2016): Residual Stresses in Thick-Section Electron Beam Welds in RPV Steels. PVP2016-63940, V06BT06A079. *In:* Ren, W., Zhu, X.-K. & Duncan, A. (eds.): Proceedings of the ASME 2016 Pressure Vessels and Piping Conference, Vol. 6B: Materials and Fabrication. Vancouver, British Columbia, Canada, July 17-21, 2016. American Society of Mechanical Engineers ASME, New York, NY.

Watkins, A.D., Kunerth, D.C. & McJunkin, T.R. (2006): Eddy Current Examination of Spent Nuclear Fuel Canister Closure Welds. *In:* ANS: 11th International High-Level Radioactive Waste Management Conference (IHLRWM 2006). Global Progress Toward Safe Disposal. Las Vegas, Nevada, April 30 - May 4, 2006. American Nuclear Society ANS, La Grange Park, Ill., 571-576.

Watkins, B., Wood, D.S. & Nichols, R.W. (1963): Effects of Prolonged Stress Relieving Treatments on the Mechanical Properties of Reactor Pressure Vessel Steels. British Welding Journal 10/2, 37-53.

Xu, K. (2012): Hydrogen embrittlement of carbon steels and their welds. *In:* Gangloff, R.P. & Somerday, B.P. (eds.): Gaseous Hydrogen Embrittlement of Materials in Energy Technologies. The problem, its characterisation and effects on particular alloy classes. (Woodhead Publishing Series in Metals and Surface Engineering, 2). Woodhead Publishing, Oxford, 526-561.

Xu, K. & Rana, M. (2008): Tensile and Fracture Properties of Carbon and Low Alloy Steels in High Pressure Hydrogen. *In:* Somerday, B.P., Sofronis, P., Jones, R. & Somerday, B. (eds.): Effects of Hydrogen on Materials. Proceedings of the 2008 International Hydrogen Conference. Jackson, WY, September 7-10, 2008. American Society for Metals ASM, Materials Park, Ohio, 349-356.

Yoshikawa, H., Gunji, E. & Tokuda, M. (2008): Long term stability of iron for more than 1500 years indicated by archaeological samples from the Yamato 6th tumulus. Journal of Nuclear Materials 379/1-3, 112-117. DOI: 10.1016/j.jnucmat.2008.06.009.

Zawierucha, R. & Xu, K. (2005): Hydrogen pipeline steels. *In:* Petrovic, J.J., Anderson, I.E., Adams, T.M., Sandrock, G., Legsdins, C.F., Stevenson, J.W. & Yang, Z. (eds.): Materials for Hydrogen Economy Symposium. Proceedings of the Materials Science & Technology 2005 Conference, vol. 4. Pittsburgh, PA, September 25-28, 2005, 79-90.

Zhang, C.L., Laurich, B., Zhang, C.-L. & Laurich, B. (2020): Mechanical behavior of sandy facies of Opalinus Clay under different load conditions. Journal of Rock Mechanics and Geotechnical Engineering 12/2, 223-241. DOI: 10.1016/j.jrmge.2019.09.005.

App. A SF and RP-HLW data

In this Appendix, SF and RP-HLW data that are relevant to the canister design are presented (Nagra 2023b). The maximum dimensional data and total average mass per FA type for existing reactors are given in Tab. A-1. The fuel quantities arising over 60 years of reactor operation time (KKM with a 49-years operating lifetime) are given in Tab. A-2. Tab. A-3 gives the numbers of SF-PWR and SF-BWR disposal canisters. The numbers of canisters have been calculated based on the maximum thermal loading at the time of disposal of 1,500 W and the assumption of 4 PWR FAs per SF-PWR canister and 12 BWR FAs per SF-BWR canister. The details of the HLW flasks are given in Tab. A-4 and the number of RP-HLW canisters, assuming 3 flasks per canister, in Tab. A-5.

Tab. A-1: FA data

	KKL BWR fuel	**KKM BWR fuel**	**KKG PWR fuel**	**KKB PWR fuel**
FA length, mm	4,481	4,475	4,296	3,518
FA width, mm	139 × 139	139 × 139	215 × 215	198 × 198
FA mass, kg	296	266	664	479
No. of FAs	7,710	1,177	1,760	1,801

Tab. A-2: SF quantities

	BWR	**PWR**
No. FA	8,887	3,561

Tab. A-3: Numbers of SF canisters

Type	**No. of canisters**
SF-PWR	1,039
SF-BWR	891

Tab. A-4: RP-HLW flask data

Flask type	**AREVA**	**BNFL**
Flask length (mm)	1,335	1,335
Flask diameter (mm)	430	430
Overlap when stacked (mm)	67	67
Flask mass (kg)	493	474
No. of flasks	436	196

Tab. A-5: Number of RP-HLW canisters

	AREVA and BNFL
No. of canisters	211

App. B Weld process selection

B.1 Weld process selection for top lid closure weld

For the selection of a suitable welding process for the welding of the top lid of SF and RP-HLW disposal canisters, two welding processes were considered: EB and NG-TIG.

Although NG-TIG welding has long been used for high integrity welded joints for nuclear applications, in terms of this particular application there is a feature that would present relatively high-level disadvantages in terms of a requirement for a “right first time”, remote automated process. NG-TIG is not proven in a fully automated environment. In particular, the process is multi-pass, and the as-welded metal will generate silicates attached to the weld surface after each welding run. These will need to be mechanically cleaned between welding runs to ensure good fusion of the successive run and to eliminate flaws. This cleaning process is generally completed manually, and no automatic cleaning approach has yet been developed. While the process can deliver high integrity welds, in practical application there are many potential failure modes related to the failure of machine parts or operator error in bead placement. While these can easily be corrected in most applications where manual intervention is possible, minimal manual intervention is required here, and satisfactory results could not be easily achieved. NG-TIG also relies on an excavated weld preparation. In order to make the weld, some welding consumable is needed to back-fill the weld preparation. As such, there is a requirement for discrete quantities of filler wire to be fed close to the operating head. Feeding wire over long distances presents a risk of wire-snagging faults. These reels of wire will need changing and setting up in between spools being used and local intervention will be necessary. Similarly, the tungsten electrode, though not regarded as a welding consumable in that it does not melt to create the weld, will periodically wear and become contaminated through use. As such, it will have to be periodically changed or replaced in a large circumferential weld, again requiring manual intervention.

EB welding is an in-vacuum fusion welding process that uses a high energy, focused electron beam as a heat source. Welds can be produced either as fully penetrating welds where the beam penetrates the entire material thickness and excess energy passes through the joint, or as partially penetrating welds where the joint face is fused but penetration is controlled to a fixed depth.

A decision matrix analysis was used to select the most suitable welding process for the closure weld of the canisters. The two welding processes were scored against 25 weighted criteria. These criteria are listed to the left of Tab. B-1. A numerical score was assigned to each welding process against these 25 criteria using a consistent scoring system, in which 1 represented low confidence and 10 represented high confidence, for each criterion. An overall rating was obtained by multiplying each score by its corresponding factor. A total score for each welding process was then calculated by adding all the overall ratings, which is shown in Tab. B-1 in the last row.

Tab. B-1 indicates that EB welding scores higher than the NG-TIG welding process and is thus selected. This is predominantly due to its higher productivity and reliability for remote operation. Although hardness and toughness properties after welding are more of a challenge, heat treatment is expected to restore these properties.

B.2 Weld process selection for bottom lid

A study was performed to select a suitable welding process for the welding of the bottom lid of SF and RP-HLW canisters. For this evaluation, a similar approach as for the top lid closure weld was followed.

The criteria and the relevant rating factors are described below:

1. Tolerance to variance in fit up: adaptability of welding process to variation/non-uniformity in fit-up/set-up before start of welding (1 = tight tolerance required, 5 = wide tolerance allowed).
2. Susceptibility to flaws for the material/process combination: possibilities of weld imperfections and defect formation and their effect on the quality of the canister (1 = highly susceptible to flaws, 5 = less susceptible to flaws).
3. Difficulty of repair: methodology and technique to be applied to remove the defects found in the weld by means of relevant non-destructive examination (NDE) and subsequent re-welding (fill up) without producing any additional defects (1 = very difficult, 5 = less difficult).
4. Suitability for inspection: suitability for inspection of weld during and after welding including visual inspection and other NDE such as RT, UT and UT variations, etc. (1 = unsuitable for inspection, 5 = suitable for inspection and easy operation).
5. Number of operators required: total number of technicians/operators required to operate welding activity e.g., welder, welding operator, any supporting technician etc. (1 = more operators required, 5 = fewer operators required (ideally 1 per equipment or 1 handling more than 1 piece of equipment)).
6. Possible process welding positions: welding can be carried out in different positions such as vertical, horizontal, overhead, etc. Not all the processes can be used for all positional welding: for example, SAW cannot be used for overhead welding due to granular flux falling under gravity and the associated lack of weld shielding; TIG and MIG welding processes can be used for all positional welding mainly due to gas shielding (1 = limited positions available, 5 = all positional welding available).
7. Weld edge preparation requirement: dimensions and shape of the area on canister at which welding will be carried out (1 = precise control of dimensional requirement, 5 = less stringent tolerance on dimensions).
8. Capacity for remote operation/automation: ability of the welding process to be automated and availability of the equipment in market (1 = restriction on automation or no automation possible, 5 = full automation possible).
9. Expected mechanical properties of weld (after PWHT, e.g., percentage of recovery of base material properties): mechanical properties of welding (filler) wire after weld deposition and its response to subsequent PWHT. Variation in the mechanical properties of weld and adjacent parent plate (1 = wide variation in mechanical properties, 5 = uniform mechanical properties).
10. Permissible window of operation: more control over deposition via equipment control and variations (1 = no, less and/or restricted control, 5 = better flexibility and good control).
11. Typical deposition rate: amount of weld metal deposited in kg every hour while welding arc is on. This applies to arc welding processes. For EB welding, no filler wire is added (1 = low metal deposition in $kg \cdot h^{-1}$, 5 = higher deposition $kg \cdot h^{-1}$).

12. Ease of access for torch/energy source: welding torch or energy source conveniently and accurately reaching expected location in the weld groove (1 = poor access usually with standard torch (bulky unit), 5 = good access usually with specialised torch suitable for narrow groove).
13. Distortion: variation in the dimensions of a welded part after completion of weld compared to expected/final design. This is a result of residual stress (1 = high distortion after welding, 5 = low distortion after welding).
14. Health and safety requirements: welding is an energy intensive process. Worker protection is important. Arc welding produces mainly heat, light, noise and fumes while EB welding creates X-rays (1 = severe adverse effect(s) on operator, 5 = no or minimal adverse effect(s) on operator).
15. Joint width: opening of the welding groove. The size of the welding torch defines the required extent of opening. A smaller and thinner torch requires a narrower opening and a smaller volume of metal deposition (1 = wider width/opening, 5 = narrow width).
16. Joint tracking availability: this part is covered under automation. This function helps to maintain the accuracy of the welding arc or power beam following the intended location within the weld groove (1 = no tracking available, 5 = full tracking available).
17. Welding consumable (filler wire): grade of welding filler wire having composition and behaviour close to parent material. EB welding does not require filler wire (1 = unavailability of filler chemistry matching parent metal and considerable difference in the weld metal properties compared to parent metal, 5 = exact matching filler wire chemistry and weld metal properties).
18. Diameter of welding filler wire: a larger diameter results in increased deposition rate and hence increased productivity (1 = significant limitations on filler wire diameter (small wire diameter), 5 = few limitations on filler wire diameter (larger filler wire diameter)).
19. Approximate weld metal weight (kg): amount of weld metal required to complete the weld groove. Filler wire consumption correlates to this (1 = high amount of weld metal required for weld completion, 5 = low or no weld metal requirement).
20. Approximate time for completion: calculated as ratio of total amount of weld metal required to be deposited for weld completion (kg) to the weld metal deposition rate ($kg \cdot h^{-1}$) (1 = longer time, 5 = shorter time).

The criteria, weighting factors, scores and rating factors for the assessed weld processes (EB, TIG-C, TIG-H, SAW-S, SAW-M, MAG-S, MAG-M) are shown in Tab. B-2 to Tab. B-8.

Tab. B-1: Decision matrix analysis for weld process selection for the closure weld

Criteria	Weighting	NG-TIG comment	NG-TIG score	NG-TIG rating factor (weight × score)	EB comment	EB score	EB rating factor (weight × score)
Can the process be carried out automatically and remotely?	10	NG-TIG is not a fully automatic process. It is mechanised and will need some remote operator control.	5	50	Yes, automatic processing is standard as it has to be in a vacuum chamber.	10	100
Can the process be operated in a 2G welding position?	10	Reduction in deposition rates in 2G/PC compared to 1G/PA.	8	80	Yes, 2G welding is the best option for fully penetrating welding of > 25 mm.	10	100
Is the process suitable for application to Nagra's joint design?	10	Arc process of choice for high quality nuclear work.	10	100	Yes, EB welding would be suitable for Nagra's design.	10	100
The likelihood of that given process producing zero weld defects.	10	On assumption that all processes will fail intermittently but can be repaired. NG-TIG has a track record of producing welds with no defects.	8	80	On assumption that all processes will fail intermittently but can be repaired. EB has a track record of producing very high quality welds with almost no defects. Any flaws present would normally pass inspection and would not be classified as a defect.	7	70
Is the process likely to produce low magnitude tensile residual stresses at the surfaces of the weld zone?	10	Patel et al. (2012) shows that yield magnitude hoop stresses are generated through NG-TIG welding from the surface to 3/4 weld depth.	1	10	Patel et al. (2012) shows that relatively low magnitude stresses (~ 180 MPa) are generated at the surface due to EB welding, with yield magnitude tensile hoop stresses developed in the mid-section and near the root.	6	60

Tab. B-1: Cont.

Criteria	Weighting	NG-TIG comment	NG-TIG score	NG-TIG rating factor (weight × score)	EB comment	EB score	EB rating factor (weight × score)
Is the given process also capable of producing no weld defects when it starts and/or stops?	9	Defects will occur and will require a repair strategy. Stop/starts more prone than other locations but possible to ramp in/out at start/stops to reduce.	8	72	In an EB weld, there is an increased risk of flaws on weld termination (e.g., root porosity), procedures would need to be developed for the slope out areas.	7	63
Is the welding equipment capable of continuous operation? If consumables need frequent replacement this will require a lower score and the downtime associated with carrying out repairs.	8	Equipment problems can occur during any long term arc on time use but can be mitigated by proper maintenance. Wire feeding units in particular can fail. Non-consumable tungsten electrodes will need to be replaced and/or re-prepared after a couple of hours of use.	8	64	EB equipment can be operated continuously during a normal shift pattern (8 hours) at up to 15 kW. A normal weld would take ~ 2 hours.	10	80
Can the processing equipment be rotated around a fixed canister/lid assembly in that position?	8	Yes. Heads are relatively compact and lightweight.	10	80	Yes. A prototype with a head going around 450 degrees already exists.	10	80
In the case of multiple pass processes, can interpass cleaning be avoided?	8	Interpass cleaning will be required between runs to remove silicates.	2	16	No interpass cleaning required as it is a single-pass process.	10	80
Do relevant welding procedure qualification standards for that process exist already?	8	Yes.	10	80	Yes.	10	80

Tab. B-1: Cont.

Criteria	Weighting	NG-TIG comment	NG-TIG score	NG-TIG rating factor (weight × score)	EB comment	EB score	EB rating factor (weight × score)
Is the process likely to produce an acceptable weld in terms of low hardness?	8	Heat inputs are low but the multipass nature of the welds generates HAZ refinement and reduced hardness.	9	72	Low heat input overall but the single-pass process means there is no opportunity for interpass refinement of welds.	5	40
Is the technology readiness level (TRL) of the process high?	7	High TRL in industrial and nuclear pressure vessel usage proven to production.	10	70	High TRL in industrial and nuclear pressure vessel usage proven to production. Thick section weld for wind turbines, gas turbines, pressure vessels.	10	70
Can the processing equipment be exposed to radioactive environments?	7	The amount of gamma radiation generated by the canister is expected to be low. However, this radiation will degrade any plastic, electronics or optics. Some lead shielding can be positioned but maintenance of the equipment will be required at regular intervals. There are suppliers available for such protective casings. The welding head/nozzle tips may require some parts to be changed frequently due to radiation if they cannot be protected. These could be supplied and automatically replaced. It would also be recommended to include redundancy in the system.	10	70	All EB welding equipment generates high levels of X-radiation > 400 mSv/h. Normal EB machines are lead-shielded to protect the operator, and the electronic equipment is outside the vacuum chamber. Depending on the design EB equipment is similar in nature and resilient to X-ray degradation.	10	70

Tab. B-1: Cont.

Criteria	Weighting	NG-TIG comment	NG-TIG score	NG-TIG rating factor (weight × score)	EB comment	EB score	EB rating factor (weight × score)
Can the associated process monitoring equipment be exposed to radioactive environments?	7	The equipment, particularly the electronics and optics, would need to be protected from deposition of irradiated particles or welding fumes etc. generated during the process. There are suppliers available for such protective casings. The cameras and electronics would need special casing. It may be necessary to replace certain equipment after a certain period of welding time. It would also be recommended to include redundancy in the system.	5	35	EB welding using a moving chamber has been built previously where all process monitoring was outside the high radiation environment, i.e., the vacuum chamber. Current EB equipment of a different form can be exposed to a radioactive environment without major difficulties. However, access is periodically required for maintenance.	10	70
Can the process cope with any residual magnetism?	7	Residual magnetism, if present will cause arc deflection and parts will need to be assessed and demagnetised.	1	7	Yes, but the residual magnetism level must be below 5 Gauss (5×10^{-4} Tesla) for continued high quality welds.	3	21
Can the process be used without preheat?	7	TIG is a low hydrogen process by nature and should not require preheating.	9	63	Yes. EB welding is a low hydrogen process (in vacuum and no filler).	9	63
Is the process tolerant to variation in fit up?	6	Tolerant to 0-1 mm variation.	5	30	Tolerant to 0-0.25 mm gap. Above 0.25 mm, there is a risk of an underflush weld. This tolerance is commonly achieved in the industry.	3	18

Tab. B-1: Cont.

Criteria	Weighting	NG-TIG comment	NG-TIG score	NG-TIG rating factor (weight × score)	EB comment	EB score	EB rating factor (weight × score)
Does the process provide matching weld strength?	6	Matching joint strength capability.	10	60	Typically, up to 95% of the parent metal; in some materials up to 100%.	8	48
Is the process low maintenance?	4	Intermittent and routine servicing essential. Daily equipment checks required.	5	20	Daily check of optic glass (1/2 hour). Weekly check of the standard maintenance items (2 hours) and monthly gun maintenance (1 day).	9	36
Is the finished weld bead that the process produces suitable for inspection and coating?	4	Produces relatively smooth surface at cap with no crevices. May impede UT but should be suitable for coating.	7	28	The weld cap would probably require a wash pass or cosmetic weld with lower energy to give an appropriate weld bead. This is a second activity after the main weld. This pass should allow UT inspection but may not be suitable for coating.	5	20
Can the process be carried out with minimal cleaning? Is the process tolerant of contaminants?	4	Joint cleanliness will need to be very good. Machined and free of surface oils, oxides, dust and other contaminants.	1	4	Machining fluid oil grease and other contaminants will need to be removed, otherwise an increased flaw generation (porosity) has to be expected.	1	4
The estimated welding time of the process.	4	Estimated arc on time is 50 hours per canister single head at conservative deposition rates. At 80% utilisation for required interpass cleaning, this is 63 hours.	0	0	Setting up, tacking, intermittent welding, EB would take up to 5 hours per canister, including the cosmetic pass.	10	40

Tab. B-1: Cont.

Criteria	**Weighting**	**NG-TIG comment**	**NG-TIG score**	**NG-TIG rating factor (weight × score)**	**EB comment**	**EB score**	**EB rating factor (weight × score)**
Does the process produce joints with acceptable joint toughness?	4	Good toughness.	10	40	Fracture toughness in as-welded condition can be a little low in the fusion area.	5	20
Can the process be made without any filler wire additions?	3	No, it requires filler wire.	1	3	Yes, it requires no filler wire.	10	30
Can the process be made without gas shielding?	3	No, it requires gas shielding.	1	3	Yes, EB is a medium vacuum process.	10	30
TOTAL			1137	TOTAL			1393

Tab. B-2: Scoring table for reduced pressure electron beam (EB) for weld process selection for the bottom lid

Criteria	**Weighting**	**Comment**	**Score**	**Rating factor (weight × score)**
Tolerance to variance in fit-up	4	0 – 0.25 mm	2	8
Susceptibility to flaws for the material/process combination	5	Possibility of spatter and porosity	2	10
Difficulty of repair	4	Medium	3	12
Suitability for inspection of main weld	5	High	4	20
Number of operators required	1	1 machine operator, automatic welding	5	5
Process welding positions possible	2.5	Horizontal preferred [2G]	5	12.5
Weld edge preparation requirement	4.5	Simple machined square edge, 3.2 µm Ra	1	4.5
Capacity for remote operation/automation	2	Remote operation is the norm as is automatic weld processing	5	10
Expected mechanical properties of weld after PWTH	5	Low HI compared to arc welds but lack of interpass re-heating due to single pass. 95% parent strengths typical. With PWHT impact properties improve.	4	20
Permissible window of operation	3	CNC controlled parameters, continuous 8-hour operation possible [< 2 hours per weld]	5	15
Typical deposition rate ($kg \cdot h^{-1}$)	2.5	None, as no wire needed	5	12.5
Ease of access for torch / energy source	4.5	No torch, line of sight access needed but can be 200-500 mm away	5	22.5
Distortion	5	Low distortion, low heat input	5	25
Health and safety requirements	4	X-ray generation, stopped by vacuum chamber	4	16
Joint width	2	10 mm	4	8

Tab. B-2: Cont.

Criteria	Weighting	Comment	Score	Rating factor (weight × score)
Joint tracking availability	5	Visual tracking or electron optical tracking via CNC program	5	25
Welding consumable (filler wire) EN 10250-2 S235J2G3 EN 10222-2 P245GH	3	None	5	15
Filler wire diameter (mm)	2.5	None	5	12.5
SF disposal canister				
Approximate weld metal weight (kg)	2	Autogenous	5	10
Approximate time for completion (h)	3	Less than 5 hours for all set-up/welding	5	15
RP-HLW disposal canister				
Approximate weld metal weight (kg)	2	Autogenous	5	10
Approximate time required for completion (h)	3	Less than 5 hours for all set-up/welding	5	15
Process comments	-	High integrity welding process chosen by nuclear and aerospace industries. No interpass cleaning required as it is a single pass autogenous welding process. Tolerant of high radiation environments.	-	-
TOTAL				**303.5**

Tab. B-3: Scoring table for narrow gap tungsten inert gas - cold wire (TIG-C) for weld process selection for the bottom lid

Criteria	**Weighting**	**Comment**	**Score**	**Rating factor (weight × score)**
Tolerance to variance in fit-up	4	0 – 1 mm	3	12
Susceptibility to flaws for the material/process combination	5	Lack of sidewall fusion	1	5
Difficulty of repair	4	Medium	3	12
Suitability for inspection of main weld	5	High	4	20
Number of operators required	1	1 per welding torch	3	3
Process welding positions possible	2.5	All	5	12.5
Weld edge preparation requirement	4.5	Joint requires J-prep machining	3	13.5
Capacity for remote operation/automation	2	Vision system used for remote in-process monitoring	5	10
Expected mechanical properties of weld after PWTH	5	Lower HI relative to sub arc. More number of passes, better impact properties expected than SAW and MAG.	5	25
Permissible window of operation	3	Higher requirement on setup. Correlated with tolerance.	3	9
Typical deposition rate ($kg \cdot h^{-1}$)	2.5	1.5 – 2.5	1	2.5
Ease of access for torch / energy source	4.5	Specialised torches available for application	3	13.5
Distortion	5	Lower	4	20
Health and safety requirements	4	Open arc. PPE.	3	12
Joint width	2	8.5 – 20 mm	4	8
Joint tracking availability	5	Laser line scanning not possible due to depth Usually vision system with operator	4	20

Tab. B-3: Cont.

Criteria	Weighting	Comment	Score	Rating factor (weight × score)
Welding consumable (filler wire) EN 10250-2 S235J2G3 EN 10222-2 P245GH	3	EN ISO 14341 A (38 or 42 or 46) 2 (Z or M or C) 3Si1	4	12
Filler wire diameter (mm)	2.5	1.6, 2.4	-	-
SF disposal canister				
Approximate weld metal weight (kg)	2	~ 46 – 60	3	6
Approximate time for completion (h)	3	~ 20 – 26	3	9
RP-HLW disposal canister				
Approximate weld metal weight (kg)	2	~ 30 – 39	3	6
Approximate time require for completion (h)	3	~ 13 – 17	3	9
Process comments	-	Arc process of choice for high-quality nuclear work.	-	-
TOTAL				**240**

Tab. B-4: Scoring table for narrow gap tungsten inert gas - hot wire (TIG-H) for weld process selection for the bottom lid

Criteria	**Weighting**	**Comment**	**Score**	**Rating factor (weight × score)**
Tolerance to variance in fit-up	4	0 – 1 mm	3	12
Susceptibility to flaws for the material/process combination	5	Lack of sidewall fusion	1	5
Difficulty of repair	4	Medium	3	12
Suitability for inspection of main weld	5	High	4	20
Number of operators required	1	1 per welding torch	3	3
Process welding positions possible	2.5	All	5	12.5
Weld edge preparation requirement	4.5	Joint requires J-prep machining	3	13.5
Capacity for remote operation/automation	2	Vision system used for remote in-process monitoring	5	10
Expected mechanical properties of weld after PWTH	5	Lower HI relative to sub arc. More number of passes, better impact properties expected than SAW and MAG.	5	25
Permissible window of operation	3	Higher requirement on setup. Correlated with tolerance.	3	9
Typical deposition rate ($kg \cdot h^{-1}$)	2.5	3 – 6.5	1	2.5
Ease of access for torch / energy source	4.5	Specialised torches available for application	3	13.5
Distortion	5	Lower	4	20
Health and safety requirements	4	Open arc. PPE	3	12
Joint width	2	8.5 – 20 mm	4	8
Joint tracking availability	5	Laser line scanning not possible due to depth Usually vision system with operator	4	20

Tab. B-4: Cont.

Criteria	Weighting	Comment	Score	Rating factor (weight × score)
Welding consumable (filler wire) EN 10250-2 S235J2G3 EN 10222-2 P245GH	3	EN ISO 14341 A (38 or 42 or 46) 2 (Z or M or C) 3Si1	4	12
Filler wire diameter (mm)	2.5	1.6, 2.4	-	-
SF disposal canister				
Approximate weld metal weight (kg)	2	~ 46 –60	3	6
Approximate time for completion (h)	3	~ 9 – 12	3	9
RP-HLW disposal canister				
Approximate weld metal weight (kg)	2	~ 30 – 39	3	6
Approximate time require for completion (h)	3	~ 5 – 7	3	9
Process comments	-	Arc process of choice for high quality nuclear work. Additional power source required for hot wire - not always achievable with welding equipment dependent on delivery mechanism.	4	-
TOTAL				**240**

Tab. B-5: Scoring table for narrow gap submerged arc welding - single wire (SAW-S) for weld process selection for the bottom lid

Criteria	**Weighting**	**Comment**	**Score**	**Rating factor (weight × score)**
Tolerance to variance in fit-up	4	0 – 2 mm	4	16
Susceptibility to flaws for the material/process combination	5	Lack of sidewall fusion, slag inclusion	3	15
Difficulty of repair	4	Medium	3	12
Suitability for inspection of main weld	5	High	4	20
Number of operators required	1	1 per welding torch	3	3
Process welding positions possible	2.5	Flat only	3	7.5
Weld edge preparation requirement	4.5	Joint requires J-prep machining	3	13.5
Capacity for remote operation/automation	2	No sight of weld under flux - requires post-weld inspection/inspection of bead some distance behind weld pool.	3	6
Expected mechanical properties of weld after PWTH	5	Possibly lower hardness/lower strength - depends on heat input/metallurgy & PWHT. Higher deposition rate, lesser number of passes.	4	20
Permissible window of operation	3	Lower requirement on setup. Correlated with tolerance.	4	12
Typical deposition rate ($kg \cdot h^{-1}$)	2.5	6.5 – 10	5	12.5
Ease of access for torch / energy source	4.5	Specialised torches available for application	3	13.5
Distortion	5	Higher	3	15
Health and safety requirements	4	Arc hidden. Conventional PPE.	4	16
Joint width	2	18 – 50 mm	3	6
Joint tracking availability	5	Mechanical off sidewall - no vision	3	15

Tab. B-5: Cont.

Criteria	Weighting	Comment	Score	Rating factor (weight × score)
Welding consumable (filler wire) EN 10250-2 S235J2G3 EN 10222-2 P245GH	3	EN ISO 14171 A: S 42 2 AB S2	4	12
Filler wire diameter (mm)	2.5	4, 5	-	-
SF disposal canister				
Approximate weld metal weight (kg)	2	~ 76	4	8
Approximate time for completion (h)	3	~ 8.5	4	12
RP-HLW disposal canister				
Approximate weld metal weight (kg)	2	~ 50	4	8
Approximate time require for completion (h)	3	~ 5.5	4	12
Process comments	-	1. Flux coverage does not allow to see real time deposition activity 2. Access and welding from opposite side is required to back machine and do the weld root. 3. High productivity.		-
TOTAL				**255**

Tab. B-6: Scoring table for narrow gap submerged arc welding - multi wire (SAW-M) for weld process selection for the bottom lid

Criteria	**Weighting**	**Comment**	**Score**	**Rating factor (weight × score)**
Tolerance to variance in fit-up	4	0 – 2 mm	4	16
Susceptibility to flaws for the material/process combination	5	Lack of sidewall fusion, slag inclusion	3	15
Difficulty of repair	4	Medium	3	12
Suitability for inspection of main weld	5	High	4	20
Number of operators required	1	1 per welding torch	3	3
Process welding positions possible	2.5	Flat only	3	7.5
Weld edge preparation requirement	4.5	Joint requires J-prep machining	3	13.5
Capacity for remote operation/automation	2	No sight of weld under flux - requires post-weld inspection/inspection of bead some distance behind weld pool.	3	6
Expected mechanical properties of weld after PWTH	5	Possibly lower hardness/lower strength - depends on heat input/metallurgy & PWHT. Higher deposition rate, lesser number of passes.	4	20
Permissible window of operation	3	Lower requirement on setup. Corelated with tolerance.	4	12
Typical deposition rate ($kg \cdot h^{-1}$)	2.5	8.5 – 20	5	12.5
Ease of access for torch / energy source	4.5	Specialised torches available for application	3	13.5
Distortion	5	Higher	3	15
Health and safety requirements	4	Arc hidden. Conventional PPE.	4	16
Joint width	2	18-50 mm	3	6

Tab. B-6: Cont.

Criteria	Weighting	Comment	Score	Rating factor (weight × score)
Joint tracking availability	5	Mechanical off sidewall - no vision	3	15
Welding consumable (filler wire) EN 10250-2 S235J2G3 EN 10222-2 P245GH	3	EN ISO 14171 A: S 42 2 AB S2	4	12
Filler wire diameter (mm)	2.5	4, 5	-	-
SF disposal canister				
Approximate weld metal weight (kg)	2	~ 76	5	10
Approximate time for completion (h)	3	~ 5	5	15
RP-HLW disposal canister				
Approximate weld metal weight (kg)	2	~ 50	5	10
Approximate time require for completion (h)	3	~ 3.3	5	15
Process comments	-	1. Flux coverage does not allow to see real time deposition activity 2. Access and welding from opposite side is required to back machine and do the weld root. 3. High productivity.	-	-
TOTAL				**265**

Tab. B-7: Scoring table for narrow gap metal active gas welding – single wire (MAG-S) for weld process selection for the bottom lid

Criteria	**Weighting**	**Comment**	**Score**	**Rating factor (weight × score)**
Tolerance to variance in fit-up	4	0 – 2 mm	4	16
Susceptibility to flaws for the material/process combination	5	Possibility of spatter, lack of sidewall fusion	3	15
Difficulty of repair	4	Medium	3	12
Suitability for inspection of main weld	5	High	4	20
Number of operators required	1	1 per welding torch	3	3
Process welding positions possible	2.5	All	5	12.5
Weld edge preparation requirement	4.5	Joint requires J-prep machining	3	13.5
Capacity for remote operation/automation	2	Vision system used for remote in-process monitoring	5	10
Expected mechanical properties of weld after PWTH	5	Lower HI relative to sub arc. Expected properties between SAW and TIG.	5	25
Permissible window of operation	3	Lower requirement on setup. Correlated with tolerance.	4	12
Typical deposition rate ($kg \cdot h^{-1}$)	2.5	3.5 – 6	3	7.5
Ease of access for torch / energy source	4.5	Specialised torches available for application	3	13.5
Distortion	5	Higher	3	15
Health and safety requirements	4	Open arc. PPE	3	12
Joint width	2	18 – 50 mm	3	6
Joint tracking availability	5	Laser line scanning not possible due to depth Usually vision system with operator	4	20

Tab. B-7: Cont.

Criteria	Weighting	Comment	Score	Rating factor (weight × score)
Welding consumable (filler wire) EN 10250-2 S235J2G3 EN 10222-2 P245GH	3	EN ISO 14341 A (38 or 42 or 46) 2 (Z or M or C) 3Si1	4	12
Filler wire diameter (mm)	2.5	1.2, 1.6	-	-
SF disposal canister				
Approximate weld metal weight (kg)	2	~ 60	4	8
Approximate time for completion (h)	3	~ 17.5	4	12
RP-HLW disposal canister				
Approximate weld metal weight (kg)	2	~ 39	4	8
Approximate time require for completion (h)	3	~ 11	4	12
Process comments	-	Less experience with this technique - may require development (difficulties with achieving e.g., sidewall fusion via wire oscillation or magnetic stirring)	-	-
TOTAL				**265**

Tab. B-8: Scoring table for narrow gap metal active gas welding – multi wire (MAG-M) for weld process selection for the bottom lid

Criteria	**Weighting**	**Comment**	**Score**	**Rating factor (weight × score)**
Tolerance to variance in fit-up	4	0 – 2 mm	4	16
Susceptibility to flaws for the material/process combination	5	Possibility of spatter, lack of sidewall fusion	3	15
Difficulty of repair	4	Medium	3	12
Suitability for inspection of main weld	5	High	4	20
Number of operators required	1	1 per welding torch	3	3
Process welding positions possible	2.5	All	5	12.5
Weld edge preparation requirement	4.5	Joint requires J-prep machining	3	13.5
Capacity for remote operation/automation	2	Vision system used for remote in-process monitoring	5	10
Expected mechanical properties of weld after PWTH	5	Lower HI relative to sub arc. Expected properties between SAW and TIG.	5	25
Permissible window of operation	3	Lower requirement on setup. Correlated with tolerance.	4	12
Typical deposition rate ($kg \cdot h^{-1}$)	2.5	7 – 13.5	3	7.5
Ease of access for torch / energy source	4.5	Specialised torches available for application	3	13.5
Distortion	5	Higher	3	15
Health and safety requirements	4	Open arc. PPE	3	12
Joint width	2	18 – 50 mm	3	6
Joint tracking availability	5	Laser line scanning not possible due to depth Usually vision system with operator	4	20

Tab. B-8: Cont.

Criteria	Weighting	Comment	Score	Rating factor (weight × score)
Welding consumable (filler wire) EN 10250-2 S235J2G3 EN 10222-2 P245GH	3	EN ISO 14341 A (38 or 42 or 46) 2 (Z or M or C) 3Si1	4	12
Filler wire diameter (mm)	2.5	1.2, 1.6	-	-
SF disposal canister				
Approximate weld metal weight (kg)	2	~ 60	4	8
Approximate time for completion (h)	3	~ 7	4	12
RP-HLW disposal canister				
Approximate weld metal weight (kg)	2	~ 39	4	8
Approximate time require for completion (h)	3	~ 4.5	4	12
Process comments	-	Less experience with this technique - may require development (difficulties with achieving e.g., sidewall fusion via wire oscillation or magnetic stirring)	-	-
Total				**265**

App. C Preliminary weld procedure specifications

This Appendix consists of drafts of the preliminary weld procedure specifications (pWPS) covering the information needed for the SF and the RP-HLW disposal canisters, in accordance with BS EN ISO 15609-3 (BSI 2004). It concerns the top closure weld on both the SF and RP-HLW canisters, a 140 mm thick circumferential butt joint, welded using reduced pressure EB, see Fig. 3-15. Since the pWPS for the two canister types are very similar, a single document is presented below with any differences between the SF and RP-HLW canisters specifically highlighted. In addition, probable activities for the welding of an actual canister during the manufacturing and sealing stage, which includes activities in and outside of the hot cell, are discussed. Furthermore, data on the potential controls and/or parameter variations that can be used to minimise flaws in thick section welds especially at the start-stop position are included. In addition, the inspection and assembly requirements for the canister both inside and outside of the hot cell environment including initial fit-up limits are addressed.

C.1 Qualification activities

This document complies with the requirements of BS EN ISO 15609-3:2004 'Specification and qualification of welding procedures for metallic materials – welding procedure specification – Part 3: Electron beam welding.' (BSI 2004).

To qualify the welding procedure, weld tests should be performed and assessed in accordance with BS EN ISO 15614-11:2002 "Specification and qualification of welding procedures for metallic materials – Welding procedure test – Part 11: Electron and laser beam welding".

In order to take into account the service performance needs of the products, the qualification should be assessed to one of the acceptance levels B, C or D as defined in BS EN ISO 13919-1:2019. The quality level should be specified by the application standard or the responsible designer.

Welding operator qualifications shall be prepared in accordance with the requirements of BS EN ISO 14732-:2013 "Welding personnel — Qualification testing of welding operators and weld setters for mechanized and automatic welding of metallic materials".

C.2 Equipment specifications

Outline

The equipment described below is based on TWI's "1EB" machine, which is a fixed gun with a rotary table. Another system configuration, which TWI has designed and built previously, is a fixed canister with a movable welding head. The vacuum chamber can be connected to the canister via sliding seals and inflatable couplings, or it can be a conventional vacuum chamber.

Description

A high-power reduced-pressure electron beam facility will be used for the welding process (process 51). The equipment is a 100 kW 150 kV EB machine with a laser-heated 3.4 mm LaB_6 filament, which will be used in reduced pressure vacuum mode (~ 5×10^{-2} mbar). This can be achieved within approximately 30 minutes after starting the pumping sequence.

The system is fitted with a fully programmable Siemens 840D CNC, which controls the electrical and mechanical axes of the machine and can be used to enable automatic welding. The electron gun is fitted with a digital beam deflection system, which can produce numerous deflection patterns that can be used to alter weld shapes and control penetration. For this work it is intended that the gun will be used in the PC or horizontal weld orientation.

Tolerances on welding parameters

The following tolerances on welding parameters are assured via calibration:

Beam current	± 1%
Accelerating voltage	± 1%
Welding speed	± 1%
Working distance	± 1 mm
Oscillation amplitude	± 5%
Oscillation frequency	± 5%
Focus coil current	± 0.5%
Slope time	± 0.5%

C.3 Material

Forged material as specified will be used for the welding of the canister lid and body (Section 3.4). No filler material is intended to be used during the welding process. A fronting bar of mild steel is to be used as a weld bead support feature.

C.4 Inspection and assembly

Inspection outside the hot cell

Inspection of the parts and the joint fit-up should be performed prior to the canister entering the hot cell:

1. A canister body and lid need to be selected for the following inspection activities. They should be clearly marked with individual serial numbers to enable full tracing of inspection records.
2. The parts should be checked to ensure that surface oxide/mill scale have been removed from 25 mm around the joint line. The area is initially cleaned with isopropyl alcohol to remove any corrosion protection coating.
3. The surface finish of the faying faces should also be assessed according to the requirements on the component drawings and/or as stated below.
4. The radial gap between the integral spigot of the lid and the canister bore should be measured and recorded. All values should be less than the amount specified below.
5. After an initial cleaning of the joint faces with isopropyl alcohol, the joint gap should be measured by trial assembly of the joint. The measured joint gap should be recorded in approximately eight equally spaced places around the circumference of the canister. It should be less than the amount specified on the component drawings and/or as stated below.
6. The relative position of the lid and the canister body should be marked via a scribe line or dot punch.

7. The mismatch across the joint should also be measured and recorded in approximately eight equally spaced places around the circumference of the canister. All values should be less than the range specified below.
8. The parts should then be reassembled with a stainless steel TIG wire that has a diameter of 1.6 mm inserted into the joint in at least 3 places, to give a consistent joint gap around the canister.
9. A Gauss meter probe can then be used to scan the joint for residual magnetism. The level of residual magnetism should be checked in a minimum of eight equally spaced positions around the circumference of the joint. Demagnetisation can be required if the joint readings are above 15 Gauss.
10. The weld bead support ring should be cleaned and checked for residual magnetism. Demagnetisation will be required if the surface readings are over 5 Gauss.
11. The weld bead support ring should be lowered into position on the canister body. It should be secured in place using an appropriate clamping collar to prevent it from moving during welding. Its position should be checked as per Tab. C-1 below.
12. Following the inspection stages of the process the canister body and lid can be moved into the hot cell environment.

Assembly after waste loading

Following the filling of the canister body with waste and the assembly of the inner lid, the final cleaning and assembly can be completed.

13. The canister body should be moved into position onto the rotary table and fixed in place.
14. When in position, the canister run-out on the rotary fixture should be checked, via a touch probe, to ensure it is less than 3 mm. If it is more than 3 mm the canister should be removed, rotated and replaced onto the rotary fixture to be measured again.
15. The assembly should also be checked for level with respect to the rotary fixture, again by a touch probe. The assembly will be level to 1.0 $mm \cdot m^{-1}$.
16. Final cleaning of joint faces with isopropyl alcohol will be carried out to remove any traces of contamination on and around the joint, which may have occurred during final assembly.
17. The lid should be lowered onto the canister body to ensure the alignment marks/scribe lines coincide.

No clamping is required as self-weight loading from the lid alone should be sufficient to hold the parts in intimate contact until EB tack welding is performed.

Tab. C-1: Fit-up limits

Feature	Allowable range
Radial spigot clearance	0.25 to 0.75 mm
Circumferential joint gap	0 to 0.25 mm
Surface mismatch	- 0.5 to 0.5 mm
Surface finish	< 3.2 µm R_a
Fronting bar position	7 mm down from joint
Joint run-out on fixture	-1.5 to 1.5 mm
Surface level	1.0 mm·m^{-1}

C.5 Welding sequence

The welding operations will be conducted in the following sequence:

1. Tacking (stitch tacks)
2. Tacking (full 360° circumferential tack)
3. Welding (full 360° circumferential weld)

Procedure

1. If no welding has been performed within the last five days, a standard test plate will be welded to check machine operation, welding parameters and weld penetration. Penetration shall be a minimum of 140 mm + 20 mm. Welding shall only commence once the machine operation, welding parameters and weld penetration have been verified.
2. The chamber will be evacuated to a vacuum of 5×10^{-2} mbar or better. Helium bleed gas will be started at 0.6 L·min^{-1}.
3. No preheating is expected to be used and the start temperature is expected to be between 15 °C and 50 °C.
4. The electron gun will be conditioned at 160 kV for a period of 5 minutes after which time the EB will be deposited onto beam dump at an appropriate beam current level (minimum 5 mA) for a period of 30 minutes immediately prior to welding. During this period the machine will undergo 2 ramp-up and ramp-down beam current cycles (at least 50 mA). This operation will be repeated each time the vacuum chamber has been vented or after a sustained high voltage arc has occurred.
5. The centre axis of the assembly shall be confirmed to be in line with the beam to within ± 3 mm using the visual optics of the machine.
6. The joint shall be checked for run-out using a tracer beam (~ 0.5 mA), Z positions every 45° should be noted for CNC program compilation.
7. Stitch tacks will be made at eight locations around the circumference of the joint in a sequence such that consecutive tack welds are diametrically opposite, see Tab. C-2 and Fig. C-1.
8. Following stitch tacking, the joint will be tacked continuously around its circumference. The 0° start position shall be at the previously scribed/spot punch-marked location, see Tab. C-3, Fig. C-2 and Fig. C-3.

9. After tacking, a full penetration weld will be produced using the welding conditions shown in Tab. C-4.
10. Slope-up and slope-down positions will be as illustrated in Fig. C-4 and Fig. C-5.
11. After welding, the chamber will be vented and the assembly allowed to cool naturally in air.

C.6 Unplanned shutdowns and repair options

In the event of an unplanned machine shutdown (due to infrastructure failure) or a sustained high voltage arc, which shuts off the beam, a defect in the area of concern should be expected. If this occurs during tacking operations, the location should be noted, and the tacking process can continue where it left off. The beam should be sloped in before the flaw ensuring a small 1° overlap and the weld allowed to complete the tacking operation.

If the shutdown event occurred during the main weld pass, then a similar repair option is possible. The location should be noted for future inspection, then the main weld sequence can be restarted 31° back from the edge of the flaw. The beam will ramp up and the weld will overlap the flaw and continue to complete the full cycle.

Once the canister has cooled down, any noted regions should be inspected carefully to ensure all defects have been completely repaired. If the defect persists then discussions need to be held on whether to attempt another autogenous repair with the EB or perform a weld repair with filler wire.

C.7 Inspection

After the assembly has cooled, the canister will be subjected to examinations. Should the visual examination show the weld to be unsatisfactory, the next steps (repair weld/concession) will be determined. The welded assembly will be subjected to UT in accordance with the developed procedure. In the event that a weld is found to be defective, the next steps (repair weld/concession) will be determined.

C.8 Equipment alterations

No changes to the specified equipment or its configuration, as described above, are allowed. If any change becomes necessary, the level of testing to achieve requalification will be defined. Any significant change will invalidate the weld procedure qualification.

C.9 Records

All weld record documents shall be completed and retained for each weld.

C.10 Preliminary welding procedure specification

Full penetration butt joint into integral backing type weld - joint depth of 140 mm plus 20 mm minimum

Outside diameter: 1100 mm for the SF canister and 720 mm for the RP-HLW canister

Tab. C-2: Stitch tack welding conditions

Essential parameter	**Values**		**Allowable range***
Welding position	PC		± 5° slope ± 10° rotation
CNC program number	SF	34781-W001-ST	-
	RP-HLW	34781-W002-ST	
Accelerating voltage	150 kV		± 1%
Beam current	15 mA		± 5%
Focus coil currents	-		-
Top lens	1032 mA		± 2%
Bottom lens	950 mA		± 2%
Working distance	200 mm		± 1 mm·min^{-1}
Beam deflection	Circle CW		-
Amplitude	1.25 mm		± 0.1 mm
Frequency	70 Hz		± 1%
Welding speed, F	200 mm/min		± 1%
Slope conditions	-		-
Slope-up	SF	10 mm (1.04°) [3 s]	–0/+1 mm
	RP-HLW	10 mm (1.59°) [3 s]	
Weld length	SF	50 mm (5.21°) [15 s]	–0/+1 mm
	RP-HLW	50 mm (7.96°) [15 s]	
Slope-down	SF	10 mm (1.04°) [3 s]	–0/+1 mm
	RP-HLW	10 mm (1.59°) [3 s]	
Minimum temperature before start of welding	15 °C		-
Maximum inter-pass temperature	50 °C		-
Post weld heat treatment	None		-
Material specification	Nagra specification		Group 1 metals

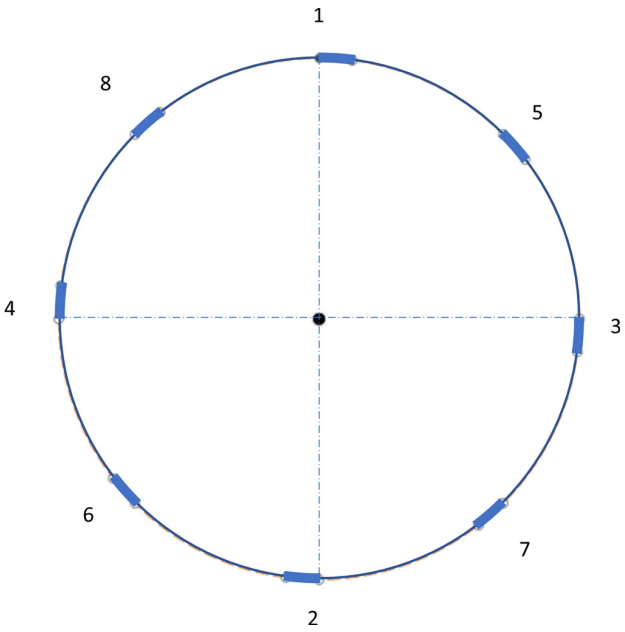

Fig. C-1: Stitch tacking positions and sequence

Tab. C-3: Tack welding conditions

Essential parameter	**Actual values**		**Allowable range**
Welding position	PC		± 5° slope ± 10° rotation
CNC program number	SF	34781-W001-T	-
	RP-HLW	34781-W002-T	
Accelerating voltage	150 kV		± 1%
Beam current	30 mA		± 5%
Focus coil currents	-		-
Top lens	1,032 mA		± 2%
Bottom lens	950 mA		± 2%
Working distance	200 mm		± 1 mm/min
Beam deflection	Circle CW		-
Amplitude	1.25 mm		± 0.1 mm
Frequency	70 Hz		± 1%
Welding speed	200 mm/min		± 1%
Start position	0°		± 0.1°
Slope conditions	-		-
Slope-up	SF	10 mm (1.04°) [3 s]	–0/+1 mm
	RP-HLW	10 mm (1.59°) [3 s]	
Weld length	SF	3,455.8 mm (360°) [1,036.7 s]	–0/+1 mm
	RP-HLW	2,262 mm (360°) [678.6s]	
Slope-down	SF	10 mm (1.04°) [3 s]	–0/+1 mm
	RP-HLW	10 mm (1.59°) [3 s]	
Minimum temperature before start of welding	15 °C		-
Maximum inter-pass temperature	50 °C		-
Post weld heat treatment	None		-
Material specification	Nagra specification		Group 1 metals

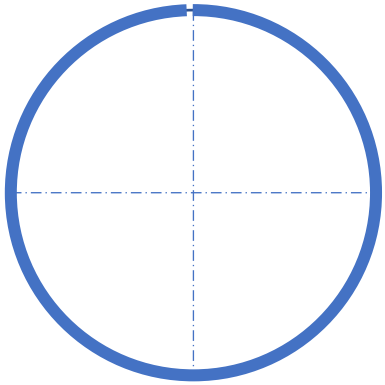

Fig. C-2: Tack welding diagram

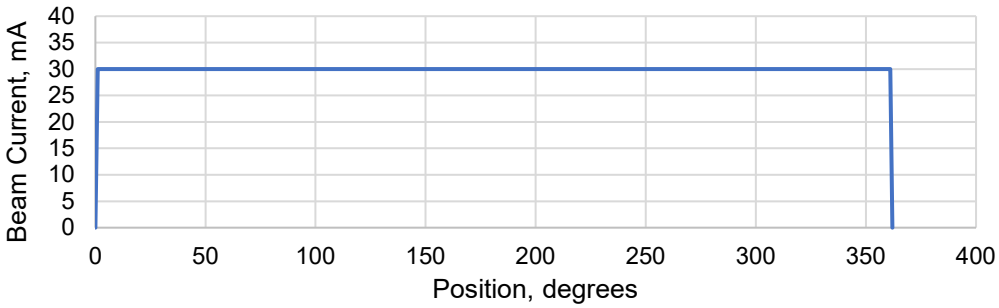

Fig. C-3: Welding current progression for tack weld

Tab. C-4: Full current welding conditions

Essential parameter	**Actual values**		**Allowable range**
Welding position	PC		± 5° slope ± 10° rotation
CNC program number	SF	34781-W001-M	-
	RP-HLW	34781-W002-M	
Accelerating voltage	150 kV		± 1%
Beam current	225 mA		± 5%
Focus coil currents	-		-
Top lens	1,032 mA		± 2%
Bottom lens	950 mA		± 2%
Working distance	200 mm		± 1 mm/min
Beam deflection	Circle CW		-
Amplitude	1.25 mm		± 0.1 mm
Frequency	70 Hz		± 1%
Welding speed	80 mm/min		± 1%
Start Position	0°		± 0.1°
Slope conditions	-		-
Slope-up	SF	288 mm (30°) [216 s]	–0/+1 mm
	RP-HLW	188.5 mm (30°) [141.4 s]	
Weld length including overlap	SF	3,465.4 mm (361°) [2599 s]	–0/+1 mm
	RP-HLW	2,268.2 mm (361°) [1701.2 s]	
Slope-down	SF	576 mm (60°) [432 s]	–0/+1 mm
	RP-HLW	377 mm (60°) [282.8 s]	
Minimum temperature before start of welding	15 °C		-
Maximum inter-pass temperature	50 °C		-
Post weld heat treatment	600 °C		-
Material specification	Nagra specification		Group 1 metals

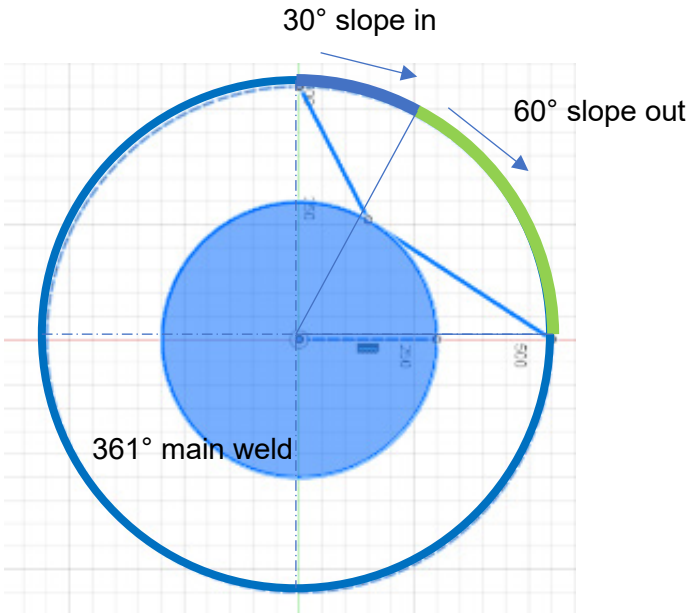

Fig. C-4: Welding positions for main weld including slope in and slope out

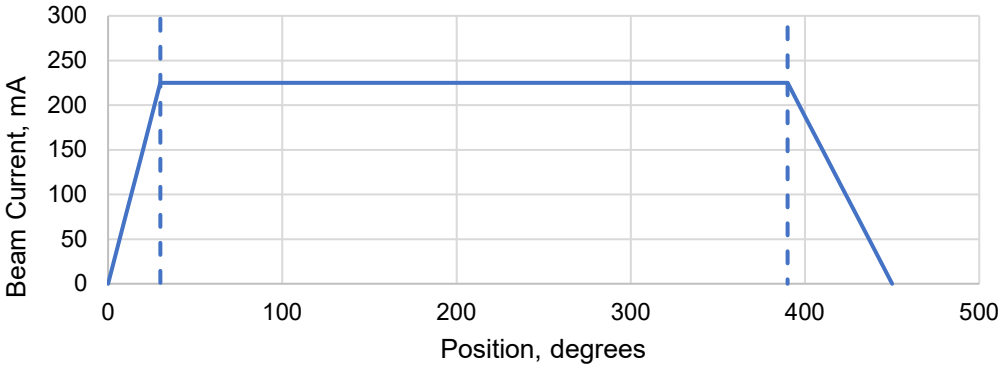

Fig. C-5: Welding current progression for main weld

C.11 Modifications to slope out conditions for improved weld quality

Slope out rate

Depending on the specific welding parameters used there is a possibility of flaws presenting in the slope down area of the weld. Typically, these flaws can be a mixture of root flaws caused by the changing weld power in the slope-out region, which influences the stability of the keyhole at the root of the weld.

The normal course of action is to reduce the rate of change in the beam power and hence smooth out the instabilities. This is accomplished via changes to the slope-out length, with longer slope-outs usually eliminating the issues. Initially a 60° slope-out is suggested as the normal 30° slope out may not prove long enough to avoid flaws in the thick section weld of the canister.

Focus control

Some flaws in the weld can also be caused by a change in the beam focus position as the power is reduced. The focus point of the weld moves and effectively widens the weld in certain areas. This can lead to solidification type cracks in the slope-out region where locally wider fusion zones are made at the root of the weld.

One remedy is to change the focus position with beam current as the weld is terminating. This tracking of beam focus position with power can remove the locally wider sections of the weld and remove the solidification cracks.

Deflection control

Most thick section EB welds are made with some form of beam deflection. This can be circular or linear but its objective is to widen the root area to help stabilise the keyhole and prevent keyhole collapse type flaws. These types of flaws are typically root porosity and cold shuts. The frequency and size of the beam deflection are the main parameters and the values used herein are those used before with good results. However, if increased root porosity is seen in the slope out region changes to the parameters can be made to improve the stability (increased frequency or larger amplitudes).

App. D Stress relaxation

This appendix contains the stress-strain curves determined from P245GH parent metal specimens at various temperatures and the data used to establish the stress relaxation model for FEA. Fig. D-1 below is limited to 2% strain to demonstrate the discontinuous yield behaviour up to 500 °C. This is considered in the construction of the Option 2 FAD.

A literature review was conducted to establish the necessary inputs for FEA activities within the framework of the testing programme. A total of 40 specimens were manufactured from a normalised P245GH plate with a thickness of 80 mm, a width of 500 mm and a length of 1 m to support tensile and stress relaxation tests

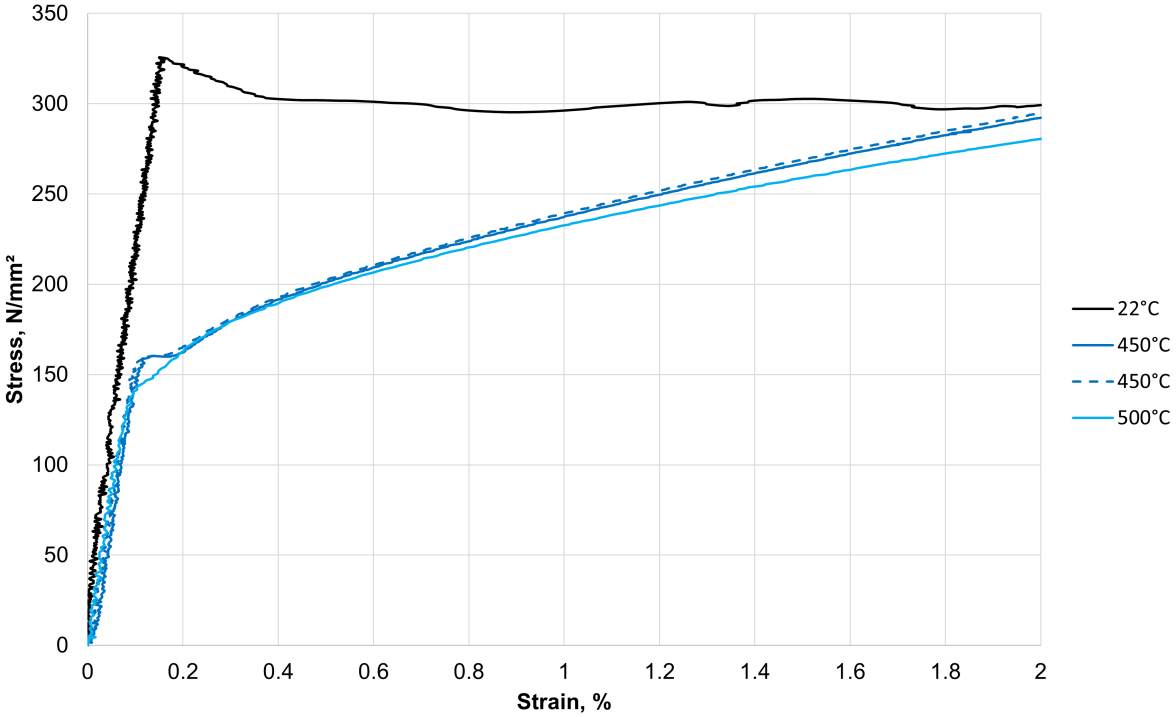

Fig. D-1: Elevated stress-strain curves capped at 2% strain

D.1 Detailed approach to establish stress relaxation properties

Identification of the viscoplastic strain rate ($\dot{\varepsilon}_0$), the quasi-static elastic limit (σ_{elss}), the parameter used to calibrate the variation of train rate with stress (σ_0), the coefficient describing the back stress due to dislocation density (β), the recovery parameter c_1, and the coefficient giving the variation of dislocation density with viscoplastic strain (c_2) could be achieved using a stress-strain curve obtained at a known strain rate. With a total strain rate of 1.4×10^{-5} s^{-1}, the variation of stress predicted by the model can be described as:

$$\dot{\sigma} = E\left[\dot{\varepsilon}_T - \dot{\varepsilon}_0 \sinh\left(\frac{\sigma - \sigma_{elss} - R}{\sigma_0}\right)\right] \quad [16]$$

where $\dot{\varepsilon}_T$ is the total strain rate, equal to 1.4×10^{-5} s^{-1} for the experimental data.

The model does not include a factor following the Arrhenius' law for dependency on temperature. This is because the different parameters do not vary with the temperature in the same way, so that obtaining a linear variation with temperature was not possible. Therefore, the parameters were calibrated from the tensile test data for each of the test temperatures from 450 °C to 600 °C.

Stress-strain curves were generated in Excel spreadsheets using an explicit formulation for the differential Equation [16]. Validation of the stress-strain curves was completed by comparing predicted and experimental relaxation curves:

- 600 °C shown in Fig. D-2;
- 575 °C shown in Fig. D-3;
- 550 °C shown in Fig. D-4;
- 500 °C shown in Fig. D-5;
- 450 °C shown in Fig. D-6.

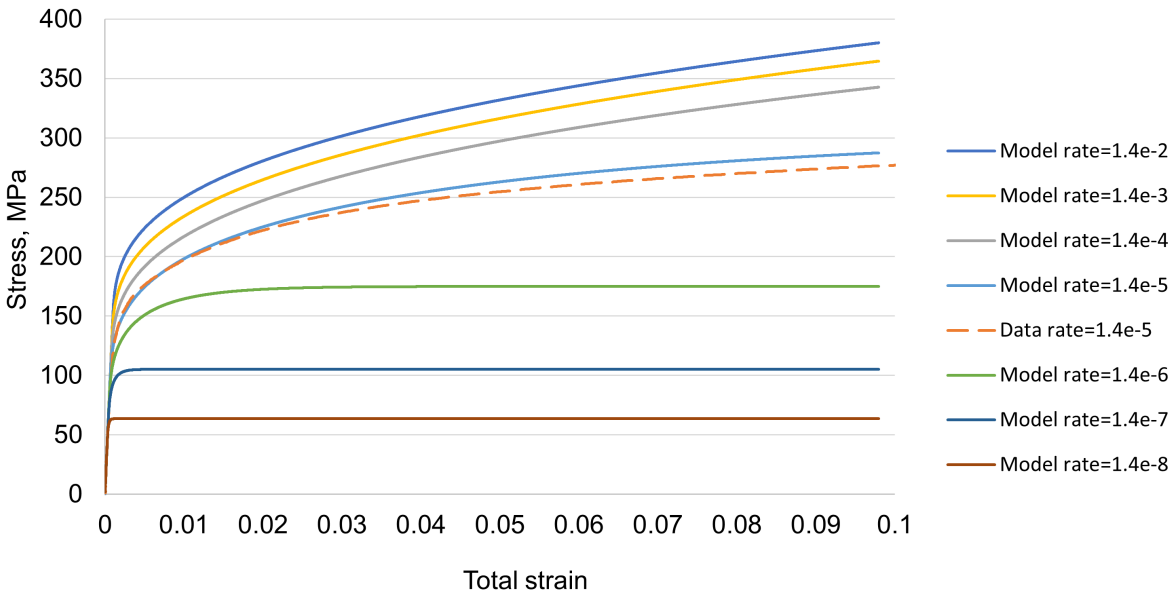

Fig. D-2: Stress-strain curves at different strain rates for 600 °C

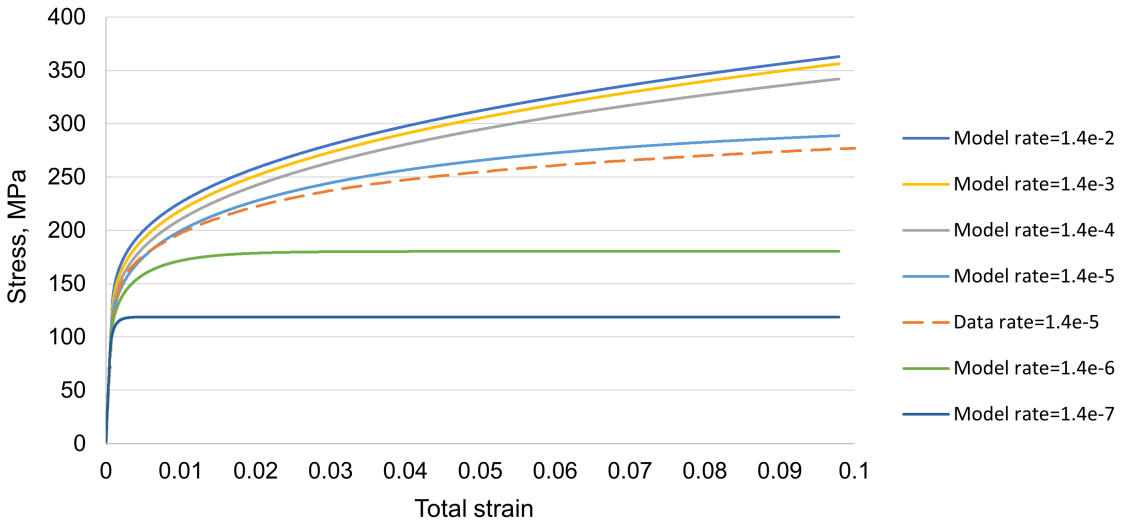

Fig. D-3: Stress-strain curves at different strain rates for 575 °C

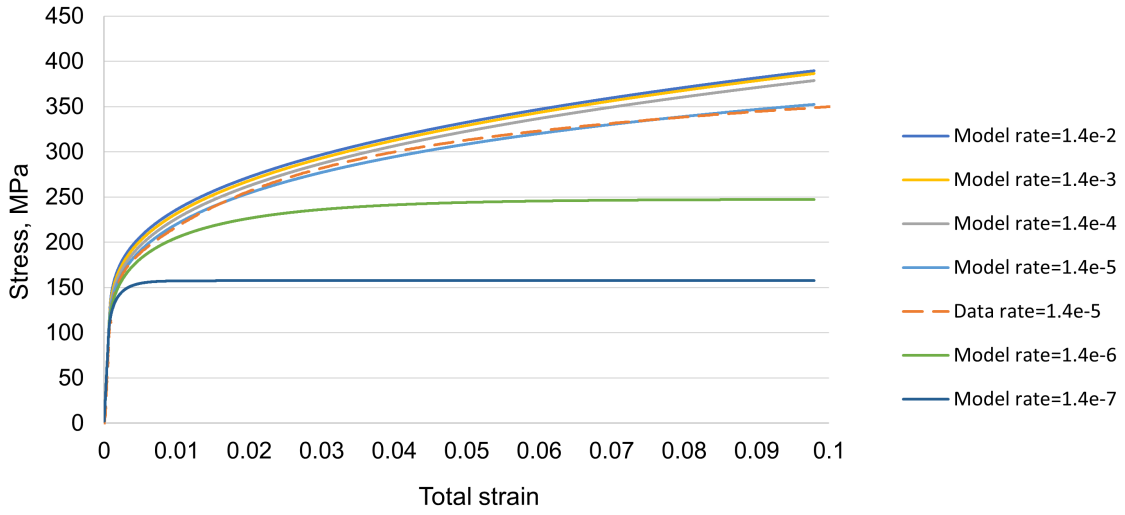

Fig. D-4: Stress-strain curves at different strain rates for 550 °C

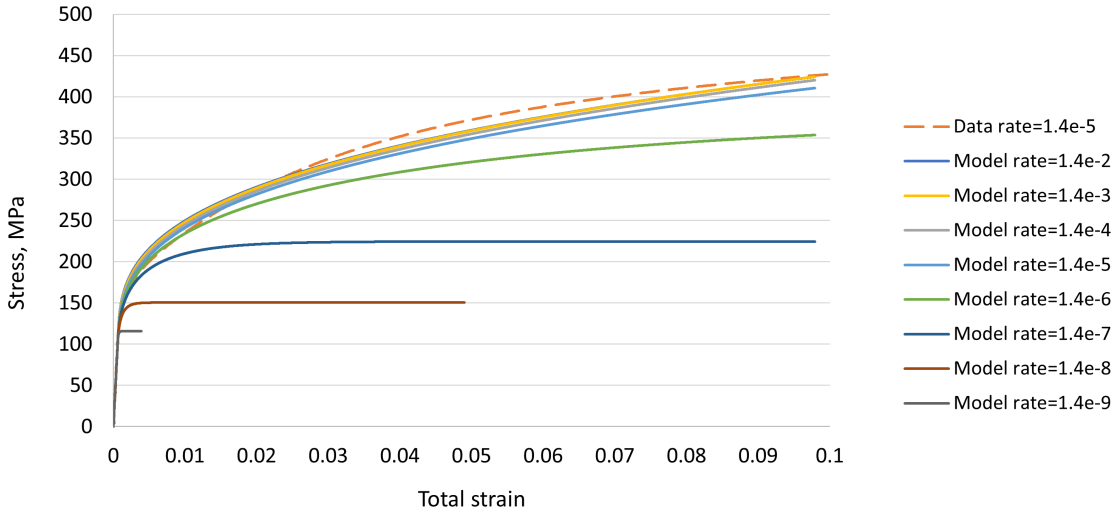

Fig. D-5: Stress-strain curves at different strain rates for 500 °C

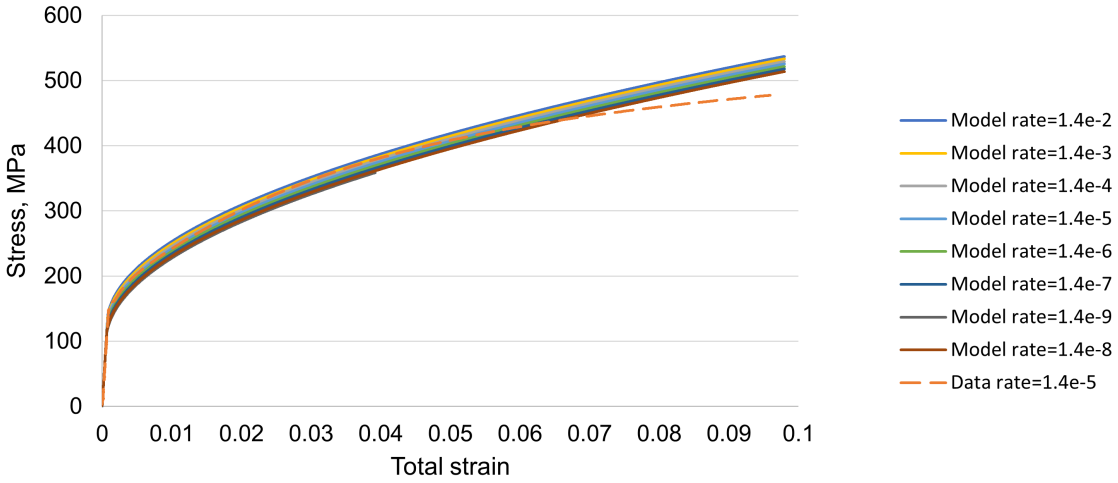

Fig. D-6: Stress-strain curves at different strain rates for 450 °C

The parameters determined from the Dyson & McLean (1990) model were then used to validate experimental stress relaxation behaviour at various temperatures, as seen in Fig. D-7 to Fig. D-11.

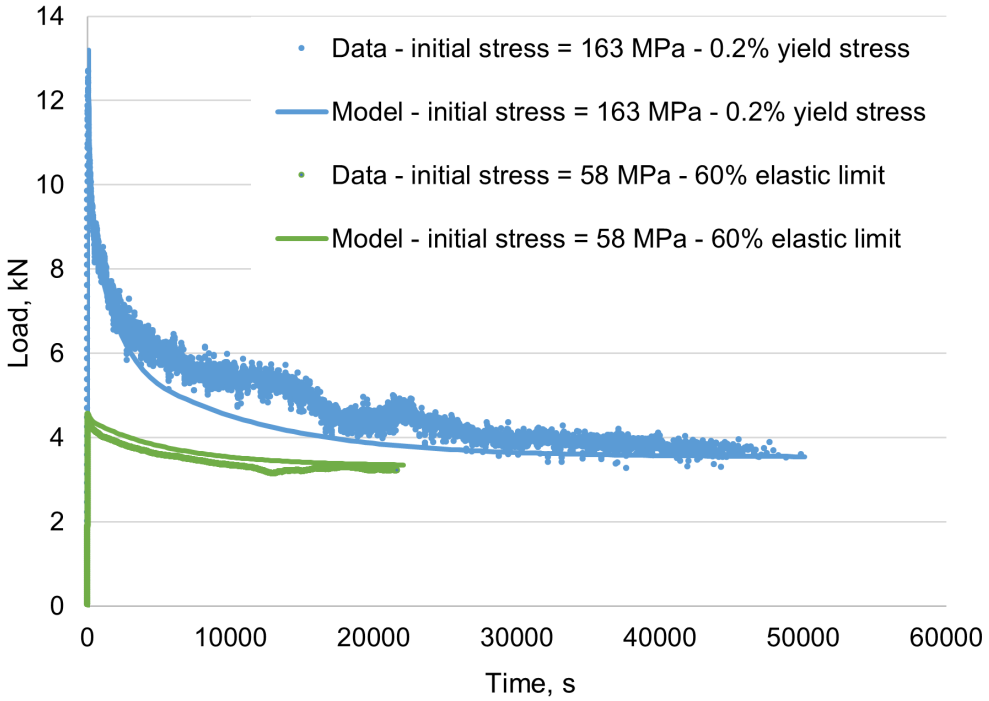

Fig. D-7: Experimental and predicted stress relaxation behaviour at 600 °C

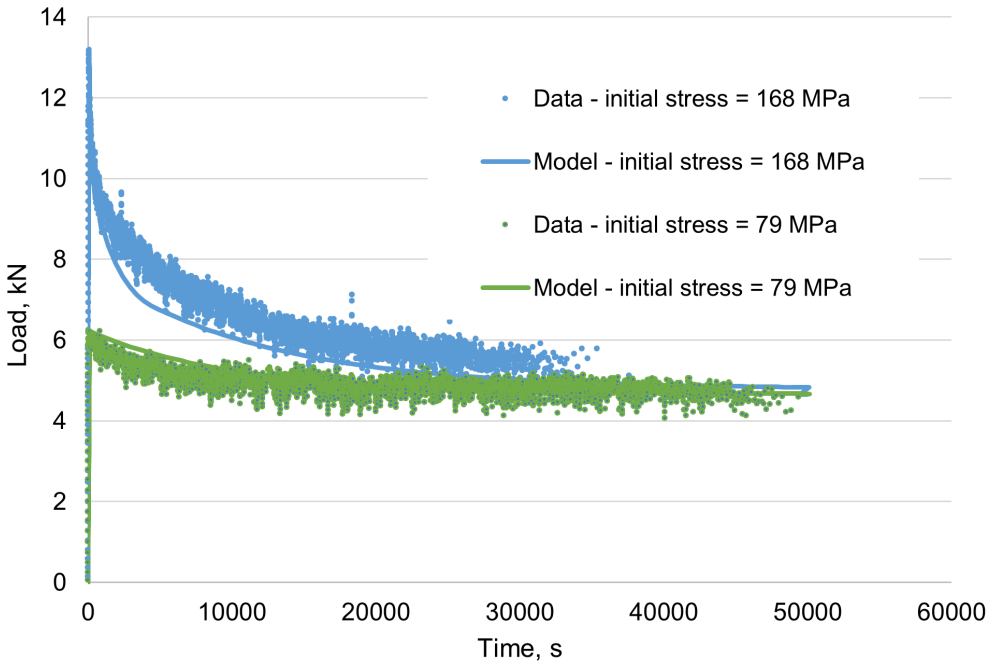

Fig. D-8: Experimental and predicted stress relaxation behaviour at 575 °C

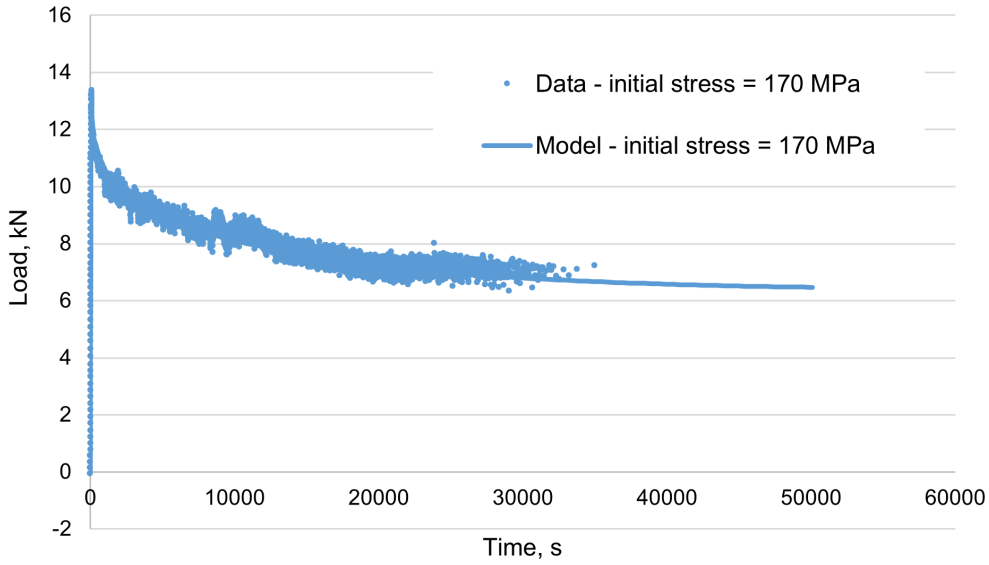

Fig. D-9: Experimental and predicted stress relaxation behaviour at 550 °C

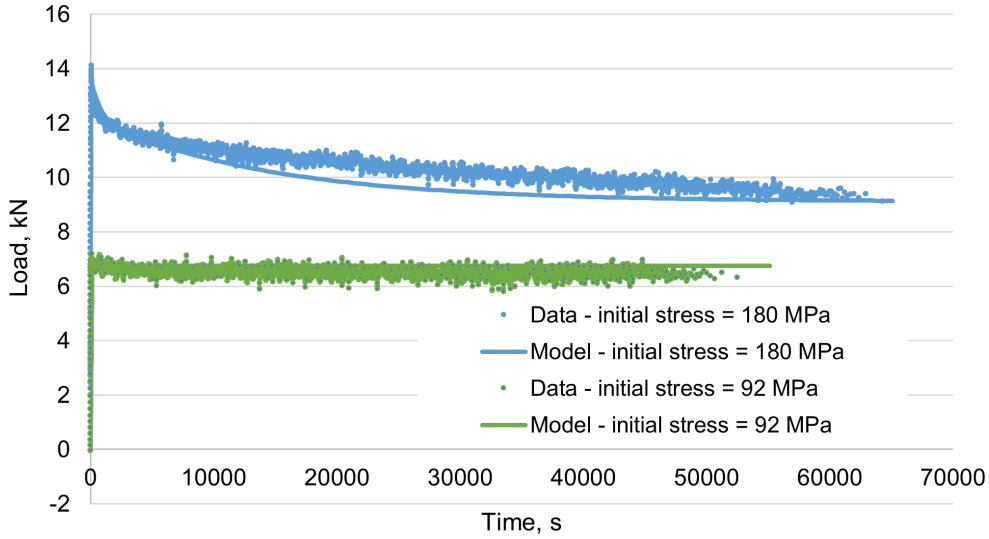

Fig. D-10: Experimental and predicted stress relaxation behaviour at 500 °C

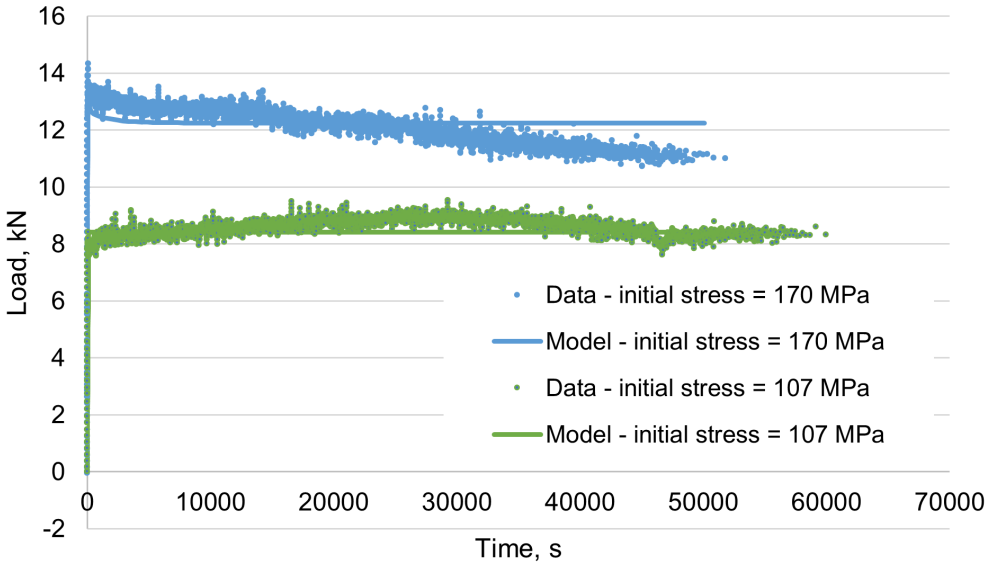

Fig. D-11: Experimental and predicted stress relaxation behaviour at 450 °C

The strain-rate-dependent behaviour was invoked in the PWHT analysis to predict the stress relaxation. It was also used in the welding process model so that the plastic behaviour was adapted to high strain rates during welding and low strain rates during cooling.

D.2 Stress relaxation model

The yield strength of materials is often given or referred to as the 0.2% proof strength. This value can be determined from tensile stress-strain curves, in particular when the onset of plasticity is not clear from the experimental data. For example, in BS 7910 (BSI 2019b), the estimate of residual stresses for the calculation of the fracture parameter is based on the 0.2% proof strength. However, in order to give an accurate description of the plastic behaviour of the material in FE analyses, it is better to use data from the onset of plastic yielding, starting from the elastic limit (when the material behaviour deviates from linearity), see Fig. D-12. In addition, constitutive equations usually employ the elastic limit rather than the 0.2% proof strength. The engineering stress-strain curves presented in Fig. D-13 were converted into true stress-strain curves using the equations below:

$$\varepsilon_{eng} = \Delta l / l_0 \quad [17]$$

$$\sigma_{eng} = F / S_0 \quad [18]$$

$$\varepsilon_{true} = ln(1 + \varepsilon_{eng}) \quad [19]$$

$$\sigma_{true} = \sigma_{eng}(1 + \varepsilon_{eng}) \quad [20]$$

The plastic strain was determined using:

$$\varepsilon_p = \varepsilon_{true} - \sigma_{true}/E \quad [21]$$

where ε_{eng} is the engineering strain, l_0 the initial gauge length, Δl the change in gauge length, σ_{eng} the engineering stress, F the applied load, S_0 the initial cross sectional area of the test specimen, ε_{true} the true strain, ε_p the plastic strain, and E the elastic modulus.

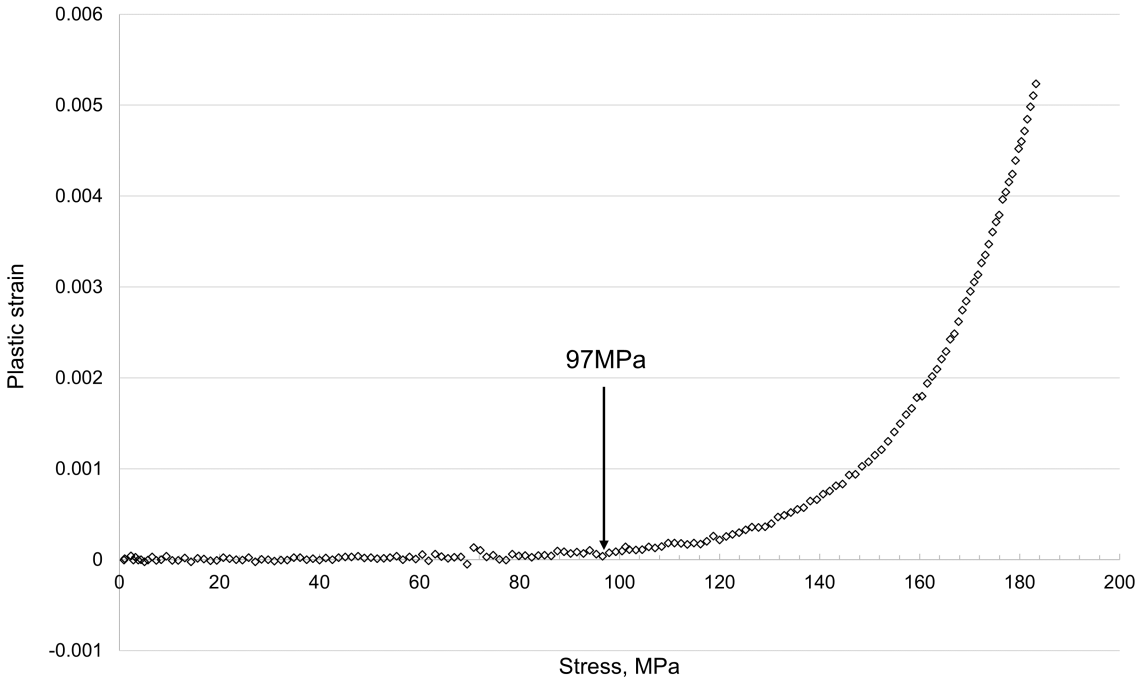

Fig. D-12: Determination of the rate-dependent elastic limit at 600 °C for a rate of 1.4×10^{-5} s^{-1}

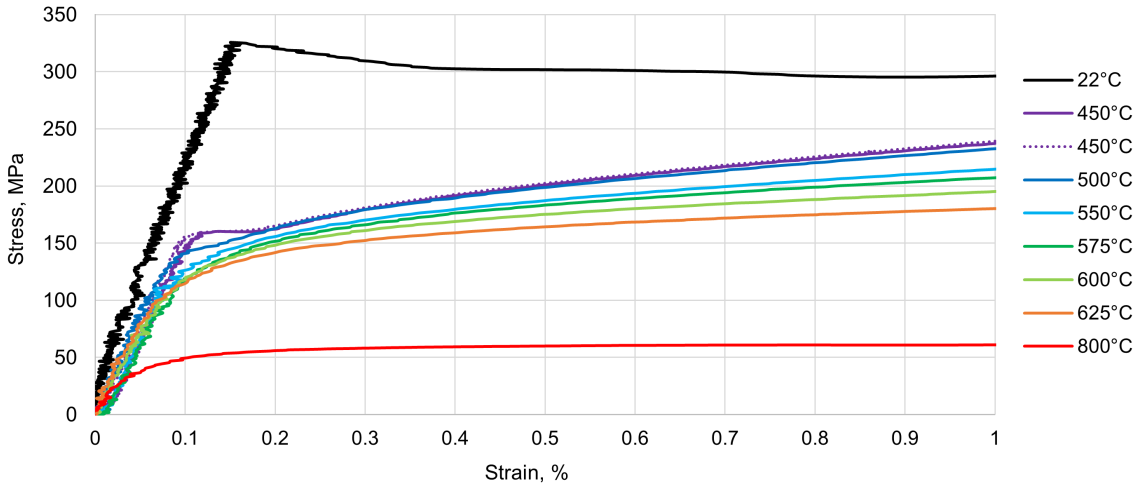

Fig. D-13: Stress-strain curves determined from tensile tests

Stress relaxation is activated by the same mechanisms as creep (mainly primary and secondary), since relaxation is the effect of viscoplasticity at a constant total strain:

$$\dot{\varepsilon}_e + \dot{\varepsilon}_{vp} = 0 = \frac{\dot{\sigma}}{E} + \dot{\varepsilon}_{vp}(\sigma) \text{ in uniaxial loading} \quad [22]$$

where $\dot{\varepsilon_{vp}}$ is the viscoplastic strain rate, $\dot{\varepsilon}_e$ is the elastic strain rate, σ is the applied von Mises stress, and E is the Young's modulus.

The secondary viscoplastic strain rate can, for example, be chosen to vary with stress following a single power law (Norton-Hoff), or to vary following an exponential or a hyperbolic sine function. It is usually observed from experiments that the secondary creep strain rate increases more with stress than with what would be predicted by a single power law. Therefore, the hyperbolic sine function is preferred to capture the variation of the secondary strain rate for a wider range of applied stress, as used by Dyson & McLean (1990).

In relaxation, part of the initial elastic strain applied during loading is converted into a permanent viscoplastic strain. The total strain applied during relaxation can therefore be small in magnitude; hence, it is more rigorous to account for the mechanism that causes primary creep, since it takes place at small strain as well. Primary creep can take place when the stress applied to a multi-phased material is partitioned between harder and softer phases until a homogeneous strain rate is achieved, or when the material is subject to strain hardening when the number of dislocations increases with plastic strain or when the precipitates make it more difficult for dislocations to move in the grains (Basoalto 2001).

It was assumed that strain hardening is caused by the increased number of dislocations from plasticity, generating a back-stress R that decreases the viscoplastic strain rate. The number of dislocations can also decrease with time due to the probability of dislocations of opposite sign to recombine and cancel each other out. This recovery is more likely to occur when the temperature and the number of dislocations are higher.

The equations used to describe the viscoplastic behaviour are as follows:

$$\dot{\varepsilon_{vp}} = \dot{\varepsilon_0} sinh\left(\frac{\sigma - \sigma_{elss} - R}{\sigma_0}\right) \quad [23]$$

$$R = \beta \sqrt[3]{\rho} \quad [24]$$

$$\dot{\rho} = c_2 \dot{\varepsilon_{vp}} - c_1 \rho^n \quad [25]$$

where:

ρ is a work-hardening parameter similar to a dislocation density

It is dependent on the parameter $\dot{\varepsilon}_0$. In more complex models, this parameter can vary with the density of mobile dislocations, which is a ratio of the total density of dislocations ρ. However, in the model used here, the no distinction is made between mobile and fixed dislocations, so that the parameter $\dot{\varepsilon}_0$ is identified as a whole. In theory, $\dot{\varepsilon}_0$ increases with temperature for identical values of the creep driving force (term in *sinh*).

σ is the applied von Mises stress.

σ_{elss} is the quasi-static elastic limit. This is the value of the stress where a tensile curve obtained at very low strain rate deviates from linearity.

R is the back-stress caused by work hardening. It depends on the density of fixed dislocations, on the parameter β, and is caused by the friction of the mobile dislocations in the network of fixed dislocations, slowing down the creep rate. Since no distinction between fixed and mobile dislocations is made in the model, R depends on the total density of dislocations ρ. For the same density of dislocation, the resistance of the dislocations network, and thus β, should decrease with temperature.

$c_2\dot{\varepsilon_{vp}}$ is the variation of the hardening parameter with viscoplastic strain. It is directly related to the increase in strain caused by the dislocations, since they are defects in the crystal lattice and lower the density. c_2 should be constant with temperature and the size of the defects caused by the dislocations is expected to vary with thermal expansion of the material.

$-c_1\rho^n$ is a recovery term, describing the variation of the hardening parameter with time. c_1 is related with the probability for two dislocations of opposite sign to combine and annihilate each other. c_1 should increase with temperature as the dislocations become more mobile. In the constitutive equation used, n has been set equal to 1.

In the Dyson & McLean (1990) model, the work hardening variable R varies with $\sqrt{\rho}$. However, it was found when identifying the parameters, that using $\sqrt[3]{\rho}$ gave a better prediction of the behaviour when the material starts yielding, which can be important for the modelling of relaxation, as the viscoplastic strain is small (lower that 1%).

When this model is applied to describe creep, the initial value of the hardening parameter is set as an initial density of dislocations when the material has not experienced work hardening, assumed to be in the order of 10^9 dislocations per cm^2 in steels (Kang & Kim 2019). When the load is applied, the hardening parameter increases with the viscoplastic strain, in turn increasing the corresponding back stress and causing the viscoplastic strain rate to decrease. This is what happens when primary creep is observed in a creep test, where the increase of creep strain is gradually lowered until a constant secondary strain rate is achieved. In the model, the secondary strain rate corresponds to the hardening parameter, reaching an asymptotic value when its increase due to the viscoplastic strain is balanced by its decrease due to recovery. In this case, the variation of hardening parameter ρ in Equation [25] is zero.

During loading of a relaxation test, or prior to PWHT of a structural weld, the initial strain at the beginning of relaxation is not fully elastic. This is particularly the case for PWHT when the residual stresses are caused by strain hardening taking place during cooling, and when relaxation tests are carried out with a high initial stress. For these cases, the value of the hardening parameter is higher than 10^9 at the beginning of the relaxation step.

When the material is in the viscoplastic regime, the Dyson & McLean (1990) model should be able to predict stress-strain curves, creep, and relaxation. Identification of the six parameters $(\dot{\varepsilon}_0, \sigma_{elss}, \sigma_0, \beta, c_1, c_2)$ could be achieved using a stress-strain curve obtained at the known strain rate. Knowing that the experimental stress-strain curve was obtained using a total strain rate of 1.4×10^{-5} s^{-1}, the variation of stress predicted by the model can be deduced from Equation [9] and described as:

$$\dot{\sigma} = E\left[\dot{\varepsilon}_T - \dot{\varepsilon}_0 \sinh\left(\frac{\sigma-\sigma_{elss}-R}{\sigma_0}\right)\right] \quad [26]$$

where $\dot{\varepsilon}_T$ is the total strain rate, equal to 1.4×10^{-5} s^{-1} for the experimental data.

Stress-strain curves were generated in Excel spreadsheets using an explicit formulation for the differential Equation [27]. The six parameters were identified in order to obtain a good match between the predicted stress-strain curve and the experimental data. Then, stress-strain curves were generated at different strain rates to create a database for the rate-dependent plasticity model in Abaqus. Validation was completed by comparing predicted and experimental relaxation curves at 450 °C, 500 °C, 550 °C, 575 °C and 600 °C.

The parameters identified for each of the six tests are listed in Tab. D-1 below. Note that the value of the parameter β at 450 °C is significantly different compared to the values at the higher temperatures. This is because the work hardening R varies with $\sqrt{\rho}$ at 450 °C rather than with $\sqrt[3]{\rho}$. The coefficient β is given in MPa.cm^m with m equal to either 2 or 3.

Tab. D-1: Values of $\dot{\varepsilon}_0, \sigma_0, \sigma_{elss}, \beta, c_1, c_2$ at each temperature of interest

Temperature [°C]	$\boldsymbol{\sigma_{elss}}$ [MPa]	$\boldsymbol{\sigma_0}$ [MPa]	$\boldsymbol{\dot{\varepsilon}_0}$ [s^{-1}]	$\boldsymbol{\beta}$ [MPa $cm^{-1/m}$]	$\boldsymbol{c_1}$	$\boldsymbol{c_2}$ [$cm^2\,s^{-1}$]
450	104	1.7	4.0×10^{-9}	2.75×10^{-4}	0.0	2.3×10^{-13}
500	87	1.4	8.0×10^{-9}	2.30×10^{-2}	2.0×10^{-5}	2.8×10^{-13}
550	74	2.4	4.0×10^{-9}	2.02×10^{-2}	8.0×10^{-5}	2.8×10^{-13}
575	56	3.7	3.0×10^{-9}	1.80×10^{-2}	2.3×10^{-4}	2.8×10^{-13}
600	25	7.5	2.8×10^{-9}	1.73×10^{-2}	2.0×10^{-4}	2.7×10^{-13}

The parameters determined from the Dyson & McLean (1990) model were then used to validate experimental stress relaxation behaviour at various temperatures.

App. E Material properties for FE simulations

Appendix E contains the material properties used in the FE simulations undertaken as part of this work.

The thermal model of the EB weld required the thermal properties of the canister, given in Tab. E-1 to Tab. E-3. The thermal material properties (e.g., thermal conductivity and specific heat capacity) of similar grades of steel to the canister material were used. These properties were compared to other sources (Fratini et al. 2012, Plansee Composite Materials 2024, Piekarska et al. 2011, Piekarska et al. 2012) and were confirmed to be within the range found in the literature.

The mechanical models, used to obtain the residual stresses in the as-welded state and after PWHT, used the mechanical properties (i.e. the elastic, plastic and thermal expansion coefficient) displayed in Tab. E-4 to Tab. E-5. The elastic and plastic properties were obtained from extensive material testing, see App. D.

The PWHT simulation required the thermal properties for the internal components of the canisters. For the SF models, the basket was assigned the same material properties as the canister. The spent fuel was assigned the properties of uranium dioxide (see Tab. E-6, Tab. E-7 and Tab. E-8). These properties were compared to literature (Popov et al. 2000) and found to be comparable. Additional material properties of the stainless steel handles of the FAs, the flasks containing the vitrified waste and the glass are shown in Tab. E-9 to Tab. E-20.

Tab. E-1: Thermal conductivity of the canister material used in the thermal weld simulation and the PWHT models for the SF and RP-HLW disposal canisters

Temperature [°C]	**Thermal conductivity** [mW/mm.K]
25	54
125	51
225	47
1,000	26.5
1,477	33.5
1,502	34
1,527	34

Tab. E-2: Specific heat capacity of the canister material used in the thermal weld simulation and the PWHT models for the SF and RP-HLW disposal canisters

Temperature [°C]	**Specific heat** [mJ/tonne.K]
150	519,000,000
200	536,000,000
250	553,000,000
350	595,000,000
400	595,000,000
450	662,000,000
500	662,000,000
550	754,000,000
600	754,000,000
850	846,000,000

Tab. E-3: Other material properties of the canister material used in the thermal weld simulation and the PWHT models for the SF and RP-HLW disposal canisters

Material property	
Density (tonne/mm^3)	7.86×10^{-9}
Latent heat of solidification (mJ/tonne)	2.70×10^{11}
Solidus temperature (°C)	1,477
Liquidus temperature (°C)	1,527

Tab. E-4: Elastic mechanical properties of the canister material obtained from material testing (App. D)

Temperature [°C]	**Young's modulus** [MPa]	**Poisson's ratio**
22	205,000	0.3
300	188,000	0.3
450	173,000	0.3
500	167,000	0.3
550	161,000	0.3
575	157,000	0.3
600	153,000	0.3
800	115,228	0.3
1,000	61,800	0.3
1,150	9,680	0.3

Tab. E-5: Thermal expansion coefficient of the canister material
(BSI 2024a)

Temperature [°C]	**Expansion coefficient** [mm/(mm.°C)]
20	6×10^{-6}
100	1.25×10^{-5}
200	1.29×10^{-5}
300	1.33×10^{-5}
400	1.37×10^{-5}
500	1.41×10^{-5}
600	1.45×10^{-5}
700	1.49×10^{-5}
750	1.51×10^{-5}
751	1.5×10^{-5}
800	1.41×10^{-5}
860	1.31×10^{-5}
900	1.34×10^{-5}
1,000	1.41×10^{-5}
1,100	1.46×10^{-5}
1,200	1.51×10^{-5}
1,527	1.5×10^{-8}

Tab. E-6: Thermal conductivity of the SF used in the PWHT models for SF-BWR and SF-PWR disposal canisters

Temperature [°C]	**Thermal conductivity** [mW/mm.K]
250	3
500	2.65
750	2.5
1,000	2.2

Tab. E-7: Specific heat capacity of the SF used in the PWHT models for SF-BWR and SF-PWR disposal canisters

Temperature [°C]	**Specific heat** [mJ/tonne.K]
26.85	236,580,000
126.85	264,320,000
226.85	281,530,000
326.85	292,990,000
426.85	300,710,000
526.85	305,840,000
626.85	309,180,000
726.85	311,400,000

Tab. E-8: Density of the SF used in the PWHT models for SF-BWR and SF-PWR disposal canisters

Material property	**Corrected density** [tonne/mm^3]
BWR	2.70×10^{-9}
PWR	2.96×10^{-9}

Tab. E-9: Thermal conductivity of the AISI 304L stainless steel handle used in the PWHT models for the SF-BWR disposal canister

The properties were averaged from Kim (1975), Luo et al. (2020), Geng et al. (2019) and Filoni & Rocchini (1987).

Temperature [°C]	**Thermal conductivity** [mW/mm.K]
25	15.05
200	18.4
400	20.46
600	22.59

Tab. E-10: Specific heat capacity of the AISI 304L stainless steel handle used in the PWHT models for the SF-BWR disposal canister

The properties were averaged from Kim (1975), Luo et al. (2020), Geng et al. (2019) and Filoni & Rocchini (1987)

Temperature [°C]	**Specific heat** [mJ/tonne.K]
25	496,420,000
200	526,330,000
400	561,490,000
600	601,780,000

Tab. E-11: Density of the AISI 304L stainless steel handle used in the PWHT models for the SF-BWR disposal canister

The properties were averaged from Kim (1975), Luo et al. (2020), Geng et al. (2019) and Filoni & Rocchini (1987)

Material property	
Density (tonne/mm^3)	7.83×10^{-9}

Tab. E-12: Thermal conductivity of the AISI 321 stainless steel handle used in the PWHT models for the SF-PWR disposal canister

The properties were averaged from Perović et al. (1995), Schwartzberg et al. (1970), Ho & Chu (1977) and thyssenkrupp Materials (UK) (2017)

Temperature [°C]	**Thermal conductivity** [mW/mm.K]
25	14.6
200	15.7
400	18.8
600	21.8

Tab. E-13: Specific heat capacity of the AISI 321 stainless steel handle used in the PWHT models for the SF-PWR disposal canister

The properties were averaged from Perović et al. (1995), Schwartzberg et al. (1970), Ho & Chu (1977) and thyssenkrupp Materials (UK) (2017)

Temperature [°C]	**Specific heat** [mJ/tonne.K]
20	496,000,000
100	503,000,000
300	544,000,000
500	574,000,000
600	588,000,000

Tab. E-14: Density of the AISI 321 stainless steel handle used in the PWHT models for the SF-PWR disposal canister

The properties were averaged from Perović et al. (1995), Schwartzberg et al. (1970), Ho & Chu (1977) and thyssenkrupp Materials (UK) (2017)

Material property	
Density (tonne/mm^3)	8.59×10^{-9}

Tab. E-15: Thermal conductivity of the glass used in the PWHT models for the RP-HLW disposal canister

Temperature [°C]	**Thermal conductivity** [mW/mm.K]
100	1.22
200	1.3
300	1.37
400	1.49

Tab. E-16: Specific heat capacity of the glass used in the PWHT models for the RP-HLW disposal canister

Temperature [°C]	**Specific heat** [mJ/tonne.K]
100	975,000,000
200	1,050,000,000
300	1,200,000,000
400	1,275,000,000

Tab. E-17: Density of glass used in the PWHT models for the RP-HLW disposal canister

Material property	
Density (tonne/mm^3)	2.67×10^{-9}

Tab. E-18: Thermal conductivity of the AISI 309 stainless steel flasks used in the PWHT models for the RP-HLW disposal canister

The thermal properties were averaged from Barth et al. (2020) and manufacturing datasheets from Sirius and Rolled alloys.

Temperature [°C]	**Thermal conductivity** [mW/mm.K]
19.85	12.79
119.85	14.38
219.85	16.37
319.85	17.56
419.85	18.75
519.85	19.94
619.85	21.17
648.85	21.59

Tab. E-19: Specific heat capacity of the AISI 309 stainless steel flasks used in the PWHT models for the RP-HLW disposal canister

The thermal properties were averaged from Barth et al. (2020) and manufacturing datasheets from Sirius and Rolled alloys.

Temperature [°C]	**Specific heat** [mJ/tonne.K]
20	4.88×10^{8}
100	5.03×10^{8}
200	5.23×10^{8}
400	5.64×10^{8}
600	6.06×10^{8}
800	6.47×10^{8}

Tab. E-20: Density of the AISI 309 stainless steel flasks used in the PWHT models for the RP-HLW disposal canister

The thermal properties of 309 were averaged from Barth (2020) and manufacturing datasheets from Sirius and Rolled alloys.

Material property	
Density (tonne/mm^3)	7.85×10^{-9}

App. F Inputs and results of ECA calculations

This appendix summarises the inputs and results of ECA calculations. The two main categories include:

- Long term structural integrity assessment, in which critical flaw sizes are established for each canister design and flaw type; and
- Demonstration of structural integrity performance assuming a flaw with fixed sizes that can remain in the canisters after inspection.

The ECA cases to determine critical flaw sizes included in this report are summarised in Tab. F-1, and the critical flaw sizes are illustrated in Fig. F-1 to Fig. F-4. Fig. F-1 illustrates the critical surface flaw sizes in SF canisters. Fig. F-2 illustrates the critical embedded flaw sizes with a ligament greater than 2 mm in SF canisters. Fig. F-3 illustrates the critical surface flaw sizes in RP-HLW canisters. Fig. F-4 illustrates the critical embedded flaw sizes with a ligament greater than 2 mm in RP-HLW canisters.

Tab. F-1: Critical flaw size ECA calculation cases

ECA case	Canister type	Loading	Flaw type
1-SF-surface	SF	Long term	Surface
1-SF-long-surface			Long surface
1-SF-embedded			Embedded with p = 3 to 21 mm
2-HLW-surface	RP-HLW		Surface
2-HLW-long-surface			Long surface
2-HLW-embedded			Embedded with p = 3 to 14 mm

Demonstration of structural integrity performance assuming the largest flaws missed by inspection is presented as follows. Two different flaw sizes are considered here:

- 1 × 10 mm on the OD
- 4 × 15 mm on the ID

Right after completion of closure weld and PWHT, the canisters will not experience any primary stresses. In the case of secondary stress acting alone, consistent with R6, $K_{\mathrm{r}}^{\mathrm{P}}$ (fracture ratio of applied primary K value to K_{mat}, where K_{mat} is the material fracture toughness measured by stress intensity factor) and ρ are set to zero, or V to unity, and the assessment then uses $K_{\mathrm{J}}^{\mathrm{S}}$ (elastic-plastic stress intensity factor) as determined using Annex R of BS 7910 (BSI 2013). Hence, the contribution to K_{r} from secondary stress, $K_{\mathrm{r}}^{\mathrm{S}}$ is derived from $K_{\mathrm{J}}^{\mathrm{S}}/K_{\mathrm{mat}}$ in Clause 7.

The steps for determining the effective elastic-plastic stress intensity factor, $K_{\mathrm{J}}^{\mathrm{S}}$, for secondary loading alone, are given as follows:

$$K_{\mathrm{J}}^{\mathrm{S}} = \left(\frac{a_{\mathrm{eff}}}{a}\right)^{0.5} K_{\mathrm{I}}^{\mathrm{S}}(a) \qquad [28]$$

Equation above modifies the elastic stress intensity factor, K_I^S, based on the calculated plastic zone size where the effective crack size a_{eff} is given by:

$$a_{eff} = a + \left(\frac{1}{2\pi\beta}\right)\left(\frac{K_I^S(a)}{\sigma_Y}\right)^2 \quad [29]$$

where:

β =1 for plane stress

β =3 for plane strain

Note that a_{eff} may exceed the section thickness in some cases.

This route leads to values of K_J^S that are greater than K_I^S and hence it could produce conservative results in cases where it is judged that K_J^S is less than K_I^S. That is where significant plastic relaxation of stress occurs.

The assessment point $K_r = K_J^S/K_{mat}$ is established according to the procedure above.

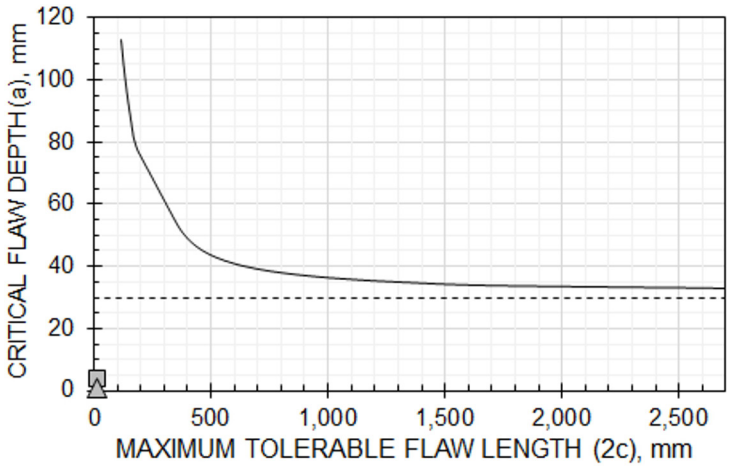

Fig. F-1 Modified critical surface flaw sizes (solid line) and critical long surface flaw size (dashed line) for SF disposal canisters

The square symbol represents the inner surface detection limit and the triangle symbol, the outer surface detection limit.

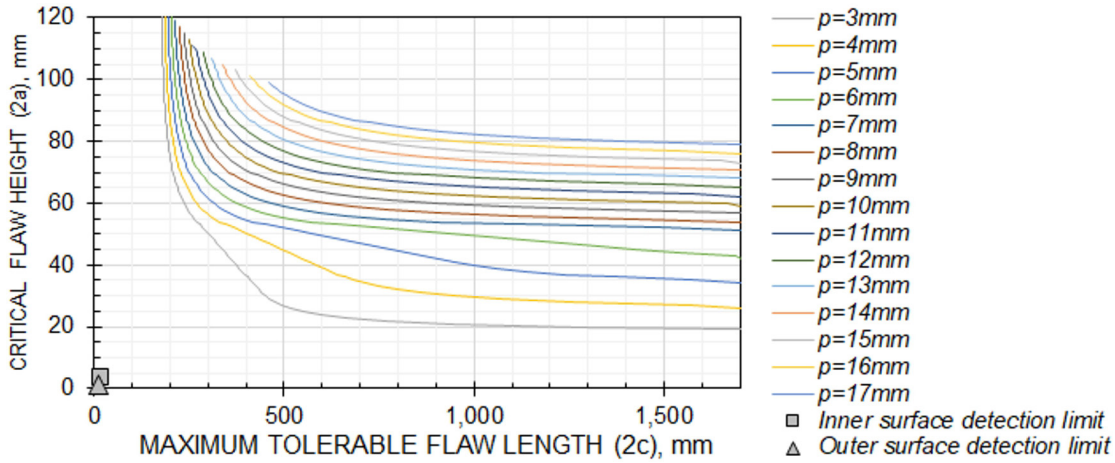

Fig. F-2 Modified critical embedded flaw sizes, with ligaments ≥ 3 mm for SF disposal canisters

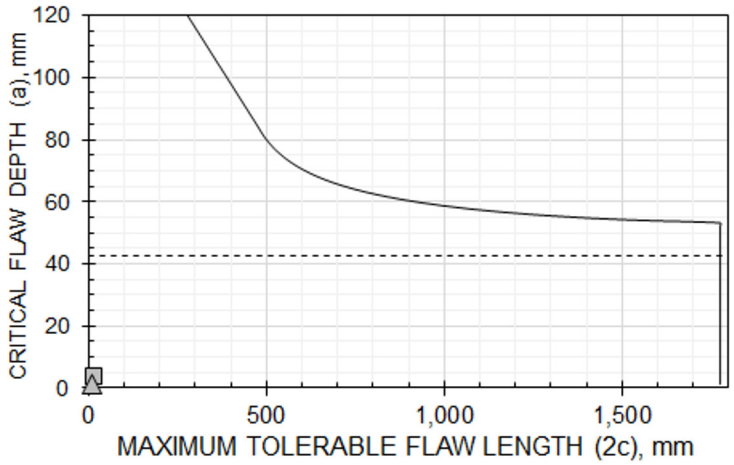

Fig. F-3 Modified critical surface flaw sizes (solid line) and critical long surface flaw size (dashed line) for RP-HLW disposal canisters

The square symbol represents the inner surface detection limit and the triangle symbol, the outer surface detection limit.

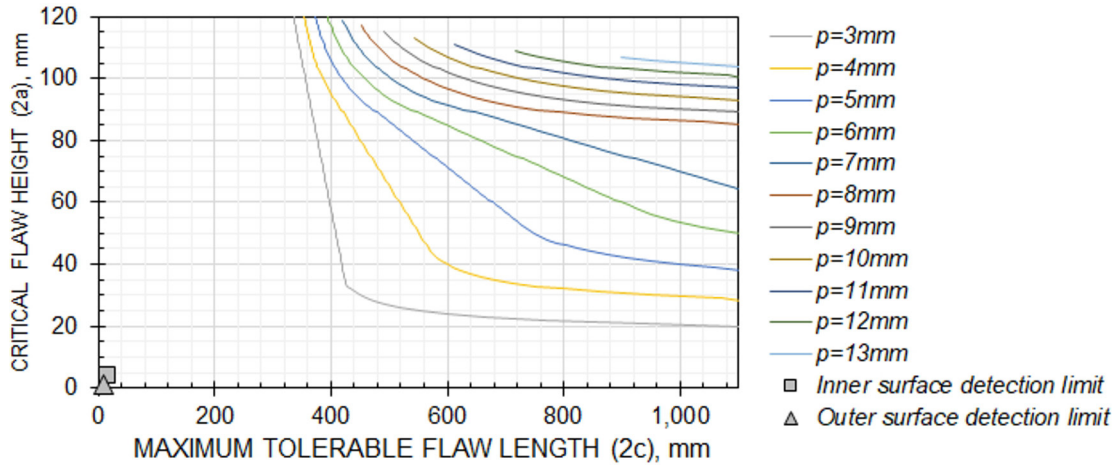

Fig. F-4 Modified critical embedded flaw sizes, with ligaments ≥ 3 mm for RP-HLW disposal canisters